Characterisation of Dosimetry in Electron Radiotherapy under different Bolus Applications.

Lindsay James Tremethick

BApp.Sc. (University of South Australia)

A thesis submitted in partial fulfilment of the requirements for the degree of

Master of Applied Science (Medical and Health Physics)

School of Applied Sciences,

College of Science, Engineering and Health

RMIT University

Melbourne, Australia

March 2012

Declaration

Except where acknowledgements are made in the text, all work described in this thesis is that of the author.

This thesis has not previously been submitted in whole or in part for any academic award to any Institute or University.

The content of this thesis is the result of work carried out since the official commencement date of the approved research program.

Lindsay J. Tremethick

Acknowledgement

The following thesis would not have been completed if not for the support and constant encouragement of many others.

I would like to thank my many supervisors for what may have been one of your most frustrating students. Firstly Jamie Trapp for listening to my generalised thoughts and ideas of a possible Masters topic and believing them suitable, starting me along what has been a long and at times almost torturous path.
The departure of Jamie from RMIT lumbered Peter Johnston and Rick Franich with me as an additional student to their already full student supervision lists. Despite what must have been an imposition on their personal time they afforded me unconditional support whenever I requested assistance.
Peter Johnston's departure from RMIT landed me squarely and solely on Rick Franich's now excessively bloated student supervision list. I certainly appreciated Rick's continued support and also the provision of appropriate advice when for personal reasons I opted to exercise an initial period of Leave of Absence which became extended through unavoidable circumstances. It was only through Rick's tireless efforts that my forced extended Leave of Absence, and what was then an “in limbo” Masters programme, was resurrected by his approach to Moshi Geso to act as my supervisor. Without Moshi's generous acceptance of me as a student and the provision of his time, often at my request, along with his advice and direction my thesis may not have commenced.

I also wish to thank my employer Radiation Oncology Victoria (now part of GenesisCare) and in particular Bill Patterson for the constant support provided in both time and resources. Bill has provided many hours of his personal time both proof reading my writings and supporting my efforts. Bill's constant reminders of the ultimate deadline, his time spent listening to, and providing suggestions for my, at times, hair brained ideas, and his assistance with some of my day to day duties has aided me immensely to complete the thesis.

Finally I must thank my wife and children for putting up with me during the course of this

Masters particularly in the last year. I know at times I must have been like a “bear with a sore head”.

To my wife Anne, who must have been bored to almost tears reading many drafts of my writings and repeatedly corrected the same grammatical errors plus finding those spelling errors a word processor never does, I owe you many thanks. To my boys Samuel and Edward that is the end of study for me!

Table of Contents

Declaration....ii

Acknowledgement....iii

Illustration Index....vii

Index of Tables....x

0. ABSTRACT....1

1. INTRODUCTION....2

1.1 Radiotherapy....2
1.2 Electron Interactions....7
1.2.1 Stopping Powers....8
1.3 Electron Beam Therapy....11
1.4 Modulated Electron Radiotherapy....12
1.5 Aims....14
2 METHODOLOGICAL DESIGN....15

2.1 Equipment & General Data Collection Conditions....15
2.2 Clinical Electron Beam Characteristics....19
2.2.1 Central Axis Percentage Depth Dose....22
2.2.1.1 PDD Dependence on Energy....23
2.2.1.2 PDD Dependence on Field Size....25
2.2.1.3 PDD Dependence on Angle of incidence....25
2.3 Ionisation Chambers....27
2.3.1 Thimble Chambers....29
2.3.2 Parallel Plate Chambers....30
2.4 Data Collection....32
2.4.1 Depth Ionisation to Depth Dose Conversion....34
2.5 Specific Measurement Conditions....35
2.5.1 Effective Point of Measurement (EPOM)....37
2.6 Bolus Materials....40
2.7 Smoothing Algorithms....44
3. RESULTS....46

3.1 Beam Quality Comparison....47
3.2 Spatial resolution as a function of chamber IC-15, CC-04 and PPC-40(Roos Type)....48
3.3 Bolus on the Applicator....51
3.3.1 Full Bolus....53
3.3.1.1 Full Bolus Perspex....54
3.3.1.2 Full Bolus Teflon....56
3.3.1.3 Full Bolus Aluminium....58
3.3.2 Partial Bolus....60
3.3.2.1 Partial Bolus Perspex....61
3.3.2.2 Partial Bolus Teflon....63
3.3.2.3 Partial Bolus Aluminium....65
3.3.3 Strip Bolus....67

3.3.3.1 Strip Bolus Teflon....68
3.3.4 Higher Z Grids....70
3.3.4.1 Aluminium Mesh....71
3.3.4.2 Stainless Steel Mesh....73
3.4 Bolus on Surface....75
3.4.1 Perspex....76
3.4.2 Teflon....77
4. DISCUSSION....78
4.1 Beam Quality....78
4.3 Bolus on Applicator....80
4.3.1 Full Bolus....80
4.3.2 Partial Bolus....83
4.3.3 Strip Bolus....85
4.3.4 Higher Z Grids....86
4.4 Bolus on Surface....88
5. CONCLUSION....90
6. BIBLIOGRAPHY....91
APPENDIX....100

Illustration Index

Illustration 1: Electron Interactions a) excitation, b) ionisation, c) bremsstrahlung, d) characteristic radiation production (Khan, 1991).....7
Illustration 2: Stopping Power – Collisional/Radiative (physics.nist.gov/PhysRefData/Star/Text/ESTAR.html).....9
Illustration 3: Depth–dose curves in water for electron beams,(solid curves), cf depth–dose curves for5 MV (small-dashed line) and 22 MV (long-dashed line) x-ray beams (Farmer, 1962, Hogstrom and Almond, 2006).....11
Illustration 4: Varian 21EX Linac (Image courtesy of Varian Medical Systems, Inc. All rights reserved.).....15
Illustration 5: 3D Blue Phantom, “water tank” (Wellhöfer, IBA Dosimetry, Germany).....16
Illustration 6: Linac Axis (Emma Viviers - www.medphysfile.com).....17
Illustration 7: 9MeV 10x10cm Field Size (Podgorsak, 2005).....20
Illustration 8: 20 MeV 10x10 cm Field (Podgorsak, 2005).....20
Illustration 9: Electron PDD Curve (Podgorsak, 2005).....21
Illustration 10: PDD: 6MV photon, 8MeV electron 22
Illustration 11: PDI Electron beams Field Size 15x15cm.....23
Illustration 12: PDD 20MeV by Field Size (Podgorsak, 2005).....25
Illustration 13: PDD at various beam angles (a) 9MeV (b) 15MeV (Podgorsak, 2005).....26
Illustration 14: Simplified Ionisation Chamber (Wikipedia).....27
Illustration 15: Farmer Chamber (Podgorsak, 2005).....29
Illustration 16: Parallel Plate Chamber (IAEA).....31
Illustration 17: IC-15 (CC-13) Compact Ionisation Chamber (Wellhöfer IBA Dosimetry Germany)…32
Illustration 18: CC-04 Compact Ionisation Chamber (Wellhöfer, IBA Dosimetry, Germany).....33
Illustration 19: Water Surface Alignment.....36
Illustration 20: CC-04 Chamber Dimensions.....39
Illustration 21: Image of Varian electron applicator and insert (maestro-research.org).....51
Illustration 22: Full Bolus on LMA insert Set up.....53
Illustration 23: Partial Bolus on LMA insert Set up.....60
Illustration 24: Example Inplane Scan from raw data.....60
Illustration 25: Strip Bolus on LMA insert Set up.....67
Illustration 26: Example inplane scan from raw data.....67
Illustration 27: Mesh (grid) Bolus on LMA insert Set up.....70
Illustration 28: 9MeV Thesis and Commissioning Depth Ionisation for Table 7.....102
Illustration 29: 20MeV Thesis and Commissioning Depth Ionisation PDI for Table 7.....103
Illustration 30: 6MeV Roos and CC-04 Chamber Depth Ionisation Table 8.....105
Illustration 31: 9MeV Roos, CC-04 & IC-15(green) Chamber Depth Ionisation Table 8.....106
Illustration 32: 12MeV Roos and CC-04 Chamber Depth Ionisation Table 8.....107
Illustration 33: 16MeV Roos and CC-04 Chamber Depth Ionisation Table 8.....108
Illustration 34: 20MeV Roos, CC-04 & IC-15(green) Depth Ionisation Chamber Table 8.....109
Illustration 35: 9MeV Inplane-Net 15x15cm field size CC-04.....111
Illustration 36: 9MeV Inplane-Net 15x15cm field size IC-15.....112
Illustration 37: 20MeV Inplane-Net 15x15cm field size CC-04.....113
Illustration 38: 20MeV Inplane-Net 15x15cm field size IC-15.....114
Illustration 39: 9MeV Isodose Overlay IC-15 (solid) CC-04 (dotted).....115
Illustration 40: 20MeV Isodose Overlay IC-15 (solid) CC-04 (dotted).....116
Illustration 41: Full Bolus on Applicator Depth Ionisation- Perspex 9MeV from Table 11 118
Illustration 42: Full Bolus on Applicator Depth Ionisation- Perspex 20MeV from Table 12.....119
Illustration 43: 9MeV Open Field for Table 13.....120
Illustration 44: Full Bolus 9MeV 1x6mm Perspex for Table 13.....121
Illustration 45: Full Bolus 9MeV 2x6mm Perspex for Table 13.....122
Illustration 46: Full Bolus 9MeV 3x6mm Perspex for Table 13.....123

Illustration 47: 6MeV Open Field Table 13.....124
Illustration 48: 20MeV Open Field Table 13.....125
Illustration 49: Full Bolus 20MeV 1x6mm Perspex for Table 13.....126
Illustration 50: Full Bolus 20MeV 2x6mm Perspex for Table 13.....127
Illustration 51: Full Bolus 20MeV 3x6mm Perspex for Table 13.....128
Illustration 52: 16MeV Open Field Table 13.....129
Illustration 53: Full Bolus on Applicator Depth Ionisation - Teflon 9MeV from Table 15.....131
Illustration 54: Full Bolus on Applicator Depth Ionisation -Teflon 20MeV from Table 16.....132
Illustration 55: Full Bolus 9MeV 1x3mm Teflon for Table 17.....133
Illustration 56: Full Bolus 9MeV 2x3mm Teflon for Table 17.....134
Illustration 57: Full Bolus 20MeV 1x3mm Teflon for Table 17.....135
Illustration 58: Full Bolus 20MeV 2x3mm Teflon for Table 17.....136
Illustration 59: Full Bolus on Applicator Depth Ionisation - Aluminium 9MeV from Table 19.....138
Illustration 60: Full Bolus on Applicator Depth Ionisation - Aluminium 20MeV from Table 20.....139
Illustration 61: Full Bolus 9MeV 2.5mm Aluminium for Table 21.....140
Illustration 62: Full Bolus 9MeV 5.0mm Aluminium for Table 21.....141
Illustration 63: Full Bolus 20MeV 2.5mm Aluminium for Table 21.....142
Illustration 64: Full Bolus 20MeV 5.0mm Aluminium for Table 21.....143
Illustration 65: Partial Bolus Perspex Depth Ionisation - Central Axis – 9MeV from Table 23.....145
Illustration 66: Partial Bolus Perspex Depth Ionisation - +3.5cm inplane – 9MeV from Table 23.....146
Illustration 67: Partial Bolus Perspex Depth Ionisation - Central Axis – 20MeV from Table 24.....147
Illustration 68: Partial Bolus Perspex Depth Ionisation - +3.5cm inplane – 20MeV from Table 24....148
Illustration 69: Partial Bolus 9MeV 1x6mm Perspex for Table 25.....149
Illustration 70: Partial Bolus 9MeV 2x6mm Perspex for Table 25.....150
Illustration 71: Partial Bolus 9MeV 3x6mm Perspex for Table 25.....151
Illustration 72: Partial Bolus 20MeV 1x6mm Perspex for Table 25.....152
Illustration 73: Partial Bolus 20MeV 2x6mm Perspex for Table 25.....153
Illustration 74: Partial Bolus 20MeV 3x6mm Perspex for Table 25.....154
Illustration 75: Partial Bolus Teflon Depth Ionisation - Central Axis – 9MeV from Table 28.....156
Illustration 76: Partial Bolus Teflon Depth Ionisation - +3.5cm inplane – 9MeV from Table 28.....157
Illustration 77: Partial Bolus Teflon Depth Ionisation - Central Axis – 20MeV from Table 29.....158
Illustration 78: Partial Bolus Teflon Depth Ionisation - +3.5cm inplane – 20MeV from Table 29.....159
Illustration 79: Partial Bolus 9MeV 1x3mm Teflon for Table 30.....160
Illustration 80: Partial Bolus 9MeV 2x3mm Teflon for Table 30.....161
Illustration 81: Partial Bolus 9MeV 2x5mm Teflon for Table 30.....162
Illustration 82: Partial Bolus 20MeV 1x3mm Teflon for Table 30.....163
Illustration 83: Partial Bolus 20MeV 2x3mm Teflon for Table 30.....164
Illustration 84: Partial Bolus 20MeV 2x5mm Teflon for Table 30.....165
Illustration 85: Partial Bolus Aluminium Depth Ionisation - Central Axis – 9MeV from Table 33.....167
Illustration 86: Partial Bolus Aluminium Depth Ionisation - +3.5cm inplane – 9MeV from Table 33 168
Illustration 87: Partial Bolus Aluminium Depth Ionisation - Central Axis – 20MeV from Table 34...169
Illustration 88: Partial Bolus Aluminium Depth Ionisation - +3.5cm inplane – 20MeV from Table 34
.....170
Illustration 89: Partial Bolus 9MeV 2.7mm Aluminium for Table 35.....171
Illustration 90: Partial Bolus 9MeV 5.1mm Aluminium for Table 35.....172
Illustration 91: Partial Bolus 20MeV 2.7mm Aluminium for Table 35.....173
Illustration 92: Partial Bolus 20MeV 5.1mm Aluminium for Table 35.....174
Illustration 93: Strip Bolus Teflon Depth Ionisation - Open, -4cm, CA,+4cm inplane – 9MeV from
Table 38.....176
Illustration 94: Strip Bolus Teflon Depth Ionisation - Open, -4cm, CA,+4cm inplane – 9MeV from
Table 39.....177
Illustration 95: Strip Bolus 9MeV 2x5mm Teflon for Table 40.....178
Illustration 96: Strip Bolus 20MeV 2x5mm Teflon for Table 40.....179

Illustration 97: Depth Ionisation Scans Higher Z Grids 9MeV.pdf from Table 42.....182
Illustration 98: Depth Ionisation Scans Higher Z Grids 20MeV.pdf from Table 43.....183
Illustration 99: Aluminium Mesh on Applicator 1xsheet 9MeV from Table 44.....184
Illustration 100: Aluminium Shim on Applicator 1xsheet 9MeV from Table 44.....185
Illustration 101: Aluminium Shim on Applicator 2xsheet 9MeV from Table 44.....186
Illustration 102: Aluminium Mesh on Applicator 1xsheet 20MeV from Table 44.....187
Illustration 103: Aluminium Sheet on Applicator 1xsheet 20MeV from Table 44.....188
Illustration 104: Aluminium Sheet on Applicator 2xsheet 20MeV from Table 44.....189
Illustration 105: Stainless Steel Mesh on Applicator Depth Ionisation 9MeV from Table 46.....190
Illustration 106: Stainless Steel Mesh on Applicator Depth Ionisation 20MeV from Table 47.....191
Illustration 107: Stainless Steel Mesh on Applicator 1xsheet 9MeV for Table 48.....192
Illustration 108: Stainless Steel Mesh on Applicator 2xsheet 9MeV for Table 48.....193
Illustration 109: Stainless Steel Mesh on Applicator 3xsheet 9MeV for Table 48.....194
Illustration 110: Stainless Steel Mesh on Applicator 4xsheet 9MeV for Table 48.....195
Illustration 111: Stainless Steel Mesh on Applicator 1xsheet 20MeV for Table 48.....196
Illustration 112: Stainless Steel Mesh on Applicator 2xsheet 20MeV for Table 48.....197
Illustration 113: Stainless Steel Mesh on Applicator 3xsheet 20MeV for Table 48.....198
Illustration 114: Stainless Steel Mesh on Applicator 4xsheet 20MeV for Table 48.....199
Illustration 115: Perspex Bolus on Surface Depth Ionisation 9MeV from Table 50.....201
Illustration 116: Perspex Bolus on Surface Net 1xSheet 9MeV for Table 51.....202
Illustration 117: Perspex Bolus on Surface Net 2xSheet 9MeV for Table 51.....203
Illustration 118: Perspex Bolus on Surface Net 3xSheet 9MeV for Table 51.....204
Illustration 119: Bolus on Surface Teflon 1, 2 x5mm sheet Depth Ionisation 9MeV for Table 53.....205
Illustration 120: Bolus on Surface Teflon 1, 2 x5mm sheet Depth Ionisation 20MeV for Table 54....206
Illustration 121: Full Bolus Perspex with 9MeV surface shift 0.6cm.....209
Illustration 122: Full Bolus Perspex with 9MeV surface shift 1.22cm.....210
Illustration 123: Full Bolus Perspex with 9MeV surface shift 1.83cm.....211
Illustration 124: Full Bolus Perspex with 20MeV surface shift 0.6cm.....212
Illustration 125: Full Bolus Perspex with 20MeV surface shift 1.27cm.....213
Illustration 126: Full Bolus Perspex with 20MeV surface shift 1.9cm.....214
Illustration 127: Full Bolus Teflon with 9MeV surface shift 0.6cm.....216
Illustration 128: Full Bolus Teflon with 9MeV surface shift 1.15cm.....217
Illustration 129: Full Bolus Teflon with 9MeV surface shift 1.83cm.....218
Illustration 130: Full Bolus Teflon with 20MeV surface shift 0.58cm.....219
Illustration 131: Full Bolus Teflon with 20MeV surface shift 1.19cm.....220
Illustration 132: Full Bolus Teflon with 20MeV surface shift 2.1cm.....221
Illustration 133: Full Bolus Aluminium with 9MeV surface shift 0.65cm.....223
Illustration 134: Full Bolus Aluminium with 9MeV surface shift 1.21cm.....224
Illustration 135: Full Bolus Aluminium with 20MeV surface shift 0.69cm.....225
Illustration 136: Full Bolus Aluminium with 20MeV surface shift 1.32cm.....226

Index of Tables

Table 1: Wellhöfer, IBA Dosimetry Compact Ionisation Chambers.....30
Table 2: Wellhöfer, PPC-40 Roos Type PP Chamber.....31
Table 3: Wellhöfer Electron Effective Point of Measurement IC-15.....38
Table 4: Perspex Water Equivalent Depths.....41
Table 5: Teflon Water Equivalent Depths.....42
Table 6: Aluminium Water Equivalent Depths.....43
Table 7: R50,ion g/cm2 R80,ion g/cm2 Project & Commissioning.....47
Table 8: R50,ion g/cm2 & R80,ion g/cm2 for thesis chambers.....48
Table 9: R50 g/cm2 & R80 g/cm2 for thesis chambers.....49
Table 10: Material used for bolus.....52
Table 11: 9MeV Perspex full bolus on LMA insert.....54
Table 12: 20MeV Perspex full bolus on LMA insert.....54
Table 13: File Number Depth Inplane Ionisation Nets Perspex full bolus.....54
Table 14: Penumbra and Therapeutic Region Dose Width, Full Bolus - Perspex.....55
Table 15: 9MeV, Teflon bolus on LMA insert.....56
Table 16: 20MeV, Teflon bolus on LMA insert.....56
Table 17: Depth Inplane Ionisation Nets Teflon full bolus.....56
Table 18: Penumbra and Therapeutic Region Dose Width, Full Bolus - Teflon.....57
Table 19: 9MeV, Aluminium full bolus on LMA insert.....58
Table 20: 20MeV, Aluminium full bolus on LMA insert.....58
Table 21: Depth Inplane Ionisation Nets Aluminium full bolus.....58
Table 22: Penumbra and Therapeutic Region Dose Width, Full Bolus - Aluminium.....59
Table 23: 9MeV, Perspex partial bolus on LMA insert.....61
Table 24: 20MeV, Perspex partial bolus on LMA insert.....61
Table 25: Depth Inplane Ionisation Nets Perspex partial bolus.....61
Table 26: Penumbra and Therapeautic Region Dose Width, Partial Bolus - Perspex.....62
Table 27: Penumbra and Therapeautic Region Dose Width, Partial Bolus - Perspex.....62
Table 28: 9MeV, Teflon partial bolus on LMA insert.....63
Table 29: 20MeV, Teflon partial bolus on LMA insert.....63
Table 30: Depth Inplane Ionisation Nets Teflon partial bolus 63
Table 31: Penumbra and Therapeautic Region Dose Width, Partial Bolus - Teflon.....64
Table 32: Penumbra and Therapeautic Region Dose Width, Partial Bolus – Teflon.....64
Table 33: 9MeV, Aluminium partial bolus on LMA insert.....65
Table 34: 20MeV, Aluminium partial bolus on LMA insert.....65
Table 35: Depth Inplane Ionisation Nets Aluminium partial bolus.....65
Table 36: Penumbra and Therapeautic Region Dose Width, Partial Bolus - Aluminium.....66
Table 37: Penumbra and Therapeautic Region Dose Width, Partial Bolus - Aluminium.....66
Table 38: 9MeV, Teflon strip bolus on LMA insert.....68
Table 39: 20MeV, Teflon strip bolus on LMA insert.....68
Table 40: Depth Inplane Ionisation Nets Teflon strip bolus.....68
Table 41: Penumbra and Therapeautic Region Dose Width, Strip Bolus - Teflon.....69
Table 42: 9MeV Aluminium mesh bolus on LMA insert.....71
Table 43: 20MeV Aluminium mesh bolus on LMA insert.....71
Table 44: Depth Inplane Ionisation Nets Higher Z Grid bolus.....71
Table 45: Penumbra and Therapeutic Region Dose Width, Full Bolus – Al Mesh/Sheet.....72
Table 46: 9MeV, Stainless Steel mesh bolus on LMA insert.....73
Table 47: 20MeV Stainless Steel mesh bolus on LMA insert.....73

Table 48: Depth Inplane Ionisation Nets Stainless Steel Mesh.....73
Table 49: Penumbra and Therapeutic Region Dose Width, Full Bolus – Stainless Steel Mesh 74
Table 50: Bolus on Surface Perspex depth ionisation 9MeV.....76
Table 51: Depth Inplane Ionisation Nets Perspex Full surface bolus 76
Table 52: Penumbra and Therapeutic Region Dose Width, Full surface Bolus - Perspex.....76
Table 53: Bolus on Surface Teflon 9MeV, ...77
Table 54: Bolus on Surface Teflon 20MeV 77

0. ABSTRACT

Radiation therapy with electron beams is a technique that continues to be used by many clinics. The characteristic depth dose with a dose build up and rapid dose drop off beyond the peak dose permits a lesion to be treated with a relatively uniform dose whilst sparing deeper normal tissue.

There are three general methods employed to modulate electron beams; a)Intensity Modulated Electron Therapy b) Segmented-field Electron Conformal Therapy, c) Bolus Electron Conformal Therapy, which can be used to achieve one or a combination of three aims; 1) level an irregular surface and improve dose distributions (missing tissue compensator), 2) reduce the penetration of the electron beam in certain areas (shaping isodoses closer to the distal edge of the target volume), 3) increase the surface dose at energies below 10MeV.

The most commonly employed method in a general radiotherapy practice to modify an electron beam is the application of a tissue like material (bolus) to the skin surface, in the strictest sense this is not Bolus Electron Conformal Therapy (BolusECT) but rather an element of the method as the bolus applied usually lacks sophisticated contouring. The first two methods mentioned are both technically and resource challenging for a general radiotherapy clinic. Unfortunately the application of bolus does have some limitations; it is not usually sterile and the daily application in areas where there may be ulcerated, necrotic or haemorrhaging tissue can lead to an unhygienic situation. In addition there are times when it is difficult to mould or reproducibly position the bolus to the particular surface irregularities leading to suboptimal treatment delivery.

Moving the bolus to the applicator level alleviates the contact and positional reproducibility difficulties however it does introduce new challenges in understanding how this will affect the electron beam dosimetry for the clinical treatment. This thesis provides the reader with some of the information necessary to understand the new challenges.

1. INTRODUCTION

1.1 Radiotherapy

Radiotherapy, Radiation Therapy, Radiation Treatment and Radiation Oncology are all terms used to describe the same process, which is the treatment of cancer using ionising radiation.

Ionising radiation transfers energy to the molecules of the material with which it interacts. In biological material this can result in damage to the cell in two ways; direct or indirect. Although the distinction between whether direct or indirect effects have occurred is not always clear, direct action is generally associated with high Linear Energy Transfer (LET) type particles where the ionisation event occurs in the Deoxybonucleic Acid (DNA) (McMillan, 2003, Halperin et al., 2008). Indirect action tends to be the predominant process accounting for approximately two thirds of the biological damage with low LET radiation e.g. electrons (Panglossi, 2007, Halperin et al., 2008). As the cell is made up of approximately 85% water(Halperin et al., 2008)(Halperin et al., 2008). Water is ionised and extremely reactive free radicals (water ion & hydroxyl radical) are formed which can then go on to damage other molecules in particular Deoxyribonucleis Acid (Podgorsak, 2005, Hall and Giaccia, 2012).

The radiation can result in a wide range of cell actions including; no effect, adaptive responses, mutation, reproductive failure, division delay or damage which includes single and/or double (lethal) DNA strand breaks, base and sugar damage and crosslinks between macromolecules (Read, 1957, Alper, 1963, McMillan, 2003, Podgorsak, 2005, Halperin et al., 2008, Hall and Giaccia, 2012).

Radiotherapy has had a history only marginally shorter than Röntgen's discovery of X-rays.

In December 1895 Wilhelm Conrad Röntgen (1845 -1923) reported to The Wurzburg Medical Physics Society; “On a new Type of Ray; A Preliminary Communication”. News of the discovery rapidly spread throughout Europe crossing the Atlantic to New York and Chicago (USA) resulting in more than 1000 oral and written communications on X-rays in 1896. Röntgen's only public demonstration of X-rays was the imaging of one of his university colleagues, (Albert von Köllicker), hand. Röntgen made a further two communications in 1896 and 1897 which further described his observations on the properties of X-rays (Bernier,

1995).

In 1896 Henri Becquerel (Antoine Henri Becquerel 1852 -1908) somewhat accidentally discovered natural radioactivity. At the time Becquerel was working with uranium salts investigating whether there was any connection between X-rays and naturally occurring phosphorescence. Becquerel had already demonstrated exposure of photographic plates, enveloped in black paper, to what he thought were the result of phosphorescence of his uranium and potassium salts. He exposed his experimental set-up to several hours of sunlight believing that the uranium absorbed sunlight and emitted X-Rays. However when he repeated his experiment a few days later, there was a decided lack of sunlight which resulted in the experimental device being kept mainly in a drawer. After a few days of disappointing weather Becquerel decided to process the photographic plate expecting to only see a very faint shadow, rather what he saw a was very clear image and he concluded that the unknown rays existed even in darkness (Allisy, 1996).

Becquerel's discovery led to further scientific investigation. In 1898 Marie Skłodowska Curie (1867-1934) and Pierre Curie (1859-1906), working with pitchblend from Joachimsthal in Bohemia, which exhibited a radioactivity greater than could be explained by the Uranium alone, presented their findings to the Academy of Sciences on the discovery of a new metal and suggested it was called Polonium. Through further work the Curie's became aware of a second substance, also highly radioactive and again announced their discovery however it was not until some 45 months later that Marie Curie was able to prepare 1 decigramme of radium chloride and later pure radium (Bernier, 1995).

Following Röntgen's discovery it was soon recognised that X-ray radiation may have an appreciable effect on normal tissue albeit detrimental. Several reports of injuries began to emerge although because of the latency not always attributed to the radiation. Emil H. Grubbé in his paper to Radiology (Grubbé, 1933) reported that he believed he was the first person to recognise that cumulative exposure to x-rays had resulted in his dermatitis. This however did lead Grubbé to investigate the use of the radiation in the treatment of carcinoma and some 60 days after Röntgen's initial communication, therapeutically delivered radiation to two patients. Within a few years of Röntgen's and then Becquerel's discovery, it was realised that the effects of radiation on superficial tumours required further investigation (Williams and Thwaites, 1993). Possibly the first documented “cure” of cancer by x-rays was by Dr Thor Stenbeck of

Stockholm in 1899 of a basel cell carcinoma on the nose of a woman (Bernier, 1995).

Progress in Radiotherapy was principally determined by the development of satisfactory sources, the work by the Curies and improvements in the X-ray producing instruments both aided the field however the major advances in radiotherapy only came about around the late 1930's to early 1940's. The development of the Van de Graaff (1930's) and betatron accelerators(1940's), the later being able to accelerate electrons up to tens of MeV, were able to produce both X-Ray radiation and also electron beams (Farmer, 1962, Hogstrom and Almond, 2006).

In the 30's the physical properties and possible advantages of high energy electron beams for therapeutic use had been reported. Different studies had identified a reduced surface dose (relative to the existing superficial and orthovoltage X-rays), the relatively broad dose maximum and rapid fall off of dose at depth, (dependent on electron energy) which suggested possible applications in dermatology (Bernier, 1995). Although there had been some developmental work, electrons remained with limited applications because of the low accelerating potential (2MeV restricting their use to mainly surface lesions) and large machine size (Karzmark, 1993, Hogstrom and Almond, 2006).

In 1934 Bill (William) Hansen returned from a brief period at MIT to Stanford University as assistant Professor of Physics and was soon immersed in researching methods of accelerating particles (principally electrons) up to an order of a million volts. Hansen believed that existing static accelerators such as the Van de Graaff generator would be limited by technical problems such as insulation. He began to explore resonant cavities along the ideas of Sloan at Berkeley, plus with additional knowledge gained from his time at MIT, eventually developed a more practical and efficient Sloan accelerator called a Rhumbatron by Stanford.

At a similar time a graduate student, Russell Varian, began work at Stanford with Hansen. By 1936 cities in Spain and China were being bombed by air and Russell's brother Sigurd, a pilot, was aware of the threat of the rapidly growing German Air Force and its participation with the Nationalists (rebels) in the Spanish Civil War. At the time Sigurd believed that the destruction occurring in Spain may spread to the United States (US) because of the support provided by volunteers to the Republican Government forces and Sigurd knew there was no method to combat or even detect aeroplane raids should they be launched from Central America on cities in the United States. Discussions between the brothers lead Russell to realise the potential of

the Rhumbatron as a radio tube capable of producing waves suitable to be used in what is now know as RADAR. With aid provided through Stanford University (ie. room, Bill Hansen & faculty plus $100) a royalty agreement was established and the Varian brothers commenced their development. Within a few months, Russell presented an idea which was evaluated by Bill Hansen and found to be promising.

The first functioning model, built by Sigurd Varian, of the Klystron occurred in 1937. At a similar time considerable work was being conducted in England on the development of a circular microwave generator (magnetron). Adapting the idea of multiple resonance cavities, from the US, lead to the development by J.T. Randall & H.A. Boot of a 0.1MW magnetron in 1939 (Ginzton et al., 1948, Ginzton et al., 1957, Ginzton and Nunan, 1985, Karzmark, 1993, Bernier, 1995). However World War II interfered with further development of Hansen's accelerator ideas.

In 1940 Professor Donald.W. Kerst developed the first betatron (an electron accelerator) for basic physics research (Klevenhagen, 1993). The betatron was capable of accelerating electrons up to tens of MeV and its therapeutic usefulness was recognised with the first patient treatment occurring in 1948 at the University of Illinois (Klevenhagen, 1993). Whilst the betatron had the majority of the world market in the early years around 1968 (Hogstrom and Almond, 2006), and although considerable pioneering research had been conducted by many researchers including K. Gund, W. Paul, F. Wachsmann and J.S. Laughlin et al (Bernier, 1995), their sheer size, limited beam output and small field size eventually drove them to obsolescence with the emerging technology of the microwave linear accelerator (Podgorsak, 2005, Hogstrom and Almond, 2006, Khan, 2010).

Following World War II two principal groups, one in the US the other in the United Kingdom (UK), lead by W.W. Hansen and D.D Fry respectively, began independently developing microwave electron accelerators. The two groups progressively leapfrogged each other with their accelerators each time achieving higher electron energies. Towards the later part of 1948 the British Ministry of Health arranged the collaboration of UK research groups for the construction of an x-ray linac for clinical use. In 1953 the first patient was treated at the Hammersmith Hospital with an x-ray beam from an Microwave Electron Linear Accelerator.

Various Microwave Linear Accelerator structures were constructed in these formative years of which some built such that x-ray target could be removed and radiation treatment could be

delivered by electrons alone allowing continued research into Electron Radiotherapy (Ginzton and Nunan, 1985, Karzmark, 1993).

1.2 Electron Interactions

This introduction is not meant to be a comprehensive analysis of electron interactions in matter, rather it is intended to provide the reader with only a basic understanding of some of the predominant physical processes that affect the penetration of electrons in matter and their resulting effects for radiotherapy. A detailed analysis is beyond the scope of this thesis and best provided by other authors including (Johns and Cunningham, 1983, Khan, 1991, Klevenhagen, 1993, Khan, 2010).

Electrons and photons interact differently within tissue; a photon beam traversing tissue, whilst attenuated, effectively looses very little energy over the distances typical for radiotherapy. Conversely the electron looses energy in small increments (appearing as continual loss) as it passes in tissue.

Electrons are surrounded by a Coulomb electric field and start interacting with atoms immediately entering a material by a variety of processes. The primary interactions are i)elastic nuclear scattering, ii)inelastic collisions with orbital electrons and iii)radiative interactions with both nuclei and orbital electrons (Illustration 1).

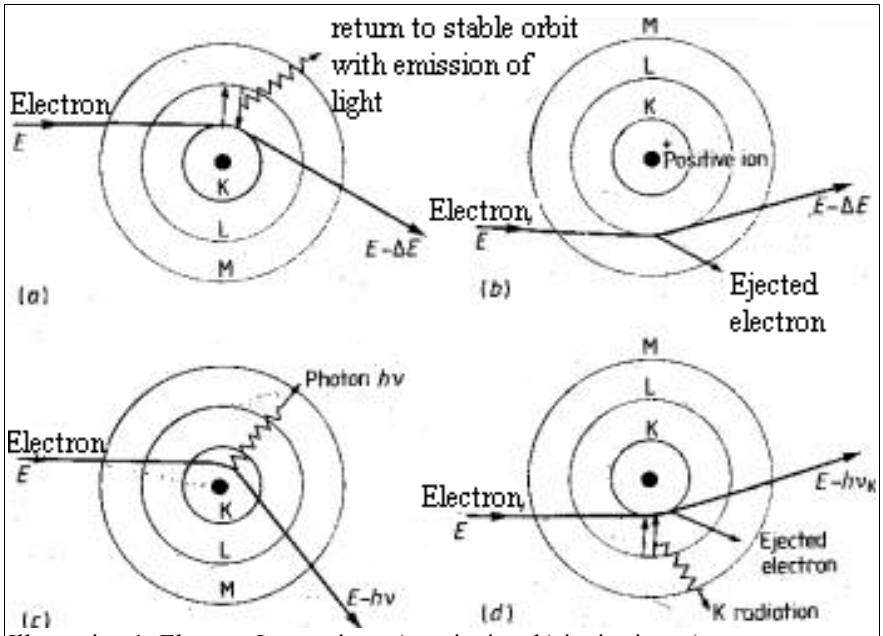

Illustration 1: Electron Interactions a) excitation, b) ionisation, c) bremsstrahlung, d) characteristic radiation production (Khan, 1991)

The interaction which occurs is determined by the energy of, and distance of, the incident electron's approach to the atom or nucleus with which it interacts (Klevenhagen, 1985, Khan, 1994).

i) In elastic collisions the electron trajectory may change (scatter) or the energy may be

redistributed among the particles emerging from the collision, however there is no kinetic energy loss (Podgorsak, 2005).

ii) With inelastic collisions, some of the electron's kinetic energy is lost and is deposited in the medium resulting in either an ionisation or excitation event with the collision atom. The probability of which process occurs depends on the atomic number of the matter and the distance and energy of the interacting electron. Generally in low atomic number matter e.g. water or tissue, electrons tend to loose energy mainly through ionising interactions with atomic atoms, whilst with higher atomic number matter e.g. lead, bremsstrahlung production becomes more important (Khan, 2010). When the distance of the electron's approach is large, relative to the dimensions of the atom, excitation occurs. Only a few eV is required to achieve excitation and hence the energy loss by the impacting electron is very small. The excited atom quickly returns to its stable state by emitting the excess energy in the form of visible radiation in a gas or as heat in a solid material. If however the distance is of the order of atomic dimensions the interaction occurs between the colliding electron and one of the atomic electrons, stripping the orbital electron from the shell resulting in ionisation of the atom (Klevenhagen, 1985).

Inelastic collisions are divided by the energy transferred from the impacting electron, most frequently the energy transfer is small and the energy of the electron appears to degrade continuously until it is captured by the material however occasionally a larger energy transfer can occur and the ejected orbital electron “delta ray” carries off energy (> about 10keV) and now becomes capable of causing ionisations or excitations in the same manner as described above (Klevenhagen, 1985, Khan, 2010).

iii) Radiative interactions occur if the electrons approach is smaller than the atomic radius. The incident electron is deflected from its incident path by the nuclear Coulomb field with the loss of energy. The energy lost is emitted as an electromagnetic radiation known as bremsstrahlung in a similar process as for the production of X-rays.

1.2.1 Stopping Powers

The energy transferred from the electron to the medium by collision or radiative processes is quantified by the use of the stopping power (S). The fraction of energy loss '*dE'* of an electron per unit of path length '*dx'* provides the quantity linear stopping power, i.e. S = *dE/ dx* (Johns and Cunningham, 1983, Klevenhagen, 1993, Metcalfe et al., 1997). The energy lost in each

interaction is very small which results in the appearance of the electron continuously loosing energy and it is convenient to consider the stopping power as representing the average rate of energy loss (Klevenhagen, 1985). In radiation dosimetry the thicknesses of materials are usually described in mass units therefore it is advantageous to define the stopping properties of the absorbing medium in terms of the mass stopping power. The total mass stopping power $(1/\rho)(S_{tot})$ - (defined as the quotient dE by ρdl *where* dE is the energy lost by a charged particle in traversing a distance in the medium of density ρ)(ICRU, 1980)- is given by the relationship:

$$(1/\rho)S_{tot} = (1/\rho)S_{rad} + (1/\rho)S_{coll}$$

including the components due to radiative (S_{rad}(ICRU, 1980)) and collisional (S_{coll}) interactions.

The stopping power increases with depth as the interacting electron looses energy as it moves further into the water. As has been noted above in *Chapter:1.2 Electron Interactions* the predominant interaction in a low density medium such as water is collisional (Illustration 2).

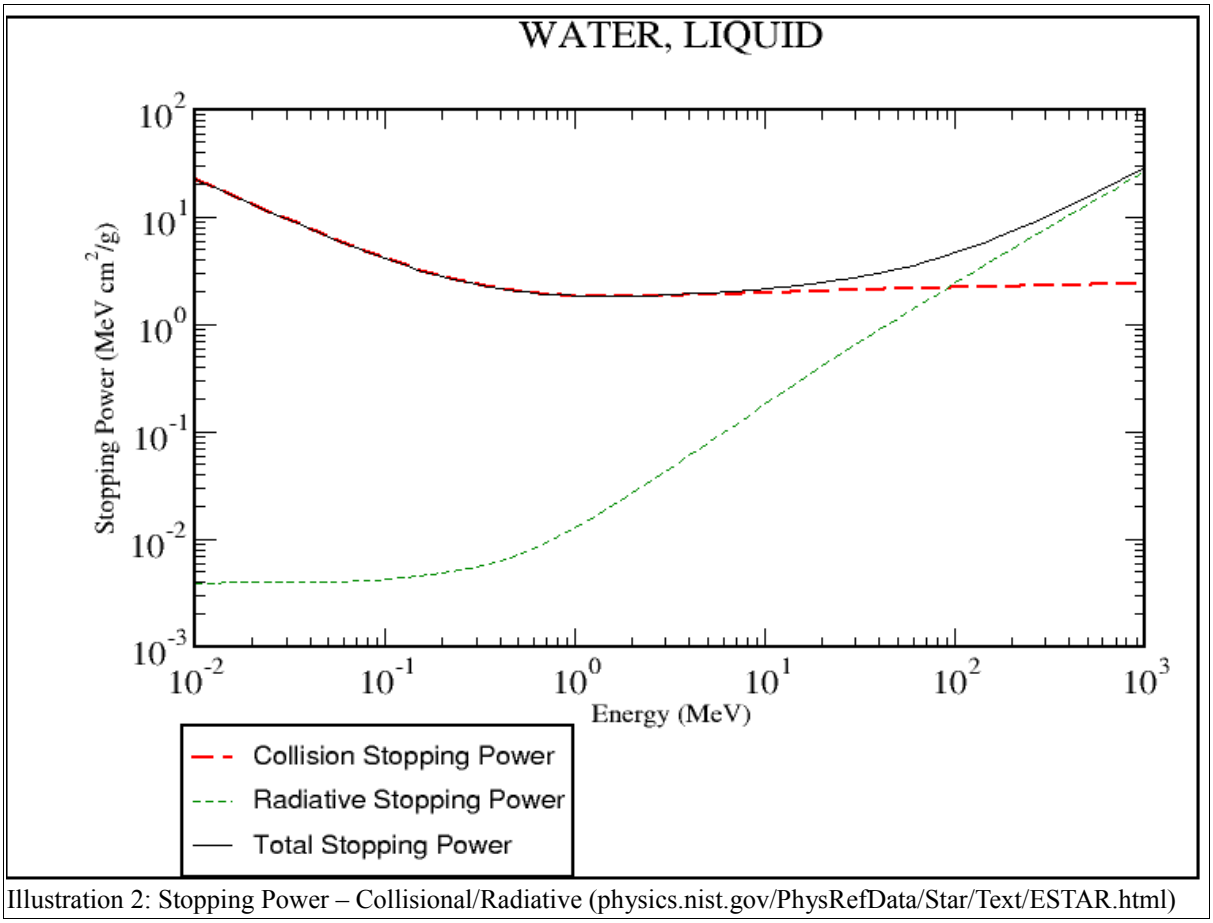

Illustration 2: Stopping Power – Collisional/Radiative (physics.nist.gov/PhysRefData/Star/Text/ESTAR.html)

To determine a dose at a point in the water phantom from the depth ionisation data it is

necessary to only consider the energy that is deposited locally therefore interactions which result in large amounts of energy being transferred (hard collisions) to secondary electrons or delta rays and carried away from the position can be ignored and the ionisation value is simply multiplied by the restricted collision stopping power. Use of the unrestricted collision stopping power would result in an overestimation of the dose deposited at the location (see further discussion Page 27 *Chapter:2.3 Ionisation Chambers*).

1.3 Electron Beam Therapy

The most clinically useful therapeutic electron beams are in the range 6-20MeV. At energies beyond 20MeV there is less of a characteristic dose drop off and the beams start to exhibit properties similar to photon beams (Illustration 3). Within the range, the electrons can be used to treat superficial tumours to depths of approximately 5-6cm and still exhibit a rapid dose fall off at depths beyond the tumour. Whilst it may be possible to treat these shallow lesions with other modalities such as brachytherapy, superficial or tangential photon beams, electrons can provide a reasonably uniform dose in the target and minimise the dose to deeper tissue (Starkschall et al., 1993, Khan, 2010) which may result in a more efficient treatment delivery.

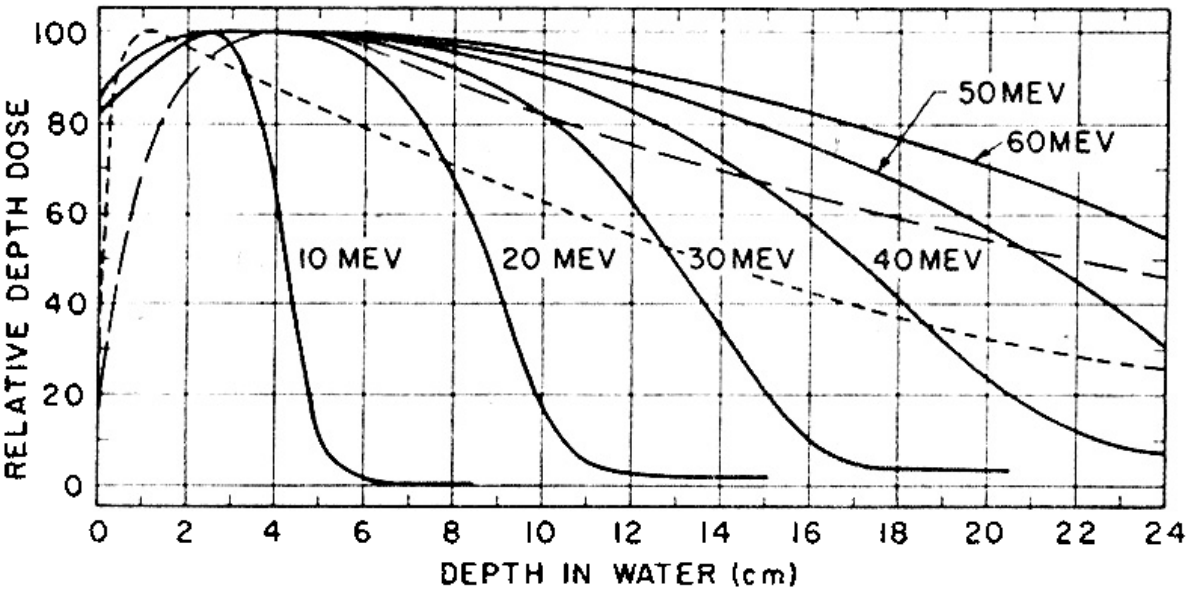

Illustration 3: Depth–dose curves in water for electron beams,(solid curves), cf depth–dose curves for5 MV (small-dashed line) and 22 MV (long-dashed line) x-ray beams (Farmer, 1962, Hogstrom and Almond, 2006).

Although electrons are commonly used for the treatment of superficial tumours often the target occurs on irregular body parts such as the head and face or in areas where surgical procedures have caused defects which can lead to significant dose heterogeneity in underlying tissue (Hogstrom and Almond, 1983). Additionally the target rarely extends to a single fixed depth below the surface, it may not be located in homogeneous tissue and often there are normal radio sensitive structures in close distal proximity making uniform dose delivery challenging. It therefore becomes necessary to manipulate(modulate) the electron beam characteristics to account for these situations (Hyodynmaa et al., 1996).

1.4 Modulated Electron Radiotherapy

Electron Conformal Therapy (ECT) (Hogstrom et al., 2003) is similar in many aspects to photon conformal therapy. The aim of 'Conformal Therapy' is to deliver the radiotherapy dose to the target as homogeneously as possible whilst minimising the dose to the surrounding tissue. This is achieved with photons by using custom blocking and compensation for multiple fields. In a similar fashion some superficial tumours can be conformally treated with one or multiple electron beams, custom blocking and compensation (Starkschall et al., 1993, Hogstrom and Almond, 2006, Halperin et al., 2008, Alexander et al., 2011).

An ideal electron beam plan is where; a) the distal 90% dose surface conforms and contains the planning target volume (PTV), b) the dose delivered is as homogeneous as possible or a prescribed heterogeneous dose distribution is delivered to the PTV, c) underlying normal and critical structures receive minimal dose (Hogstrom et al., 2003, Zeidan et al., 2011).

ECT can be achieved by energy modulation and/or intensity modulation, otherwise known as Modulated Electron Therapy (MET). There are three general methods to deliver MET; a)Intensity Modulated Electron Therapy (IMET) b) Segmented-field ECT, c) BolusECT (Hogstrom et al., 2003). Different authors (Korevaar et al., 1999, Ma et al., 2000, Lee et al., 2000, Lee et al., 2001, Ma et al., 2003, Das et al., 2004, Hogstrom and Almond, 2006) have eloquently illustrated the first two methods, however they remain technically and resource challenging for the average radiotherapy facility. The third (BolusECT) remains the technique most commonly practised in general radiotherapy centres.

BolusECT is achieved by placing a tissue equivalent material on the patients skin to achieve one or more of 3 actions; 1) level an irregular surface and improve dose distributions (missing tissue compensator), 2) reduce the penetration of the electron beam in certain areas (shaping isodoses closer to the distal edge of the target volume), 3) increase the surface dose at energies below 10MeV (Williams and Thwaites, 1993, Galbraith and Rawlinson, 1984, Gunhan et al., 2003, Demir et al., 2009).

The use of BolusECT is not a new technique and although it is fairly well described in literature (Archambeau et al., 1981, Low et al., 1995, Perkins et al., 2001), it is not without shortcomings, and it can be challenging depending on the tumour site. “Design of electron bolus for head and neck tumors is unique in that the PTV has a more complex shape, the

critical structures and their relationship to the PTV are different, and the patient surface is more irregular" (Kudchadker et al., 2003).

1.5 Aims

Bolus, in general, is not sterile and placement on the tissue surface can be unhygienic (Vatanen et al., 2009) especially when the bolus has to be in contact with ulcerated lesions, necrotic tissue or haemorrhaging lesions (Hernandez et al., 2010). Additionally it is not always possible to mould the bolus to surface irregularities introducing air gaps which can alter dose distributions (Sharma and Johnson, 1993, Kong and Holloway, 2007).

The aim of this thesis was to investigate and characterise the effect on electron dosimetry that localising different forms of bolus, both approximately tissue equivalent and non tissue equivalent, in a non conventional, although reproducible locations, (ie not on the phantom surface). A series of experiments were derived to compare the differences in beam characteristics between the recognised conventional method of locating bolus on the surface to that of bolus supported by the Low Melting point Attenuator (LMA) Electron insert. The experiments performed used the LMA insert to support the bolus resulted in an air cavity of approximately 5cm where as conventional bolus, being on the skin surface, ideally does not have any air cavity effect.

2 METHODOLOGICAL DESIGN

2.1 Equipment & General Data Collection Conditions

All experimental data was obtained on a Varian 21EX Linear Accelerator (Linac) Serial #3072 (Varian Medical Systems, Inc. Palo Alto, CA USA) (see Illustration 4) at Radiation Oncology Victoria's (ROV), Murray Valley Radiation Oncology Centre(MVROC) over a series of measurement sessions each linked by “comparison” scans . The Linac, locally referred to as W2, provides 6 & 15MV x-rays (BJR Supplement 11 (Cohen, 1972)) and 6, 9, 12, 16 & 20MeV electron beams.

Illustration 4: Varian 21EX Linac (Image courtesy of Varian Medical Systems, Inc. All rights reserved.)

Measurements were taken with the linac gantry and collimator set at 0°(Varian IEC (601-2-1) scale, radiation beam pointing at floor) and performed in a Wellhöfer 3D Blue Phantom

(Wellhöfer, IBA Dosimetry Schwarzenbruck Germany.) “water tank” (Illustration 5) with a variety of ionisation chambers (see Page 27 *Chapter:2.3 Ionisation Chambers* for discussion), Wellhöfer IC-15 (now called CC-13) Serial: 3343 & 3353, Wellhöfer CC-04 serial: 4167 & 4168 compact cylindrical ionisation chambers and Wellhöfer PPC-40 serial: 318 Roos parallel plate ionisation chamber.

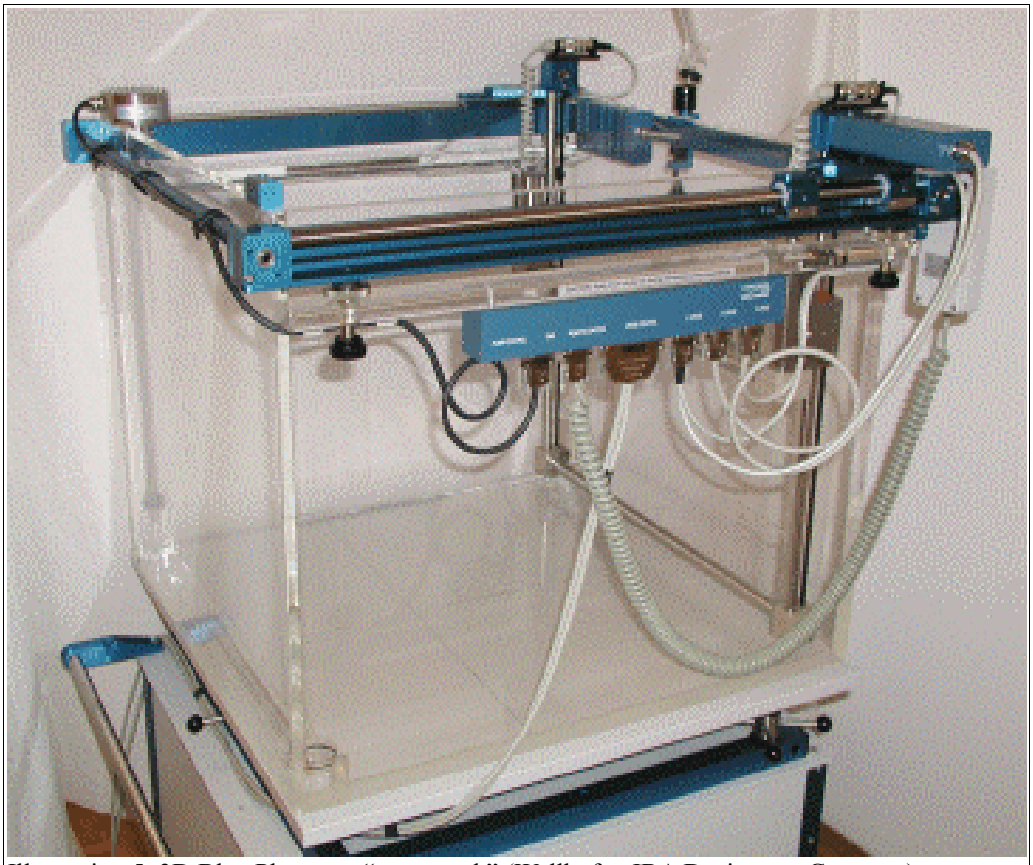

Illustration 5: 3D Blue Phantom, “water tank” (Wellhöfer, IBA Dosimetry, Germany)

Data was acquired utilising the Wellhöfer WP700 (V3.51) 3D beam scanning software and the accompanying CU500E Serial: 5989 controller/electrometer.

The Wellhöfer CU500E system was permitted to approach thermal stability by energising the system, bias voltage set to zero, prior to filling the water tank. The bottom surface of the water tank has an etched cross hair axis (faintly visible in illustration 5) which indicates two of the principal axis' of motion, inplane and crossplane axis' (illustration 6), and is used as an alignment tool to ensure the tank is positioned correctly under the Linac. The water tank was elevated to a height close to what was required and aligned such that the tank etched cross hair that indicates the inplane direction was parallel with the shadow of the linac lower jaw

face. The chamber carriage mechanism, consisting of stainless steel rails, which can be seen at the top of the tank walls in illustration 5, were levelled with a precision spirit level and then filling of the tank with water commenced (approx 20min). The water tank undergoes a regular quality assurance and maintenance program to ensure that the mechanical motions remain within acceptable tolerances. Ionisation chambers (field and reference) were attached and set in their appropriate holders following the manufacturers recommendations which included defining the water surface and isocentre in the Wellhöfer software. The reference chamber, which remains stationary in the field, is required when measuring the radiation from a Linac principally because the beam is not continuous, like the radiation emission from an isotope, but rather pulsed. The CU500E samples signal from the ionisation chambers at a fixed rate which may not correspond to when the linac is producing radiation. The use of a reference detector helps to correct for both the instantaneous fluctuations or drifts in the incident beam output and also ensures that signal is only recorded when it occurs in both the reference and field chamber. (Das et al., 2008)

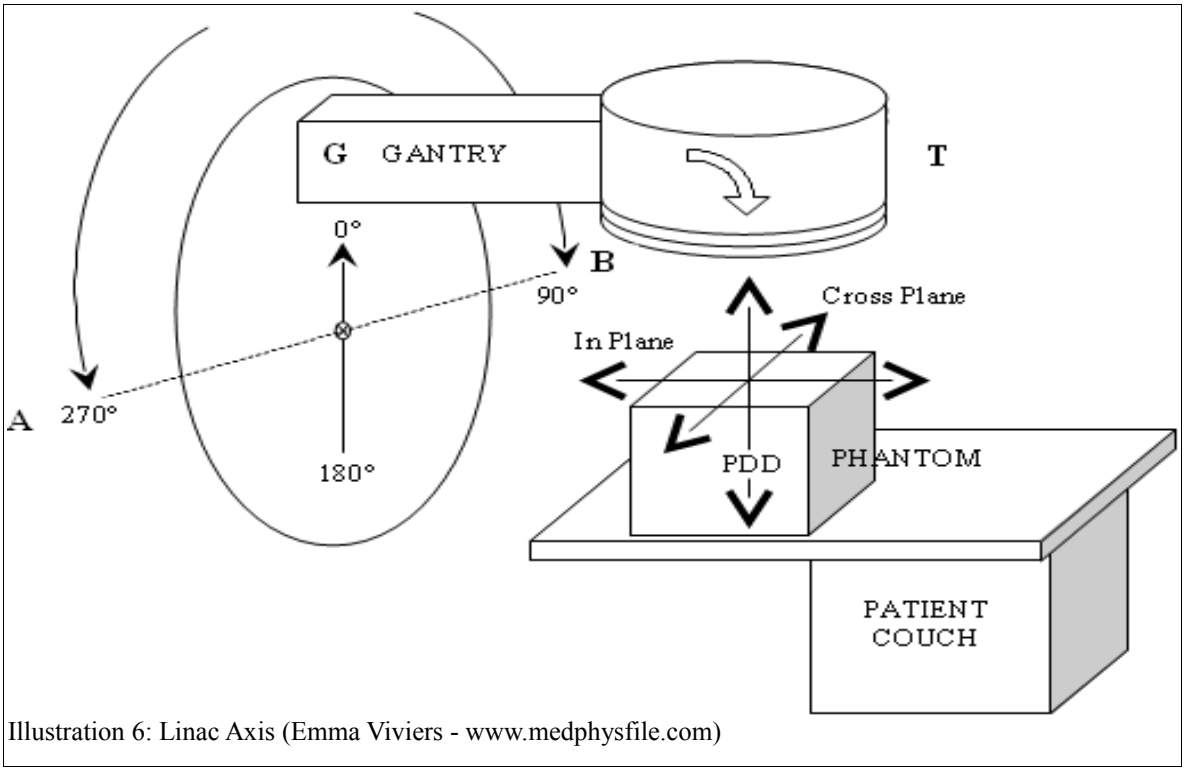

Illustration 6: Linac Axis (Emma Viviers - www.medphysfile.com)

When the tank was filled and an electron applicator attached, the tank mechanical limits were checked to ensure that the chamber could move sufficiently in the horizontal and vertical planes about the the centre axis of the electron beam for the measurements planned. The

central axis correction process within the WP700 software was not run as the set zero position of the chamber, although not at the exact zero position of the field would not affect the experimental results.

All chambers were pre-irradiated with a minimum of 1000MU before any measurements were taken to ensure that the chambers provided a stable reading (Almond et al., 1999, Andreo, 2000, McCaffrey et al., 2005). The CU500E electrometer was adjusted to provide a recorded field signal between 110-115% at the depth of maximum ionisation for the low energy electron beam (2cm for 9MeV nominal). The radiation was switched off and the inbuilt background subtraction process was run. Setting the response of the electrometer in this manner permitted measurement of the high energy electron beam (20MeV nominal) without the need to readjust and re-perform the background subtraction correction.

Air pressure and the temperature of water & air were checked before, during and after each of the long measurement sessions (8 & 12 hrs). These were found to remain constant (temp) or not vary significantly (<=2 hPa) and therefore were ignored. Additionally several scans were repeated during each data acquisition session to check for any other drift introduced by unexpected causes.

All scans; electron depth ionisation curve, electron ionisation inplane profiles and electron ionisation inplane-nets (2D ionisation scan), were obtained using the standard Varian 15x15cm electron applicator and insert with a source to surface of the water phantom distance at 100 cm (SSD technique). This approach was the result of the Varian Acceptance document defined conditions for beam quality measurement. Whilst this is contrary to general recommendation as defined by the IAEA (Andreo, 2000), the use of a smaller applicator is acceptable if the depth of the 50% dose (R_{50}) does not change by greater than $0.1 g/cm^2$. This condition had been previously determined to be satisfied from measurements performed at ROV.

2.2 Clinical Electron Beam Characteristics

When an electron beam treatment is prescribed, to directly treat a particular cancer (eg skin, lips, nose) or as a boost irradiation to an area partially treated with another modality such as photons (eg breast, scars, nodes), the Radiation Oncologist would normally choose an electron beam energy that enables a relatively uniform therapeutic dose (generally considered as 85% (Brahme and Svensson, 1976) to 90% (Khan et al., 1991b) of maximum dose) to be delivered from the surface to a depth that encompasses the target whilst still sparing underlying tissue. To appreciate the most effective clinical use of electron beams it is necessary to have a basic understanding of their isodose distributions in water and heterogeneous media (Halperin et al., 2008). Different accelerators may produce very different dose distributions for the same nominal energy used for electron therapy due to differences in construction which results in the lack of a single universal electron beam beam description. However it is still possible to describe electron beams in general terms which can provide useful information applicable to expected dose distributions (ICRU, 1984). There are two principle components of interest to a clinicial when prescribing an electron beam, namely the isodose distribution and the percentage depth dose (PDD).

The electron beam isodose distribution exhibits a characteristic shape remarkably different to that seen with a photon beam. As was already noted in Chapter 1.2 Electron Interactions as the electron beam traverses a medium, constant scattering and energy loss occurs which in turn results in an increase in electron scattering angle and consequentially the beam expands at depth. The spread of the lower value isodose curves is influenced by several factors including the isodose level, energy, field size and beam collimation (Podgorsak, 2005). The term penumbra is used to describe the region of isodose lines between approximately 80% and 20% (ICRU, 1984) or 90% to 10% (Halperin et al., 2008). The penumbra is a function of depth and is the root mean square addition of two penumbral components, SSD (air gap) and water scatter (Hogstrom et al., 1981, Khan et al., 1991a, Werner et al., 1983). The relationship is complex however it is demonstrated that air gap is more significant at lower energies whilst scatter in water dominates at higher energies (Podgorsak, 2005, Halperin et al., 2008). Because of the depth dependence the penumbra is typically defined at a single depth which the ICRU recommends as that defined by R_{85} /2, where R_{85} is the depth of the 85% isodose level beyond Z_{max} on the electron beam central axis (Podgorsak, 2005).

Whilst considering the electron beam isodose distribution it is worthy to note the lateral constriction (as a result of lack of lateral scatter equilibrium (Gerbi et al., 2009)) of the high level isodose (>80%) with energies >15MeV. These effects of expansion and constriction can be seen in the following illustrations of a 10x10cm field size electron beam for 9MeV and 20MeV respectively. It can seen in illustration 7 that the penumbra of the 9MeV beam is smaller than that associated with the 20MeV beam illustration 8, whilst the 90% isodose region is larger for the 9MeV beam (Podgorsak, 2005).

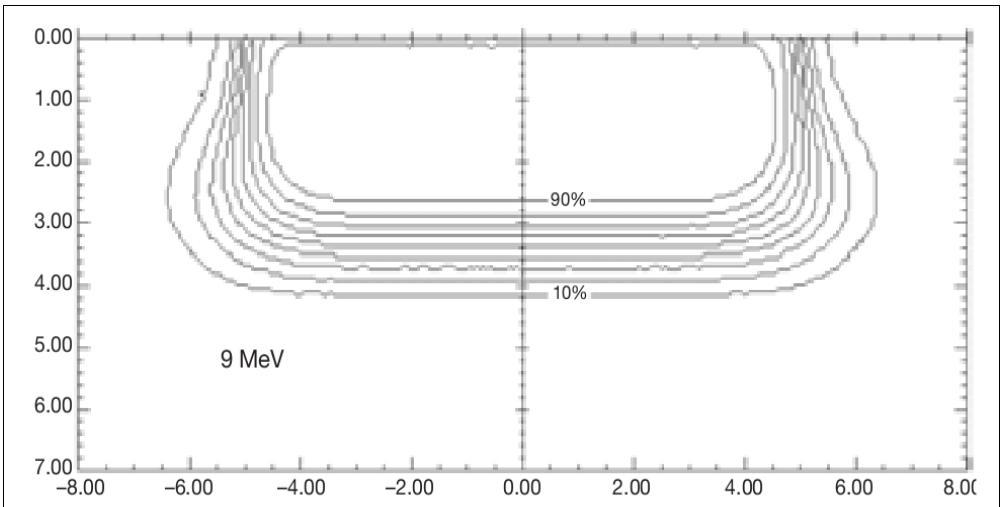

Illustration 7: 9MeV 10x10cm Field Size (Podgorsak, 2005)

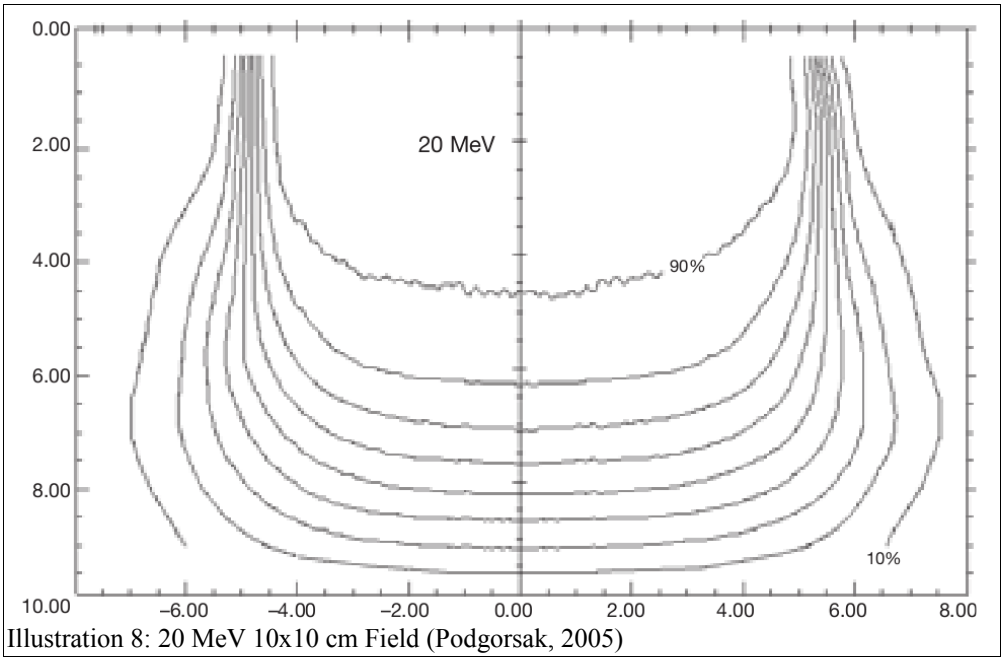

Illustration 8: 20 MeV 10x10 cm Field (Podgorsak, 2005)

Observing a generic central axis PDD distribution (Illustration 9) it can be seen that there are several parameters that need to be considered including, the relative surface dose ($\%D_S$), the maximum dose (Zmax), the therapeutic range (R_{90}), the depth of the 50% dose (R_{50}) and the practical range (R_P) (Podgorsak, 2005, Halperin et al., 2008).

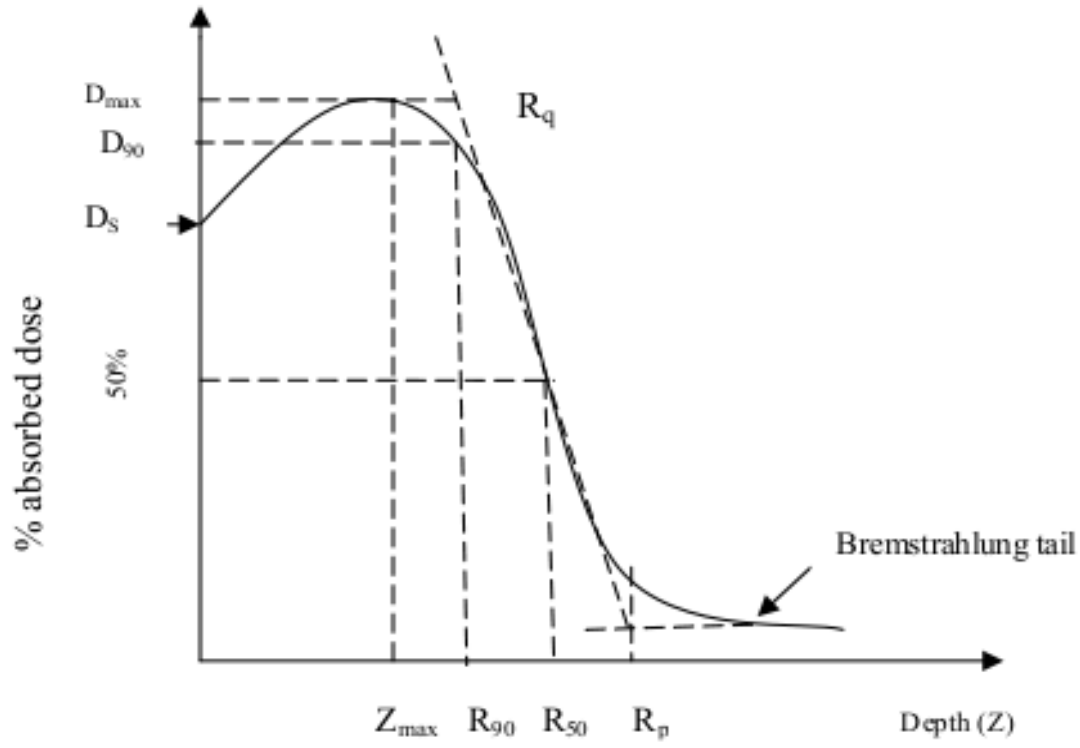

Illustration 9: Electron PDD Curve (Podgorsak, 2005)

Although each of these parameters can be affected by small differences in energy, field size, scattering foils, and source to surface distance, during machine acceptance testing these are measured, recorded and evaluated for future clinical use (Brahme and Svensson, 1976, Khan et al., 1991b, Hogstrom and Almond, 2006, Halperin et al., 2008).

2.2.1 Central Axis Percentage Depth Dose

The general shape of the electron central axis percentage depth dose (PDD) displays a high surface dose, a short build up region to a relatively broad near maximum dose and a steep dose fall off region to a non zero bremsstrahlung tail. The illustrated example (Illustration 10) shows a 6MV photon beam with an 8MeV electron beam.

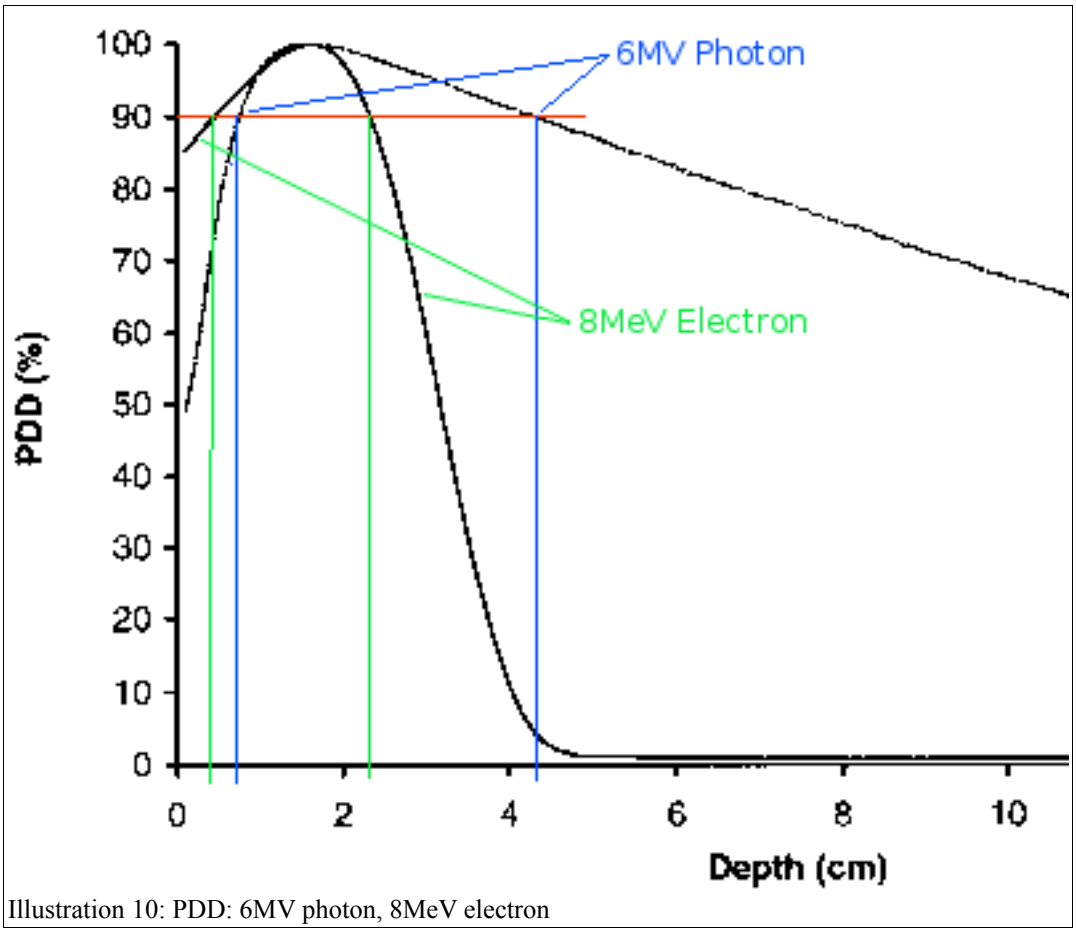

Illustration 10: PDD: 6MV photon, 8MeV electron

It can be noted that the photon and electron beams display similar depth for their maximum dose, with the photon beam (blue markers) providing almost twice the therapeutic depth (at the 90% PDD) of that of the electron beam (green markers), however the surface dose and dose at depth are remarkably different.

The PDD can not be directly measured with an ionisation chamber (see also additional discussion in *Chapter 2.5.1 Effective Point of Measurement (EPOM)*), rather a depth ionisation curve is obtained which is then converted to a corresponding depth dose distribution by applying the appropriate stopping power ratios water to air at depths in a phantom $s_{w,air}$ (Klevenhagen, 1985, Klevenhagen, 1993, Andreo, 2000, Das et al., 2008, Gerbi et al., 2009). The changes that occur for the conversion are not large for low energy electrons

but become significant at 10MeV and above (Klevenhagen, 1985, Klevenhagen, 1993, Andreo, 2000, Das et al., 2008, Gerbi et al., 2009).

It is known that other factors such as Energy, Source to Surface Distance, Angle of Incidence and Field Size can all affect the shape of an electron PDD (Brahme and Svensson, 1976, Klevenhagen, 1985, Khan et al., 1991b, Hogstrom and Almond, 2006).

2.2.1.1 PDD Dependence on Energy

Illustration 11 shows a series of Percentage Depth Ionisation curves (field size 15x15cm) obtained during commissioning of the Linac for electron beam energies 6, 9, 12, 16, 20MeV (left to right red, blue, green, cyan, black respectively).

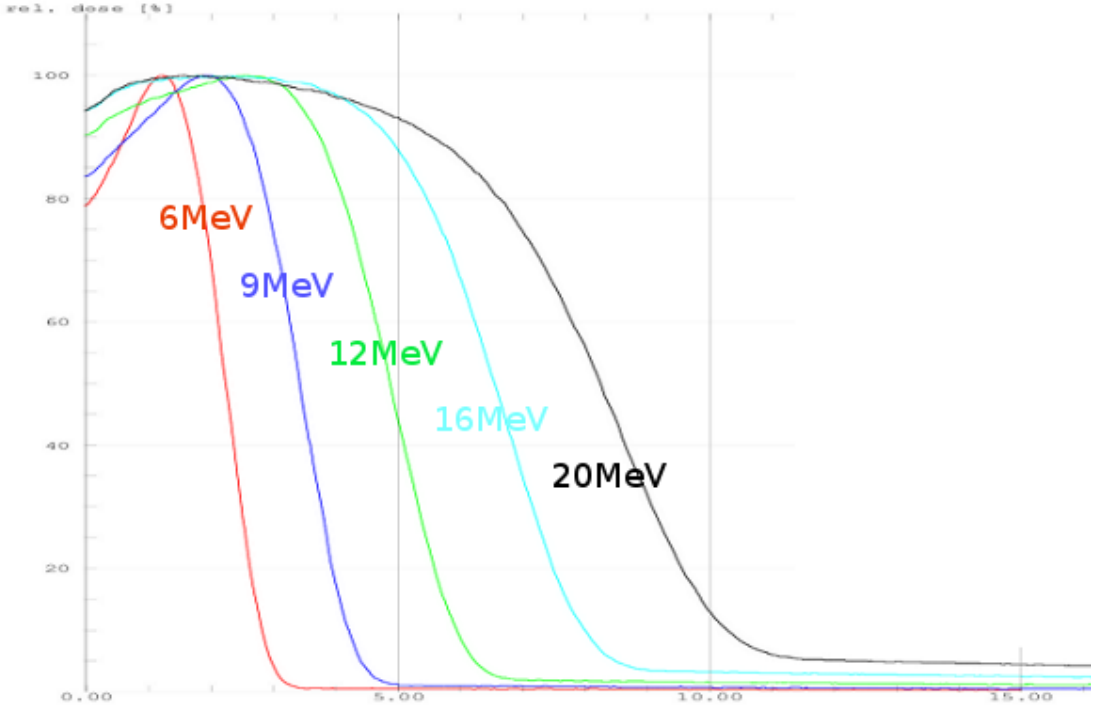

Illustration 11: PDI Electron beams Field Size 15x15cm

It can be observed that for each subsequently higher electron energy there is a correspondingly higher relative surface dose with the dose ranging from approximately 80% to 95%. The depth of the dose maximum generally increases as does the width of the therapeutic (R_{90}) region.

These effects can be explained by the nature of electron interactions and scatter. Assuming a parallel incident electron fluence on a water surface, as soon as the electron beam interacts with the water energy is deposited and scattering begins. At lower initial energies, electrons are more easily scattered (resulting in further energy loss) and through larger angles. As the

energy degrades the scattering becomes easier and the electron paths becoming more oblique to the initial direction. This causes the dose build up to occur more rapidly and over shorter distances. The reason for this is the multiple scattering that results in an increase of electron beam fluence along the central axis (Khan, 1991, Klevenhagen, 1985, Gunhan et al., 2003, Khan, 2010).

At a higher electron energy, the initial angle of scatter is less oblique than before, that is the electrons initially follow a relatively straight path compared to the low energy electrons. As the beam penetrates the medium its energy degrades scattering increases and the electron paths become more oblique to their original axis.

The bremsstrahlung tail also increases from about 1% for the 6MeV beam to approximately 5% for the 20MeV beam. The Bremsstrahlung is a result of the electron beam passing through and interacting with the accelerator exit window, scattering foils, monitor chambers, collimators and air.

The curves presented in this sub section are not dissimilar to curves published by other authors (Klevenhagen, 1985, Hogstrom and Almond, 2006, Khan, 2010).

2.2.1.2 PDD Dependence on Field Size

Electrons are known to display a field size dependence (Klevenhagen, 1993, Podgorsak, 2005, Khan, 2010) as shown in the example in Illustration 12.

For all energies when the field size is reduced the surface dose generally increases and the depth of the dose maximum moves towards the surface. These changes affect the clinically relevant portion of the electron beam. Distinguishing between large and small field sizes is dependant upon the electron range, The field is considered small if the cross section is small compared to the electron range in the medium. If the distance between the central axis and field edge is less than the lateral range of scattered electrons, lateral scatter equilibrium cannot exist and the central axis dosimetric quantities are affected (Klevenhagen, 1985, Klevenhagen, 1993).

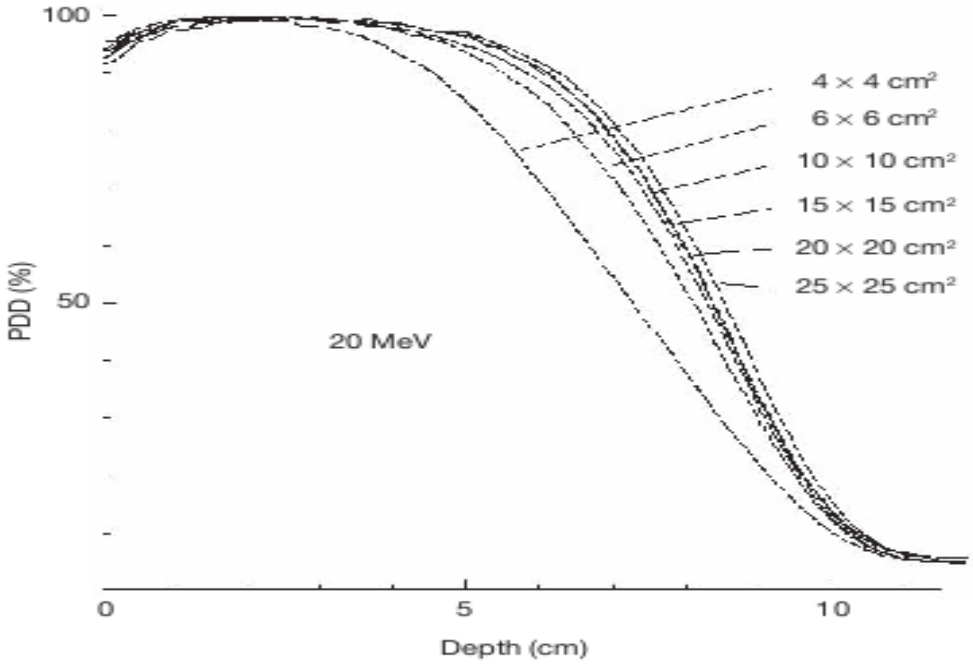

Illustration 12: PDD 20MeV by Field Size (Podgorsak, 2005)

2.2.1.3 PDD Dependence on Angle of incidence

Oblique beam incidences that exceed 20° to 30° with the water/patient surface have an effect on the the PDD characteristics (Ekstrand and Dixon, 1982, Klevenhagen, 1993, Chow and Grigorov, 2007, Khan, 2010). The distribution of electron scattering is perturbed with an increase in the laterally scattered electrons at d_{MAX} which become more influential on the generation of the PDD curve.

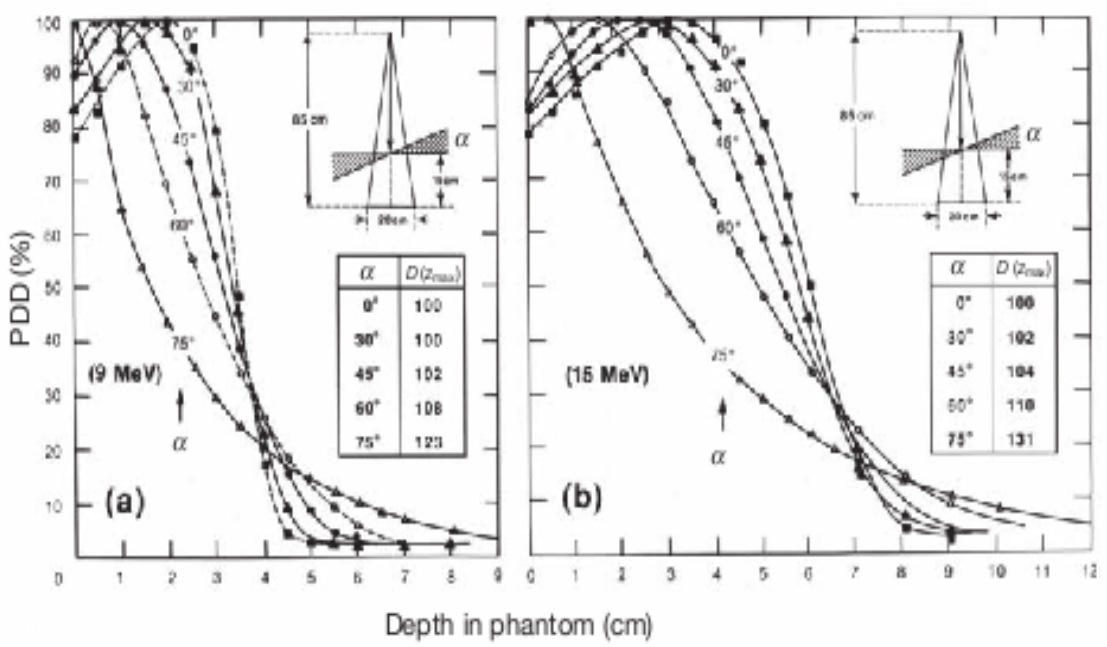

Illustration 13: PDD at various beam angles (a) 9MeV (b) 15MeV (Podgorsak, 2005)

llustration 13 demonstrates that as the angle of incidence increases the characteristic PDD shape changes with the d_{MAX} moving towards the surface. At angles that exceed 60° the PDD looses it characteristic shape and the definition of R_P can no longer be applied (Klevenhagen, 1993, Podgorsak, 2005, Levitt et al., 2006, Khan, 2010).

To avoid or minimise the complications that are described in 2.2.1.1 PDD Dependence on Energy to 2.2.1.3 PDD Dependence on Angle of incidence it was decided to limit this thesis to 2 electron energies, a single field size and 0° incident beam.

2.3 Ionisation Chambers

Radiotherapy dosimetry is typically carried out with ionisation chambers and a variety of different designs are available for different purposes. The two of particular interest being the thimble chamber and parallel plate chamber. These are, in principle, simple gas filled detectors, (Illustration 2) consisting of a non conducting gas sandwiched between a pair of electrodes. When a voltage is applied across the electrodes an electric field is established

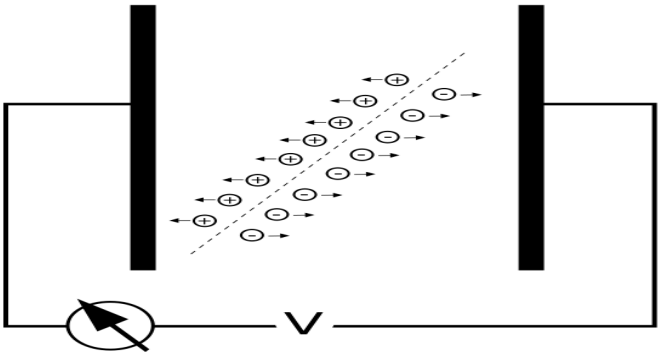

Illustration 14: Simplified Ionisation Chamber (Wikipedia)

between the electrodes which causes any charges created within the cavity (by the passage of ionising radiation), to migrate to the electrodes resulting in a current between the electrodes. Ideally, the collected charge is proportional to the dose that would have been delivered in free space (Mann et al., 1980, Van Dyk, 1999). Whilst this may apply simplistically in air, what is required is the measurement of dose within tissue. Ideally the dosimeter should be at the very least tissue equivalent in terms of atomic composition, homogeneity, and density . Clearly this is not the case for a gas filled cavity within tissue and invites the need for some relationship between what may be measured in the gas cavity and what would have been measured if the cavity was filled completely with tissue (Higginbotham, 1996, Knoll, 2000). The Bragg-Gray principle/theory is the method by which adsorbed dose in tissue can be deduced from the ionisation in the gas cavity (Knoll, 2000).

Utilising The Bragg-Gray Cavity Theory it is assumed that:

(a) the introduction of a sufficiently small cavity into the medium does not perturb the radiation field within the phantom.

(b) the ionisation collected within the gas filled cavity is deposited solely by charged particles crossing the cavity, that is it is proportional to the energy absorbed in the

surrounding medium, at the same location if the chamber was not present.

The first assumption a) is very difficult to achieve as the introduction of a cavity always results in an alteration of the number or distribution of electrons present and hence there is always the need to apply appropriate perturbation correction factors.

The second assumption b) requires conditions satisfied by the particles depositing dose within the cavity are created outside of the cavity, completely pass across the cavity, are not created in the cavity and do not stop in the cavity (Van Dyk, 1999, Podgorsak, 2005, Khan, 2010).

The quantity that determines how much energy is deposited, (discussed in *Chapter: 1.2.1 Stopping Powers*), in the cavities active volume of the chamber is the stopping power S. As already discussed in *Chapter:1.2 Electron Interactions*, charged particles can not only cause local ionisations and bremsstrahlung but can also interact in hard collisions resulting in the production of delta (secondary) rays (electrons), with sufficient energy to cause further ionisations, some of which escape the cavity carrying away energy from the original particle track. The Spencer-Attix cavity theory, an extension to the Bragg-Gray cavity theory, is a more general formulation that applies the Bragg-Gray conditions to both the primary and secondary particle fluence. The theory ignores the contribution of locally deposited energy from delta electrons with energy greater than a threshold by restricting the stopping power to delta electrons with energies below this threshold. (Van Dyk, 1999). Whilst Spencer-Attix theory starts to account for the actual situation it does not correct for every non ideal parameter and several other correction factors have to be introduced especially in the case of Absolute Dosimetry.

These corrections can include; (Andreo, 2000)

- Wall Correction factor (P_{wall}) - accounting for the non-medium equivalence of the chamber wall;
- Recombination Correction (k_S) - correction of the response due to the lack of complete charge collection;
- Temperature, Pressure and Humidity Corrections;
- Cavity Correction (p_{CAV}) - to account for in-scattering of electrons that makes the fluence inside the cavity different from that in the medium;
- Central Electrode Correction (p_{cel}) – accounting for non air equivalence of a thimble chamber central electrode.
- Displacement Correction (p_{dis}) – corrects for the effect of replacing a volume of water

with the detector cavity when the reference point of the chamber is taken to be at the centre of the chamber.

It is not the intention of this thesis to discuss or investigate these correction factors rather to simply alert the reader of their existence and to additionally illustrate that the calculation of dose in a medium with an ionisation chamber is a non trivial process.

Despite these necessary complex process', ionisation chambers remain the most commonly used instruments for measurement of dose. They are readily available, portable, and easy to use; and measurements performed with them are highly reproducible (Khan et al., 1991a).

2.3.1 Thimble Chambers

Probably the most common cylindrical ionization chamber is the 0.6 cm3 chamber designed by Farmer (with modifications in 1972) and whilst it was originally manufactured by Baldwin, is now available from many manufacturers. The chamber's sensitive volume is somewhat similar in shape to a thimble, and hence the Farmer type chamber is also referred to as a thimble chamber (Podgorsak, 2005).

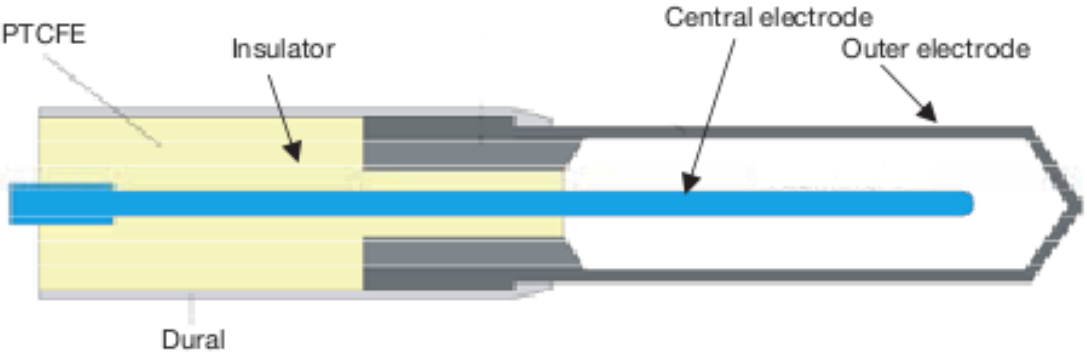

Illustration 15: Farmer Chamber (Podgorsak, 2005)

In the picture (Illustration 15) the chamber is shown to be constructed of an outer electrode (thimble) and the inner or central electrode. These electrodes can be constructed of different materials, such as graphite, Shonka plastic and aluminium, all of which can affect how the chamber responds. The chambers need to be robust and respond consistently to a variety of poly-energetic beams from nominal useful energy range of 30keV to 50MeV depending on their intended application.

The thimble type chambers used in this thesis are of similar design although somewhat more compact than the Farmer Type.

Compact chambers have arisen out of a need to measure more accurately small fields and high

dose gradient regions of beams.

The Wellhöfer IC-15 (CC-13) and Wellhöfer CC-04 Compact Ionisation Chambers are designed for scanning in the Wellhöfer Blue Phantom. The chambers feature high spatial resolution and a Shonka air-equivalent C552 thimble & electrode. Venting is accomplished through the waterproofing sheath and the chamber connector (Wellhöfer, IBA Dosimetry Schwarzenbruck Germany). A summary of the chambers key characteristics are included in table 1 see also Illustration 17 & 18

Model	**IC-15**	**CC-04**
Volume:	0.13 cc	0.04 cc
Sensitivity:	0.044 nC/cGy	0.013 nC/cGy
Active length:	5.8 mm	3.6 mm
Inner diameter:	6.0 mm	4.0 mm
Wall:	C552, 0.4 mm thick, 70 mg/cm2	C552, 0.4 mm thick, 70 mg/cm2
Electrode:	C552, 1 mm diameter	C552, 1 mm diameter

Table 1: Wellhöfer, IBA Dosimetry Compact Ionisation Chambers

2.3.2 Parallel Plate Chambers

A parallel-plate ionisation chamber design is more complex than a thimble and whilst it consists of two plane walls, in an arrangement much along the lines in the diagrammatical representation of Illustration 2 their separation is only of the order of 1-2mm.

One of the parallel plates acts as the entrance window (polarising electrode) and the other becomes the back wall (collecting electrode) the complexity is the addition of a guard ring system, outside the collection electrode, and sometimes backscatter material.

The guard ring has two functions;

a) it is at the same potential as the collection electrode and thus ensures a homogeneous electric field between the electrodes, it also,

b) if sufficiently wide, prevents electrons, scattered from the chamber walls from being collected (Van Dyk, 1999, Podgorsak, 2005).

A schematic (Illustration 16) of the parallel plate chamber shows the collecting electrode (denoted as 2) and the guard ring (denoted as 3).

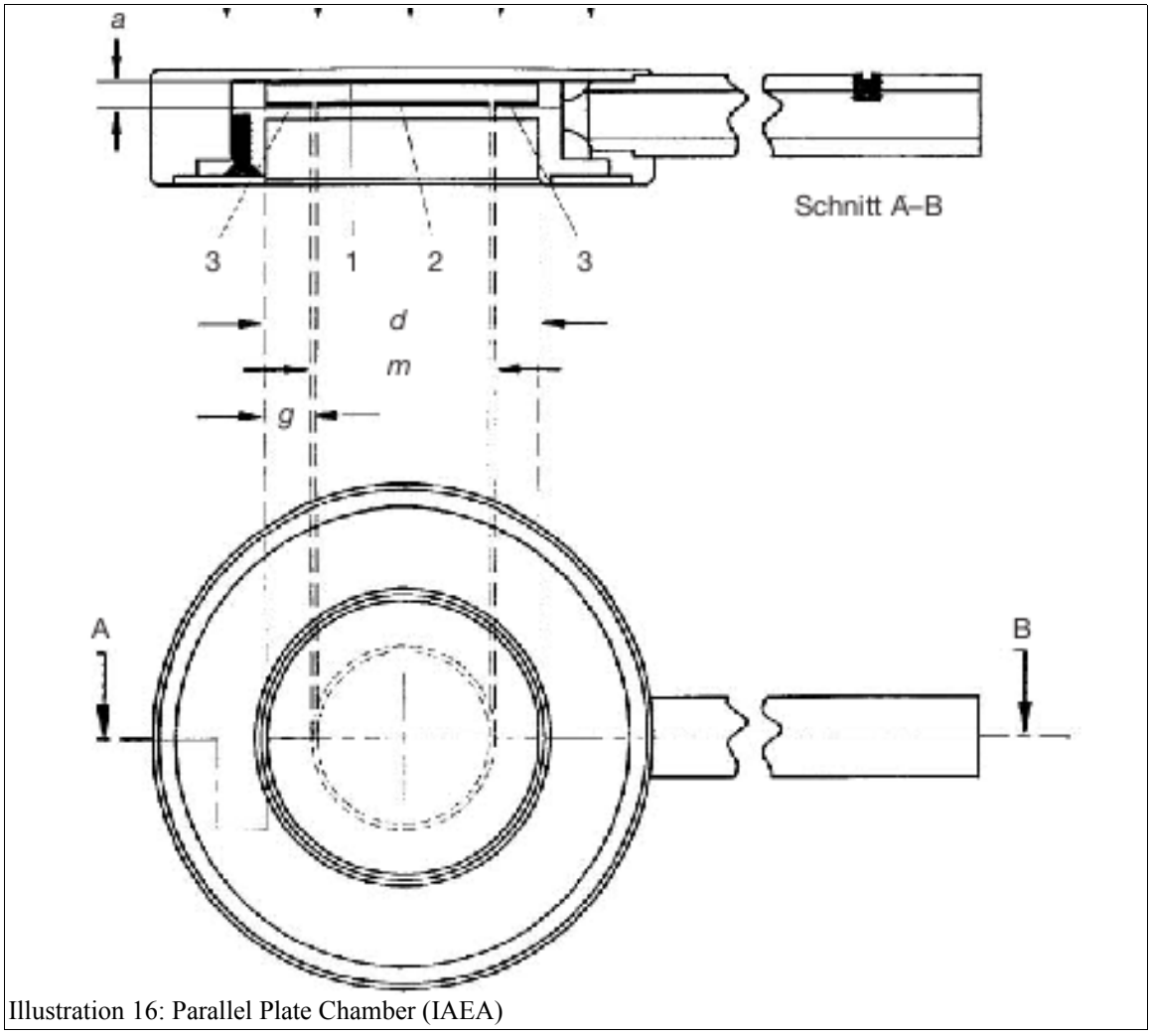

Illustration 16: Parallel Plate Chamber (IAEA)

Ideally the chamber is constructed in a material that is of a similar composition of the medium in which the chamber is intended to be used, thus avoiding interface problems (Van Dyk, 1999).

The parallel-plate chamber is recommended for dosimetry of electron beams with energies below 10 MeV (Andreo, 2000). Characteristics of the parallel plate chamber used in this thesis Wellhöfer PPC-40 Roos Type are summarised in table 2.

	PPC40
Volume (nominal):	0.4 cm3
Cylinder Height:	2.0mm
Front Window Thickness:	1.0 mm PMMA 118gm/cm^2
Diameter of Inner Electrode:	16.0 mm
Guard Ring Width:	4.0 mm

Table 2: Wellhöfer, PPC-40 Roos Type PP Chamber

2.4 Data Collection

All data collected was performed with ionisation chambers as outlined in *Chapter:2.1 Equipment & General Data Collection Conditions*. Initially an IC-15 chamber depth ionisation curve was obtained for both the 9 and 20MeV (nominal energy) beams and the R_{80} compared with ROV's existing data (circa 1999). Although the IC-15 (now called CC-13) chambers may be considered relatively large (6mm inner diameter, volume 0.13cc) (Illustration17) for obtaining measurements of this type, their use permitted direct comparison with existing institutional data with which all Linacs at ROV are matched and beam models generated in the Radiotherapy Treatment Planning System (RTPS).

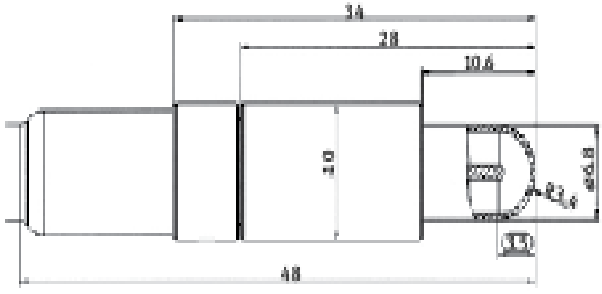

Model CC13 (formerly IC-15, IC-10)
Volume: 0.13 cc
Sensitivity: 0.044 nC/cGy
Active length: 5.8 mm
Inner diameter: 6.0 mm
Wall: C552, 0.4 mm thick, 70 mg/cm²
Electrode: C552, 1 mm diameter

Illustration 17: IC-15 (CC-13) Compact Ionisation Chamber (Wellhöfer IBA Dosimetry Germany)

The depth ionisation scan is a semi-automatic function within the Wellhöfer scanning software where the system constantly measures the dose whilst the ionisation chamber is driven from a set depth towards the surface along the central axis of the beam.

Scanning of the beam in this direction reduces the effect of meniscus formation on the chamber. It is necessary to control the speed of ascent of the chamber whilst the scan is being taken, permitting many data points to be obtained in areas of particular interest. Scan speeds that are too great can affect the accuracy of the measurements (further discussed in *Chapter 2.7 Smoothing Algorithms*) and need to be optimised in regions such as near D_{MAX}. especially for low energy electron beams where the D_{MAX} curve tends to be peaked. It is also recommended that smoothing software should be applied to ALL measured data whenever possible to minimise noise and small variations in the readings (Khan et al., 1991b, Andreo, 2000, Gerbi et al., 2009).

A series of inplane profile scans, (the chamber is driven along the inplane axis at fixed depth), were taken at 1cm intervals from 15cm to 0.5cm depth as a dual purpose;

a) to act as a 'check set' to ensure any scans extracted from the measured inplane-nets (2D scan where the chamber is driven along the inplane axis at sequential depths generating a grid) were not corrupted by either the acquisition or extraction process,

b) to provide scans for further comparison with existing data.

Similar to the depth ionisation scans it is necessary to control the chamber speed to ensure the scanning speed does not result in either noisy scans or ripples in the acquired data due to wave motion induced by the movement of the scanning arm (Das et al., 2008).

The inplane-nets measured with the IC-15 chamber had the central axis of the chamber positioned along the inplane direction of the machine and parallel to the water surface with the chamber sensitive volume/stem arranged in a target/gun orientation respectively (see Illustration 17).

The CC-04 inplane-nets were also taken in the inplane direction however the chamber was orientated in the vertical position with the sensitive volume towards the water surface. The construction of the CC-04 chamber, (Illustration 18) the stem being larger than active volume, may have resulted in a disturbance of the water surface during the inplane-net measurements before the sensitive volume had reached the water surface potentially affecting results.

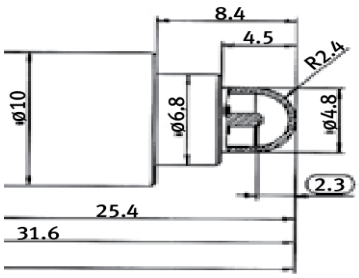

Model CC04 (formerly IC-04)
Volume: 0.04 cc
Sensitivity: 0.013 nC/cGy
Active length: 3.6 mm
Inner diameter: 4.0 mm
Wall: C552, 0.4 mm thick, 70 mg/cm²
Electrode: C552, 1 mm diameter

Illustration 18: CC-04 Compact Ionisation Chamber (Wellhöfer, IBA Dosimetry, Germany)

To ensure that the orientation of the chamber did not affect results significantly depth ionisation scans were also obtained with the CC04 chamber in a horizontal orientation, as per IC-15 chamber, and found to be indistinguishable within experimental tolerances.

The inplane-net scans, (IC-15 and CC-04 chambers), movement limits were adjusted to ensure that the maximum depth extended beyond the nominal energy practical range (R_P) by a

minimum of 4cm and in the inplane direction the scans were extended beyond the 1% isodose value at all depths with the distance between any two subsequent scans set at a 1mm spacing. All data acquired was saved in an unaltered "raw" form for future analysis.

2.4.1 Depth Ionisation to Depth Dose Conversion

It was noted in Chapter 2.2.1 Central Axis Percentage Depth Dose that it was not possible to measure a depth dose directly with an ionisation chamber in an electron beam. The chapter mentioned the need to convert the Depth Ionisation to Depth Dose by converting with the Stopping Power Ratio $s_{w,air}$. Whilst the Chapter was particularly considering the conversion for the Percentage Depth Dose it is by extension, also necessary to make similar conversions of the Depth Ionisation Nets obtained later in this thesis.

The $s_{w,air}$ ratios have been the interest of several authors over the years with Berger & Seltzer acknowledged as the pioneers in using Monte Carlo simulation of electron fluence in the application of $s_{w,air}$ calculation. Their work has been published as Recommendations by the Nordic Association of Clinical Physicists (NACP) 1980, and was based on monoenergetic-beam data particular for a mean electron energy determined at the phantom surface which is not representative of a typical clinical beam or current dosimetry protocol approach (Andreo, 2000, Mayles, 2007). Work subsequent to Berger & Seltzer, have developed newer stopping power ratio data which is more representative of clinical electron beams currently in use ((Malamut et al., 1991, Ding, 1995, Burns et al., 1996).

To apply the stopping power ratios over a range of depths other than just R_{50} the data was fitted to an equation of the form

$$s_{w,air}(z) = \frac{a + bx + cx^2 + dy}{1 + ex + fx^2 + gx^3 + hy}$$

where $x = \ln(R_{50})$ and $y = z / R_{50}$ is the relative depth.

with a = 1.075 b = -0.5087 c = 0.0887 d = -0.084

e = -0.4281 f = 0.0646 g = 0.00309 h = -0/125

The ionisation point is multiplied by the correction factor resulting in the dose point at a particular position at depth.

2.5 Specific Measurement Conditions

All measurements were performed on a Varian 21EX Linac as described in *Chapter 2.1 Equipment & General Data Collection Conditions*. All measurements were taken in the same configuration as that used for the collection of commissioning data for each available electron energy specifically 6, 9, 12, 16, 20MeV at 100cm nominal source to water surface distance using the standard 15x15cm applicator.

Data was collected with the Linac beaming continuously at a high repetition rate (600MU/minute) using one of three ionisation chamber combinations;

a) IC-15 Field and Reference chamber;
b) CC-04 Field and Reference chamber;
c) PPC-40 Field & IC-15 Reference chamber.

In each combination the reference chamber active volume was located in a position above LMA insert but beyond the corner of the exposed 15x15cm field. The clinical electron field size as defined by the final 15x15cm collimating insert, above the insert the electron field is approximately 1cm larger in both crossplane and inplane dimensions. By placing the reference chamber in this location, permits the reference chamber to be irradiated by the electron beam whilst being shadowed from the clinical field by the LMA insert and hence any perturbations caused by the chamber are primarily shadowed by the LMA insert and contribute a minimal effect on the measured beam characteristics.

It is essential that the field ionisation chamber always traverses the water tank from depth to the surface to reduce the effect of meniscus formation. The chamber must also be carefully aligned at the water surface as even small errors (1mm) can result in incorrectly calculated beam qualities.

The field chambers (IC-15 & CC-04) were inserted and clamped into their appropriate holders attached to the motion rails within the tank, this ensures that the chamber stem is perpendicular to the rail. The chamber holder was then adjusted until the chamber stem was parallel with the water surface by aligning to the reflection. The active volume of the chamber was aligned in the water tank using the Wellhöfer provided alignment cap, an opaque cylindrical plastic cap, which has a pair of perpendicular diameter lines etched on the end that continue along the length of the cylinder plus a single circumferential line approximately

5mm from the end. When the cap is on the IC-15 chamber the intersection point of the lines on the end indicates the centre of the central electrode and the circumferential line indicates the centre of the active volume.

Viewing the alignment cap through the clear tank walls, from below the water level, and with the cap rotated such that the lines are at 45° with the water surface, the chamber was moved up and down, via the tank hand control, until an image of perpendicular lines was formed.

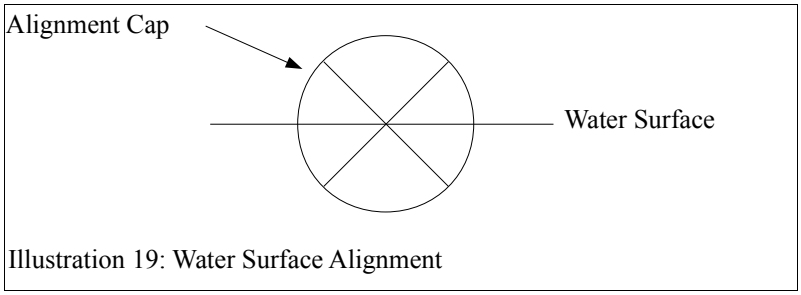

Illustration 19: Water Surface Alignment

This location was defined as the water surface via the remote control. The levelling of the tanks motion rails were confirmed by moving the chamber, with alignment cap, to the four corners horizontally and ensuring that the image of perpendicular lines remained. The alignment cap was removed for measurements and a correction for the effective point of measurement (EPOM) of the chamber was applied via the Wellhöfer software.

For the Wellhöfer PPC-40 parallel plate field chamber, an alternate chamber holder replaced the IC-15 holder and a PPC-40 specific alignment jig (a circular ring with three small inverted cones evenly spaced on the upper side) was used.

In a similar fashion to the IC-15 chamber, the PPC-40 chamber's top face was aligned to be horizontal with the water surface in the inplane and crossplane axis utilising the reflection of the jig, particularly the inverted cones, on the water surface. The chamber holder is adjusted until the tips of cones on the jig (actual and reflection) at the water surface just touch. At this position the chamber's front surface was parallel with the water surface in both the cross plane and inplane axis, the jig was removed and the chamber driven slowly upwards until the front (top) face just touched the water surface. This point was then defined as the water surface via the tank hand control. As before the correction for EPOM was included in the software.

The CU500E Electrometer/Controller was programmed according to the manufactures recommendations using continuous sampling, digital division and chamber bias voltage set at

+300V for the collecting electrode. The gain on the electrometer was adjusted such that the signal on the reference chamber channel provided a nominal level of approximately 100%. The field chamber channel gain was then adjusted to provide a signal of approximately 110%-115% with the chamber located on Central Axis at depth of approximate d_{MAX} (2cm) for the 9MeV beam.

Once the reference and field gains were adjusted as described, the beam was terminated and a background leakage subtraction process initiated.

Prior to accepting the calculated results obtained from the Wellhöfer water tank and WP700 Software, it is necessary to validate the operation/function of both the Wellhöfer software and the water tank. The numerical results presented for this thesis were all obtained from Wellhöfer calculations performed on data measured in the Wellhöfer water tank it is therefore necessary to know that the chamber positioning is as the software commands. Part of the Quality Assurance program at ROV centres include regular checks of the Wellhöfer water tank chamber positioning movements. The water tank chamber support rails have ruler markings which have previously been verified to correspond with a standards traceable ruler and the QA performed regularly checks that the chamber moves to the correct position.

2.5.1 Effective Point of Measurement (EPOM)

As indicated in *Chapter 2.3 Ionisation Chambers* the introduction of an ionisation chamber always results in a perturbation of the field for which corrections must be applied. In addition, although the chamber was set-up on the central electrode axis, it is known that this is not the point at which the chamber actually measures ionisation (Huang et al., 2010, Khan, 2010, Looe et al., 2011). For a cylindrical ionisation chamber the concept of an effective point of measurement (EPOM) was introduced. Experimentally this can be determined by comparing percentage depth-dose curves measured with a well guarded parallel plate chamber and with a thimble chamber. Considering the IC-15 chamber and referring to the dosimetry protocol (TRS-398), which defines the EPOM as being 0.5 times the internal radius of the thimble, would result in a calculated EPOM as 1.5mm above the central electrode for the chamber. Wellhöfer recommends their empirically calculated, EPOM corrections (determined by comparison measurements) are used with the IC-15 chamber, see table 3,

Energy	Displacement	% of r
4 - 8MeV	1.6mm	0.53
9 - 16MeV	1.8mm	0.6
>16MeV	2.0mm	0.66

Table 3: Wellhöfer Electron Effective Point of Measurement IC-15

which are applied automatically by the Wellhöfer WP700 system when the chamber has been correctly entered into the software and EPOM corrections selected (Degener, 1998b).

The differences between Wellhöfer EPOM, the dosimetry protocol recommendation plus the fact that the CC-04 chamber was post WP700V3.51 software particularly in the orientation used and there weren't any Wellhöfer recommended numbers, presented this thesis with an obvious question of what figures should be used for the CC-04 chamber.

Several authors have discussed the protocol recommendations (Das et al., 1998, Wang and Rogers, 2009b, Huang et al., 2010); and most recently (Looe et al., 2011). Das et al 1998 illustrated that this subject has been under discussion for a considerable time acknowledging different investigators Attix 1986, (Dutreix and Dutreix, 1966, Weatherburn and Stedeford, 1977), TG-21 1983(Almond et al., 1983), IAEA 1987 all of which have shown a range for the EPOM shift from 0.33r to 0.85r related to the energy of the beam. In their own investigation (Das et al., 1998) has suggested that the correction ranged between 0.9r to 0.5 r for 6 to 20MeV respectively. Huang (Huang et al., 2010) has also determined a shift in the EPOM although their results were completely the opposite to those of Das et al. (Das et al., 1998) for which they could not provide an explanation, they did however recommend that the position of Peff of a cylindrical chamber should be experimentally determined for each electron beam.

To complicate the issue further other authors have questioned whether the EPOM of a well guarded parallel plate chambers (eg Roos Type Chamber used in this thesis) is at the front surface of the air cavity as stated by the dosimetry protocol. Wang and Rodgers (Wang and Rogers, 2009a) suggested the effective point of measurement may be shifted toward the cavity centre by as much as one-half a millimetre. In their paper Looe et al, (Looe et al., 2011) provides a table reporting the work of several other authors Zink & Wulff, Lacroix et al (Zink and Wulff, 2009, Lacroix et al., 2010), Bruggmoser et al 2007(in German) & Looe et al 2007 (German Text) which similarly support their announced shift, for 6 and 9MeV electrons, of 0.4 ±0.1mm towards the cavity centre for the Roos chamber. Quite recently work by Ono et al

(Ono et al., 2011) provide similar figures.

Determining an appropriate EPOM for the CC-04 chamber at the different beam qualities used in this thesis, with the chamber in the vertical orientation, may be worthy of its own scientific investigation and publication however it was beyond the scope of what was required for a sub section of this thesis.

Rather than attempting to characterise the chamber, and for simplicity it was decided to apply a single EPOM for the CC-04 chamber for all electron energies accepting that at lower energies there will be some error.

With reference to the dimensions shown in Illustration 20, it was considered that the internal radius was 2.0mm, although it could be argued that there may only 1.9mm between the tip of the central electrode and inner wall of the thimble. This difference was considered within the error of what could be set with the Wellhöfer software and set-up error within the watertank.

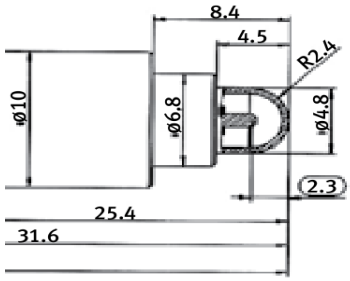

Model CC04 (formerly IC-04)
Volume: 0.04 cc
Sensitivity: 0.013 nC/cGy
Active length: 3.6 mm
Inner diameter: 4.0 mm
Wall: C552, 0.4 mm thick, 70 mg/cm²
Electrode: C552, 1 mm diameter

Illustration 20: CC-04 Chamber Dimensions

The average of the Wellhöfer percentage displacements of the IC-15 chamber (0.6r) was used providing an EPOM as 1.2mm. This figure was then used as the default displacement when the CC-04 chamber was used. Comparison of the depth ionisation scans Illustrations 30 to 34 demonstrate a very good agreement between the CC-04 and Roos chamber using the chosen EPOM for at least energies 9, 12, 16, 20MeV. The experimental results presented validate the use of the CC-04 chamber for further measurements and the confirmation of unchanged beam qualities since acceptance and commissioning data was obtained in 2005.

2.6 Bolus Materials

It is known that an electron beam will lose energy as it traverses through a material. As soon as the beam enters the material scattering and energy loss occurs. When an electron beam travels through tissue the energy decreases approximately linearly and the spectrum becomes broader with depth (Khan, 2010). As a very basic starting position for this thesis it was assumed that applying a bolus material (tissue like phantom) to the applicator would degrade the electron beam in a fashion somewhat similar to how an electron beam energy degrades with depth in tissue.

Although Podgorsak (Podgorsak, 2005) provides the simple Harder equation which relates the mean energy at depth in a water phantom Ez to the practical range Rp namely

$$Ez = E0\ (1 - z/Rp)$$

it is known that caution has to be used when applying this equation as it has limitations. The equation is only acceptably accurate for low-energy beams (<10MeV) and for shallow depths at higher energies. It is rather recommended that Monte Carlo calculations for Ez (Andreo and Brahme, 1981) independently confirmed by others (Ding and Rogers, 1996, Fernandez-Varea et al., 1996) be used (Andreo, 2000, Thwaites et al., 2003).

It must be remembered that either the Harder equation or the Monte Carlo calculations only apply to water as the medium and clearly that was not the material used as bolus in this thesis. There was a need to determine the equivalence of the thesis bolus material to that of water before the simple Harder equation could be applied. It was acknowledged that the ideal approach would have been applying a Monte Carlo approach however that exceeded the scope of the planned thesis.

For a material to be considered water equivalent its Linear Collision Stopping power, Linear Radiative Stopping Power and Linear Angular Scattering Power need to be the same as water. Investigations into the water equivalence of several materials have been studied by different authors including (Bruinvis et al., 1985, Thwaites, 1985, Low and Hogstrom, 1994, Tello et al., 1995, Thomadsen et al., 1995, Babic et al., 2002, McEwen and DuSautoy, 2003, Casar et al., 2004, Borcia and Mihailescu, 2008) all of which illustrated that there isn't an exact, although some better than others, match.

Dosimetry protocols IAEA TRS-398, AAPG TG-25 & TG-51, IPEM2003 (Andreo, 2000,

Khan et al., 1991a, Almond et al., 1999, Thwaites et al., 2003) have attempted to address this non equivalence by using a scaling procedure which converts ranges and depths measured in plastic phantoms to equivalent depths in water. Following the recommended approach of TRS-398 (Andreo, 2000) it is possible to calculate an approximate equivalent water depth for the Perspex used in this thesis by the following equation;

$$Z_W = Z_{pl}\, c_{pl} \text{ g/cm}^2 \ (Z_{pl} \text{ in g/cm}^2) \qquad Z_{pl} = \text{depth in plastic(cm) x plastic density } \rho_{pl}$$

IAEA TRS-398 provide for perspex (PMMA); c_{pl} = material scaling factor to convert ranges and depths measured in phantoms to equivalent values in water = 0.941, ρ_{pl} =1.19 (with a recommendation that ρ_{pl} is measured by the user). Having evaluated the perspex used in this thesis and finding it to be approximately 1.18 rather than the suggested density of 1.19 the equivalent depths were calculated (see table 4).

Perspex	**1 x 6mm**	**2 x 6mm**	**3 x 6mm**
Water-equivalent thickness (mm)	6.7	13.3	20

Table 4: Perspex Water Equivalent Depths

The scaling factor provided by the protocol is an average of scaling factors across the clinically useful energy range and strictly only applies to depth dose distribution and their use in scaling depth ionisation distributions is an approximate.(Andreo, 2000)

Attempting to apply a similar approach for Teflon is complicated by the fact that the dosimetry protocols do not provide any data comparable to what is listed for perspex. Teflon is not considered in any of the previously mentioned dosimetry protocols (AAPM TG25, IAEA TRS398 & IPEM2003) as a tissue substitute, although it is used by some manufacturers of radiotherapy phantoms as a “tissue like” electron density substitute for example Catphan® 504 the fact remains that there aren't factors available to calculate a water equivalent depth.

ICRU Report-35 (ICRU, 1984) does provide a method by which an approximate water-equivalent depth can be calculated utilising the Continuous Slowing Down Approximation (CSDA) range ratio of water to solid phantom. The approximation assumes that ranges in materials are proportional to the CSDA range, however this approach is limited in its approximation as it only accounts for continuous collision and radiative energy loss.

The CSDA range represents the path length of an electron track and is not the depth of penetration of the electron in a material as it does not account for multiple scattering which

can appreciably affect the penetration depths of electrons. This difference was also recognised by several authors and other scaling methods have been proposed. Grosswendt and Roos (Grosswendt and Roos, 1989) identified the scaling law developed by Harder, which took into account the relationship between ranges and path lengths utilising so called detour factors. Sorcini and Brahme (Sorcini and Brahme, 1994) also sought to improve the CSDA approach by proposing a scaling law containing ratios of CSDA ranges and detour factors. The ICRU Report 49 (ICRU, 1993) includes a section describing detour factors as an appropriate process to account for the differences between the average penetration depth and the CSDA range. (Fernandez-Varea et al., 1996)

"Detour factors have long been recognised as a parameter providing an estimation of the combined effect of continuous energy losses and multiple scattering when charged particles penetrate condensed matter" (Fernandez-Varea et al., 1996) attributing their initial identification to Bothe 1933 & Bethe et al 1938.

Tabata and Andreo have further extended the formula presented by Fernandez-Varea et al to produce two semi-empirical equations to determine detour factors in condensed materials, identifying that previously proposed formulas were not accurate enough to explain the small differences among light phantom materials used for medical purposes. Their first equation is applicable to light compounds and mixtures with a mean atomic number between 4.75 and 6.6, whilst their second equation, considered less precise, provides a formula applicable to a wide atomic number range. Whilst the second formula is considered less precise the authors have compared the deviation of the semi-empirical formula with Monte Carlo calculations and determined a maximum deviation of 0.9% (Tabata and Andreo, 1998).

Using the formula and substituting as appropriate it is possible to calculate detour factors (df) for Teflon at the two incident energies used in this thesis, at 9MeV df= 0.688 and 20MeV df=0.776. Utilising these factors and values from ICRU Report-35 an approximate range scaling can be be calculated (see table 5).

Teflon	**1 x 3mm**	**2 x 3mm**	**2 x 3mm+4.6mm**
9MeV water-equivalent thickness (mm)	6.0	11.9	21.0
20MeVwater-equivalent thickness (mm)	5.9	11.8	20.8

Table 5: Teflon Water Equivalent Depths

Similarly to the problems presented for Teflon, the dosimetry protocols mentioned do not provide any guidance for Aluminium, however by following the approach used for Teflon it is possible to calculate detour factors for the two energies namely 9MeV df= 0.60 and 20MeV df=0.70 which corresponded with figure 3 in the Tabata and Andreo paper. Again as mentioned for Teflon the calculated detour factors and CSDA data from CRU Report-35 an approximate range scaling can be be calculated.

Aluminium	**2.5/2.7mm**	**5.0/5.1mm**
9MeV water-equivalent thickness (mm)	7.5	14.2
20MeV water-equivalent thickness (mm)	7.4	14.0

Table 6: Aluminium Water Equivalent Depths

2.7 Smoothing Algorithms

Smoothing of acquired data is in effect applying a low pass filter that aims to eliminate the high frequencies, the abrupt, sharp spikes that are on the underlying signal (Das et al., 2008).

All data measured with the Wellhöfer CU500E & WP700V3.51 system has, to a varying degree, some noise which can be related to; the speed of the scan, signal sampling rate, signal processing in the electrometer and the machine output. The Linac produces radiation in a pulsed fashion and it is necessary to only record data whilst radiation is being produced. Whilst the use of a reference chamber ensures that signal is only recorded when it exists in both the reference and field channel it does not control the rate at which the signal is sampled.

Signal processing in the CU500E takes somewhere between 5-10ms between each internal hardware division and combined with the controller's time constant of 20ms results in an approximate maximum number of 20 data points delivered to the computer per second (Degener, 1998a). The speed of the chamber support arms motion in the water tank ranges between 0.1mm and 15mm per second. As the speed of the scan is increased the distance between each data point also increases, at maximum speed one data point is acquired every 0.75mm. The speed of the scan is of particular importance in regions of high dose gradient.

The Wellhöfer software provides 6 smoothing algorithms based on a selectable size moving block, as the block is increased in size so to is the smoothing increased. The smoothing algorithms available are, least square, median, arithmetic mean, geometric mean, envelope, and Bézier. Typically it is necessary to experiment with the smoothing to observe which one provides the most acceptable result without changing the basic shape (Degener, 1998b).

The Wellhöfer WP700 Software manual provides the user with a description of each of the smoothing algorithms and their operation. Wellhöfer utilises a moving block of data, with variable width, selectable by the user (3 to 31), which determines how many data points are used in one smoothing calculation. The selected block moves through the observed data by dropping 1 point on the left and adding 1 to the right, smoothing is then re-performed. As the smoothing calculations are principally based around the central point it is advisable that an odd number of points is selected.

Least Square: fits a function to the data so that the square of the differences of the abscissan between computed and observed numbers is at a minimum. Least Square is reported to be a

good smoothing algorithm as it preserves slope and the maximum is not falsified (Mironov and Elizarova, 2011, Degener, 1998b).

Median: The points in the smoothing block data are arranged in an increasing series, the middle number is taken as a pseudo mean of the moving block central point. Median can retain the slope but not the maximum.

Arithmetic Mean: Values of the moving block are added and divided by the total number of points in the block. The algorithm fails to conserve either maximum or slope.

Geometric Mean: The numbers in the moving block are multiplied and then the root is extracted to get the mean value of the central point. Results of the calculations are correct provided all the numbers are positive. The process does not preserve maximum or slope of the scan.

Envelope: A linear interpolation is performed between the first and last point in the moving block. This does not preserve max or slope.

Bézier: This is the most sophisticated smoothing tool available in the software. The Bézier parametric curve function is generated from control points which are the number of points chosen by the user i.e. the moving block. The Bézier curve in general, does not pass through any of the control points except the first and last and the curve is normally contained within the convex hull of the control points. If multiple control points are added at a single position then the curve is weighted or "pulled" towards that position. As Wellhöfer moves the smoothing block through the data the Bézier curves generated are smoothly joined at the seam of each calculation block. Bézier curves are easy to compute and stable however depending on the number of control points chosen in the moving block will control how quickly this algorithm operates as it requires the computation of higher order polynomials and factorials. The algorithm maintains both slope and maximum (Bourke, 1996, Kim et al., 1999, Kim et al., 2002, Zhu et al., 2009).

3. RESULTS

The results presented in this thesis are divided into sections that cover the following:

- verifying the relationship between thesis data and ROV commissioning data including beam quality determined by PDI, PDD
- determining effect of chamber characteristics
- addition of bolus like material on applicators
- non tissue equivalent, metal grids

3.1 Beam Quality Comparison

The field size chosen (15x15cm) for the measurements of beam quality and used in this thesis was defined by the Varian Customer Acceptance Procedure (CAP) and the Linac's departmental commissioning data. The intention of this section was to validate that the beam qualities had not changed significantly from acceptance/commissioning data.

Using the Wellhöfer IC-15 Compact Ionisation chamber in the Wellhöfer Blue Phantom Percentage Depth Ionisation scans were obtained on central axis and the results of the data analysis presented in Table 7.

ROV uses the 0.1 g/cm^2 variation in the Depth of the 80% ionisation ($R_{80,ion}$) value across all Linacs in the practice when considering whether the beam quality is unchanged. Table 7 indicates a very good agreement between this thesis, acceptance and commissioning data, validating beam energies were unchanged.

	$R_{50,ion}$ g/cm^2 IC-15			**$R_{80,ion}$ g/cm^2 IC-15**		
Energy	**Thesis**	**CAP**	**Commissioning**	**Thesis**	**CAP**	**Commissioning**
9MeV	3.52	3.46	3.51	2.95	2.90	2.96
20MeV	8.16	8.16	8.17	6.51	6.57	6.54

Table 7: $R_{50,ion}$ g/cm^2 $R_{80,ion}$ g/cm^2 Project & Commissioning

See also Illustration 28 and 29 in the appendix page 102 and 103 respectively.

Note: To enable comparison between Thesis, CAP and Commissioning data it was necessary to copy all raw Wellhöfer scans to a single data directory. This action results in changes to the original Wellhöfer file number and as a result the file numbers in the listed illustrations will not correspond with file numbers throughout the rest of this Thesis.

Thesis raw scan 9MeV <00000001> when copied became <00000011> for analysis.

Thesis raw scan 20MeV <00000024> when copied became <00000017> for analysis.

All alterations of scan file number by copying scans were recorded in the experimental data book.

3.2 Spatial resolution as a function of chamber IC-15, CC-04 and PPC-40(Roos Type)

Having confirmed that the beam qualities were unchanged from acceptance/commissioning data it was necessary to validate the use of the CC-04 chamber as an appropriate ionisation chamber for this thesis. The CC-04 chamber's smaller volume may provide a higher spatial resolution than that provided by the IC-15 chamber. However, as the chamber was not positioned in the normal, stem horizontal, orientation, it was necessary to ensure that the stem vertical orientation did not significantly affect results.

As previously indicated extreme care is required when positioning the chamber in the water tank as electron profiles are very sensitive to set-up errors in depth. In a similar fashion to the process explained previously the chamber was inserted into a holder and aligned to be vertical referenced against the bunker lasers. Using the reflection method, the tip of the chamber was aligned to the water surface and then displaced upwards to account for the chambers estimated EPOM. Wellhöfer does not provide guidance in using their chambers in such an orientation and therefore it was necessary to estimate a position following the guidance for cylindrical chambers in the dosimetery protocol TRS-398 (Andreo, 2000) and other writings (discussed previously see *Chapter 2.5.1 Effective Point of Measurement (EPOM)*).

PDI curves were measured and the results of the numerical analysis are presented in table 8. See also Illustrations 30, 31, 32, 33, 34 on pages 105 to 109 in the appendix

Comparison of the $R_{50,ion}$ and $R_{80,ion}$ g/cm^2 for the 3 chamber types IC-15, CC-04, & Roos indicate excellent agreement for electron energies above 10MeV namely 12MeV ,16MeV and 20MeV. Chamber agreement for 6MeV & 9MeV were less consistent.

	$R_{50,ion}$ g/cm^2			**$R_{80,ion}$ g/cm^2**		
	IC-15	**CC-04**	**Roos**	**IC-15**	**CC-04**	**Roos**
6MeV	-	2.28	2.39	-	1.90	2.01
9MeV	3.52	3.47	3.51	2.95	2.95	2.99
12MeV	-	4.90	4.89	-	4.14	4.17
16MeV	-	6.49	6.51	-	5.42	5.40
20MeV	8.16	8.17	8.16	6.53	6.50	6.48

Table 8: $R_{50,ion}$ g/cm^2 & $R_{80,ion}$ g/cm^2 for thesis chambers

To ensure that comparisons between $R_{50,ion}$ g/cm^2 & $R_{80,ion}$ g/cm^2 from PDI's did not mask actual differences in PDD's a further analysis was performed as shown in table 9.

	R_{50} g/cm^2			**R_{80} g/cm^2**		
	IC-15	**CC-04**	**Roos**	**IC-15**	**CC-04**	**Roos**
9MeV	3.56	3.50	3.55	3.01	2.99	3.04
20MeV	8.37	8.40	8.41	6.94	6.96	6.95

Table 9: R_{50} g/cm^2 & R_{80} g/cm^2 for thesis chambers

The differences between the R_{50} g/cm^2 & R_{80} g/cm^2 for either 9MeV or 20MeV for the different chambers is of the order of 0.5mm which is of a similar order as that seen in the comparison between thesis and acceptance/commissioning data.

The poorer agreement seen in Table 8 between the CC-04 and Roos chamber at the low energies was as expected; the IAEA does not recommend the use of thimble chamber below 10MeV.

The effects of the chamber size was further investigated with the use of inplane-nets for the open fields (CC-04, IC-15 chamber) for 9MeV and 20MeV electrons (Illustration 35, 36, and Illustration 37, 38 respectively on page 111 to 114 of the appendix).

It was found that the iso-ionisation lines, when corrected for a chamber inplane displacement, would only overlay between 2% and 80%, above this level there were subtle differences in the 9MeV scans that required further analysis. The CC-04 chamber appeared to produce, although small, a laterally larger 95%, 98% and 100% ionisation line. The slight differences in the iso-ionisation lines in the build up region were ignored as the both PDI's and PDD's had already demonstrated minor differences.

Using the Wellhöfer “isodose compare” function the calculated iso-ionisation lines for the CC-04 chamber (solid) and IC-15 chamber (Dotted) can be overlaid (Illustration 39 on page 115) and the larger lateral spread can be observed.

The differences that were observed with 9MeV nets were also investigated with 20MeV inplane-nets. An ionisation comparison between the IC-15 inplane-net and the CC-04 inplane-net for the 80-100% (Illustration 40 on page 116) demonstrated the same although more noticeable effect. The CC-04 chamber provided ionisation regions which were substantially larger (laterally) than those determined with the IC-15 chamber. It should be noted that the

ionisation lines do not significantly differ with depths below approximately 95%.

3.3 Bolus on the Applicator

This series of experiments was to determine the effect of both partial and full bolus located on the applicator (LMA insert) on electron beam characteristics. The LMA insert is the final collimating device in the Varian Electron Applicator. The standard Varian "15x15cm" insert, located at a nominal SSD of 95cm, results in a projected field of 15x15cm at the surface of the phantom.

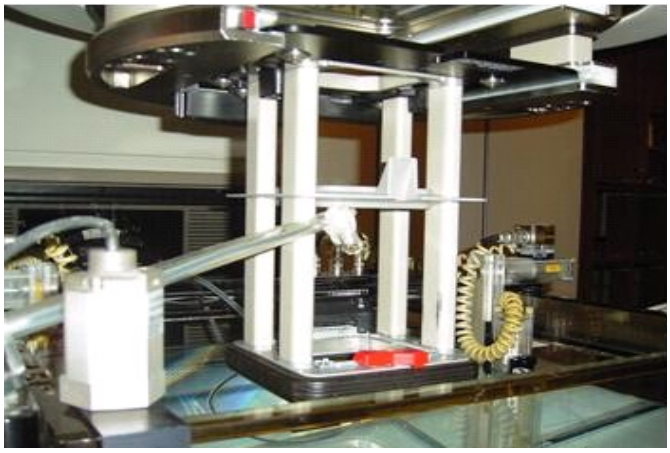

Illustration 21: Image of Varian electron applicator and insert (maestro-research.org)

Different bolus material; Perspex (Polymethylmethacrylate - PMMA), Teflon (Polytetrafluoroethylene - PTFE), Aluminium, Aluminium Mesh and Stainless Steel Mesh, of differing thicknesses, were trialled for their effects on the electron beam as presented below. Depth Ionisation scans and Inplane Depth Ionisation Nets (inplane-nets) were obtained for various arrangements of bolus as described. See table 10 for summary of material used.

The bolus materials were available in discreet thicknesses;

Perspex bolus pieces were cut from a 6mm thick sheet to an appropriate size for application on the LMA insert.

Teflon bolus pieces were cut from both 3mm, 4.6mm &5mm thick sheet to an appropriate size ffor application on the LMA insert.

Aluminiumn bolus pieces were cut from both Al flashing ~0.03mm thick and 1mm thick sheet to an appropriate size for application on the LMA insert. Table headings 2.5/2.7mm or 5.0/5.1mm are required to link the incorrectly annotated illustrations (appendix) and the actual measured thickness.

	Water		Perspex		Teflon		Aluminium		Stainless Steel	
Density g/cm^3	1.00		1.18		2.20		2.70		7.81-8.00	
R/Electron Density	1.00		1.15		1.87		2.34		6.83	
Energy MeV	**9**	**20**	**9**	**20**	**9**	**20**	**9**	**20**	**9**	**20**
LCSP MeV/cm	1.96	2.05	1.90	1.98	1.65	1.72	1.63	1.70	1.47	1.56
LRSP MeV/cm	0.16	0.41	0.14	0.36	0.17	0.43	0.25	0.64	0.46	1.14
CSDA g/cm^2	4.51	9.32	4.67	9.69	5.32	10.87	5.33	10.56	5.60	10.41
R/Electron Density – Relative Electron Density (to water) dimensionless										
LCSP - Linear Collision Stopping power LRSP - Linear Radiative Stopping Power										
CSDA – Continuous Slowing Down Approximation from ESTAR (http://physics.nist.gov/PhysRefData/Star/Text/ESTAR.html)										

Table 10: Material used for bolus

3.3.1 Full Bolus

The bolus material was placed on the LMA insert such that it covered the entire open area. Depth Ionisation scans with the CC-04 Chamber were taken. It was expected that the addition of this material would modify the beam characteristics in a manner similar to the addition of a bolus material on the surface of the phantom, accounting for the thickness and density.

Observing the LMA insert from above (Illustration 22) with an orientation reference from

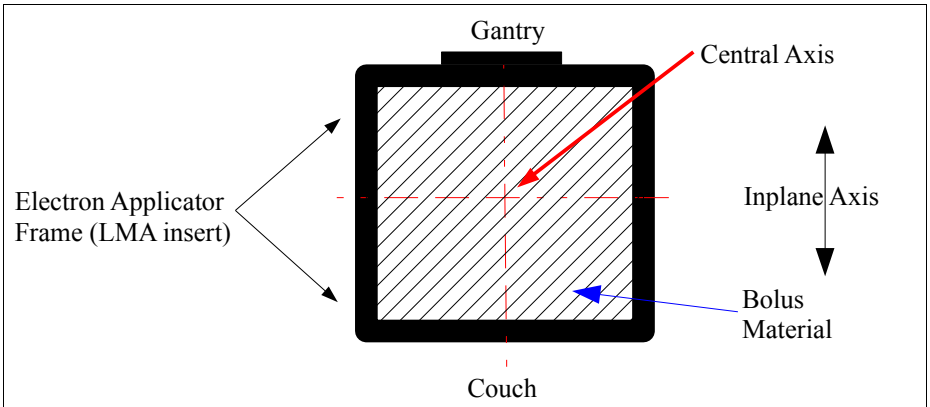

Illustration 22: Full Bolus on LMA insert Set up

Illustration 6 (page 17), the entire area is covered by the material. Data acquired from this arrangement has to be considered as a new “beam energy” as it is not possible to renormalise the distribution based on the normal Depth Ionisation curve..

3.3.1.1 Full Bolus Perspex

9MeV	9MeV Open	1x6mm	2x6mm	3x6mm	6MeV Open
$R_{30,ion}$ g/cm^2	3.80	3.19	2.56	1.93	2.53
$R_{50,ion}$ g/cm^2	3.47	2.87	2.25	1.64	2.29
$R_{80,ion}$ g/cm^2	2.95	2.33	1.73	1.14	1.92
R_P cm	4.18	3.64	2.95	2.35	2.80
File #	28	181	182	185	33
See CA depth Ionisation Scans Illustrations 41 page 118					

Table 11: 9MeV Perspex full bolus on LMA insert

20MeV	20MeV Open	1x6mm	2x6mm	3x6mm	16MeV Open
$R_{30,ion}$ g/cm^2	9.04	8.42	7.75	7.11	7.10
$R_{50,ion}$ g/cm^2	8.19	7.56	6.90	6.27	6.52
$R_{80,ion}$ g/cm^2	6.55	5.84	5.24	4.65	5.42
R_P cm	9.98	9.31	8.75	8.05	7.69
File #	138	180	183	184	42
See CA depth Ionisation Scans Illustrations 42 page 119					

Table 12: 20MeV Perspex full bolus on LMA insert

File Names for Depth Ionisation Nets in Appendix									
9MeV					20MeV				
Open	1x6mm	2x6mm	3x6mm	6MeV	Open	1x6mm	2x6mm	3x6mm	16MeV
29	261	262	265	168	26	260	263	264	169
See depth Ionisation Nets Illustrations 43 to 52 page 120 to 129									

Table 13: File Number Depth Inplane Ionisation Nets Perspex full bolus

Penumbra (20-80%) and Therapeutic Region (90%) Widths - Perspex								
	9MeV				20MeV			
	File #	**Depth cm**	**90% cm**	**20-80% cm**	**File #**	**Depth cm**	**90% cm**	**20-80% cm**
Open	**29**	1.45	14.04	0.84	**26**	3.30	13.64	1.01
1x6mm	**261**	1.15	12.26	2.25	**260**	2.97	12.55	1.64
2x6mm	**262**	0.84	10.82	3.18	**263**	2.65	12.50	1.95
3x6mm	**265**	0.55	8.28	4.32	**264**	2.36	10.73	2.57
Dose calc. from Depth Ionisation Nets Illustrations 43 to 52 page 120 to 129								

Table 14: Penumbra and Therapeutic Region Dose Width, Full Bolus - Perspex

3.3.1.2 Full Bolus Teflon

9MeV	Open	1x3mm	2x3mm	2x3mm+4.6mm	6MeV Open
$R_{30,ion}$ g/cm^2	3.80	3.23	2.66	1.94	2.53
$R_{50,ion}$ g/cm^2	3.47	2.88	2.32	1.64	2.29
$R_{80,ion}$ g/cm^2	2.95	2.31	1.75	1.12	1.92
R_P cm	4.18	3.71	3.08	2.37	2.80
File #	28	190	193	194	33
See CA depth Ionisation Scans Illustrations 53 page 131					

Table 15: 9MeV, Teflon bolus on LMA insert

20MeV	Open	1x3mm	2x3mm	2x3mm+4.6mm	16MeV Open
$R_{30,ion}$ g/cm^2	9.04	8.47	7.85	7.04	7.10
$R_{50,ion}$ g/cm^2	8.19	7.59	6.98	6.16	6.52
$R_{80,ion}$ g/cm^2	6.55	5.91	5.32	4.45	5.42
R_P cm	9.98	9.36	8.91	8.07	7.69
File #	138	191	192	195	42
See CA depth Ionisation Scans Illustrations 54 page 132					

Table 16: 20MeV, Teflon bolus on LMA insert

File Names for Depth Ionisation Nets in Appendix							
9MeV				20MeV			
Open	1x3mm	2x3mm	6MeV	Open	1x3mm	2x3mm	16MeV
29	266	270	168	26	267	271	169
See depth Ionisation Nets Illustrations 55 to 58 page 133 to 136							

Table 17: Depth Inplane Ionisation Nets Teflon full bolus

Penumbra (20-80%) and Therapeutic Region (90%) Widths - Teflon								
	9MeV				20MeV			
	File #	**Depth cm**	**90% cm**	**20-80% cm**	**File #**	**Depth cm**	**90% cm**	**20-80% cm**
Open	**29**	1.45	14.04	0.84	**26**	3.30	13.64	1.01
1x3mm	**266**	1.11	10.50	2.69	**267**	3.01	12.34	1.70
2x3mm	**270**	0.86	10.29	3.49	**271**	2.72	11.36	2.25
Dose calc. from Depth Ionisation Nets Illustrations 55 to 58 page 133 to 136								

Table 18: Penumbra and Therapeutic Region Dose Width, Full Bolus - Teflon

3.3.1.3 Full Bolus Aluminium

9MeV	Open	2.5/2.7mm	5.0/5.1mm	6MeV Open
$R_{30,ion}$ g/cm^2	3.80	3.17	2.61	2.53
$R_{50,ion}$ g/cm^2	3.47	2.82	2.26	2.29
$R_{80,ion}$ g/cm^2	2.95	2.26	1.69	1.92
R_P cm	4.18	3.65	3.06	2.80
File #	28	186	189	33
See CA depth Ionisation Scans Illustrations 59 page 138				

Table 19: 9MeV, Aluminium full bolus on LMA insert

20MeV	Open	2.5/2.7mm	5.0/5.1mm	16MeV Open
$R_{30,ion}$ g/cm^2	9.04	8.38	7.77	7.10
$R_{50,ion}$ g/cm^2	8.19	7.48	6.85	6.52
$R_{80,ion}$ g/cm^2	6.55	5.71	5.07	5.42
R_P cm	9.98	9.39	8.81	7.69
File	138	187	188	42
See CA depth Ionisation Scans Illustrations 60 page 139				

Table 20: 20MeV, Aluminium full bolus on LMA insert

File Names for Depth Ionisation Nets in Appendix							
9MeV				20MeV			
Open	2.5mm	5.0mm	6MeV	Open	2.5mm	5.0mm	16MeV
29	257	258	168	26	256	259	169
See depth Ionisation Nets Illustrations 61 to 64 page 140 to 143							

Table 21: Depth Inplane Ionisation Nets Aluminium full bolus

Penumbra (20-80%) and Therapeutic Region (90%) Widths - Aluminium								
	9MeV				20MeV			
	File #	**Depth cm**	**90% cm**	**20-80% cm**	**File #**	**Depth cm**	**90% cm**	**20-80% cm**
Open	**29**	1.45	14.04	0.84	**26**	3.30	13.64	1.01
2.5mm	**257**	1.10	10.25	3.18	**256**	2.93	11.80	2.03
5.0mm	**258**	0.82	7.80	4.48	**259**	2.60	10.71	2.72
Dose calc. from Depth Ionisation Nets Illustrations 61 to 64 page 140 to 143								

Table 22: Penumbra and Therapeutic Region Dose Width, Full Bolus - Aluminium

3.3.2 Partial Bolus

The experiment was modified to have only a portion of the field covered with the bolus material. In the inplane direction, (ie towards the couch), the bolus material covered the LMA insert from 3.0cm off central axis to the LMA insert edge.

Observing the LMA insert from above (Illustration 23), with an orientation reference from

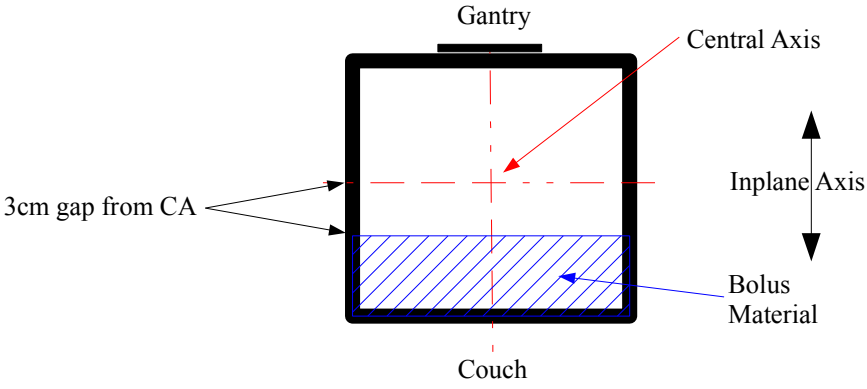

Illustration 23: Partial Bolus on LMA insert Set up

Illustration 6 (page 17), the majority of the field defined by the LMA insert was left uncovered which exposed the central axis of the beam. With this arrangement it may have been possible to rescale depth ionisation scans on the central axis, however it is known that bolus edges do perturb an electron beam and hence a point further away (~4cm inplane from CA towards the gantry) was chosen to ensure the beam was as close to the standard open field. For completeness Depth Ionisation Scans were obtained of the central axis.

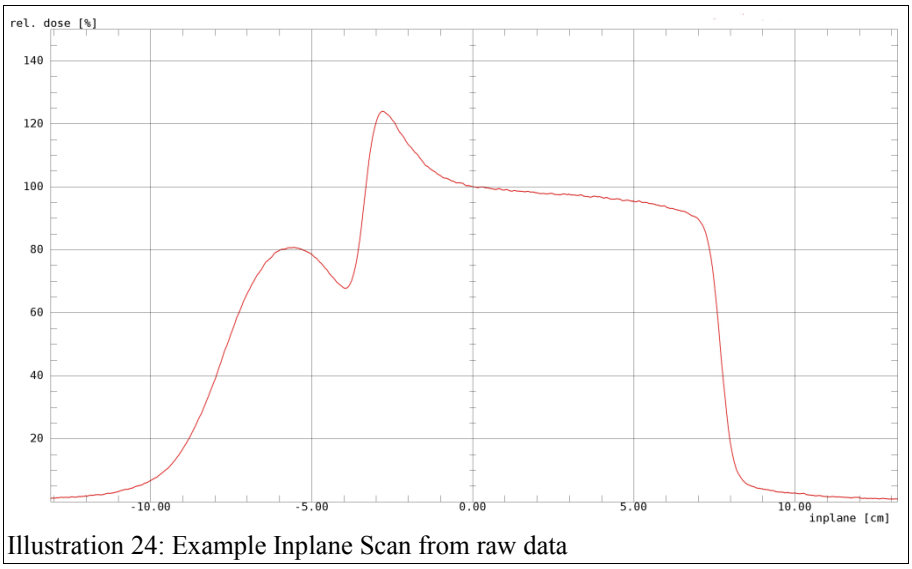

Illustration 24: Example Inplane Scan from raw data

3.3.2.1 Partial Bolus Perspex

9MeV	Open	1x6mm		2x6mm		3x6mm		6MeV Open
		CA	3.5cm	CA	3.5cm	CA	3.5cm	
$R_{30,ion}$ g/cm²	3.80	3.77	3.80	3.77	3.80	3.70	3.81	2.53
$R_{50,ion}$ g/cm²	3.47	3.43	3.48	3.43	3.47	3.45	3.48	2.29
$R_{80,ion}$ g/cm²	2.95	2.84	2.93	2.84	2.93	2.90	2.94	1.92
R_P cm	4.18	4.21	4.22	4.22	4.22	4.22	4.23	2.80
File #	28	220	221	237	239	241	240	33
3.5cm indicates inplane displacement towards gantry see illustration 23 See CA depth Ionisation Scans Illustrations 65 page 145 See 3.5cm inplane depth Ionisation Scans Illustrations 66 page 146								

Table 23: 9MeV, Perspex partial bolus on LMA insert

20MeV	Open	1x6mm		2x6mm		3x6mm		16MeV Open
		CA	3.5cm	CA	3.5cm	CA	3.5cm	
$R_{30,ion}$ g/cm²	9.04	8.99	8.98	8.99	8.98	8.96	8.98	7.10
$R_{50,ion}$ g/cm²	8.19	8.13	8.12	8.12	8.12	8.08	8.12	6.52
$R_{80,ion}$ g/cm²	6.55	6.55	6.40	6.54	6.41	6.46	6.41	5.42
R_P cm	9.98	9.89	9.96	9.96	9.93	9.94	9.96	7.69
File #	138	207	222	224	223	254	255	42
3.5cm indicates inplane displacement towards gantry see illustration 23 See CA depth Ionisation Scans Illustrations 67 on page 147 See 3.5cm inplane depth Ionisation Scans Illustrations 68 on page 148								

Table 24: 20MeV, Perspex partial bolus on LMA insert

File Names for Depth Ionisation Nets in Appendix									
9MeV					20MeV				
Open	1x6mm	2x6mm	3x6mm	6MeV	Open	1x6mm	2x6mm	3x6mm	16MeV
29	274	275	278	168	26	273	276	277	169
See depth Ionisation Nets Illustrations 69 to 74 page 149 page 154									

Table 25: Depth Inplane Ionisation Nets Perspex partial bolus

Penumbra (20-80%) and Therapeutic Region (90%) Widths – Perspex Open Area (+3.5cm from CA towards Gantry)								
	9MeV				20MeV			
	File #	Depth cm	90% cm	20-80% cm	File #	Depth cm	90% cm	20-80% cm
Open	**29**	1.45	14.04	0.84	**26**	3.30	13.64	1.01
1x6mm	**274**	1.45	6.99	0.83	**273**	3.30	6.93	1.00
2x6mm	**275**	1.45	6.97	0.85	**276**	3.30	6.93	1.01
3x6mm	**278**	1.45	6.96	0.85	**277**	3.30	6.93	1.01
Dose calc. from Depth Ionisation Nets Illustrations 69 to 74 page 149 page 154								

Table 26: Penumbra and Therapeautic Region Dose Width, Partial Bolus - Perspex

Penumbra (20-80%) and Therapeutic Region (90%) Widths – Perspex Under Bolus								
	9MeV				20MeV			
	File #	Depth cm	90% cm	20-80% cm	File #	Depth cm	90% cm	20-80% cm
Open	**29**	1.45	14.00	0.84	**26**	3.30	13.60	1.01
1x6mm	**274**	1.15	-	2.07	**273**	2.97	-	1.52
2x6mm	**275**	0.84	-	3.22	**276**	2.65	-	1.87
3x6mm	**278**	0.55	-	4.39	**277**	2.36	-	2.06
Dose calc. from Depth Ionisation Nets Illustrations 69 to 74 page 149 page 154								

Table 27: Penumbra and Therapeautic Region Dose Width, Partial Bolus - Perspex

3.3.2.2 Partial Bolus Teflon

9MeV	Open	1x3mm		2x3mm		2x5mm		6MeV Open
		CA	3.5cm	CA	3.5cm	CA	3.5cm	
$R_{30,ion}$ g/cm²	3.80	3.87	3.89	3.85	3.89	3.86	3.89	2.53
$R_{50,ion}$ g/cm²	3.47	3.54	3.56	3.51	3.56	3.51	3.56	2.29
$R_{80,ion}$ g/cm²	2.95	2.99	3.02	2.93	3.01	2.93	3.02	1.92
R_P cm	4.18	4.32	4.32	4.29	4.34	4.3	4.33	2.80
File #	28	321	322	324	323	353	354	33
3.5cm indicates inplane displacement towards gantry see illustration 23 See CA depth Ionisation Scans Illustrations 75 page.156 See 3.5cm inplane depth Ionisation Scans Illustrations 76 Page.157								

Table 28: 9MeV, Teflon partial bolus on LMA insert

20MeV	Open	1x3mm		2x3mm		2x5mm		16MeV Open
		CA	3.5cm	CA	3.5cm	CA	3.5cm	
$R_{30,ion}$ g/cm²	9.04	9.09	9.06	9.09	9.07	9.01	9.07	7.10
$R_{50,ion}$ g/cm²	8.19	8.24	8.21	8.23	8.22	8.11	8.22	6.52
$R_{80,ion}$ g/cm²	6.55	6.62	6.51	6.63	6.48	6.51	6.48	5.42
R_P cm	9.98	9.97	9.99	10.07	10.06	9.95	10.04	7.69
File #	138	308	307	337	338	340	339	42
3.5cm indicates inplane displacement towards gantry see illustration 23 See CA depth Ionisation Scans Illustrations 77 page.158 See 3.5cm inplane depth Ionisation Scans Illustrations 78 Page.159								

Table 29: 20MeV, Teflon partial bolus on LMA insert

File Names for Depth Ionisation Nets in Appendix									
9MeV					20MeV				
Open	1x3mm	2x3mm	2x5mm	6MeV	Open	1x3mm	2x3mm	2x5mm	16MeV
29	279	282	125	168	26	280	281	126	169
See depth Ionisation Nets Illustrations 79 to 84 page 160 to 165									

Table 30: Depth Inplane Ionisation Nets Teflon partial bolus

Penumbra (20-80%) and Therapeutic Region (90%) Widths – Teflon Open Area								
	9MeV				20MeV			
	File #	Depth cm	90% cm	20-80% cm	File #	Depth cm	90% cm	20-80% cm
Open	**29**	1.45	14.04	0.84	**26**	3.30	13.64	1.01
1x3mm	**279**	1.45	6.94	0.86	**280**	3.30	6.93	1.01
2x3mm	**282**	1.45	6.96	0.85	**281**	3.30	6.91	1.00
2x5mm	**125**	1.45	6.95	0.86	**126**	3.30	6.92	1.01
Dose calc. from Depth Ionisation Nets Illustrations 79 to 84 page 160 to 165								

Table 31: Penumbra and Therapeautic Region Dose Width, Partial Bolus - Teflon

Penumbra (20-80%) and Therapeutic Region (90%) Widths – Teflon Under Bolus								
	9MeV				20MeV			
	File #	Depth cm	90% cm	20-80% cm	File #	Depth cm	90% cm	20-80% cm
Open	**29**	1.45	14.00	0.80	**26**	3.30	13.60	1.00
1x3mm	**279**	1.13	-	2.35	**280**	3.01	-	1.65
2x3mm	**282**	0.86	-	3.70	**281**	2.72	-	2.06
2x5mm	**125**	No full bolus ref for rescale			**126**	No full bolus ref for rescale		
Dose calc. from Depth Ionisation Nets Illustrations 79 to 84 page 160 to 165								

Table 32: Penumbra and Therapeautic Region Dose Width, Partial Bolus – Teflon

3.3.2.3 Partial Bolus Aluminium

9MeV	Open	2.5/2.7mm		5.0/5.1mm		6MeV Open
		CA	3.5cm	CA	3.5cm	
$R_{30,ion}$ g/cm²	3.80	3.80	3.81	3.78	3.82	2.53
$R_{50,ion}$ g/cm²	3.47	3.46	3.49	3.44	3.49	2.29
$R_{80,ion}$ g/cm²	2.95	2.91	2.95	2.84	2.94	1.92
R_P cm	4.18	4.26	4.26	4.23	4.27	2.80
File	28	372	373	375	374	33
3.5cm indicates inplane displacement towards gantry see illustration 23 See CA depth Ionisation Scans Illustrations 85 page.167 See 3.5cm inplane depth Ionisation Scans Illustrations 86 Page.168						

Table 33: 9MeV, Aluminium partial bolus on LMA insert

20MeV	Open	2.5/2.7mm		5.0/5.1mm		16MeV Open
		CA	3.5cm	CA	3.5cm	
$R_{30,ion}$ g/cm²	9.04	9.03	9.01	9.03	9.02	7.10
$R_{50,ion}$ g/cm²	8.19	8.19	8.14	8.17	8.15	6.52
$R_{80,ion}$ g/cm²	6.55	6.55	6.41	6.56	6.42	5.42
R_P cm	9.98	10.00	10.02	10.02	9.97	7.69
File #	138	359	358	388	389	42
3.5cm indicates inplane displacement towards gantry see illustration 23 See CA depth Ionisation Scans Illustrations 87 page.169 See 3.5cm inplane depth Ionisation Scans Illustrations 88 Page.170						

Table 34: 20MeV, Aluminium partial bolus on LMA insert

File Names for Depth Ionisation Nets in Appendix							
9MeV				20MeV			
Open	2.5mm	5.0mm	6MeV	Open	2.5mm	5.0mm	16MeV
29	286	287	168	26	285	288	169
See depth Ionisation Nets Illustrations 89 to 92 page 171 to 174							

Table 35: Depth Inplane Ionisation Nets Aluminium partial bolus

t

Penumbra (20-80%) and Therapeutic Region (90%) Widths – Aluminium Open Area								
	9MeV				20MeV			
	File #	**Depth cm**	**90% cm**	**20-80% cm**	**File #**	**Depth cm**	**90% cm**	**20-80% cm**
Open	**29**	1.45	14.04	0.84	**26**	3.30	13.64	1.01
2.5mm	**286**	1.45	6.90	0.86	**285**	3.30	6.88	0.84
5.0mm	**287**	1.45	6.87	0.85	**288**	3.30	6.90	0.85
Dose calc. from Depth Ionisation Nets Illustrations 89 to 92 page 171 to 174								

Table 36: Penumbra and Therapeautic Region Dose Width, Partial Bolus - Aluminium

Penumbra (20-80%) and Therapeutic Region (90%) Widths – Aluminium Under Bolus								
	9MeV				20MeV			
	File #	**Depth cm**	**90% cm**	**20-80% cm**	**File #**	**Depth cm**	**90% cm**	**20-80% cm**
Open	**29**	1.45	14.04	0.84	**26**	3.30	13.64	1.01
2.5mm	**286**	1.10	-	3.18	**285**	2.93	-	2.20
5.0mm	**287**	0.82	-	6.10	**288**	2.60	-	2.30
Dose calc. from Depth Ionisation Nets Illustrations 89 to 92 page 171 to 174								

Table 37: Penumbra and Therapeautic Region Dose Width, Partial Bolus - Aluminium

3.3.3 Strip Bolus

The partial bolus experiment was modified to have only a strip of bolus material on one side of the central-axis. This arrangement left a strip of open beam on the opposite side of the bolus. It was expected that this arrangement would result in an elevated ionisation region on either side of the bolus material. As this experiment was only to illustrate the effects, only a teflon strip was measured.

Observing the LMA insert from above (Illustration 25), with an orientation reference from

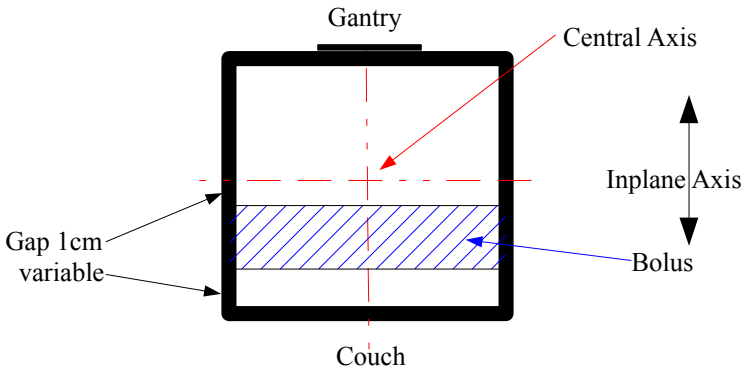

Illustration 25: Strip Bolus on LMA insert Set up

Illustration 6 (page 17)

With this arrangement it would not have been possible to rescale depth ionisation scans on the central axis, as the bolus edge is too close to the central beam and it is known that a sharp edge will perturb an electron beam causing a high dose region to be formed adjacent to the bolus edge (Shortt et al., 1986, Klevenhagen, 1993), therefore, as for the partial bolus situation, a point further away (~4cm inplane from CA towards the gantry) was chosen to ensure the beam was as close to the standard open field.

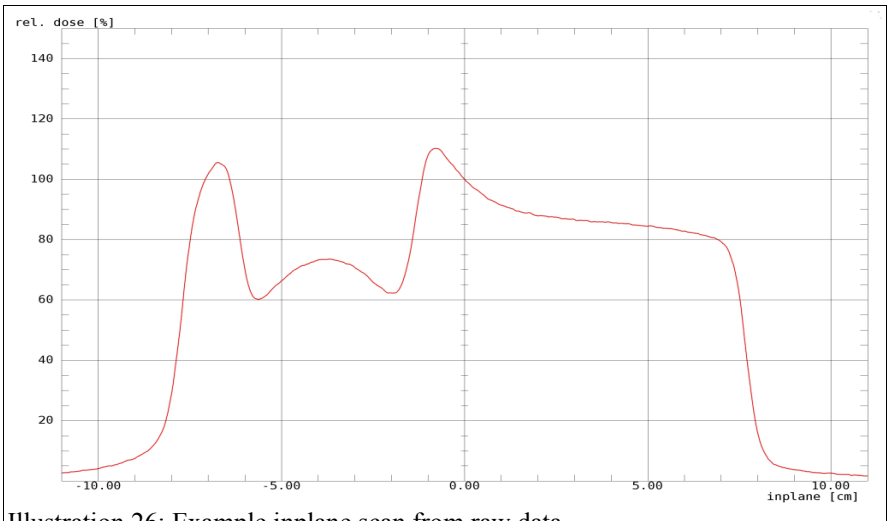

Illustration 26: Example inplane scan from raw data

3.3.3.1 Strip Bolus Teflon

9MeV	Open	2x5mm			6MeV Open
		-4cm	CA	+4cm	
$R_{30,ion}$ g/cm²	3.80	2.31	3.62	3.76	2.53
$R_{50,ion}$ g/cm²	3.47	1.99	3.2	3.42	2.29
$R_{80,ion}$ g/cm²	2.95	1.47	2.4	2.87	1.92
R_P cm	4.18	2.72	#-	#-	2.80
File #	28	75	79	83	33
# depth ionisation scan too shallow for Wellhöfer calculation +4cm indicates inplane displacement towards gantry see illustration 25					
See depth Ionisation Scans Illustrations 93 page.176					

Table 38: 9MeV, Teflon strip bolus on LMA insert

20MeV	Open	2x 5mm			16MeV Open
		-4cm	CA	+4cm	
$R_{30,ion}$ g/cm²	9.04	7.51	8.57	8.93	7.10
$R_{50,ion}$ g/cm²	8.19	6.36	7.56	8.08	6.52
$R_{80,ion}$ g/cm²	6.55	3.7	5.83	6.39	5.42
R_P cm	9.98	8.81	9.64	6.28	7.69
File #	138	53	57	64	42
+4cm indicates inplane displacement towards gantry see illustration 25					
See depth Ionisation Scans Illustrations 94 page 177					

Table 39: 20MeV, Teflon strip bolus on LMA insert

File Names for Depth Ionisation Nets in Appendix					
9MeV			20MeV		
Open	2x 5mm	6MeV	Open	2x 5mm	16MeV
29	47	168	26	46	169
See depth Ionisation Nets Illustrations 95, 96 page 178 & 179					

Table 40: Depth Inplane Ionisation Nets Teflon strip bolus

Penumbra (20-80%) and Therapeutic Region (90%) Widths – Teflon Large Open Area								
	9MeV				20MeV			
	File #	**Depth cm**	**90% cm**	**20-80% cm**	**File #**	**Depth cm**	**90% cm**	**20-80% cm**
Open	**29**	1.45	14.04	0.84	**26**	3.30	13.64	1.01
2x5mm	**47**	1.45	6.99	0.83	**46**	3.3	6.83	0.98
Dose calc. from Depth Ionisation Nets Illustrations 95, 96 page 178 & 179								

Table 41: Penumbra and Therapeautic Region Dose Width, Strip Bolus - Teflon

3.3.4 Higher Z Grids

Some authors have illustrated the use of high density materials as a surface bolus material such as tantalum, tin, lead and brass (Alasti and Galbraith, 1995, Cederbaum et al., 2001, Healy et al., 2005) the availability and use of these materials are either difficult to obtain locally, undesirable and/or expensive.

Alternate materials, which could be easily sourced from local hardware stores, were Aluminium and Stainless Steel mesh whilst the Z value is lower that the previously mentioned, their merit as an replacement was tested. It was not possible to source these alternate mesh materials with different open area to wire diameter ratios.

The bolus material was placed on the LMA insert such that it covered the entire open area.

Observing the LMA insert from above (Illustration 27) with an orientation reference from Illustration 6 (page 17).

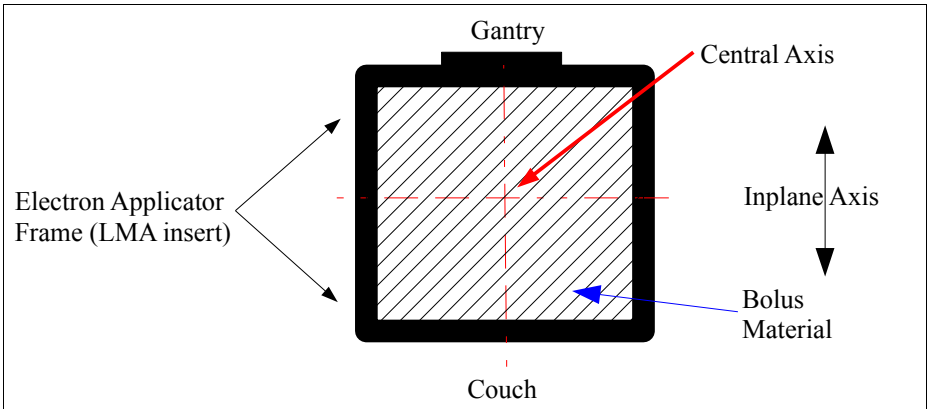

Illustration 27: Mesh (grid) Bolus on LMA insert Set up

3.3.4.1 Aluminium Mesh

9MeV	Open	1xAl Mesh	1xAl Shim	2xAl Shim	6MeV
$R_{30,ion}$ g/cm²	3.80	3.8	3.8	3.73	2.53
$R_{50,ion}$ g/cm²	3.47	3.47	3.46	3.4	2.29
$R_{80,ion}$ g/cm²	2.95	2.93	2.92	2.86	1.92
R_P cm	4.21	4.21	4.19	4.12	2.80
File #	28	414	419	422	33
See depth Ionisation Scans Illustrations 97 Page 182					
Al mesh = 0.1mm wire open area 0.94mmx0.94mm - Al Shim = 0.3mm					

Table 42: 9MeV Aluminium mesh bolus on LMA insert

20MeV	Open	1xAl Mesh	1xAl Shim	2xAl Shim	16MeV Open
$R_{30,ion}$ g/cm²	9.04	9.01	9.05	8.97	7.10
$R_{50,ion}$ g/cm²	8.19	8.17	8.17	8.1	6.52
$R_{80,ion}$ g/cm²	6.55	6.53	6.5	6.41	5.42
R_P cm	9.98	9.88	9.89	9.79	7.69
File #	138	127	420	421	42
See depth Ionisation Scans Illustrations 98 Page 183					
Al mesh = 0.1mm wire open area 0.94mmx0.94mm - Al Shim = 0.3mm					

Table 43: 20MeV Aluminium mesh bolus on LMA insert

File Names for Depth Ionisation Nets in Appendix							
9MeV				20MeV			
Open	1xAl Mesh	1xAl Sheet	2xAl Sheet	Open	1xAl Mesh	1xAl Sheet	2xAl Sheet
29	415	418	423	26	416	417	424
See depth Ionisation Nets Illustrations 99 to 104 page 184 to 189							
Al mesh = 0.1mm wire open area 0.94mmx0.94mm - Al Sheet = 0.3mm							

Table 44: Depth Inplane Ionisation Nets Higher Z Grid bolus

Penumbra (20-80%) and Therapeutic Region (90%) Widths – Al Mesh/Sheet								
	9MeV				20MeV			
	File #	**Depth cm**	**90% cm**	**20-80% cm**	**File #**	**Depth cm**	**90% cm**	**20-80% cm**
Open	**29**	1.45	14.04	0.84	**26**	3.30	13.64	1.01
1xAl Mesh	**415**	1.44	13.55	0.99	**416**	3.31	13.61	1.04
2xAl Mesh	**418**	1.43	12.92	1.28	**417**	3.31	13.45	1.13
2xAl Sheet	**423**	1.40	12.40	1.60	**424**	3.27	13.09	1.26
Dose calc. from Depth Ionisation Nets Illustrations 99 to 104 page 184 to 189								

Table 45: Penumbra and Therapeutic Region Dose Width, Full Bolus – Al Mesh/Sheet

3.3.4.2 Stainless Steel Mesh

9MeV	Open	1xSS	2xSS	3xSS	4xSS
$R_{30,ion}$ g/cm^2	3.80	3.78	3.74	3.71	3.66
$R_{50,ion}$ g/cm^2	3.47	3.45	3.40	3.35	3.31
$R_{80,ion}$ g/cm^2	2.95	2.89	2.85	2.77	2.72
R_P cm	4.18	4.22	4.18	4.19	4.12
File #	28	197	198	201	204
See depth Ionisation Scans Illustrations 105 Page.190					

Table 46: 9MeV, Stainless Steel mesh bolus on LMA insert

20MeV	Open	1xSS	2xSS	3xSS	4xSS
$R_{30,ion}$ g/cm^2	9.04	8.99	8.95	8.91	8.85
$R_{50,ion}$ g/cm^2	8.19	8.13	8.09	8.05	7.96
$R_{80,ion}$ g/cm^2	6.55	6.44	6.38	6.34	6.14
R_P cm	9.98	9.96	9.86	9.92	9.82
File #	138	196	199	200	203
See depth Ionisation Scans Illustrations 106 Page.191					

Table 47: 20MeV Stainless Steel mesh bolus on LMA insert

File Names for Depth Ionisation Nets in Appendix									
9MeV					20MeV				
Open	1xSS	2xSS	3xSS	4xSS	Open	1xSS	2xSS	3xSS	4xSS
29	303	302	295	294	26	306	299	298	291
See depth Ionisation Nets Illustrations 107 to 114 page 192 to 199									

Table 48: Depth Inplane Ionisation Nets Stainless Steel Mesh

Penumbra (20-80%) and Therapeutic Region (90%) Widths – Stainless Steel mesh								
	9MeV				20MeV			
	File #	**Depth cm**	**90% cm**	**20-80% cm**	**File #**	**Depth cm**	**90% cm**	**20-80% cm**
Open	**29**	1.45	14.04	0.84	**26**	3.30	13.64	1.01
1xSS	**303**	1.41	12.56	1.19	**306**	3.02	11.40	1.14
2xSS	**302**	1.30	11.82	1.56	**299**	2.96	10.85	1.31
3xSS	**295**	1.34	10.47	1.80	**298**	2.87	8.97	1.49
4xSS	**294**	1.31	10.56	2.13	**291**	2.86	9.65	1.63
Dose calc. from Depth Ionisation Nets Illustrations 107 to 114 page 192 to 199								

Table 49: Penumbra and Therapeutic Region Dose Width, Full Bolus – Stainless Steel Mesh

3.4 Bolus on Surface

Typically, bolus materials are placed on the patient's skin surface. This approach is well documented by several authors (Archambeau et al., 1981, Galbraith and Rawlinson, 1984, Khan et al., 1991a, Klevenhagen, 1993, Starkschall et al., 1993) To ensure that the experimental measurements obtained for this thesis were valid a subset of the bolus materials and electron energies were used with the bolus placed on the phantom surface.

The measurements obtained were compared with published data.

Depth Ionisation scans and depth ionisation nets were measured using the nominal 9MeV electron beam and the 6mm thick perspex sheet. Depth Ionisation scans using both the 9MeV and 20MeV electron beams were obtained for Teflon using 5mm sheets.

3.4.1 Perspex

9MeV	9MeV Open	1x6mm	2x6mm	3x6mm
$R_{30,ion}$ g/cm^2	3.80	3.14	2.54	2.00
$R_{50,ion}$ g/cm^2	3.47	2.81	2.2	1.67
$R_{80,ion}$ g/cm^2	2.95	2.26	1.65	1.12
R_P cm	4.21	3.57	2.96	2.45
File #	28	405	408	409
* indicates extrapolated reading				
See depth Ionisation Scans Illustrations 115 page 201				

Table 50: Bolus on Surface Perspex depth ionisation 9MeV

File Names for Depth Ionisation Nets in Appendix				
9MeV				
Open	1x6mm	2x6mm	3x6mm	6MeV
29	406	407	410	168
See depth Ionisation Nets Illustrations 116 to 118 page 202 to 204				

Table 51: Depth Inplane Ionisation Nets Perspex Full surface bolus

Penumbra (20-80%) and Therapeutic Region (90%) Widths - Perspex				
	9MeV			
	File #	Depth cm	90% cm	20-80% cm
Open	29	1.45	14.04	0.84
1x6mm	406	1.10	13.84	1.06
2x6mm	407	0.81	13.67	1.09
3x6mm	410	0.54	13.22	1.16
Dose calc. from Depth Ionisation Nets Illustrations 116 to 118 page 202 to 204				

Table 52: Penumbra and Therapeutic Region Dose Width, Full surface Bolus - Perspex

3.4.2 Teflon

9MeV	9MeV Open	1x5mm	2x5mm
$R_{30,ion}$ g/cm^2	3.80	3.08	2.10
$R_{50,ion}$ g/cm^2	3.47	2.74	1.75
$R_{80,ion}$ g/cm^2	2.95	2.11	1.14
R_P cm	4.21	3.58	2.57
File #	28	152	146
See depth Ionisation Scans Illustrations 119 page 205			

Table 53: Bolus on Surface Teflon 9MeV,

20MeV	Open	1x5mm	2x5mm
$R_{30,ion}$ g/cm^2	9.04	8.42	7.62
$R_{50,ion}$ g/cm^2	8.19	7.48	6.50
$R_{80,ion}$ g/cm^2	6.55	5.33	4.14
R_P cm	9.98	9.54	8.99
File #	138	150	148
See depth Ionisation Scans Illustrations 120 page 206			

Table 54: Bolus on Surface Teflon 20MeV

4. DISCUSSION

4.1 Beam Quality

When measuring electron beams with an ionisation chamber the results obtained are Percentage Depth Ionisation (PDI) curves as was noted in *Chapter: 2.2.1 Central Axis Percentage Depth Dose*. Ionisation in the chamber is dependent upon the energy of the electron which passes across the chamber. Unlike a photon beam, which effectively does not loose beam energy, (when compared to an electron beam), as it traverses the water phantom, the electron beam energy appears to degrade continuously at a rate of approximately 2MeV/cm in a water phantom. Photon beam interactions in water essentially generate the same energy secondary electrons at all depths which can be measured by the ionisation chamber. The electron beam however has a different energy dependent upon the depth in the phantom.

In a clinical situation the PDI curves are typically converted to Percentage Depth Dose (PDD) curves by applying the appropriate Restricted Stopping Power Ratio and used for dose calculations however, provided the chamber is unchanged, it is also possible to directly compare the PDI. This can be illustrated by considering how the Dosimetry Protocol TRS-398 beam quality index ($R_{50.}$), the half-value depth in water, for electron beams is defined. R_{50} is the depth in water (in g/cm^2) at which the absorbed dose is 50% of its value at the absorbed-dose maximum, measured with with standard conditions, SSD of 100cm and a field size at the phantom surface of at least 10 cm x 10 cm for $R_{50} \leq 7$g/cm^2 (energy $\leq$ 16MeV) and at least 20 cm x 20 cm for $R_{50} > 7$ g/cm^2(energy > 16MeV) (Andreo, 2000). Since R_{50} (dose) can be obtained from $R_{50,ion}$ (ionisation) using the simple relationships;

$$R_{50} = 1.029\ R_{50,ion} - 0.06 \text{ g/cm}^2 \ (R_{50,ion} \leq 10 \text{ g/cm}^2)$$

$$R_{50} = 1.059\ R_{50,ion} - 0.37 \text{ g/cm}^2 \ (R_{50,ion} > 10 \text{ g/cm}^2)$$

it can be seen that comparing $R_{50,ion}$ values is equally valid.

Whilst the dosimetry protocol TRS-398 (Andreo, 2000) requires a 20x20cm field for beam quality determination for beam qualities >7 g/cm^2(ie energy >16MeV) this thesis was comparing acquired data with that from acceptance/commissioning data which was obtained with the 15x15cm applicator. This variation from the protocol recommendation does not

invalidate this thesis data as the protocol also states “A field size smaller than 20 cm x 20 cm may be used provided that R50 does not change by more than around 0.1 g/cm^2 from the value measured for a 20 cm x 20 cm field.” ROV has determined previously that this condition is satisfied for the the electron beams used in this thesis.

4.3 Bolus on Applicator

4.3.1 Full Bolus

An assumption was made that applying a bolus material to the LMA insert could result in an effect similar to that of applying the same bolus material to the surface of the phantom. Observation of the figures presented in Table 11 for the $R_{30,ion}$ g/cm^2, $R_{50,ion}$ g/cm^2 and $R_{80,ion}$ g/cm^2 values, for the addition of 1, 2 & 3x6mm sheets of Perspex on the insert for the 9MeV Depth Ionisation (DI) resulted in a shift of the 9MeV DI scan towards the surface by approximately 6.1mm with each additional sheet. This observation was tested and confirmed by overlaying a surface corrected nominal 9MeV electron beam DI scan (with surface shift of 6mm, 12.2mm & 18.3mm), over the DI scans for the 1, 2 & 3x6mm Perspex sheets (on insert) respectively (see Illustrations 121 to 123, page 209 to 211). Additionally the further results obtained in *Chapter 3.4 Bolus on Surface* presented in Table 50 (also shown by Illustration 115) aid to support, in part, the assumption, although it must be noted that these DI scans are quite different in the build-up region.

It was also assumed that the 9MeV beam could be modified to be similar to the 6MeV beam and on assessment of the $R_{50,ion}$ g/cm^2 for the 2x6mm Perspex beam they are quite similar. If the simple Harder equation was applied to the initial 9MeV beam the similarities are not surprising as 12mm of Perspex was evaluated to be approximately 13mm of water depth (Table Table 4: Perspex Water Equivalent Depths) which theoretically would result in an approximate energy of 6MeV leaving the downstream side of the Perspex on the applicator. Using the TRS-398 Dosimetry Protocol electron beam quality index (Andreo, 2000) and our knowledge of the variation of $R_{50,ion}$ g/cm^2 from *Chapter 3.1 Beam Quality Comparison* for the Project, CAP and Commissioning data it could be argued that these are the same beams. However it can also be seen that the $R_{80,ion}$ g/cm^2 (Varian beam quality) does appear to diverge beyond what is acceptable for matching energies 0.1g/cm^2 .

Further, observation of the PDI curves (Illustration 41 page 118) provides a better indication of how the 9MeV has been modified to approximate the open field 6MeV beam ($R_{50,ion}$ g/cm^2 wise). This modification of the 9MeV beam may well provide some clinical benefit given that the surface dose has been increased to the therapeutic 90% ionisation level whilst maintaining a 90% ionisation level within 3mm of the 6MeV Open Field at depth.

Understanding the shift of the $R_{80,ion}$ g/cm^2 and d_{max} to a shallower level appears to indicate

that there is a higher component of low energy (scattered) electrons in the beam compared to that of the open field 6MeV. It, must be remembered, as was observed in *Chapter 3.2 Spatial resolution as a function of chamber IC-15, CC-04 and PPC-40(Roos Type),* that the depth ionisation curves recorded by the CC-04 chamber appeared to underestimate both the $R_{50,ion}$ g/cm^2 and $R_{80,ion}$ g/cm^2 values by approximately 0.1g/cm^2 for the 6MeV beam energy when compared to a Roos chamber depth ionisation.

A similar approach and assumptions were taken with the 20MeV beam, see Table 12 for these measurements. With a similar arrangement to the 9MeV beam, whilst remembering the limitations placed on the Harder equation, is was expected that 20MeV beam may also be modulated to a lower energy and hence an open field 16MeV beam was also recorded.

It is reasonably clear from these tabulated results that the 20MeV beam has been modified in a similar fashion as what occurred with the 9MeV beam. Analysis of the $R_{50,ion}$ g/cm^2 points, it can be seen that there is a shift towards the surface of 6.1mm 12.7mm & 19.0mm shift for the 1, 2 & 3x6mm Perspex Sheet scans respectively (Illustration 124 to 126 page 212 to 214). Whilst the beam was modulated, it did not degrade in a manner that may provide a clinically as useful beam. This is better seen in the PDI scans in Illustration 42 page 119.

Whilst the surface dose has been increased to approximately 98% of dose maximum for all the thicknesses of perspex modulated 20MeV beam, the beam profiles have just been shifted towards the surface resulting in what is a therapeutically less useful beam. Comparison of the degraded 20MeVbeam with the standard Open Field 16MeV beam it can be seen that the 16MeV beam provides a therapeutic region that is both larger and more homogeneous, surface ~ 94% and 90% to a water depth of 4.8cm. It is also observed that the tail of the modified 20MeV PDI has a higher x-ray contamination, being the same as the open field 20MeV beam.

The confirmation that the open beams were degraded by the perspex and using our general understanding of electron interactions in materials, necessitated further measurements to completely characterise the modulated beams. Inplane-Net scans were taken of all the degraded (1, 2 & 3x6mm perspex full bolus) set-ups for the 9MeV and 20MeV beams.

Whilst it is acknowledged that the 3x6mm Perspex modulated 20MeV beam cannot be considered as a replacement for a 16MeV beam, it does provide an indication of the effects that Perspex bolus material located on the LMA insert will cause. It can be clearly seen from

Illustrations 42 to 51 on page 119 to 128. that the addition of the Perspex has substantially increased the scattering of electrons resulting in a much wider spread of the low iso-ionisation lines. It can also be seen that there is a narrowing of the higher iso-ionisation lines.

When Teflon was substituted for the perspex on the applicator a very similar effect was observed to that seen with Perspex. The 9MeV depth ionisation scan was moved towards the surface by 0.6cm, 1.15cm and 1.83cm for the 1x3mm, 2x3mm and 2x3mm+4.6mm Teflon sheets respectively. For the 20MeV electron beam the shifts observed were 0.58cm, 1.19cm and 2.1cm respectively. In a similar fashion to what was applied to the Perspex results, this was also tested and verified by overlaying a surface corrected 9MeV and 20MeV beams on the Full Bolus Teflon results using the Wellhöfer software. See illustrations 127 to 132 page 216 to 221

Finally Teflon was replaced by two thicknesses of Aluminium manufactured from several layers of Aluminium shim of nominal thickness 0.3mm and the depth ionisation distribution measured (note; although the two thicknesses of Aluminium are referred to differently in the illustrations and tables as either 2.5/2.7mm and 5.0/5.1mm the 2.5mm and 5.0mm were only an approximate thickness used to identify scans before measurements with a vernier were completed). In a similar fashion as seen with the Perspex and Teflon the addition of Aluminium resulted in a shift of the depth ionisation scan towards the water surface. The 9MeV depth ionisation scan was moved towards the surface by 0.65cm and 1.21cm for the 2.7mm and 5.1mm Aluminium sheets respectively. For the 20MeV electron beam the shifts observed were 0.69cm and 1.32cm respectively. These shifts can be seen in Illustrations 133 to 136 on page 223 to 226.

A further analysis of the effects on the distribution was performed by converting the ionisation scans to dose and evaluating both the Therapeutic Region (90%) lateral dimension and the penumbra (20%-80%) for each bolus material see Table 14, 18 and 22 on pages 55, 57 and 59 respectively. The tables indicates that the Therapeutic region is progressively reduced from the open field whilst the penumbra increases considerably.

Considering how the electron beams are modified by each of the bolus materials, as seen with both the depth ionisation curves and depth dose curve, it appears to indicate that the approach may have some limited application, however the very large increase in penumbra and reduction of lateral therapeutic size reduces or removes any benefit.

4.3.2 Partial Bolus

It is known that sharp bolus edges can perturb the ionisation distribution and generate a complex distribution with hot and cold spots formed within the open field and below the bolus respectively. Several authors have described this effect and it is recommended that the edge of the bolus is tapered to smooth out the surface and reduce the effect (Khan, 2010, Nygaard et al., 2005, Podgorsak, 2005).

With the bolus now on the LMA insert it was necessary to measure the effect that a sharp edge would have on the distribution in the water phantom. Observing the Central Axis Depth Ionisation Curves (Illustration 65 page 145) for the 9MeV beam it is clear that the addition of each layer of perspex to the insert had some appreciable effect. Depth ionisation scans taken at a point +3.5cm (towards the gantry) beyond the central-axis do not show an appreciable change. To understand these effects depth ionisation nets were taken for the three layers of perspex (Illustration 69 to 71). When the nets are evaluated it can be seen that there is very little difference between the ionisation curves below ~95% on the open side (+ve or towards the gantry) of the insert. It can be further seen that at these ionisation levels there is no appreciable difference with the CC-04 Chamber open field 9MeV net (Illustration 35) However at central axis and on the -ve side (away from gantry & under the bolus) considerable perturbation of the distribution occurs. A hot spot up to 120% of the normalised open field occurs and the lower ionisation levels spread further from the LMA insert edge in a similar fashion that was seen in the full bolus on LMA insert.(Illustration 44 to46)

Observation of the Depth Ionisation Scans for the 20MeV beam did not display a similar effect to that seen with the 9MeV Depth Ionisation scan. However it would have been incorrect to assume that the 20MeV beam did not display a similar effect based only upon the depth ionisation scans therefore further depth ionisation nets were obtained for evaluation (Illustration 72 to 74). Comparison between the nets for the three layers of Perspex with the open field and the full bolus nets also demonstrated that there was little change in the ionisation below 95% on the open side. The hotspot was again closely associated with the bolus edge and grew to approximately 130% of the normalised open field

Exploring this effect further the Perspex was replaced with Teflon and Depth Ionisation scans and Depth Ionisation Nets measured. It was found that the 1x3mm and 2x3mm & 2x5mm Teflon Depth Ionisation Net (Illustration 79 to 84) were remarkably similar to that of the 1x6mm 2x6mm & 3x6mm Perspex Depth Ionisation Net respectively for both the 9MeV and

20MeV beams.

Finally the Teflon was replaced by Aluminium sheets as described previously and Depth Ionisation scan and Depth Ionisation Nets measured (Illustration 91 & 92). It was found that the 2.5/2.7mm Aluminium Net was very similar to the 2x6mm Perspex Net whilst the 5.0/5.1mm Aluminium Net approximated the 3x6mm Perspex Net.

In a similar approach to that followed for Chapter 4.3.1 Full Bolus an analysis of the Penumbra and Therapeutic regions for each technique was performed. To achieve a proper conversion to dose and analysis each Depth Ionisation net had to be renormalised in two different regions, I) open area and ii) under the bolus.

Depth ionisation scans had indicated that a position +3.5cm inplane did not display any perturbations as a result of the bolus edge and therefore each Depth Ionisation net was first renormalised at the +3.5cm inplane position based on the data obtained from the open field Depth Dose. It was found that in this position the Penumbra and therapeutic region did not change in width from that seen in the open field, see Table 26,31 and 36 on pages 62, 64 and 66 respectively (note the therapeutic region is only half of the full field).

To analysis the region beneath the bolus it was necessary to attempt to renormalise the Depth Dose net at a location which corresponded to a similar position for the Full Bolus Scans.

It was found that at a position of -5.5cm to -6.5cm inplane each Depth Dose Net could be renormalised and isodose lines would approximately overlay (within 2-3mm) with those seen in the Full Bolus Depth Dose Nets for the lower isodose levels.

Comparing the penumbras for the 9MeV beam and perspex showed reasonable agreement (<=2mm) however there was up to 4mm difference with the 20MeV beam. This approach was followed for Teflon and Aluminium where the agreement between the full bolus penumbra and the partial bolus penumbra varied between reasonable and extremely poor. Whilst the thinner layers of either Teflon and Aluminium bolus and particularly with the lower energy beam were approximately within 3mm, the result were not consistent bringing doubt on the reproducibility of the approach. It was found that small repositioning of the normalisation point could result in large changes in the agreement.

4.3.3 Strip Bolus

The application of a strip of bolus material (teflon 2x5mm) to the applicator, where there was an open region on either side of the strip, as expected generated two hot spots on either side of the bolus strip ranging up to 130% for the 20MeV beam (Khan, 2010).

With the bolus located closer to the CA of the beam than for the Partial Bolus setup (1cm vs 3cm) the open area on the gantry side (+ve on scans) was reduced and consequentially the shape of the high iso-ionisation lines are somewhat dissimilar, however observation of the <=80% iso-ionisation lines at +7.5cm (ie the beam edge) seen in Illustration 95 displayed an excellent match with the same iso-ionisation lines in Illustration 81 (Partial Bolus). The good match was also seen with the same iso-ionisation lines at depth for the open field region of the scan. With further inspection it was also possible to see a similar match in iso-ionisation lines between the beam edge at -1cm on Illustration 81 and -3cm in Illustration 95.

The iso-ionisation of the smaller open area (-ve side away from gantry) did not display the same depth penetration as seen on the +ve side of central axis open area however this was not surprising as the region could be considered to be quite similar to a small field where it is known that the beam characteristics can display (1) the depth of maximum dose shifts toward the surface, (2) the depth of 90% and 80% dose, become smaller, (3) the surface dose increases, and (4) the dose fall-off region becomes more gradual (Rustgi and Working, 1992, Khan, 2010).

Similar observations, which were seen for the 9MeV beam, can be made for the 20MeV depth ionisation nets Illustration 84 and 96.

An analysis of the strip bolus Depth Dose Nets open area was very similar to that seen with the Depth Dose net for the larger open area of the partial bolus scans. This was as expected as the two open areas were very similar and corresponded to the open field scan. When an analysis of the Depth Dose either under the bolus material or in the smaller open area appeared to suffer from the bolus edge effects with a higher dose in the open area and a lower dose under the bolus. An attempt was made at normalisation of the scans in both areas however the results were inconclusive as small repositioning ether in the inplane direction or depth resulted large changes.

4.3.4 Higher Z Grids

The paper by Alasti & Galbraith (Alasti and Galbraith, 1995) describes a process where a Tantalum wire mesh was used on the patients skin surface to elevate the surface dose of lower energy electron beams thereby effectively increasing the available therapeutic interval of the beam. Lambert et al (Lambert et al., 1999) provides an explanation that whilst the dual scattering foil generated electron beams of modern linear accelerators provided a dosimetric improvement of sharper dose fall off and lower doses beyond the maximum range it was at the "expense" of dose at superficial depths. Other authors have described methods by which the surface dose can be elevated including partial bolussing (Galbraith and Rawlinson, 1984), lead as surface bolus (Moyer et al., 1986) and beam spoilers (Das et al., 1991) they all have some limitations

Initial experimentation with layers of Aluminium mesh carefully stacked so that the open area of the mesh was progressively reduced provided results which were completely indistinguishable from one another. In an attempt to greatly reduce the "open area" Aluminium foil was substituted for the mesh and tested. Analysis of the depth ionisation scan for the open field and for the fields with 1xAl mesh or 1xAl shim on the applicator displayed very little difference and could easily be considered as the same beam quality remembering the results obtained earlier comparing beam qualities. The addition of the second sheet of Al Shim whilst it did appear to shift the depth ionisation scan towards the surface the move was less than 1mm.

Similar to the depth ionisation scans, analysis of the depth ionisation nets for 1xAl mesh, 1xAl Shim and 2xAl Shim (Illustration 99, 100 and 101), compared to the open field depth ionisation net (Illustration 35), were generally indistinguishable at depths for ionisation values <80%. The nets however did display a slightly increasing lateral contraction of the high percentage 90-100% ionisation lines whilst the low ionisation lines <40% displayed a lateral expansion.

For completeness the experimentation was also performed with the 20MeV electron beam and whilst there appeared to be a minor lateral contraction of the high iso-ionisation lines and a minor lateral expansion of the low iso-ionisation lines the nets were essentially indistinguishable. It was concluded that Aluminium mesh (nor shim) could not provide a suitable medium as bolus.

The Aluminium was replaced by a Stainless Steel mesh and in a similar fashion to the original experimentation with Aluminium mesh each additional layer was carefully aligned to reduce the visible open area. Observation of the depth ionisation scan for 9MeV (Illustration 105) does display a minor increase in the surface dose (approximately 84% to 88%) however this is not sufficient to utilise the beam to treat superficial malignancies. It may also be argued that the beam has lost some of it therapeutic qualities, albeit a minor change of approximately 2mm, with a shift of the 90% iso-ionisation line, beyond the peak, towards the surface.

Examination of the depth ionisation nets for 1, 2, 3 & 4xSS mesh (Illustration 107 to 110) displayed changes that were similar to those seen with the Aluminium Shim with the iso-ionisation lines greater than 50% contracting, i.e. moving in towards the central axis and the low iso-ionisation lines less than 50% laterally expanding. As before these experiments were repeated with the 20MeV beam and the same minor effects were observed.

It can be concluded for the obtained depth ionisation nets that the use of higher density meshes (Al or SS) on the applicator provides no immediate clinical benefit, such as increasing the surface dose of the electron beam, but rather could be considered as actually degrading the usefulness of the electron beam with the reduced high dose region and lateral increase in low dose area as demonstrated by tables 45 and 49.

4.4 Bolus on Surface

The effects of bolus material used on the surface has been well documented in both text books and papers by several different authors. Whether the bolus is Jeltrate Pads Elasto-gels Polyflex (Chang et al., 1992, Dubois et al., 1996, Thilmann et al., 1996, Babic et al., 2002), Tin & Lead (Moyer et al., 1986, Lambert et al., 1999, Healy et al., 2005), Wax & Perspex (Archambeau et al., 1981, Sharma et al., 1983, Low and Hogstrom, 1994, Humphries et al., 1996, Perkins et al., 2001, Kudchadker et al., 2003, Hanna et al., 2008), or exotic materials such as Tantalum mesh (Alasti and Galbraith, 1995, Cederbaum et al., 2001) their effects at the surface can be easily referenced.

With this in mind it was decided to experiment initially with perspex located on the surface of the water phantom to verify that measurements of the 9MeV electron beam obtained in the thesis conditions compared reasonably with previously published results. These measurements were then extended by substituting Teflon for the perspex.

In section *2.6 Bolus Materials* the perspex sheet was evaluated as being a water equivalent thickness of 6.7mm therefore it was expected that a depth ionisation scan taken with a single sheet of perspex material on the surface would result in shift of the scan towards the water surface by the same amount. Lambert et al (Lambert et al., 1999) illustrated that the application of tissue equivalent bolus resulted in a decrease of the therapeutic range by an equivalent amount, and Gunhan et al (Gunhan et al., 2003) demonstrated similar results. Examination of Illustration 115, it is seen that the depth ionisation curve shifts towards the surface by an amount slightly greater than its thickness when measured at the $R_{80,ion}$ g/cm^2 position. Whilst the shifts are not strictly in accordance with the water equivalent thickness calculated, it is believed that the minor differences seen particularly for the 3 layer of perspex is a result of the ionisation chamber used for data collection. Examination of the corresponding depth ionisation nets also demonstrated the simple shift of iso-ionisation lines towards the surface without any lateral alteration.

The depth ionisation scans were then repeated for Teflon at both 9MeV and 20MeV (Illustration 119 and 120 respectively). Analysis of the 9MeV scan determined that the depth ionisation curve was moved towards the surface, measured at the $R_{80,ion}$ g/cm^2 position, by 8.4mm and 18.2mm for the 5mm and 10mm thickness of Teflon respectively. For 20MeV the

respective shifts were 12.1mm and 24.1mm.

Comparison of these shifts with those calculated via the Tabata and Andreo approach for water equivalent depth (see page 42 ref table 5) displayed a much greater difference than those calculated for Perspex possibly indicating that the calculations performed in section *2.6 Bolus Materials* may well be in error and hence require further dedicated research.

Considering the results in this section for only Perspex as the bolus material and that which has been published it is reasonable to believe that the data obtained in the thesis experiments are relatively robust.

5. CONCLUSION

This thesis has demonstrated that it is possible to locate “bolus” materials (both tissue and non tissue like) on the LMA insert and modify the characteristics of the emerging electron beam. It is clear that such modifications do come at the expense of a broader beam penumbra and in many cases a significantly reduced lateral therapeutic dose region although the advantage of avoiding skin/bolus contact and positional reproducibility remains. The broader beam penumbra may not be totally disadvantageous as other authors have demonstrated the use of electron wedges to aid in beam matching (Kurup et al., 1992, Kurup et al., 1993). Should the broader beam penumbra be a problem it is known that the penumbra can be “sharpened” by using surface shielding, (Leavitt et al., 1990, Able et al., 1991, Chi et al., 2005, Chi et al., 2006, Halperin et al., 2008) however this reintroduces a skin/material contact that may result in an unhygienic situation.

In the thesis measurements the greatest potential for usefulness appeared to be with the 9MeV electron beam where it was possible to modify the electron beam to approximate the distribution of the 6MeV beam whilst increasing the available therapeutic interval. The restoration of the build up region may prove to be an advantage in some situations where there is still a desire to reduce the dose delivered to the skin.

It is quite clear that the bolus edge still has to be considered whether designing bolus for the skin surface or as in the thesis case, bolus for the applicator. This thesis did not investigate what sort of wedged edge was necessary to sufficiently reduce the generated hot spot, however it must be remembered that both the hot and cold spots may possibly be utilised if additional or less dose is required in particular areas.

It is reasonably obvious that the investigations performed with 20MeV electron beam were, in general, less productive and possibly the thesis may have been better served concentrating on the lower energy-range electrons where a build-up region remains, however that would not have allowed consideration of effects if the technique was used for treatment of deeper seated malignancies.

Whist the thesis did achieve its stated aim it did not have, nor intended to develop an appropriate mechanism by which such a technique could be introduced into the clinic. For this to be applied clinically an appropriate bolus design algorithm would need to be developed.

6. BIBLIOGRAPHY

ABLE, C. M., MILLS, M. D., MCNEESE, M. D. & HOGSTROM, K. R. 1991. Evaluation of a total scalp electron irradiation technique. *Int J Radiat Oncol Biol Phys,* 21**,** 1063-72.

ALASTI, H. & GALBRAITH, D. M. 1995. Depth dose flattening of electron beams using a wire mesh bolus. *Med Phys,* 22**,** 1675-83.

ALEXANDER, A., SOISSON, E., HIJAL, T., SARFEHNIA, A. & SEUNTJENS, J. 2011. Comparison of modulated electron radiotherapy to conventional electron boost irradiation and volumetric modulated photon arc therapy for treatment of tumour bed boost in breast cancer. *Radiother Oncol,* 100**,** 253-8.

ALLISY, A. 1996. Henri Becquerel: The Discovery of Radioactivity. *Radiation Protection Dosimetry,* 68**,** 3-10.

ALMOND, P. R., BIGGS, P. J., COURSEY, B. M., HANSON, W. F., HUQ, M. S., NATH, R. & ROGERS, D. W. 1999. AAPM's TG-51 protocol for clinical reference dosimetry of high-energy photon and electron beams. *Med Phys,* 26**,** 1847-70.

ALMOND, P. R., CUNNINGHAM, J. R., J., G. H., LOEVINGER, R., SUNTHARALINGAM, N., WRIGHT, K. A., NATH, R. & LEMPERT, G. D. 1983. A protocol for the determination of absorbed dose from high-energy photon and electron beams. *Med Phys,* 10**,** 741-71.

ALPER, T. 1963. Lethal Mutations and Cell Death. *Phys Med Biol,* 66**,** 365-85.

ANDREO, P. & BRAHME, A. 1981. Mean energy in electron beams. *Med Phys,* 8**,** 682-7.

ANDREO, P., BURNS, D.T., HOHLFELD, K., HUQ, M.S., KANAI, T., LAITANO, F., SMYTH, V., VYNCKIER, N.S. 2000. Absorbed Dose Determination in External Beam Radiotherapy: An International Code of Practice for Dosimetry based on Standards of Absorbed Dose to Water An International Code of Practice for Dosimetry", Technical Report Series no. 398. Vienna: IAEA, International Atomic Energy Agency.

ARCHAMBEAU, J. O., FORELL, B., DORIA, R., FINDLEY, D. O., JURISCH, R. & JACKSON, R. 1981. Use of variable thickness bolus to control electron beam penetration in chest wall irradiation. *Int J Radiat Oncol Biol Phys,* 7**,** 835-42.

BABIC, S., KERR, A. T., WESTERLAND, M., GOODING, J. & SCHREINER, L. J. 2002. Examination of Jeltrate Plus as a tissue equivalent bolus material. *J Appl Clin Med Phys,* 3**,** 170-5.

BERNIER, J. (ed.) 1995. *1895-1995 Radiation Oncology A Centry of Progress and Achivement*: European Society for Therapeutic Radiology and Oncology.

BORCIA, C. & MIHAILESCU, D. 2008. Are Water-Equivalent materials used in Electron Beams really water equivalent. *Rom. Journ. Phys.,* 53**,** 851-863.

BOURKE, P. 1996. *Beziér curves* [Online]. Available: http://paulbourke.net/geometry/bezier/index2.html [Accessed 30-9-2011 2011].

BRAHME, A. & SVENSSON, H. 1976. Specification of electron beam quality from the central-axis depth absorbed-dose distribution. *Med Phys,* 3**,** 95-102.

BRUINVIS, I. A., HEUKELOM, S. & MIJNHEER, B. J. 1985. Comparison of ionisation measurements in water and polystyrene for electron beam dosimetry. *Phys Med Biol,* 30**,** 1043-53.

BURNS, D. T., DING, G. X. & ROGERS, D. W. 1996. R50 as a beam quality specifier for selecting stopping-power ratios and reference depths for electron dosimetry. *Med Phys,* 23**,** 383-8.

CASAR, B., ZDESAR, U. & ROBAR, V. 2004. Evaluation of water equivalency of Plastic Water for high-energy electron beams using IAEA TRS-398 Code of Practice. *Radiol Oncol,* 38**,** 55-60.

CEDERBAUM, M., RAVKIN, A., ROSENBLATT, E. & GEZ, E. 2001. Implementing a tantalum wire mesh to increase the skin dose in low-energy electron irradiation of the chest wall. *Med Dosim,* 26**,** 275-9.

CHANG, F., CHANG, P., BENSON, K. & SHARE, F. 1992. Study of elasto-gel pads used as surface bolus material in high energy photon and electron therapy. *Int J Radiat Oncol Biol Phys,* 22**,** 191-3.

CHI, P. C., HOGSTROM, K. R., STARKSCHALL, G., ANTOLAK, J. A. & BOYD, R. A. 2005. Modeling skin collimation using the electron pencil beam redefinition algorithm. *Med Phys,* 32**,** 3409-18.

CHI, P. C., HOGSTROM, K. R., STARKSCHALL, G., BOYD, R. A., TUCKER, S. L. & ANTOLAK, J. A. 2006. Application of the electron pencil beam redefinition algorithm to electron arc therapy. *Med Phys,* 33**,** 2369-83.

CHOW, J. C. & GRIGOROV, G. N. 2007. Effect of electron beam obliquity on lateral buildup ratio: a Monte Carlo dosimetry evaluation. *Phys Med Biol,* 52**,** 3965-77.

COHEN, M. 1972. Central axis depth dose data for use in radiotherapy. General introduction. *Br J Radiol,* 11**,** Suppl 11:8-17.

DAS, I. J., CHENG, C. W., WATTS, R. J., AHNESJO, A., GIBBONS, J., LI, X. A., LOWENSTEIN, J., MITRA, R. K., SIMON, W. E. & ZHU, T. C. 2008. Accelerator beam data commissioning equipment and procedures: report of the TG-106 of the Therapy Physics Committee of the AAPM. *Med Phys,* 35**,** 4186-215.

DAS, I. J., KASE, K. R., COPELAND, J. F. & FITZGERALD, T. J. 1991. Electron beam modifications for the treatment of superficial malignancies. *Int J Radiat Oncol Biol Phys,* 21**,** 1627-34.

DAS, I. J., MCNEELEY, S. W. & CHENG, C. W. 1998. Ionization chamber shift correction and surface dose measurements in electron beams. *Phys Med Biol,* 43**,** 3419-24.

DAS, S. K., BELL, M., MARKS, L. B. & ROSENMAN, J. G. 2004. A preliminary study of the role of modulated electron beams in intensity modulated radiotherapy, using automated beam orientation and modality selection. *Int J Radiat Oncol Biol Phys,* 59**,** 602-17.

DEGENER, R. 1998a. WP700 Getting Started Version 3.50.00 with Blue Phantom. Schwarzenbruck, Germany: Wellhöfer Dosimetrie.

DEGENER, R. 1998b. WP700 Software Description. Schwarzenbruck, Germany: Wellhöfer Dosimetrie.

DEMIR, B., OKUTAN, M., CAKIR, A., GOKSEL, E. & BILGE, H. 2009. The effect of oblique electron beams to the surface dose under the bolus. *Med Dosim,* 34**,** 311-6.

DING, G. X. & ROGERS, D. W. 1996. Mean energy, energy-range relationships and depth-scaling factors for clinical electron beams. *Med Phys,* 23**,** 361-76.

DING, G. X. A. R., D.W.O, MACKIE, T.R. 1995. Calculation of stopping-power ratios using realistic clinical electron beams. *Med Phys,* 22.

DUBOIS, D., BICE, W., BRADFORD, B., SCHNEID, T. & ENGELMEIER, R. 1996. Moldable tissue equivalent bolus for high-energy photon and electron therapy. *Med Phys,* 23**,** 1547-9.

DUTREIX, J. & DUTREIX, A. 1966. [Comparative study of a series of ionization chambers within 20 and 10 MeV electron fluxes]. *Biophysik,* 3**,** 249-58.

EKSTRAND, K. E. & DIXON, R. L. 1982. The problem of obliquely incident beams in electron-beam treatment planning. *Med Phys,* 9**,** 276-8.

FARMER, F. T. 1962. Supervoltage therapy: a review of present day facilities and techniques. *Phys Med Biol,* 6**,** 505-31.

FERNANDEZ-VAREA, J. M., ANDREO, P. & TABATA, T. 1996. Detour factors in water and plastic phantoms and their use for range and depth scaling in electron-beam dosimetry. *Phys Med Biol,* 41**,** 1119-39.

GALBRAITH, D. M. & RAWLINSON, J. A. 1984. Partial bolussing to improve the depth doses in the surface region of low energy electron beams. *Int J Radiat Oncol Biol Phys,* 10**,** 313-7.

GERBI, B. J., ANTOLAK, J. A., DEIBEL, F. C., FOLLOWILL, D. S., HERMAN, M. G., HIGGINS, P. D., HUQ, M. S., MIHAILIDIS, D. N., YORKE, E. D., HOGSTROM, K. R. & KHAN, F. M. 2009. Recommendations for clinical electron beam dosimetry: supplement to the recommendations of Task Group 25. *Med Phys,* 36**,** 3239-79.

GINZTON, E. L., HANSEN, W. W. & KENNEDY, W. R. 1948. A linear electron accelerator. *Rev Sci Instrum,* 19**,** 89-108.

GINZTON, E. L., MALLORY, K. B. & KAPLAN, H. S. 1957. The Stanford medical linear accelerator. I. Design and development. *Stanford Med Bull,* 15**,** 123-40.

GINZTON, E. L. & NUNAN, C. S. 1985. History of microwave electron linear accelerators for radiotherapy. *Int J Radiat Oncol Biol Phys,* 11**,** 205-16.

GROSSWENDT, B. & ROOS, M. 1989. Electron beam absorption in solid and in water phantoms: depth scaling and energy-range relations. *Phys Med Biol,* 34**,** 509-518.

GRUBBÉ, E. H. 1933. Priority in the Therapeutic Use of X-rays. *Radiology,* 21**,** 156-162.

GUNHAN, B., KEMIKLER, G. & KOCA, A. 2003. Determination of surface dose and the effect of bolus to

surface dose in electron beams. *Med Dosim,* 28**,** 193-8.

HALL, E. J. & GIACCIA, A. J. 2012. *Radiobiology for the Radiologists*, Lippincott Williams & Wilkins a Wolters Kluwer business.

HALPERIN, E. C., PEREZ, C. A. & BRADY, L. W. (eds.) 2008. *Preez and Brady's principles and practice of radiation oncology*: Lippincott Williams & Wilkins.

HANNA, L., CROSBY, T. & MACBETH, F. 2008. *Practical Clinical Oncology*, Cambridge University Press.

HEALY, B. J., PADMANABHAN, P. & NITSCHKE, K. N. 2005. Tin foil as bolus material for therapeutic electron beams from the Varian Clinac 2100C/D. *Australas Phys Eng Sci Med,* 28**,** 8-13.

HERNANDEZ, V., SANCHEZ-REYES, A., BADAL, A., VILA, A., MUR, E., PEDRO, A. & SANCHIZ, F. 2010. Use of an electron spoiler for radiation treatment of surface skin diseases. *Clin Transl Oncol,* 12**,** 374-80.

HIGGINBOTHAM, J. F. (ed.) 1996. *Applications of New Technology: External Dosimetry,* Madison, WI: Medical Physics Publishing.

HOGSTROM, K. R. & ALMOND, P. R. 2006. Review of electron beam therapy physics. *Phys Med Biol,* 51**,** R455-89.

HOGSTROM, K. R., ANTOLAK, J. A., KUDCHADKER, R. J., MA, C. M. & LEAVITT, D. D. Year. Modulated electron therapy. *In:* PALTA, J. & MACKIE, R., eds. Intensity Modulated Radiation Therapy, The State of the Art, 2003 Colorado Springs, Colorado, USA. Madison, WI: Medical Physics Publishing.

HOGSTROM, K. R., MILLS, M. D. & ALMOND, P. R. 1981. Electron beam dose calculations. *Phys Med Biol,* 26**,** 445-59.

HUANG, Y., WILLOMITZER, C., ZAKARIA, G. A. & HARTMANN, G. H. 2010. Experimental determination of the effective point of measurement of cylindrical ionization chambers for high-energy photon and electron beams. *Phys Med,* 26**,** 126-31.

HUMPHRIES, S. M., BOYD, K., CORNISH, P. & NEWMAN, F. D. 1996. Comparison of Super Stuff and paraffin wax bolus in radiation therapy of irregular surfaces. *Med Dosim,* 21**,** 155-7.

HYODYNMAA, S., GUSTAFSSON, A. & BRAHME, A. 1996. Optimization of conformal electron beam therapy using energy- and fluence-modulated beams. *Med Phys,* 23**,** 659-66.

ICRU 1980. Radiation Quantities and Units. Bethesda USA: International Commission on Radiation Units and Measurements.

ICRU 1984. Radiation Dosimetry: Electron Beams with Energy between 1 and 50 MeV. Bethesda USA: International Commission on Radiation Units and Measurements.

ICRU 1993. Stopping powers and ranges for protons and alpha particles. Bethesda USA: International

Commission on Radiation Units and Measurements.

JOHNS, H. E. & CUNNINGHAM, J. R. 1983. *The Physics of Radiology,* Springfield, Illinois, USA, Charles C Thomas.

KARZMARK, C., NUNAN, CS & TANABE, E 1993. *Medical Electron Accelerators*, McGraw-Hill Inc.

KHAN, A., DOPPKE, K. P., HOGSTROM, K. R., KUTCHER, G. J., NATH, R., PRASAD, S. C., PURDY, J. A., ROZENFELD, M. & WERNER, B. L. 1991a. *CLINICAL ELECTRON-BEAM DOSIMETRY - REPORT OF TASK GROUP NO. 25 RADIATION THERAPY COMMITTEE,* New York, NY, USA, American Institute of Physics.

KHAN, F. M. 1991. Basic physics of electron beam therapy. *Front Radiat Ther Oncol,* 25**,** 10-29; discussion 61-3.

KHAN, F. M. 1994. *The Physics of Radiation Therapy,* Baltimore, Lippincott Williams & Wilkins.

KHAN, F. M. 2010. *The Physics of Radiation Therapy,* Baltimore, Lippincott Williams & Wilkins a Wolters Kluwer Company.

KHAN, F. M., DOPPKE, K. P., HOGSTROM, K. R., KUTCHER, G. J., NATH, R., PRASAD, S. C., PURDY, J. A., ROZENFELD, M. & WERNER, B. L. 1991b. Clinical electron-beam dosimetry: report of AAPM Radiation Therapy Committee Task Group No. 25. *Med Phys,* 18**,** 73-109.

KIM, C., KIM, W., PARK, B. U., HONG, C. & JEONG, M. 1999. Smoothing techniques via the bezier curve. *Communications in Statistics - Theory and Methods* 28.

KIM, C., PARK, B. H., KIM, W. & LIM, C. 2002. Bezier Curve Smoothing of the Kaplan-Meier Estimator. *Annals of the Institute of Statistical Mathematics,* 55**,** 359-367.

KLEVENHAGEN, S. C. 1985. *Physics of Electron Beam Therapy,* Bristol, Adam Hilger Ltd.

KLEVENHAGEN, S. C. 1993. *Physics and Dosimetry of Therapy Electron Beams*, Medical Physics Publishing.

KNOLL, G. F. 2000. *Radiation Detectoin and Measurement*, Hoboken: John Wiley & Sons, Inc.

KONG, M. & HOLLOWAY, L. 2007. An investigation of central axis depth dose distribution perturbation due to an air gap between patient and bolus for electron beams. *Australas Phys Eng Sci Med,* 30**,** 111-9.

KOREVAAR, E. W., HEIJMEN, B. J., WOUDSTRA, E., HUIZENGA, H. & BRAHME, A. 1999. Mixing intensity modulated electron and photon beams: combining a steep dose fall-off at depth with sharp and depth-independent penumbras and flat beam profiles. *Phys Med Biol,* 44**,** 2171-81.

KUDCHADKER, R. J., ANTOLAK, J. A., MORRISON, W. H., WONG, P. F. & HOGSTROM, K. R. 2003. Utilization of custom electron bolus in head and neck radiotherapy. *J Appl Clin Med Phys,* 4**,** 321-33.

KURUP, R. G., GLASGOW, G. P. & LEYBOVICH, L. B. 1993. Design of electron beam wedges for increasing the penumbra of abutting fields. . *Phys Med Biol,* 38**,** 667.

KURUP, R. G., WANG, S. & GLASGOW, G. P. 1992. Field matching of electron beams using plastic wedge

penumbra generators. *Phys Med Biol,* 37**,** 145-53.

LACROIX, F., GUILLOT, M., MCEWEN, M., COJOCARU, C., GINGRAS, L., BEDDAR, A. S. & BEAULIEU, L. 2010. Extraction of depth-dependent perturbation factors for parallel-plate chambers in electron beams using a plastic scintillation detector. *Med Phys,* 37**,** 4331-42.

LAMBERT, G. D., RICHMOND, N. D., KERMODE, R. H. & PORTER, D. J. 1999. The use of high density metal foils to increase surface dose in low-energy clinical electron beams. *Radiother Oncol,* 53**,** 161-6.

LEAVITT, D. D., EARLEY, L. & STEWART, J. R. 1990. Design and production of customized field shaping devices for electron arc therapy. *Med Dosim,* 15**,** 25-31.

LEE, M. C., DENG, J., LI, J., JIANG, S. B. & MA, C. M. 2001. Monte Carlo based treatment planning for modulated electron beam radiation therapy. *Phys Med Biol,* 46**,** 2177-99.

LEE, M. C., JIANG, S. B. & MA, C. M. 2000. Monte Carlo and experimental investigations of multileaf collimated electron beams for modulated electron radiation therapy. *Med Phys,* 27**,** 2708-18.

LEVITT, S. H., PURDY, J. A., PEREZ, C. A. & VIJAYAKUMAR, S. (eds.) 2006. *Technical Basis of Radiation Therapy Practical Clinical Applications,* Berlin Germany: Springer-Verlag.

LOOE, H. K., HARDER, D. & POPPE, B. 2011. Experimental determination of the effective point of measurement for various detectors used in photon and electron beam dosimetry. *Phys Med Biol,* 56**,** 4267-90.

LOW, D. A. & HOGSTROM, K. R. 1994. Determination of the relative linear collision stopping power and linear scattering power of electron bolus material. *Phys Med Biol,* 39**,** 1063-8.

LOW, D. A., STARKSCHALL, G., SHERMAN, N. E., BUJNOWSKI, S. W., EWTON, J. R. & HOGSTROM, K. R. 1995. Computer-aided design and fabrication of an electron bolus for treatment of the paraspinal muscles. *Int J Radiat Oncol Biol Phys,* 33**,** 1127-38.

MA, C. M., DING, M., LI, J. S., LEE, M. C., PAWLICKI, T. & DENG, J. 2003. A comparative dosimetric study on tangential photon beams, intensity-modulated radiation therapy (IMRT) and modulated electron radiotherapy (MERT) for breast cancer treatment. *Phys Med Biol,* 48**,** 909-24.

MA, C. M., PAWLICKI, T., LEE, M. C., JIANG, S. B., LI, J. S., DENG, J., YI, B., MOK, E. & BOYER, A. L. 2000. Energy- and intensity-modulated electron beams for radiotherapy. *Phys Med Biol,* 45**,** 2293-311.

MALAMUT, C., ROGERS, D. W. & BIELAJEW, A. F. 1991. Calculation of water/air stopping-power ratios using EGS4 with explicit treatment of electron-positron differences. *Med Phys,* 18**,** 1222-8.

MANN, W. B., AYRES, R. L. & GARFINKEL, S. B. 1980. *Radioactivity and Its Measurement,* Oxford, UK, Pergamon Press.

MAYLES, P., NAHUM, A. & ROSENWALD, J.C. (ed.) 2007. *Handbook of Radiotherapy Physics: Theory and Practice,* Boca Raton, FL: CRC Press, Taylor and Francis.

MCCAFFREY, J. P., DOWNTON, B., SHEN, H., NIVEN, D. & MCEWEN, M. 2005. Pre-irradiation effects on ionization chambers used in radiation therapy. *Phys Med Biol,* 50**,** N121-33.

MCEWEN, M. R. & DUSAUTOY, A. R. 2003. Characterization of the water-equivalent material WTe for use in electron beam dosimetry. *Phys Med Biol,* 48**,** 1885-93.

MCMILLAN, T. J. 2003. Principles of Radiobiology. *In:* BOMFORD, C. K. & KUNKLER, I. H. (eds.) *Walter and Miller's Textbook of Radiotherapy, Radiation Physics, Therapy and Oncology* Sixth ed.: Churchill Livingston, Elsevier Science Limited.

METCALFE, P., KRON, T. & HOBAN, P. W. 1997. *The Physics of Radiotherapy X-Rays from Linear Accelerators,* Madison, Wisconsin, USA, Medical Physics Publishing.

MIRONOV, V. O. & ELIZAROVA, M. V. 2011. An Estimation of inaccuracy in dosimetric data smoothing when installing the remote radiation therapy planning systems. *MAVE-BME International Workshop on Computer Integrated Surgery.* Budapest, Hungary.

MOYER, R. F., KING, G. A. & HAUSER, J. F. 1986. Lead as surface bolus for high-energy photon and electron therapy. *Med Phys,* 13**,** 263-6.

NYGAARD, K., ODLAND, O. H., KVINNSLAND, Y., NYGAARD, B., HEGGDAL, J. & MUREN, L. P. 2005. Measurements and treatment planning calculations of electron dose distributions below bolus edges. *Radiother Oncol,* 74**,** 217-20.

ONO, T., ARAKI, F. & YOSHIYAMA, F. 2011. Possibility of using cylindrical ionization chambers for percent depth-dose measurements in clinical electron beams. *Med Phys,* 38**,** 4647-54.

PANGLOSSI, H. V. (ed.) 2007. *Leading edge antioxidants research,* Hauppauge, New York: Nova Science Publishers.

PERKINS, G. H., MCNEESE, M. D., ANTOLAK, J. A., BUCHHOLZ, T. A., STROM, E. A. & HOGSTROM, K. R. 2001. A custom three-dimensional electron bolus technique for optimization of postmastectomy irradiation. *Int J Radiat Oncol Biol Phys,* 51**,** 1142-51.

PODGORSAK, E. B. (ed.) 2005. *Radiation Oncology Physics: A Handbook for Teachers and Students,* Austria: International Atomic Energy Agency.

READ, J. 1957. The approach of the physicist to radiation biology. *Phys Med Biol,* 1**,** 209-24.

RUSTGI, S. N. & WORKING, K. R. 1992. Dosimetry of small field electron beams. *Med Dosim,* 17**,** 107-10.

SHARMA, S. C., DEIBEL, F. C. & KHAN, F. M. 1983. Tissue equivalence of bolus materials for electron beams. *Radiology,* 146**,** 854-5.

SHARMA, S. C. & JOHNSON, M. W. 1993. Surface dose perturbation due to air gap between patient and bolus for electron beams. *Med Phys,* 20**,** 377-8.

SHORTT, K. R., ROSS, C. K., BIELAJEW, A. F. & ROGERS, D. W. 1986. Electron beam dose distributions

near standard inhomogeneities. *Phys. Med. Biol.,* 1**,** 235-249.

SORCINI, B. B. & BRAHME, A. 1994. An accurate energy-range relationship for high-energy electron beams in arbitrary materials. *Phys Med Biol,* 39**,** 795-811.

STARKSCHALL, G., ANATOLAK, J. A. & HOGSTROM, K. R. Year. Electron Beam Bolus for 3D Conformal Radiation Therapy. *In:* PURDY, J. A. & EMAMI, B., eds. 3D Radiation Treatment Planning and Conformal Therapy, 1993 1993 St. Louis, Missouri, USA. Medical Physics Publishing.

TABATA, T. & ANDREO, P. 1998. Semiemperical formulas for the detour factor of 1- to 50-MeV electrons in condensed materials. *Radiation Physics and Chemistry,* 53**,** 353-360.

TELLO, V. M., TAILOR, R. C. & HANSON, W. F. 1995. How water equivalent are water-equivalent solid materials for output calibration of photon and electron beams? *Med Phys,* 22**,** 1177-89.

THILMANN, C., ADAMIETZ, I. A., MOSE, S., SARAN, F., RAMM, U. & BOTTCHER, H. D. 1996. Increase of surface dose using wound dressings during percutaneous radiotherapy with photons and electrons. *Radiother Oncol,* 40**,** 181-4.

THOMADSEN, B., CONSTANTINOU, C. & HO, A. 1995. Evaluation of water-equivalent plastics as phantom material for electron-beam dosimetry. *Med Phys,* 22**,** 291-6.

THWAITES, D. I. 1985. Measurements of ionisation in water, polystyrene and a 'solid water' phantom material for electron beams. *Phys Med Biol,* 30**,** 41-53.

THWAITES, D. I., DUSAUTOY, A. R., JORDAN, T., MCEWEN, M. R., NISBET, A., NAHUM, A. E. & PITCHFORD, W. G. 2003. The IPEM code of practice for electron dosimetry for radiotherapy beams of initial energy from 4 to 25 MeV based on an absorbed dose to water calibration. *Phys Med Biol,* 48**,** 2929-70.

VAN DYK, J. (ed.) 1999. *The Modern Technology of Radiation Oncology,* Madison, Wisconsin USA: Medical Physics Publishing.

VATANEN, T., TRANEUS, E. & LAHTINEN, T. 2009. Enhancement of electron-beam surface dose with an electron multi-leaf collimator (eMLC): a feasibility study. *Phys Med Biol,* 54**,** 2407-19.

WANG, L. L. & ROGERS, D. W. 2009a. Replacement correction factors for cylindrical ion chambers in electron beams. *Med Phys,* 36**,** 4600-8.

WANG, L. L. & ROGERS, D. W. 2009b. Study of the effective point of measurement for ion chambers in electron beams by Monte Carlo simulation. *Med Phys,* 36**,** 2034-42.

WEATHERBURN, H. & STEDEFORD, B. 1977. Effective measuring position for cylindrical ionization chambers when used for electron beam dosimetry. *Br J Radiol,* 50**,** 921-2.

WERNER, B. L., KHAN, F. M. & DEIBEL, F. C. 1983. Model for calculating depth dose distributions for broad electron beams. *Med Phys,* 10**,** 582-8.

WILLIAMS, J. & THWAITES, D. (eds.) 1993. *Radiotherapy Physics in practice,* Oxford: Oxford University Press.

ZEIDAN, O. A., CHAUHAN, B. D., ESTABROOK, W. W., WILLOUGHBY, T. R., MANON, R. R. & MEEKS, S. L. 2011. Image-guided bolus electron conformal therapy - a case study. *J Appl Clin Med Phys,* 12**,** 3311.

ZHU, D., LI, K., GUO, L. & LIU, T. 2009. Bezier Control Points Image: A Novel Shape Representation Approach for Medical Imaging. *Conf Rec Asilomar Conf Signals Syst Comput,* 2009**,** 1094-1098.

ZINK, K. & WULFF, J. 2009. Positioning of a plane-parallel ionization chamber in clinical electron beams and the impact on perturbation factors. *Phys Med Biol,* 54**,** 2421-35.

APPENDIX

This appendix contains prints of the scans obtained during thesis measurements.

All scans from this thesis measurements were saved in raw form without smoothing or rescaling. If any analysis was performed during data acquisition this was saved as a new scan number.

All data analysis, post measurement sessions, were performed on a copy of the original experimental data set. Some file numbers (denoted with the form <000000xxx> where xxx is numerical) and listed in the prints may change for the same scan if the scan has been re-saved, copied or moved for additional analysis, a track of all file numbers and file locations was maintained in a log book.

In general all scans were smoothed with the Least Squares and/or Bézier Smoothing algorithms prior to any numerical analysis. The smoothing window size varied between 15 and 31 width depending on the amount of noise on the scan. Where scans were not significantly noisy in their raw form only a simple smoothing was required and for numerical analysis, the Bézier Algorithm with window 11 was used.

Where Depth-Inplane Ionisation Nets were rescaled this was performed by referencing the net to a single appropriate Depth Ionisation scan. Depth-Inplane Ionisation Iso Nets were obtained from calculated arrays with an interpolation width of 0.1mm in scan direction and 0.1mm in other direction with included array smoothing by the Wellhöfer software.

All scan plots were produced by printing to a pdf driver PDFCreator and file conversion to png format using GNU Image Manipulation Program (GIMP Software).

A.1 Project and Commissioning/Acceptance Quality Comparison

- **9MeV Thesis and Commissioning Depth Ionisation for Table 7**
- **20MeV Thesis and Commissioning Depth Ionisation PDI for Table 7**

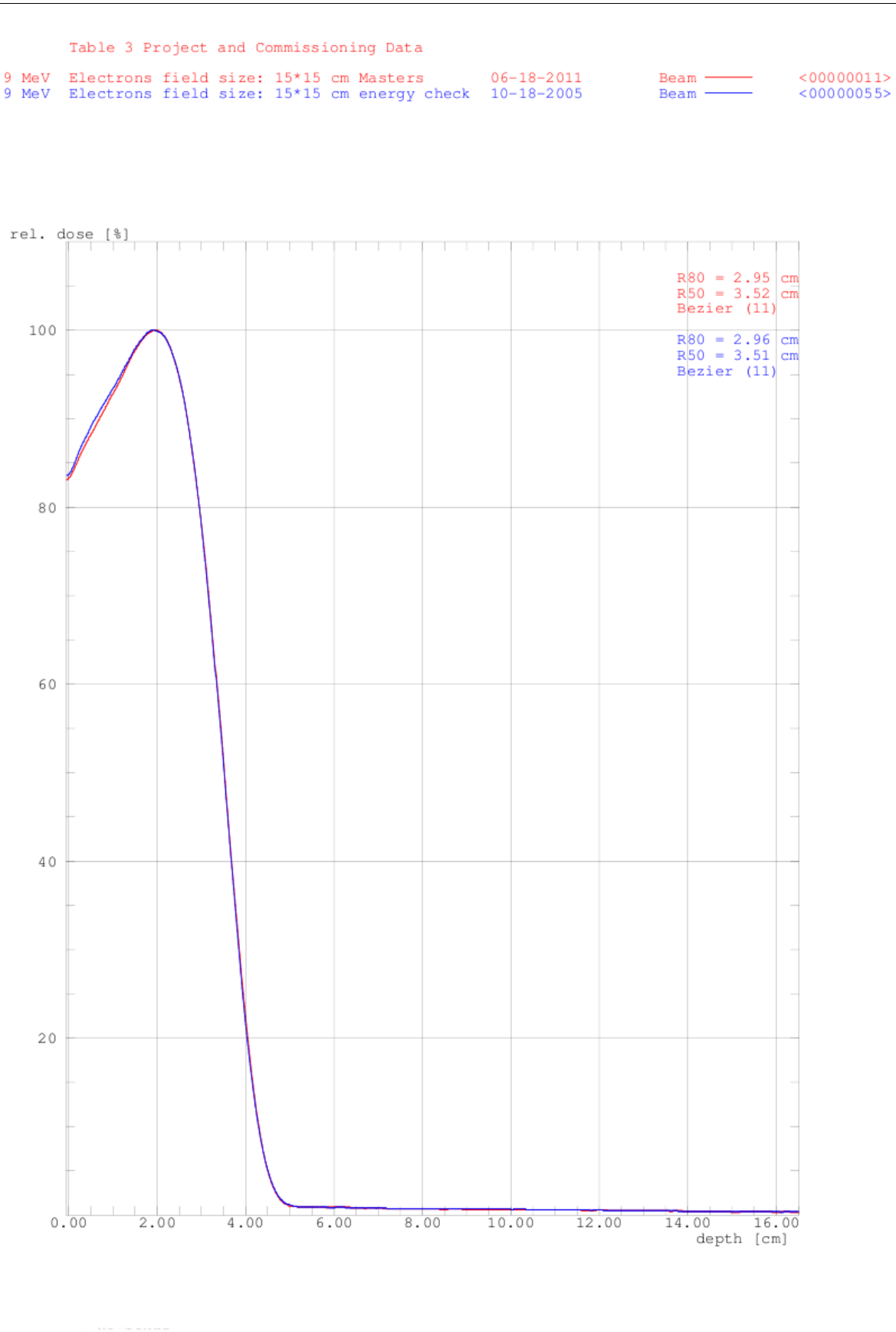

Illustration 28: 9MeV Thesis and Commissioning Depth Ionisation for Table 7

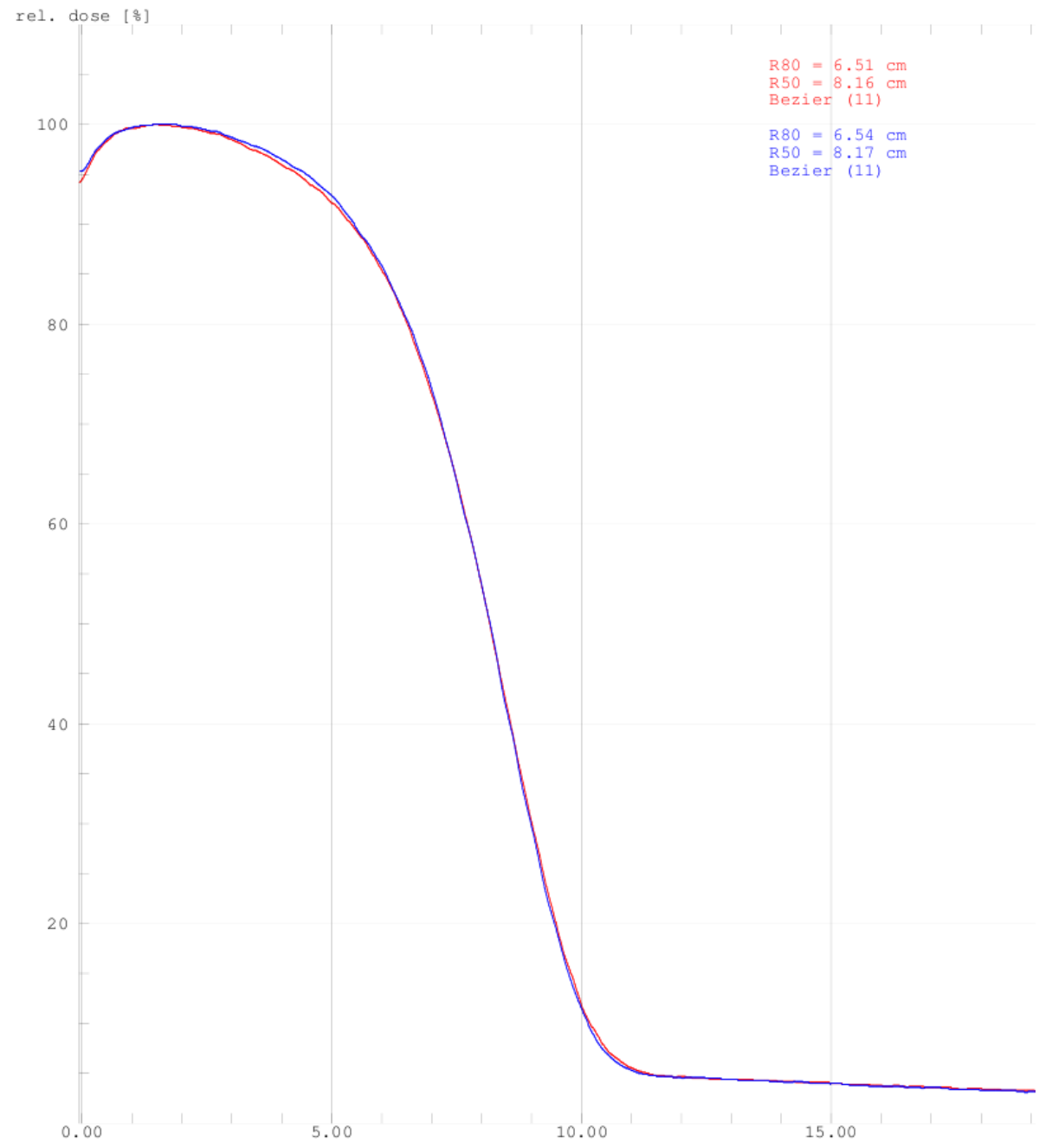

Illustration 29: 20MeV Thesis and Commissioning Depth Ionisation PDI for Table 7

A.2 Roos, CC-04 and IC-15 Chamber Comparisons for energy

- **6MeV Roos and CC-04 Chamber Depth Ionisation Table 8**
- **9MeV Roos, CC-04 & IC-15(green) Chamber Depth Ionisation Table 8**
- **12MeV Roos and CC-04 Chamber Depth Ionisation Table 8**
- **16MeV Roos and CC-04 Chamber Depth Ionisation Table 8**
- **20MeV Roos, CC-04 & IC-15(green) Depth Ionisation Chamber Table 8**

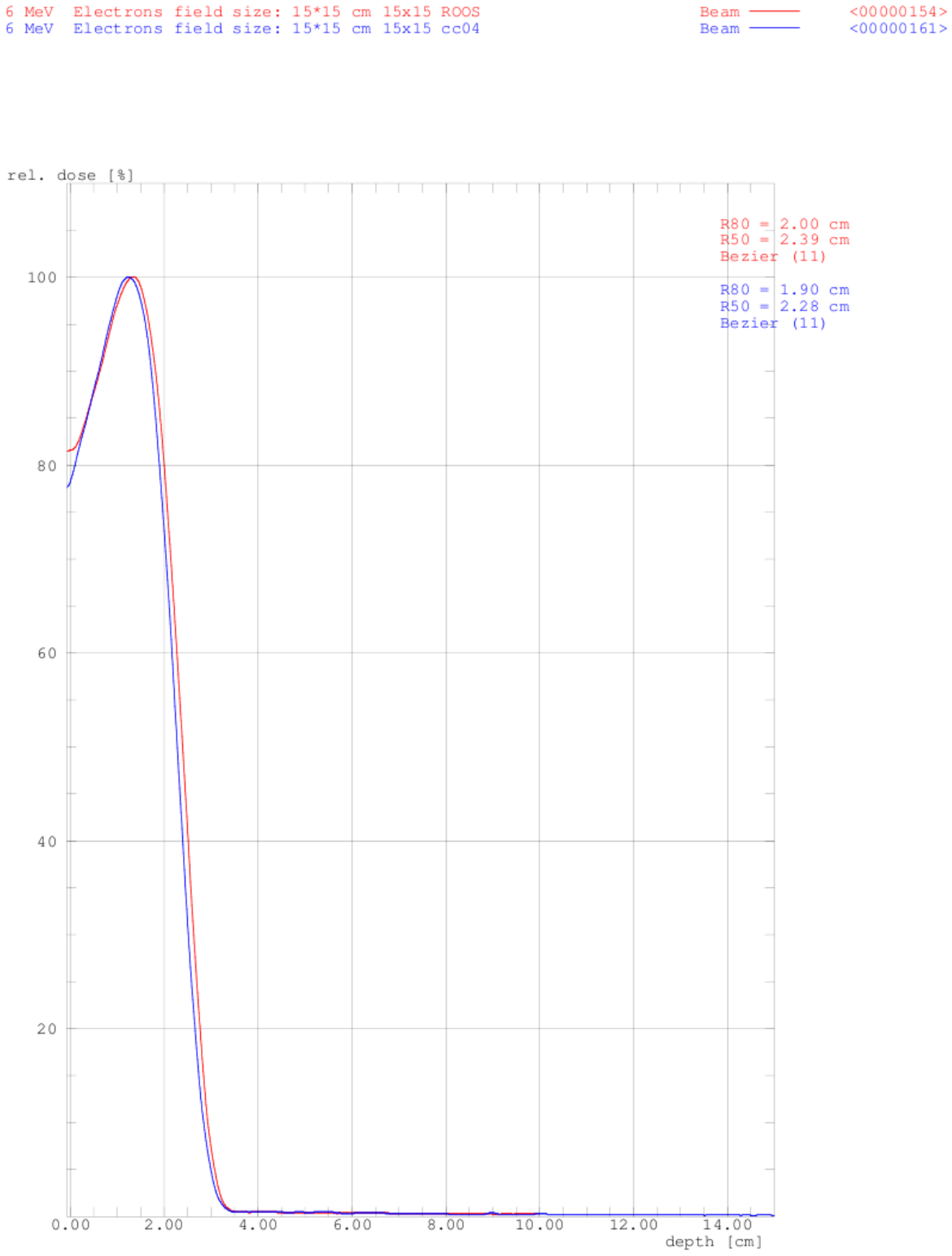

Illustration 30: 6MeV Roos and CC-04 Chamber Depth Ionisation Table 8

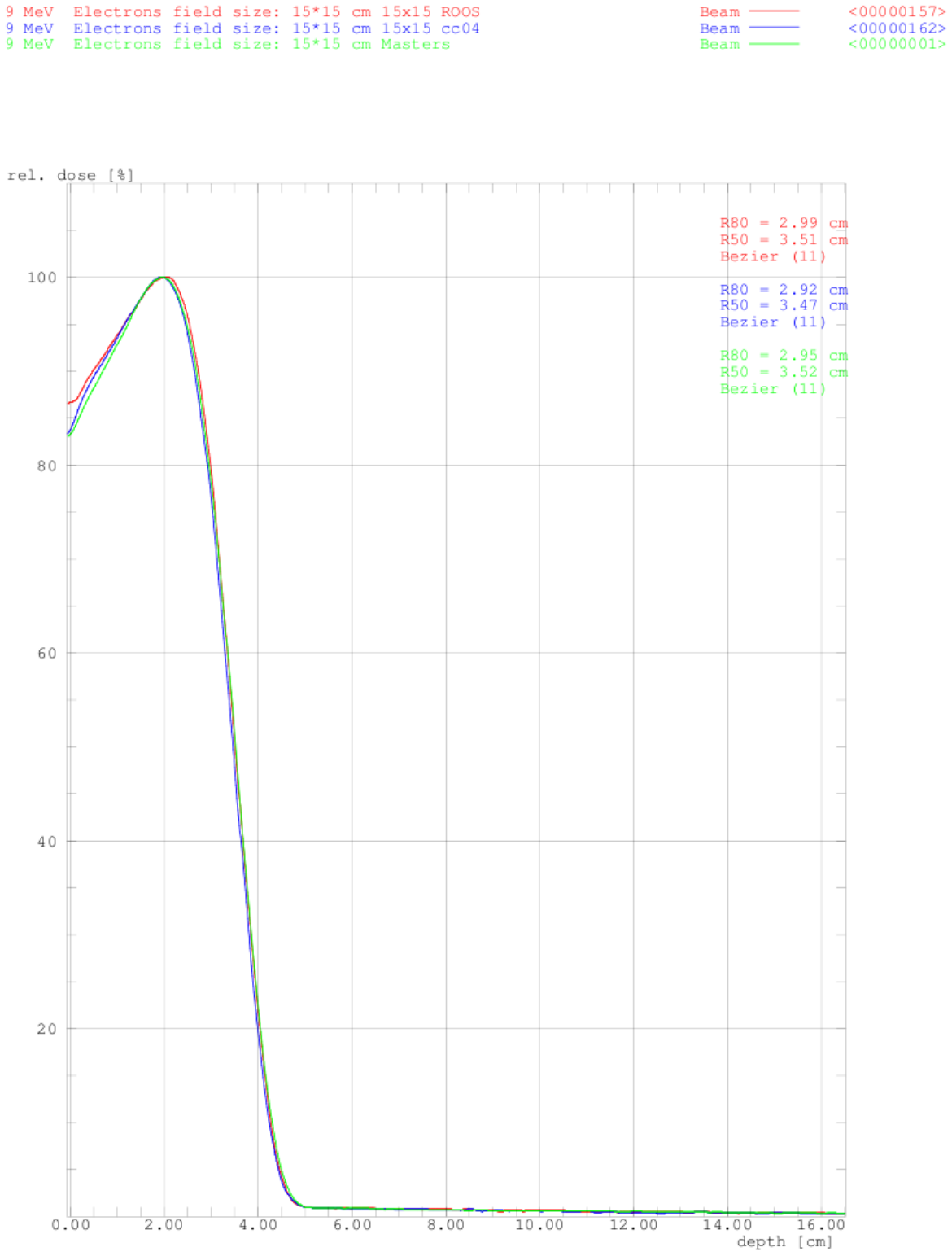

Illustration 31: 9MeV Roos, CC-04 & IC-15(green) Chamber Depth Ionisation Table 8

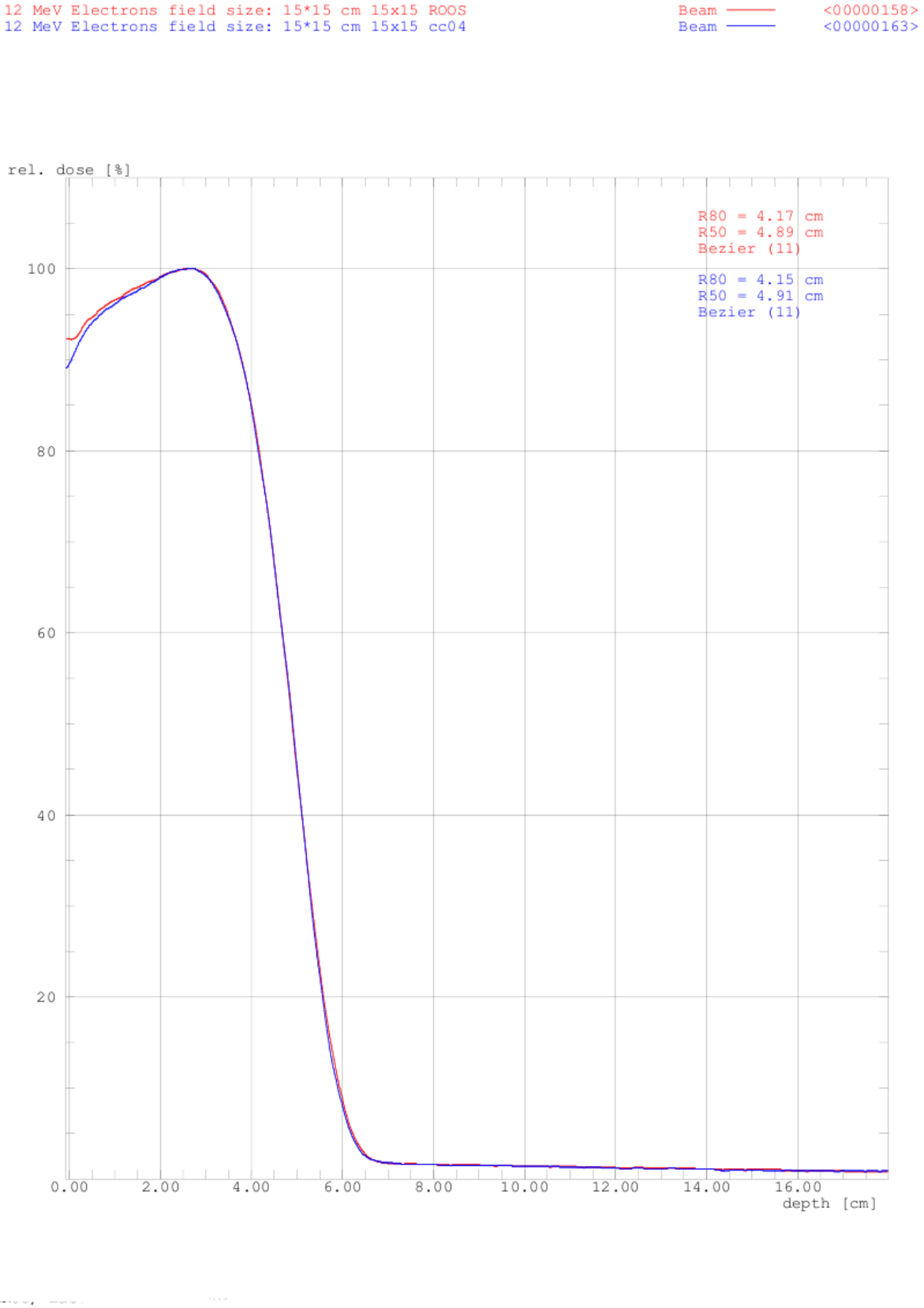

Illustration 32: 12MeV Roos and CC-04 Chamber Depth Ionisation Table 8

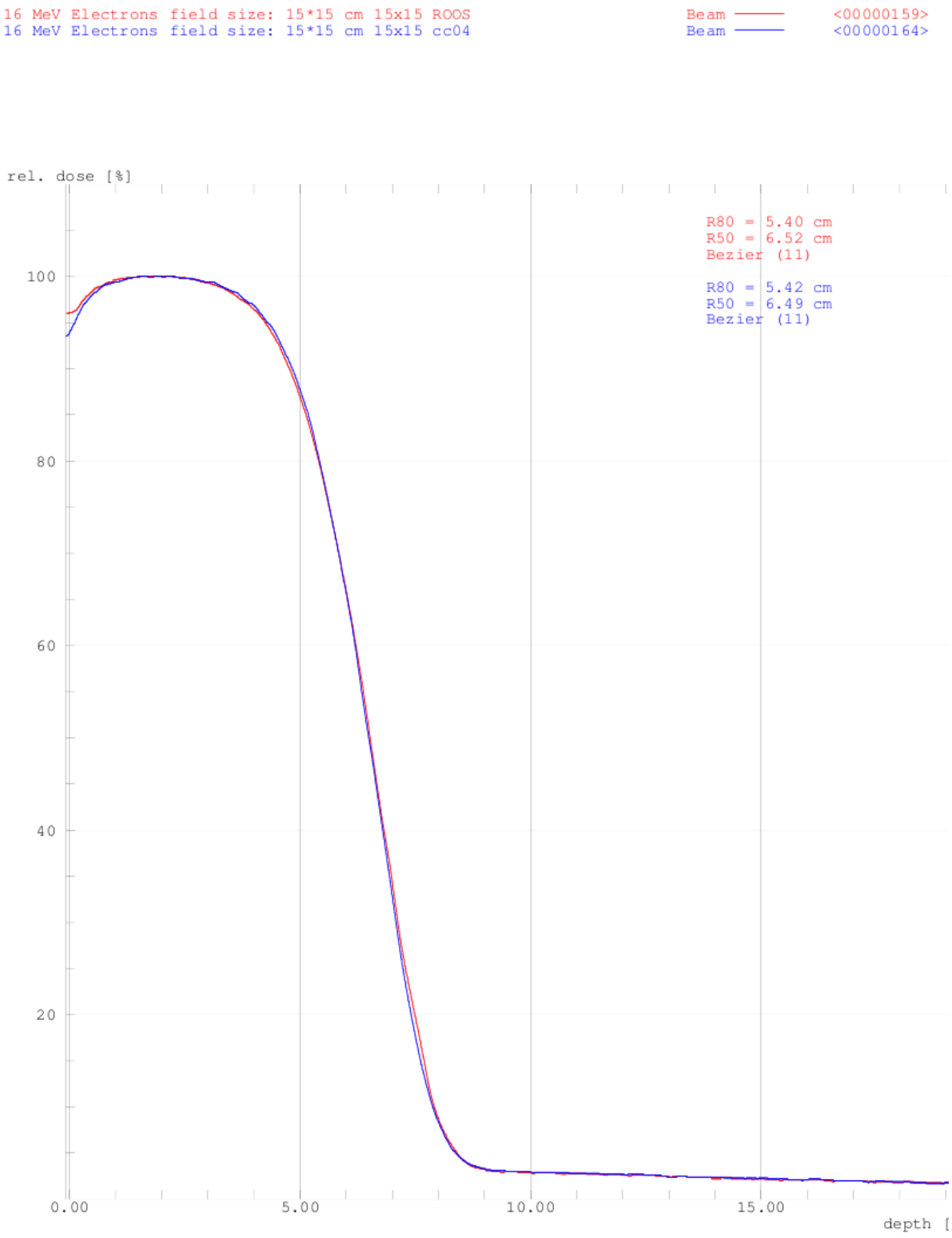

Illustration 33: 16MeV Roos and CC-04 Chamber Depth Ionisation Table 8

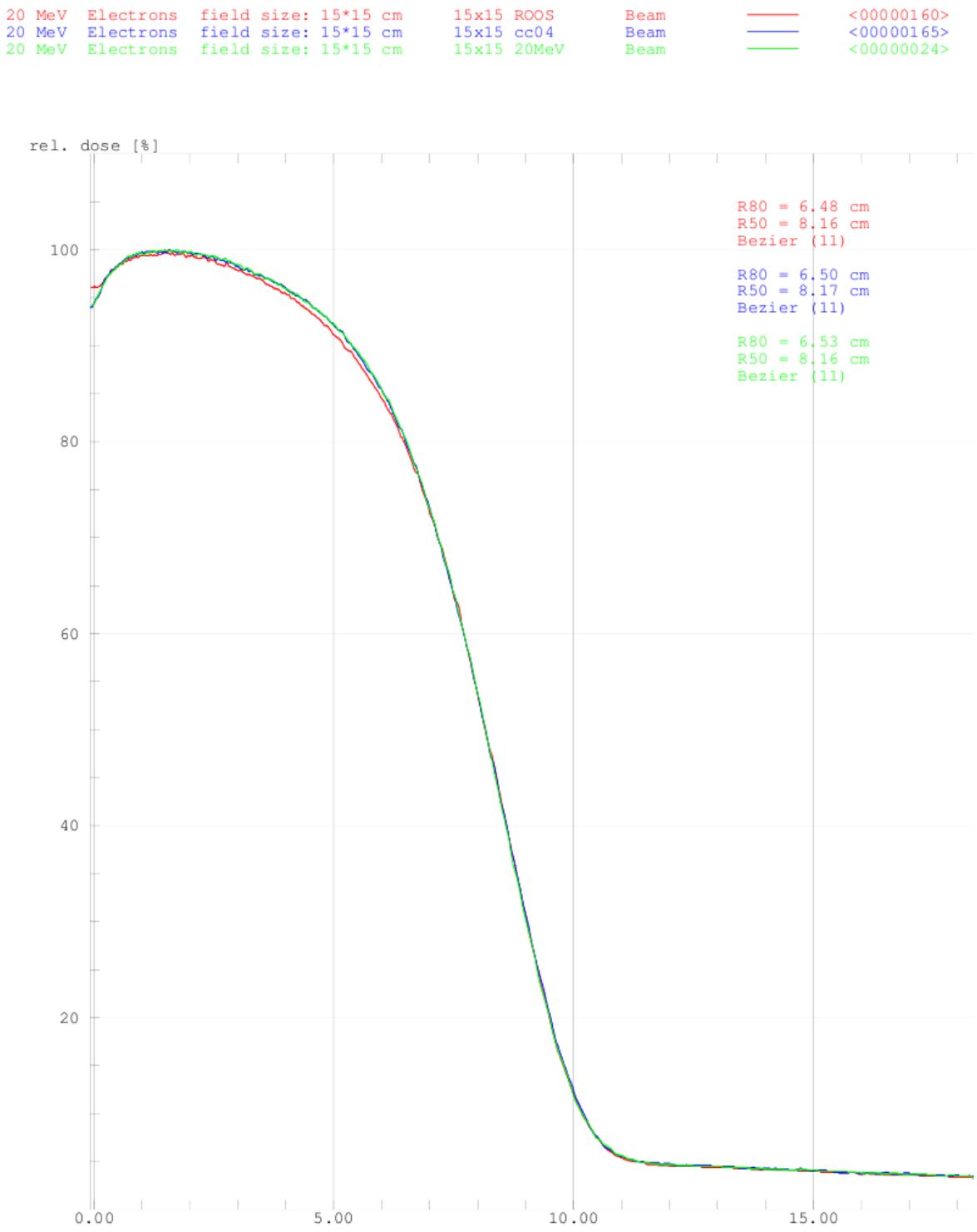

Illustration 34: 20MeV Roos, CC-04 & IC-15(green) Depth Ionisation Chamber Table 8

A.2.a Spatial Resolution CC-04 and IC-15 Chamber 9MeV

- **9MeV Inplane-Net 15x15cm field size CC-04**
- **9MeV Inplane-Net 15x15cm field size IC-15**

A.2.b Spatial Resolution CC-04 and IC-15 Chamber 20MeV

- **20MeV Inplane-Net 15x15cm field size CC-04**
- **20MeV Inplane-Net 15x15cm field size IC-15**

A.2.c Spatial Resolution Comparison Charts 9 & 20MeV

- **9MeV Isodose Overlay IC-15 (solid) CC-04 (dotted)**
- **20MeV Isodose Overlay IC-15 (solid) CC-04 (dotted)**

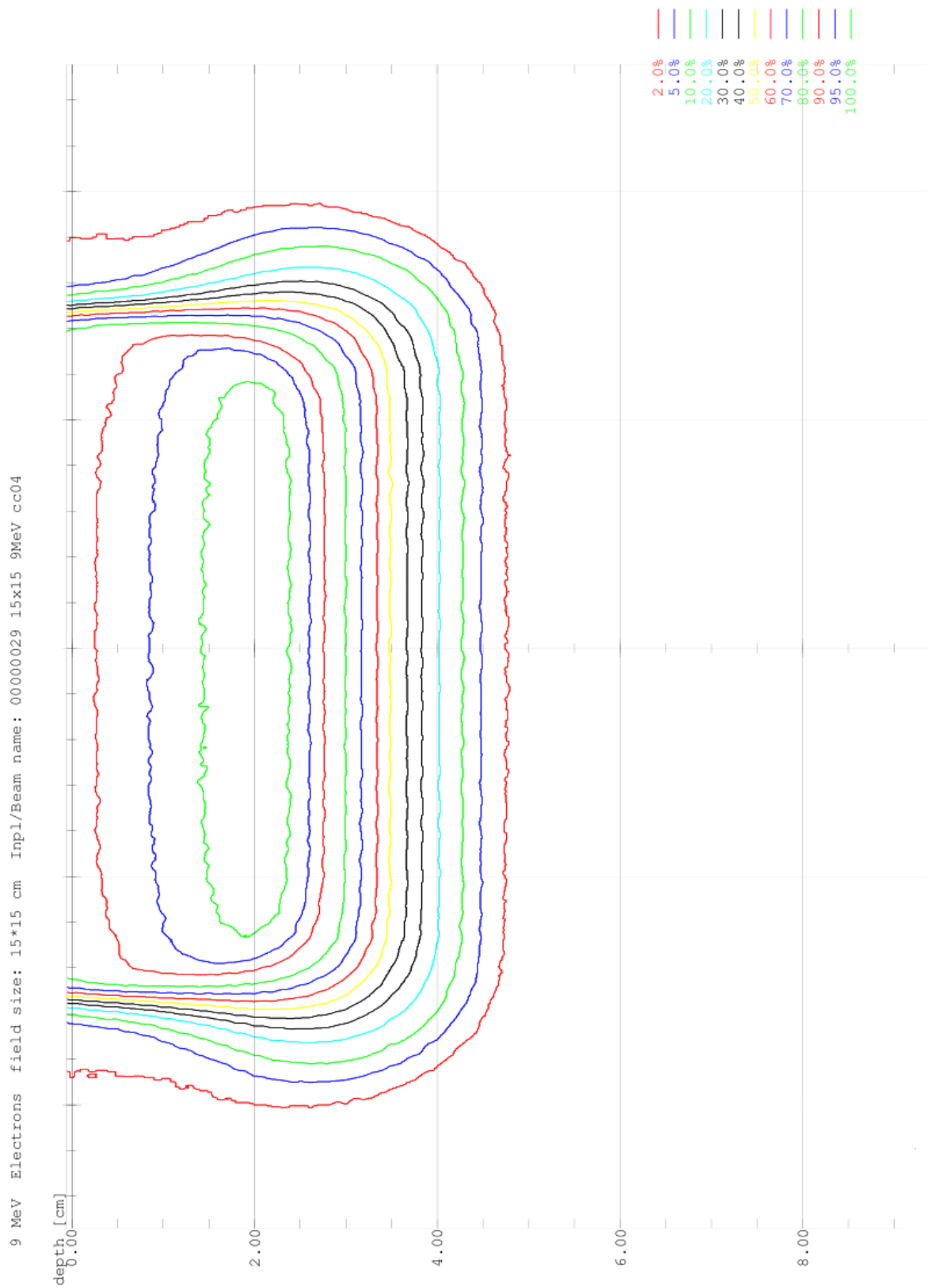

Illustration 35: 9MeV Inplane-Net 15x15cm field size CC-04

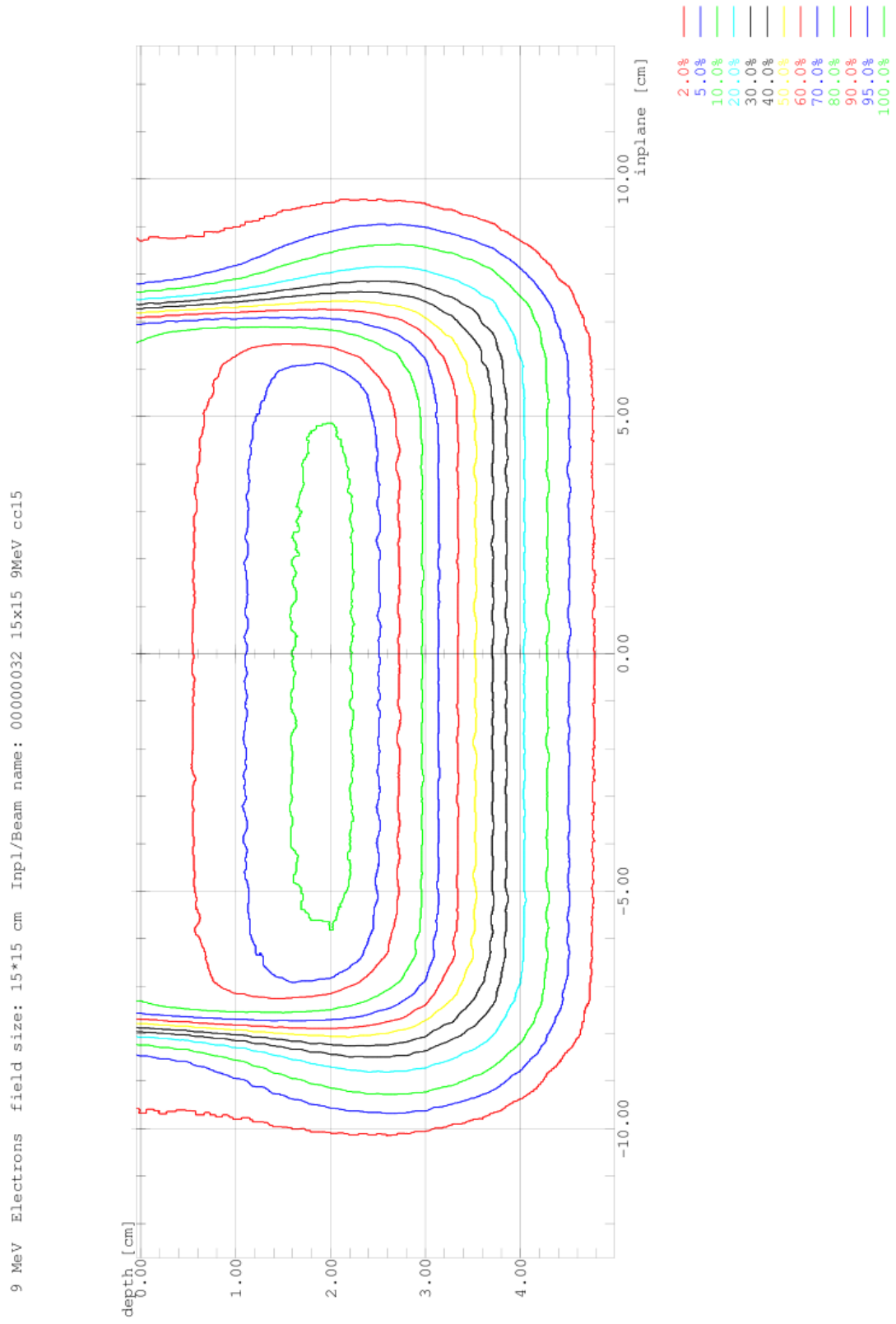

Illustration 36: 9MeV Inplane-Net 15x15cm field size IC-15

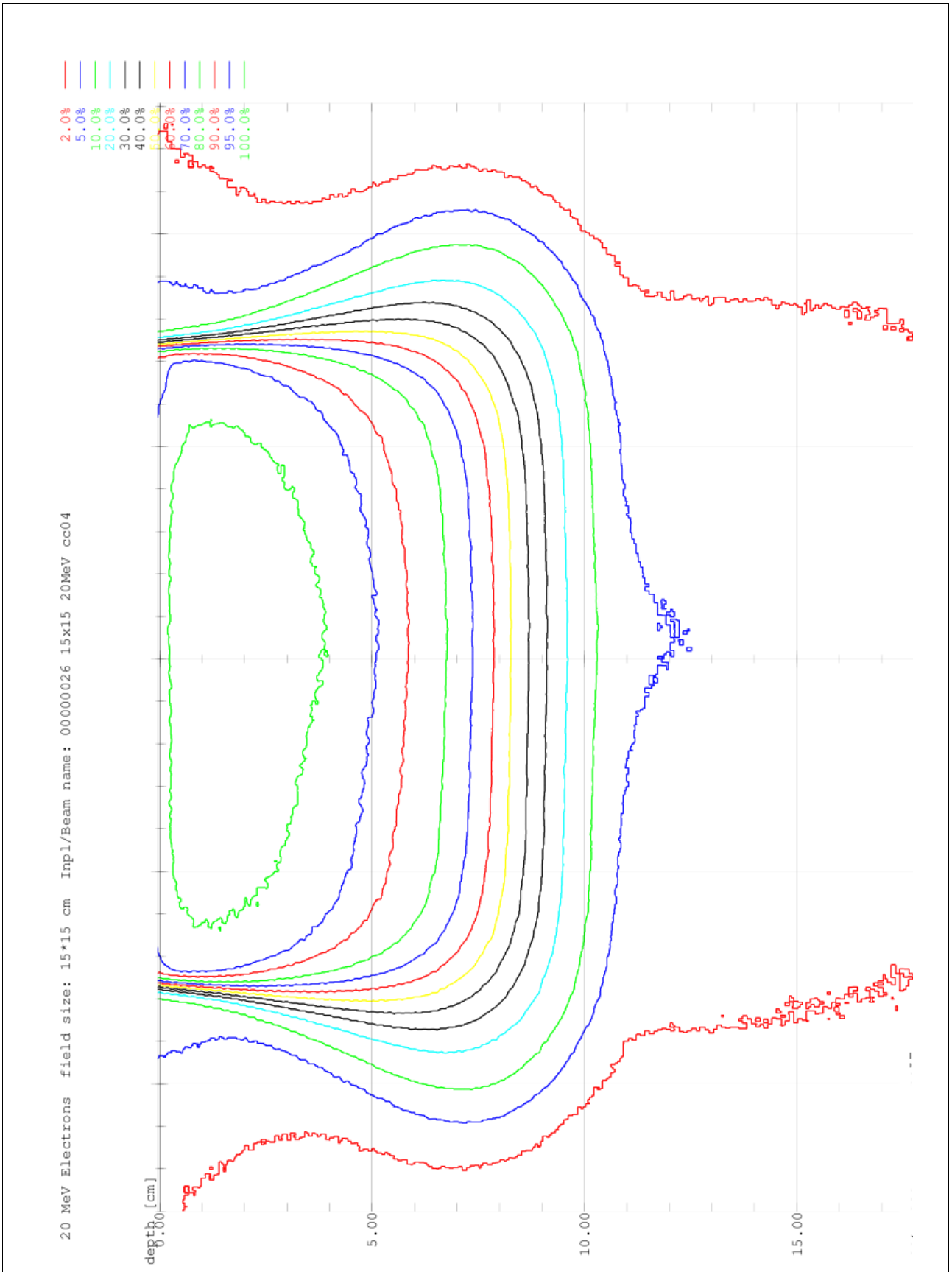

Illustration 37: 20MeV Inplane-Net 15x15cm field size CC-04

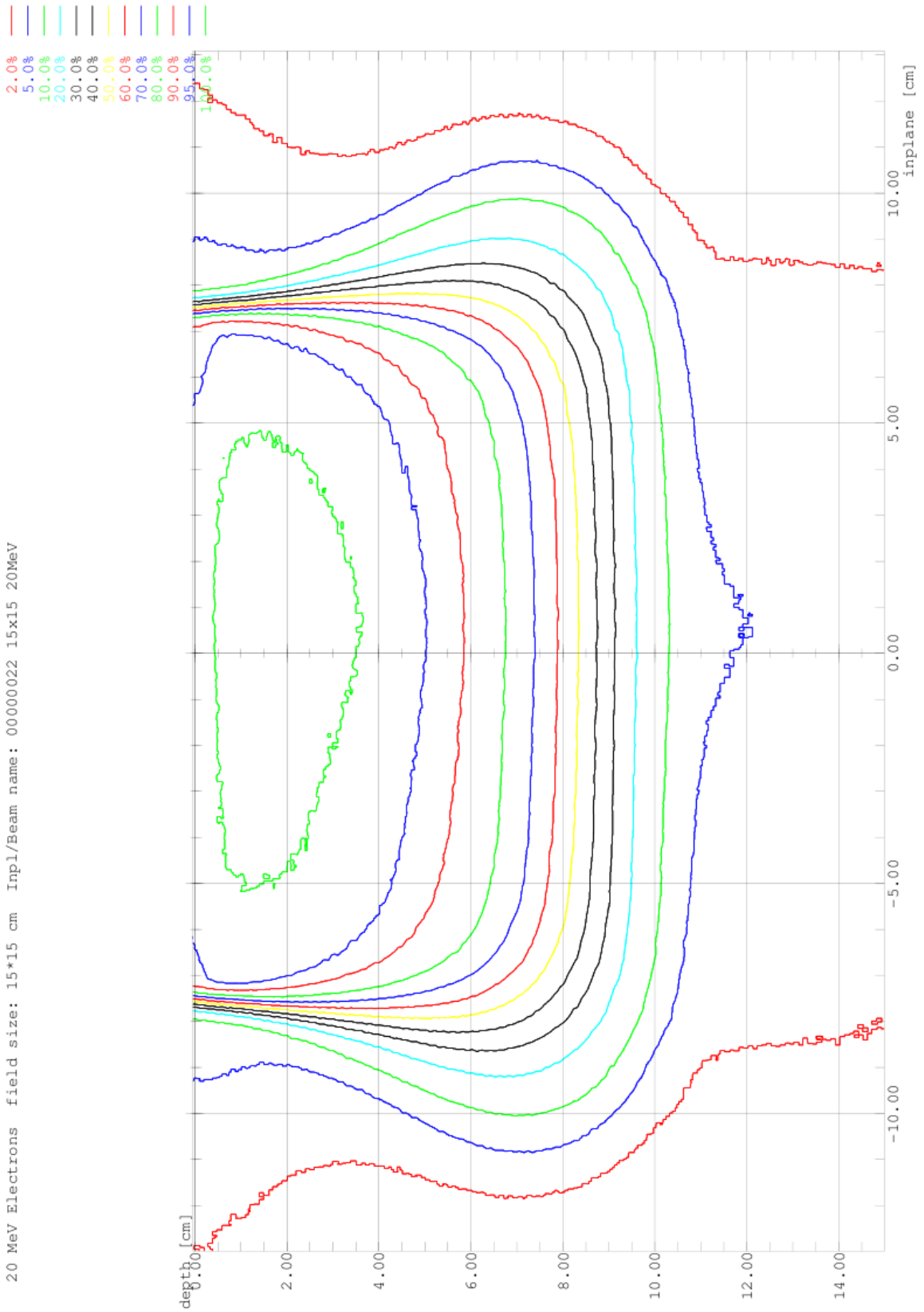

Illustration 38: 20MeV Inplane-Net 15x15cm field size IC-15

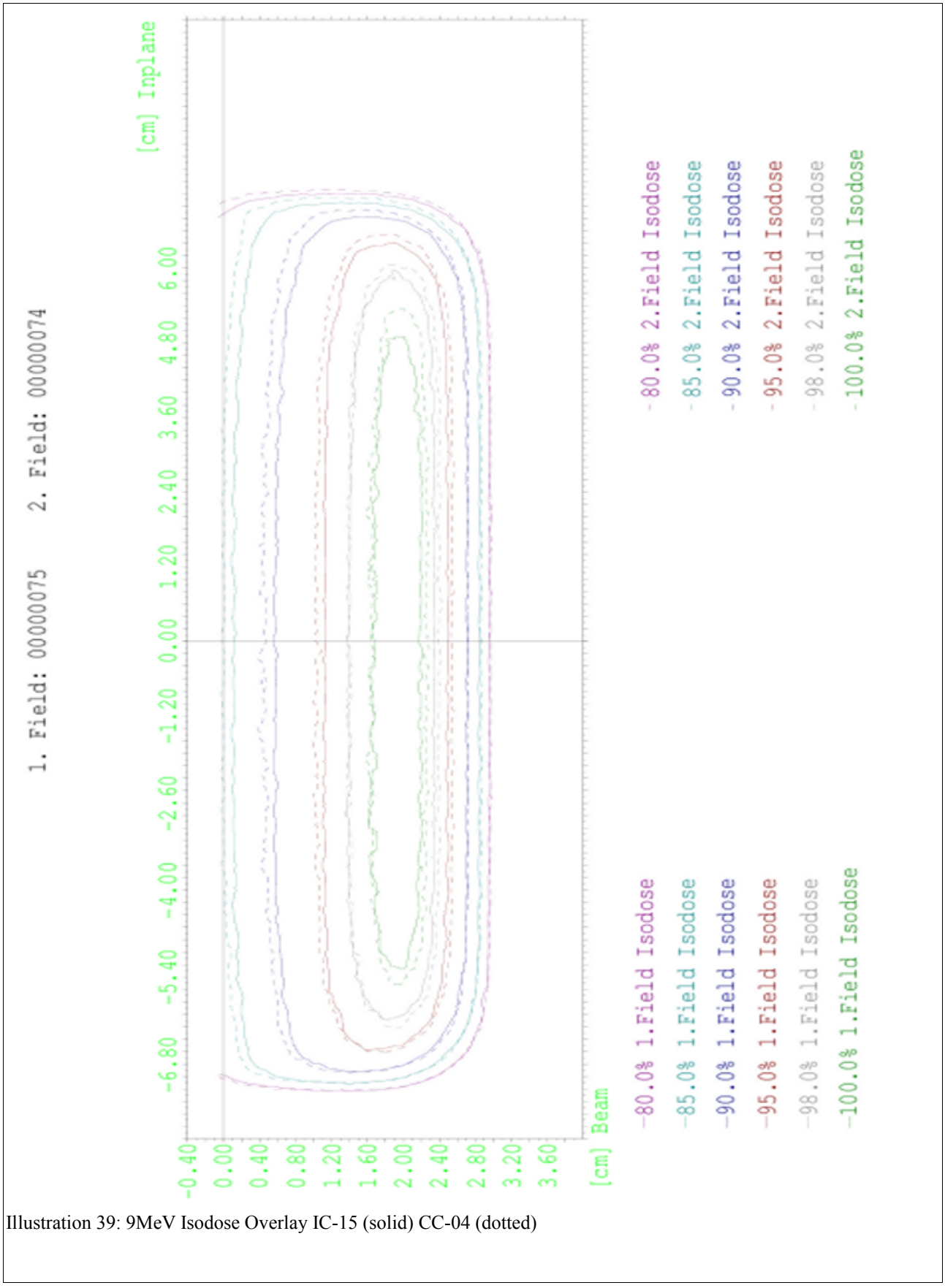

Illustration 39: 9MeV Isodose Overlay IC-15 (solid) CC-04 (dotted)

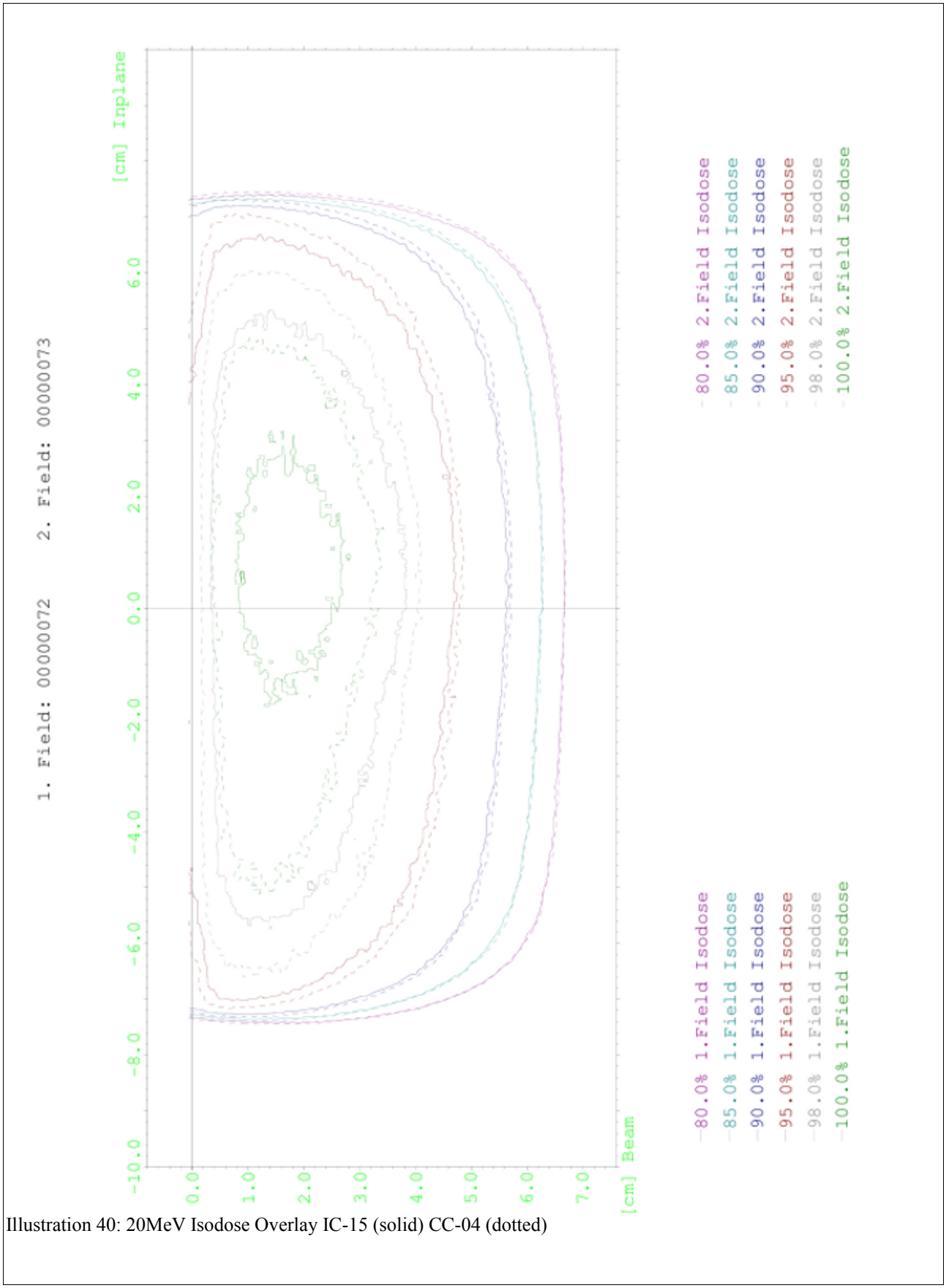

Illustration 40: 20MeV Isodose Overlay IC-15 (solid) CC-04 (dotted)

A.3.1.1 Bolus on Applicator FULL BOLUS – PERSPEX 9 & 20MeV

- **Illustration 41: Full Bolus on Applicator Depth Ionisation- Perspex 9MeV from Table 11**
- **Illustration 42: Full Bolus on Applicator Depth Ionisation- Perspex 20MeV from Table 12**
-
- **Illustration 43: 9MeV Open Field for Table 13**
- **Illustration 44: Full Bolus 9MeV 1x6mm Perspex for Table 13**
- **Illustration 45: Full Bolus 9MeV 2x6mm Perspex for Table 13**
- **Illustration 46: Full Bolus 9MeV 3x6mm Perspex for Table 13**
- **Illustration 47: 6MeV Open Field Table 13**
- **Illustration 48: 20MeV Open Field Table 13**
- **Illustration 49: Full Bolus 20MeV 1x6mm Perspex for Table 13**
- **Illustration 50: Full Bolus 20MeV 2x6mm Perspex for Table 13**
- **Illustration 51: Full Bolus 20MeV 3x6mm Perspex for Table 13**
- **Illustration 52: 16MeV Open Field Table 13**

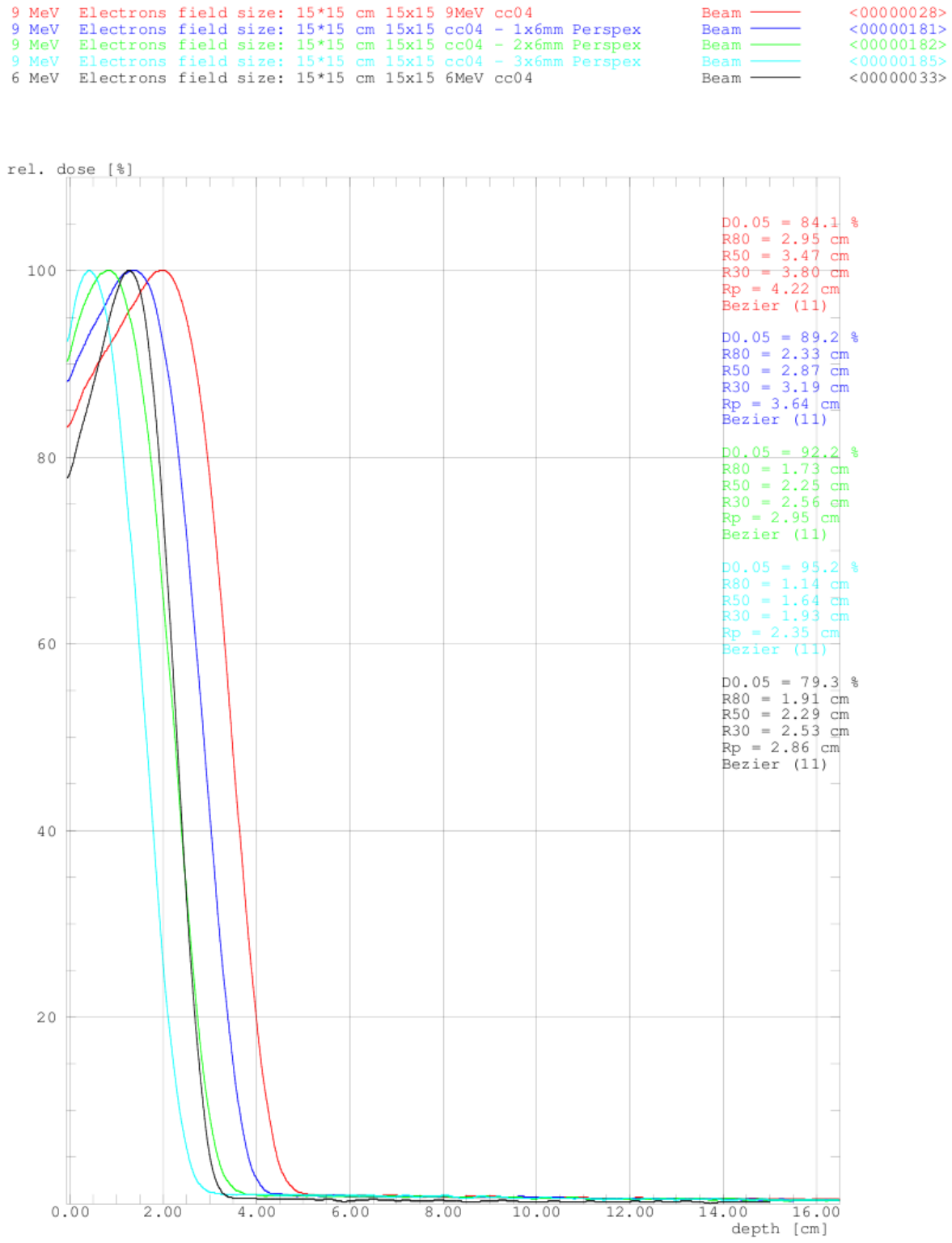

Illustration 41: Full Bolus on Applicator Depth Ionisation- Perspex 9MeV from Table 11

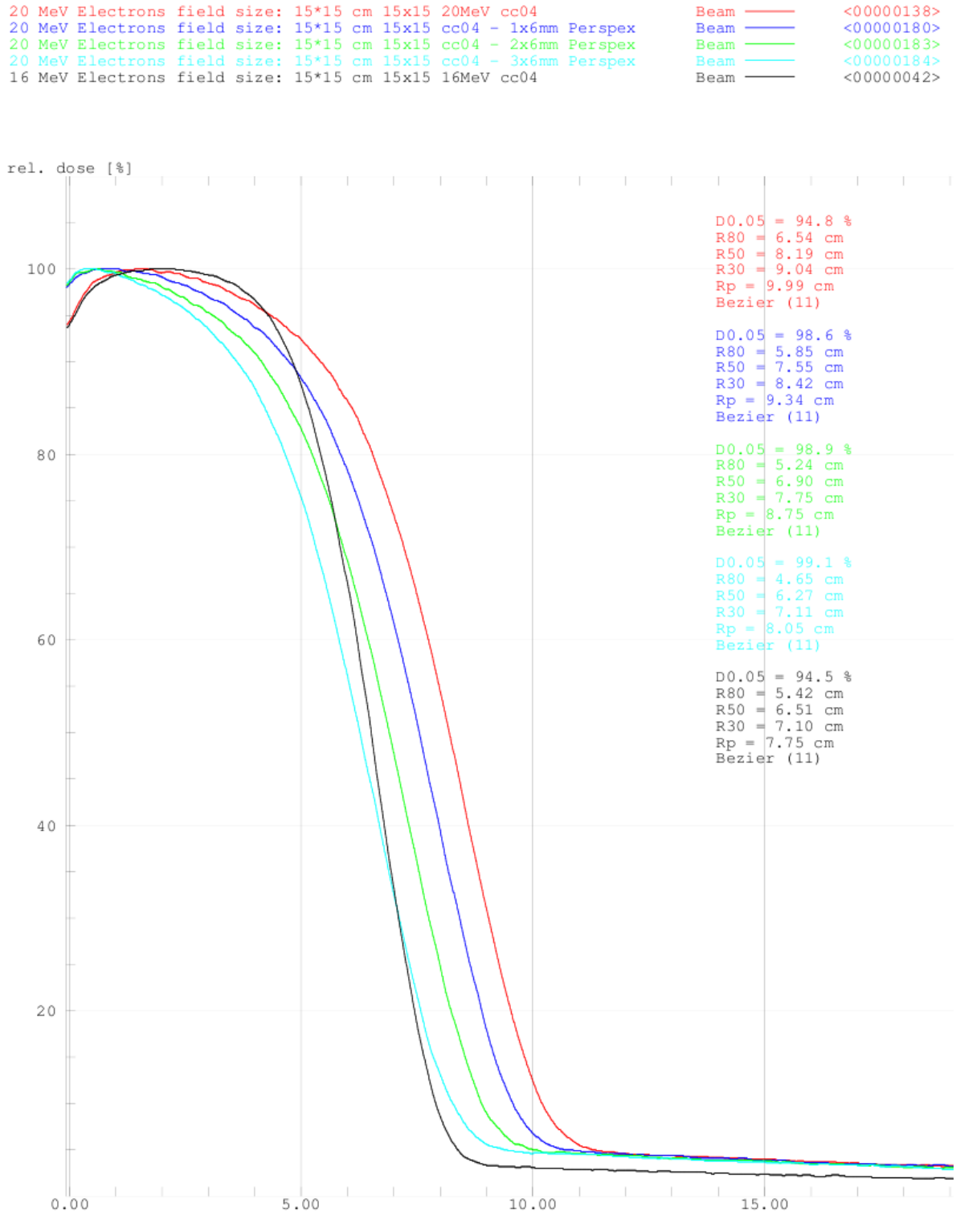

Illustration 42: Full Bolus on Applicator Depth Ionisation- Perspex 20MeV from Table 12

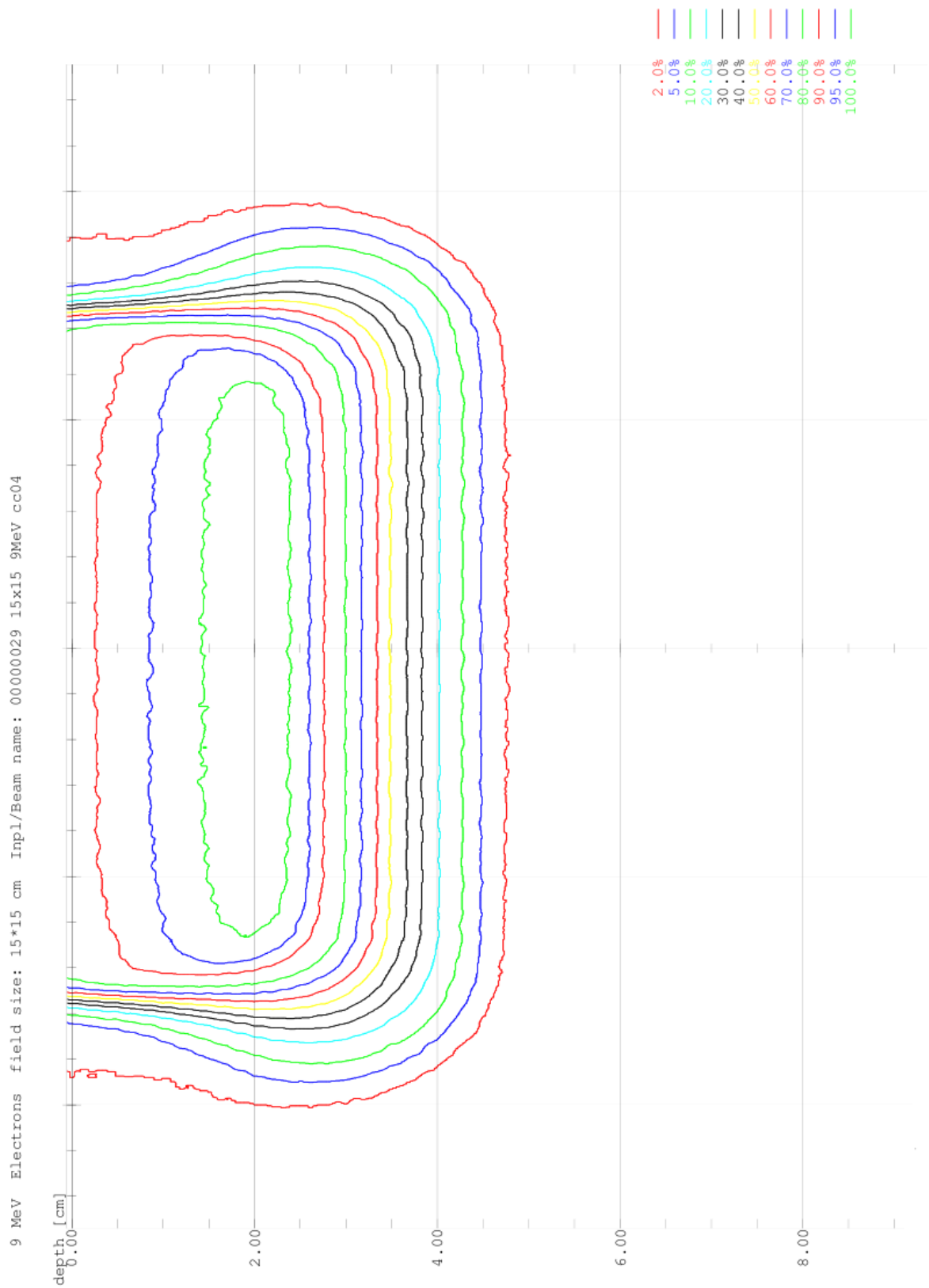

Illustration 43: 9MeV Open Field for Table 13

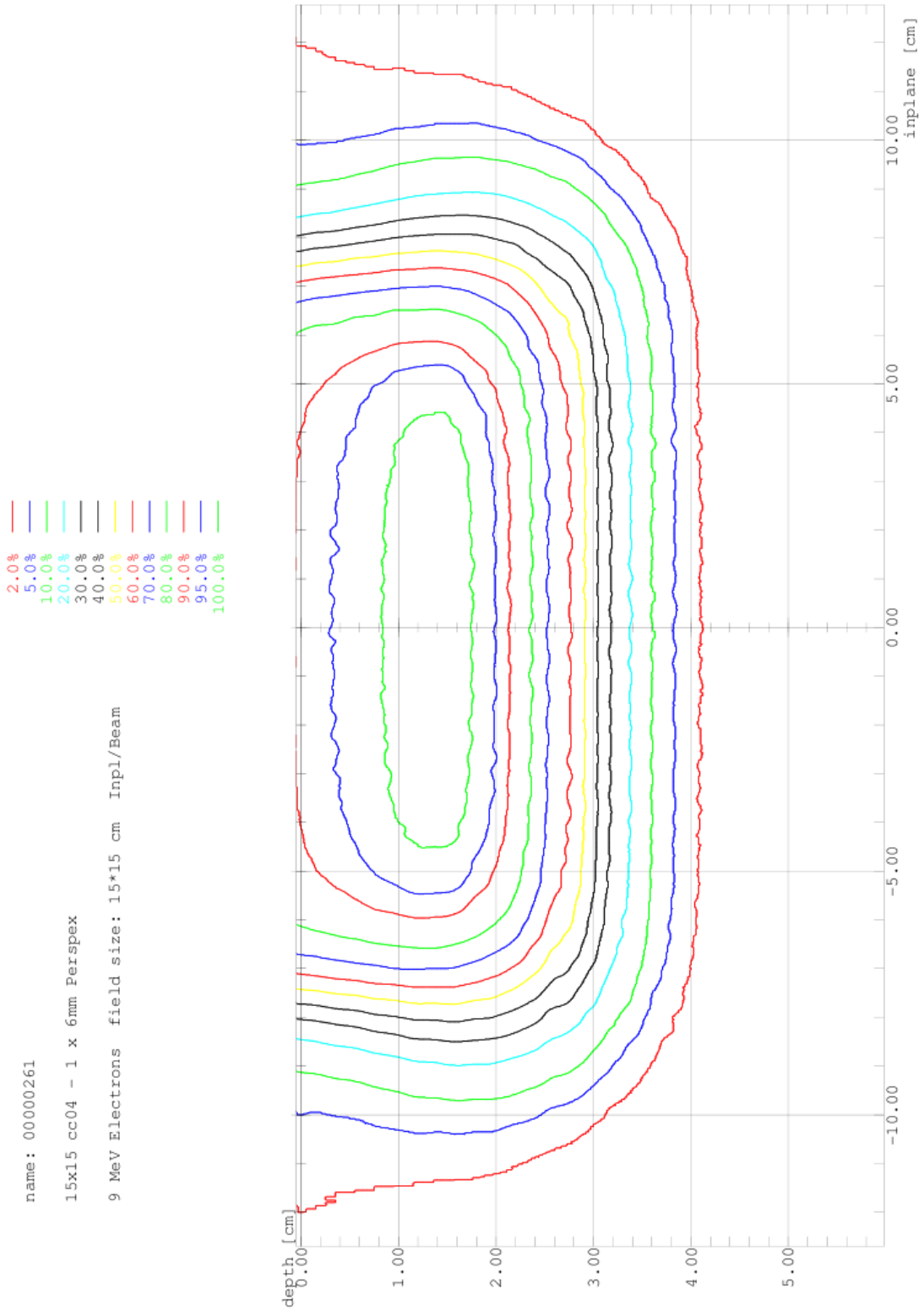

Illustration 44: Full Bolus 9MeV 1x6mm Perspex for Table 13

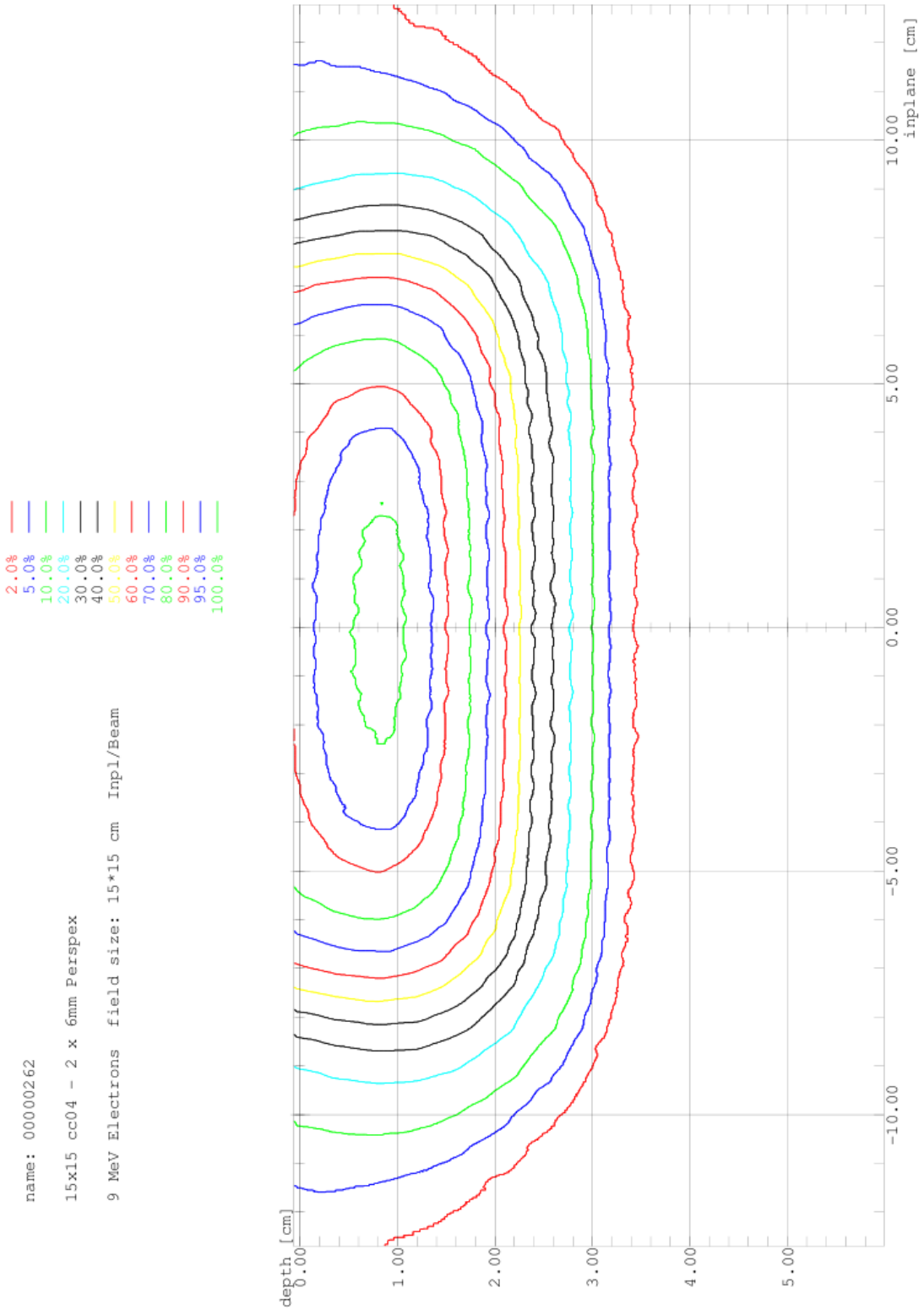

Illustration 45: Full Bolus 9MeV 2x6mm Perspex for Table 13

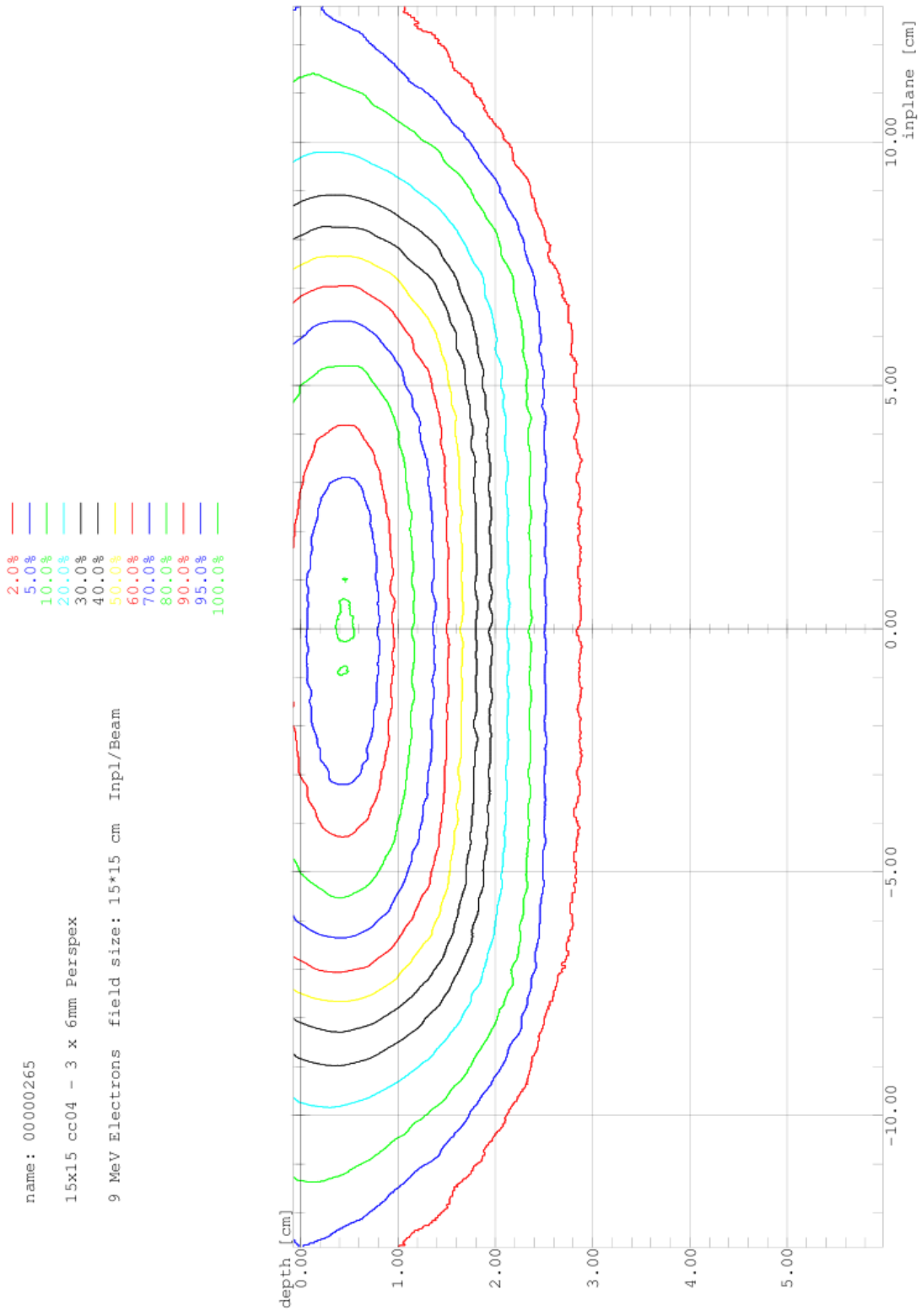

Illustration 46: Full Bolus 9MeV 3x6mm Perspex for Table 13

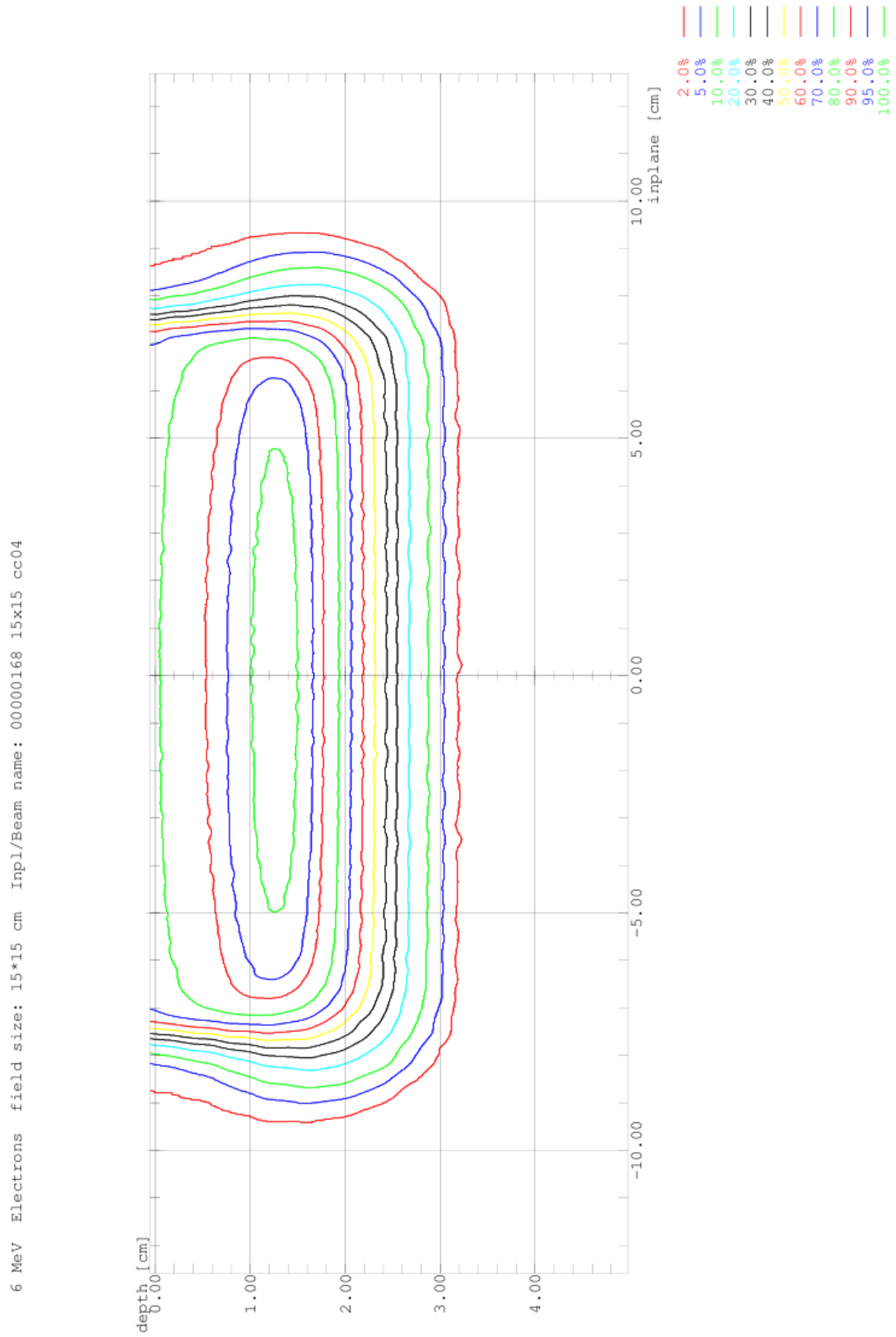

Illustration 47: 6MeV Open Field Table 13

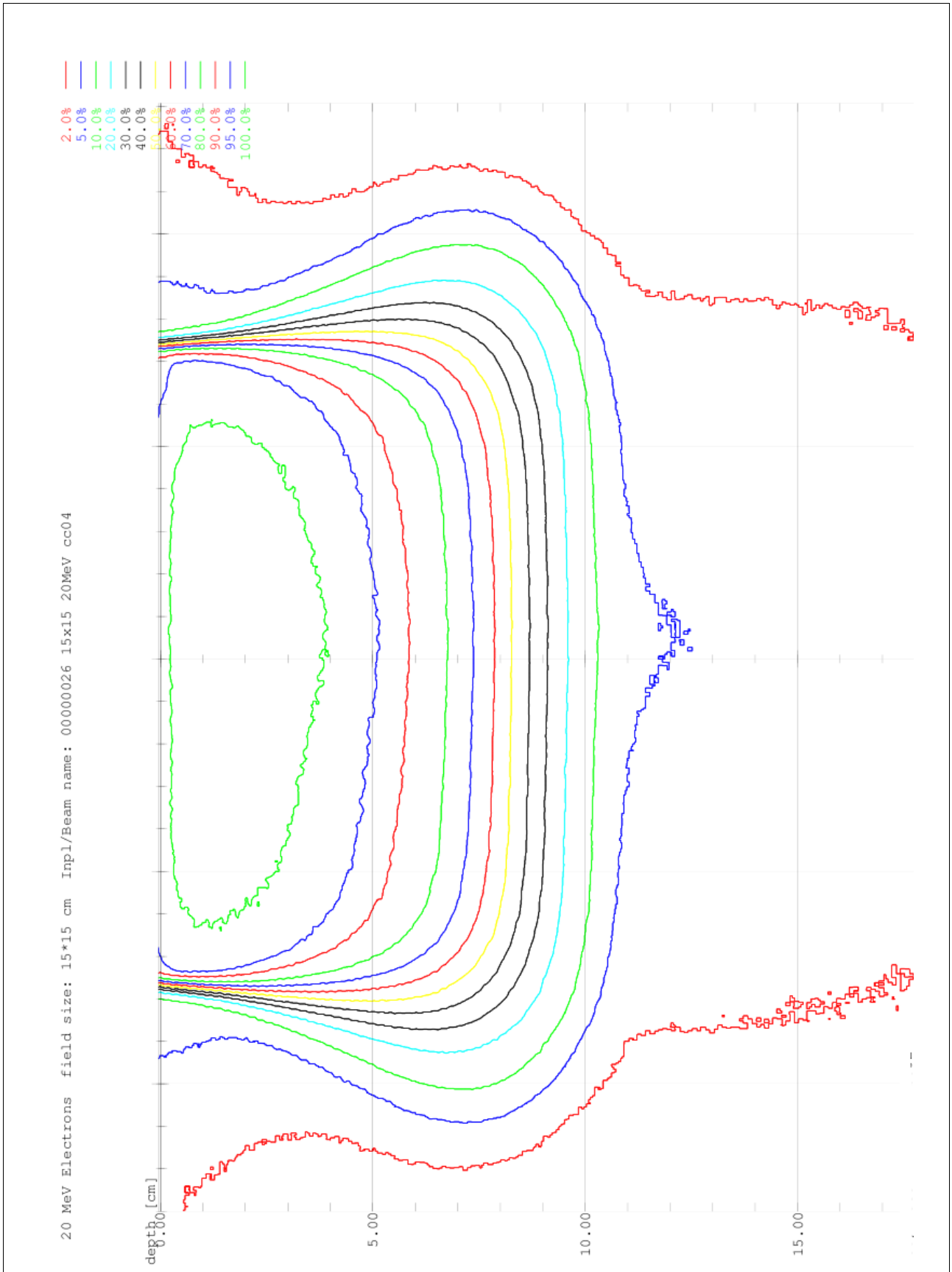

Illustration 48: 20MeV Open Field Table 13

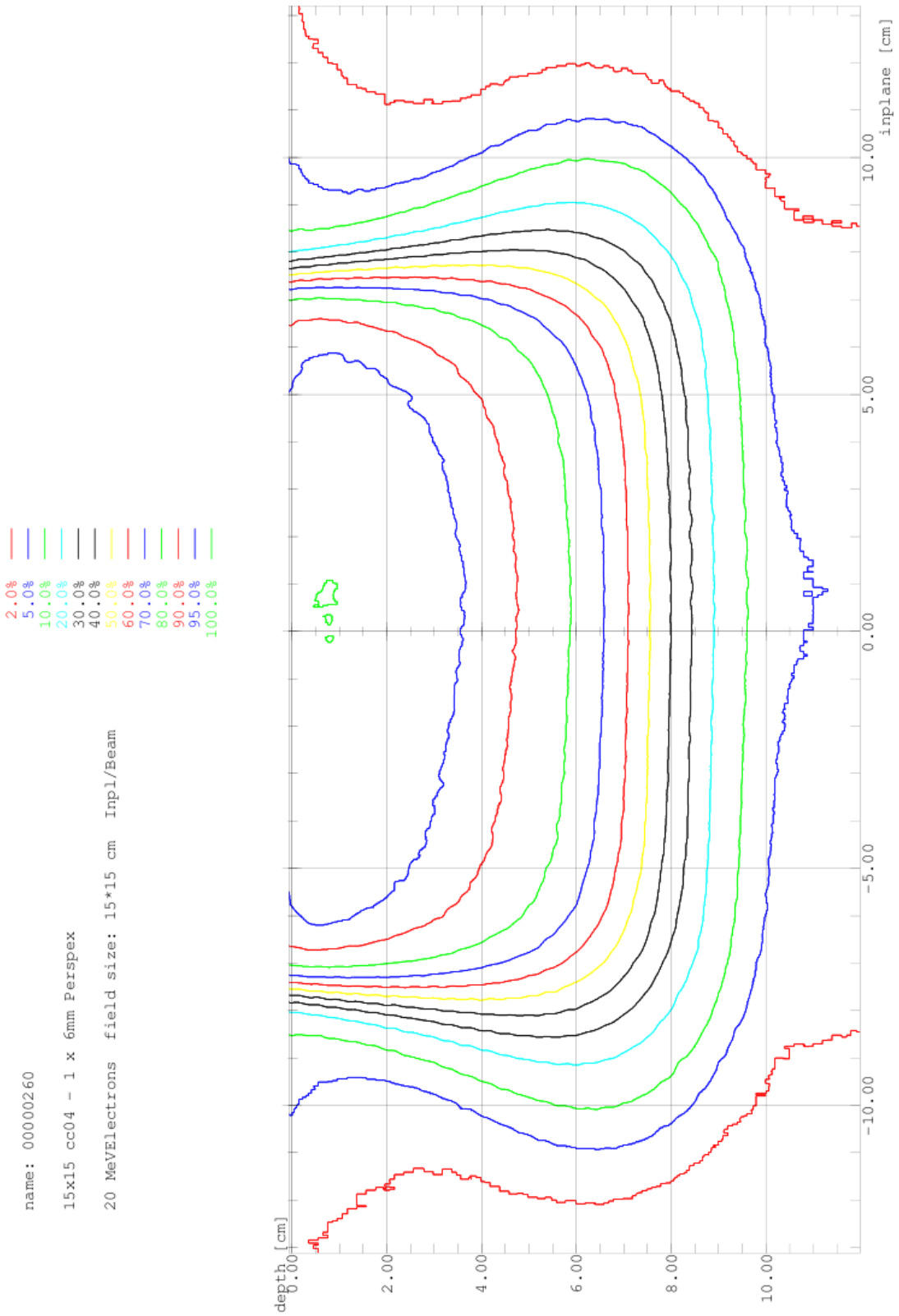

Illustration 49: Full Bolus 20MeV 1x6mm Perspex for Table 13

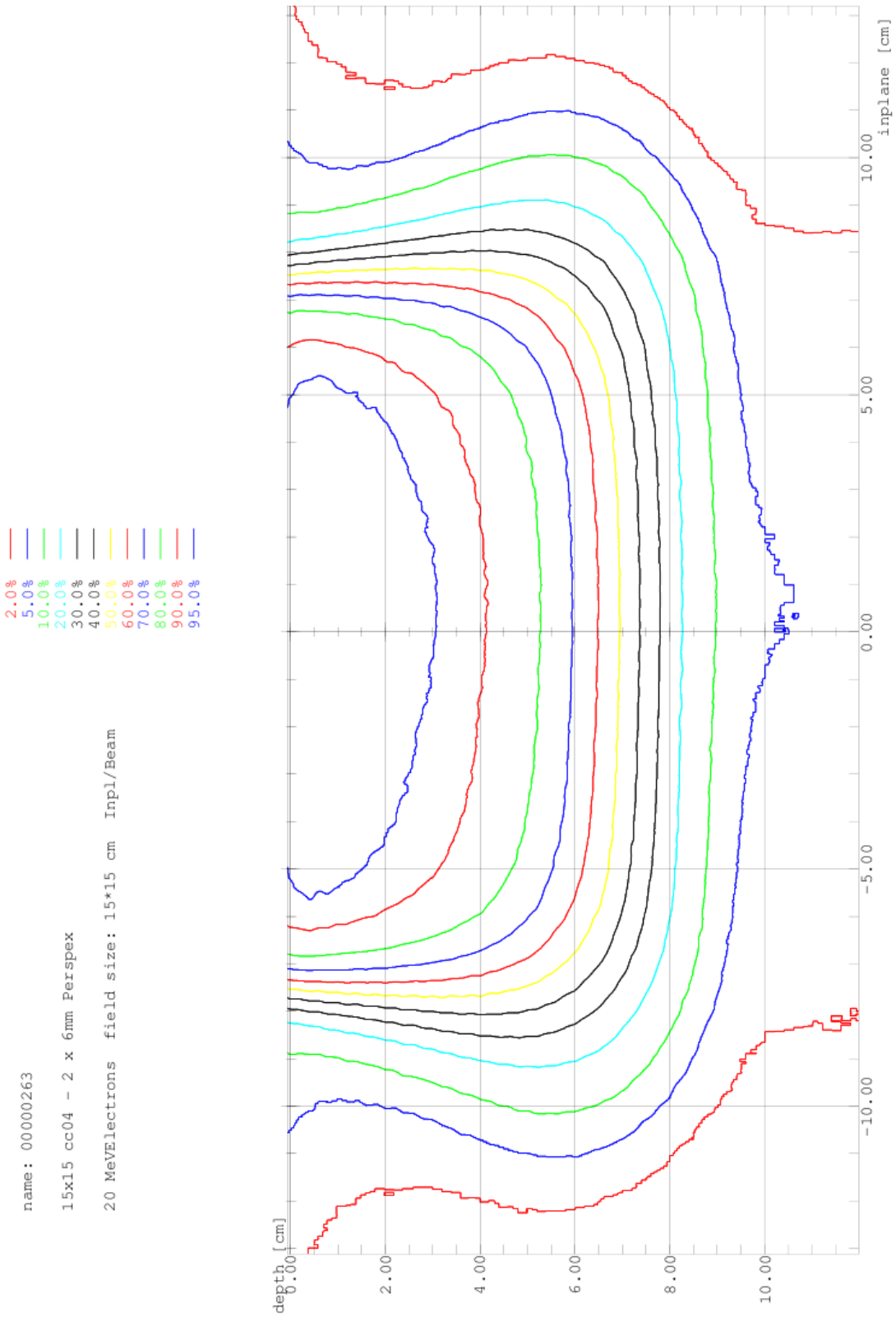

Illustration 50: Full Bolus 20MeV 2x6mm Perspex for Table 13

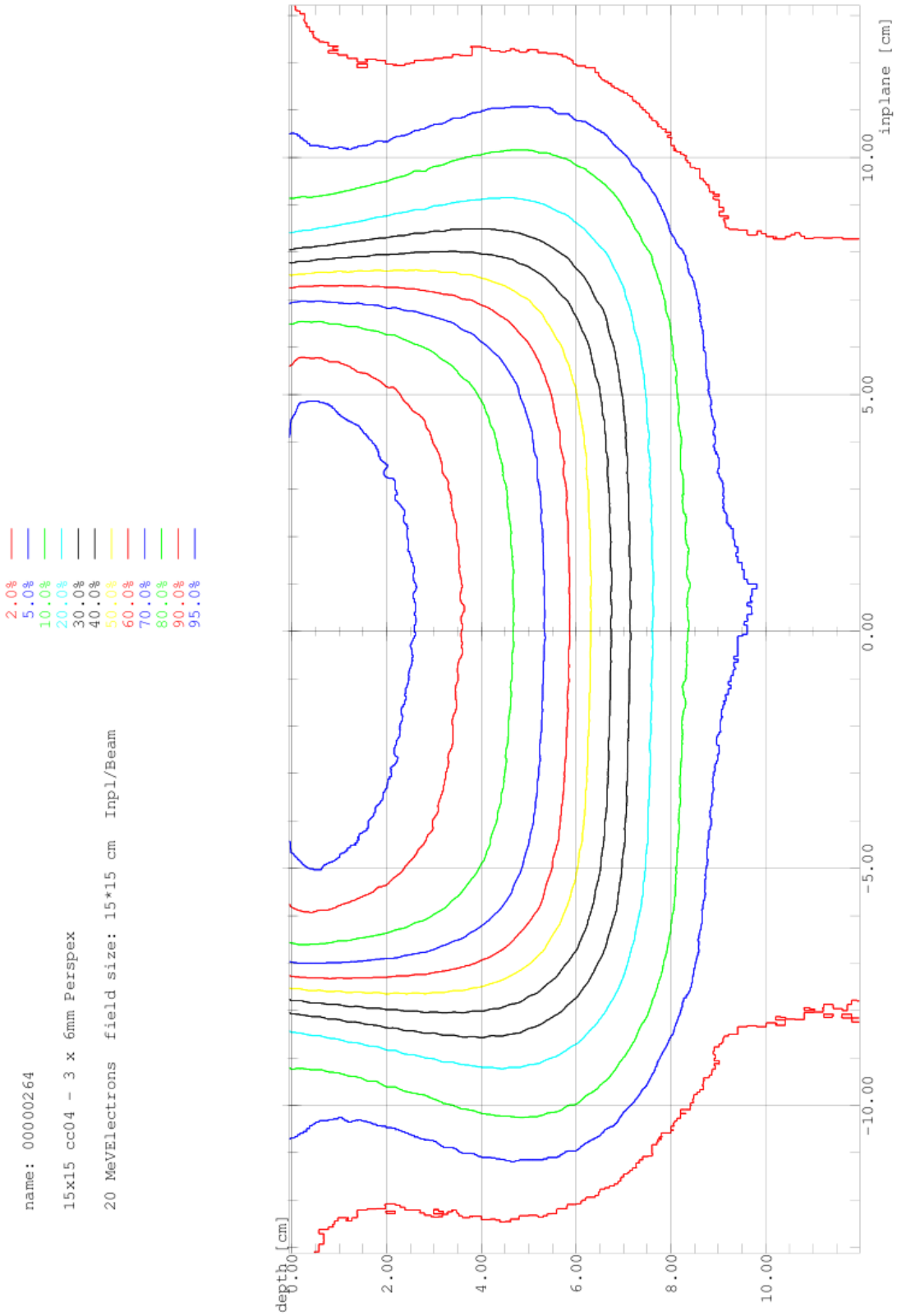

Illustration 51: Full Bolus 20MeV 3x6mm Perspex for Table 13

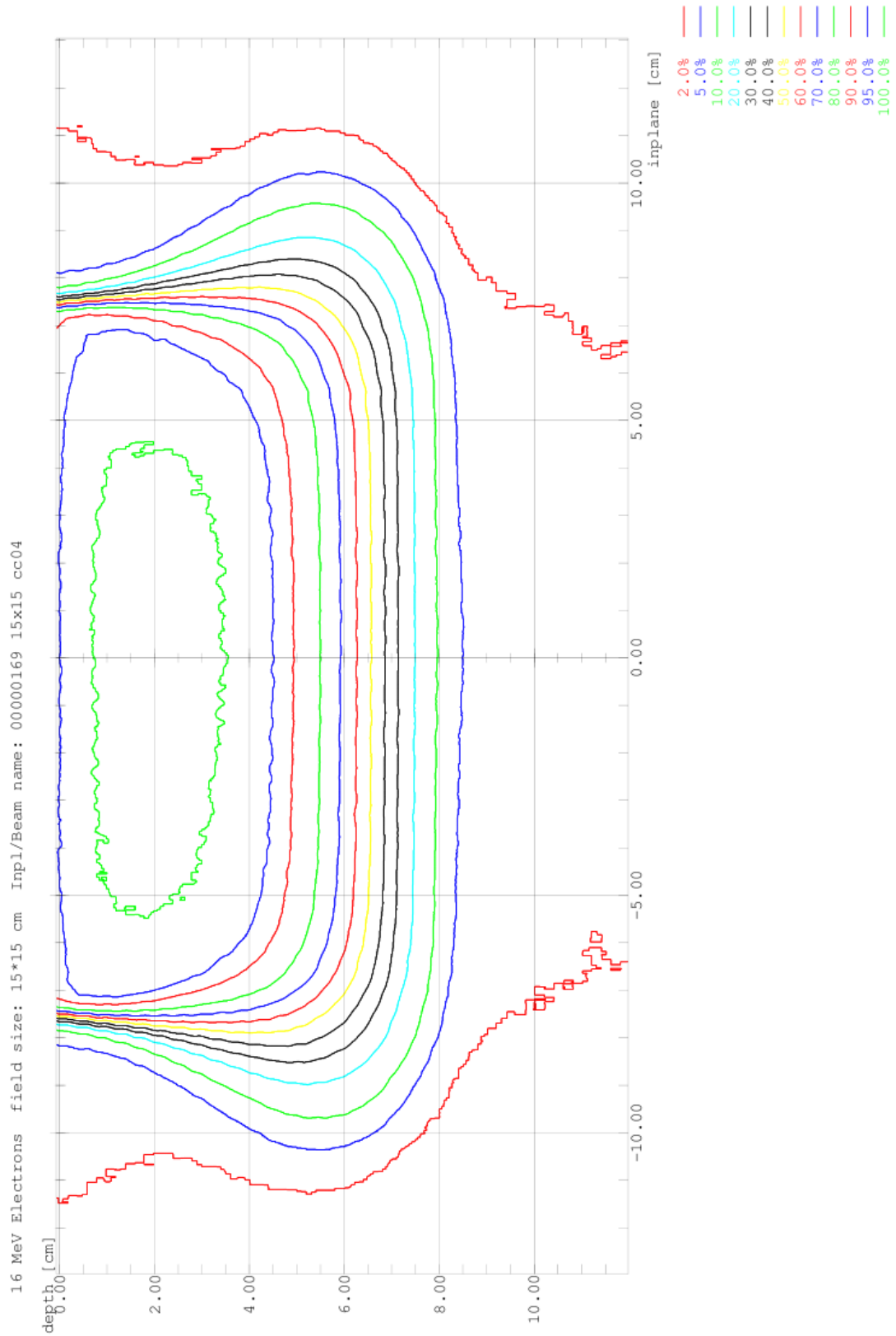

Illustration 52: 16MeV Open Field Table 13

A.3.1.2.Bolus on Applicator FULL BOLUS – TEFLON 9 & 20MeV

- **Illustration 53: Full Bolus on Applicator Depth Ionisation - Teflon 9MeV from Table 15**
- **Illustration 54: Full Bolus on Applicator Depth Ionisation -Teflon 20MeV from Table 16**
- **Illustration 55: Full Bolus 9MeV 1x3mm Teflon for Table 17**
- **Illustration 56: Full Bolus 9MeV 2x3mm Teflon for Table 17**
- **Illustration 57: Full Bolus 20MeV 1x3mm Teflon for Table 17**
- **Illustration 58: Full Bolus 20MeV 2x3mm Teflon for Table 17**

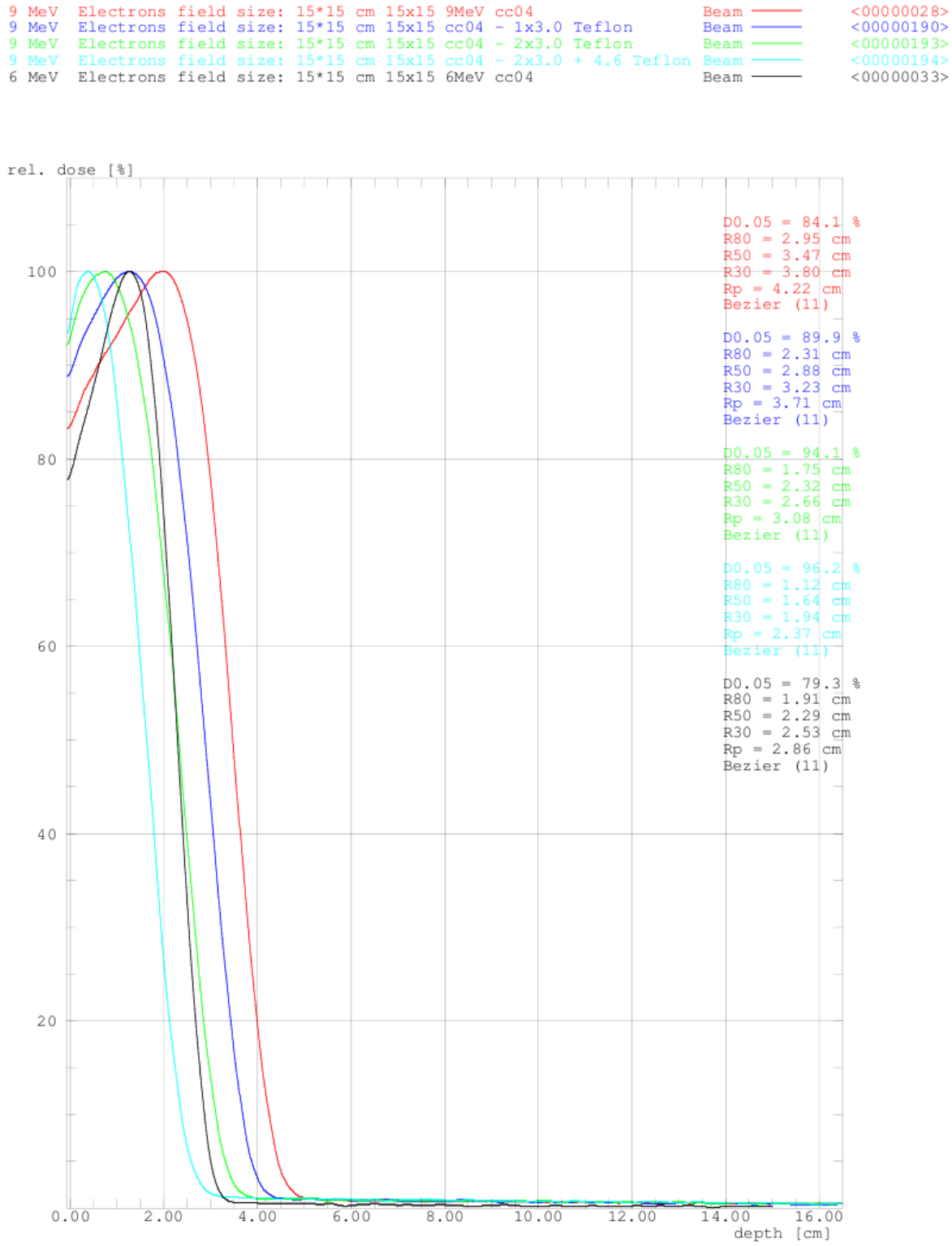

Illustration 53: Full Bolus on Applicator Depth Ionisation - Teflon 9MeV from Table 15

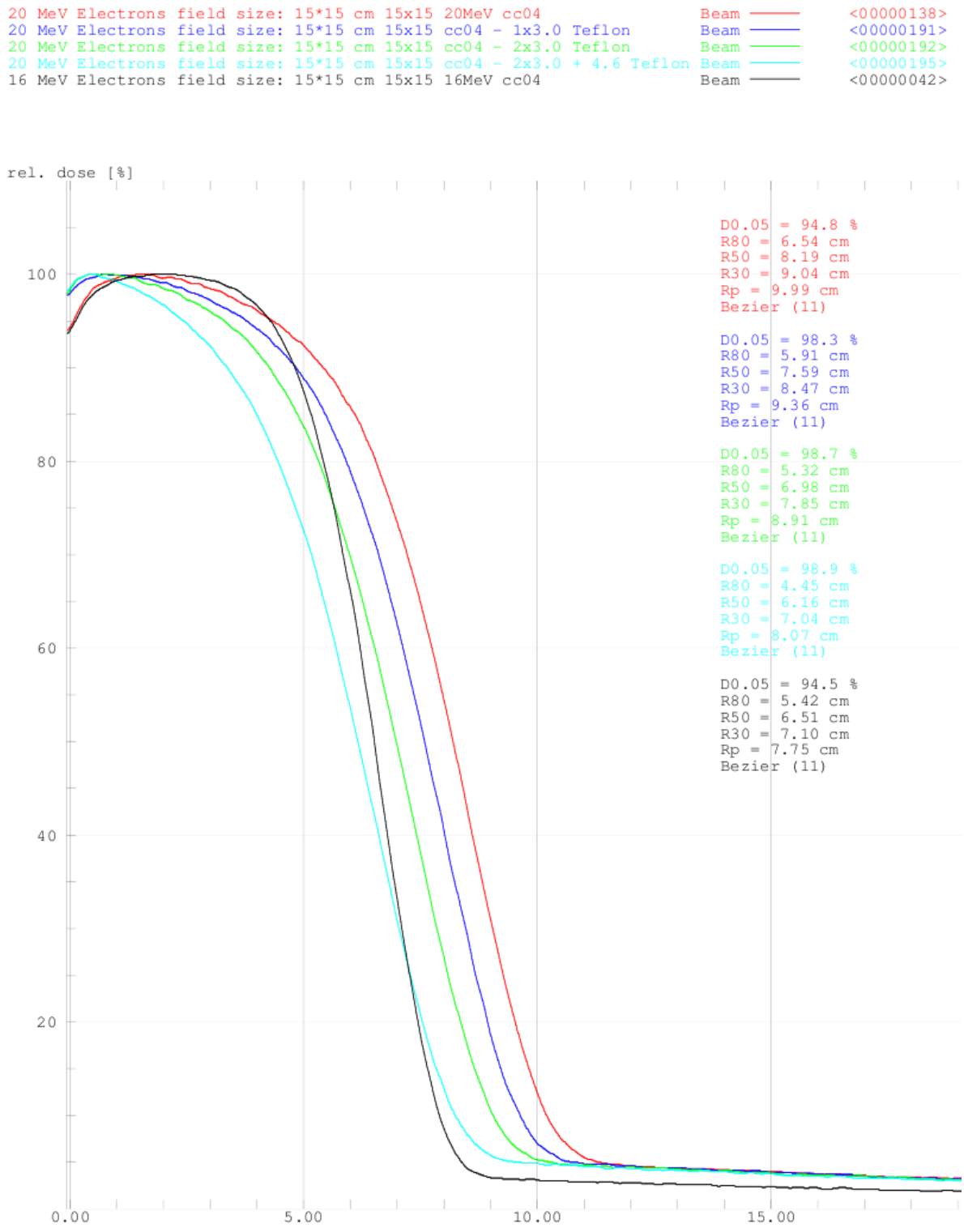

Illustration 54: Full Bolus on Applicator Depth Ionisation -Teflon 20MeV from Table 16

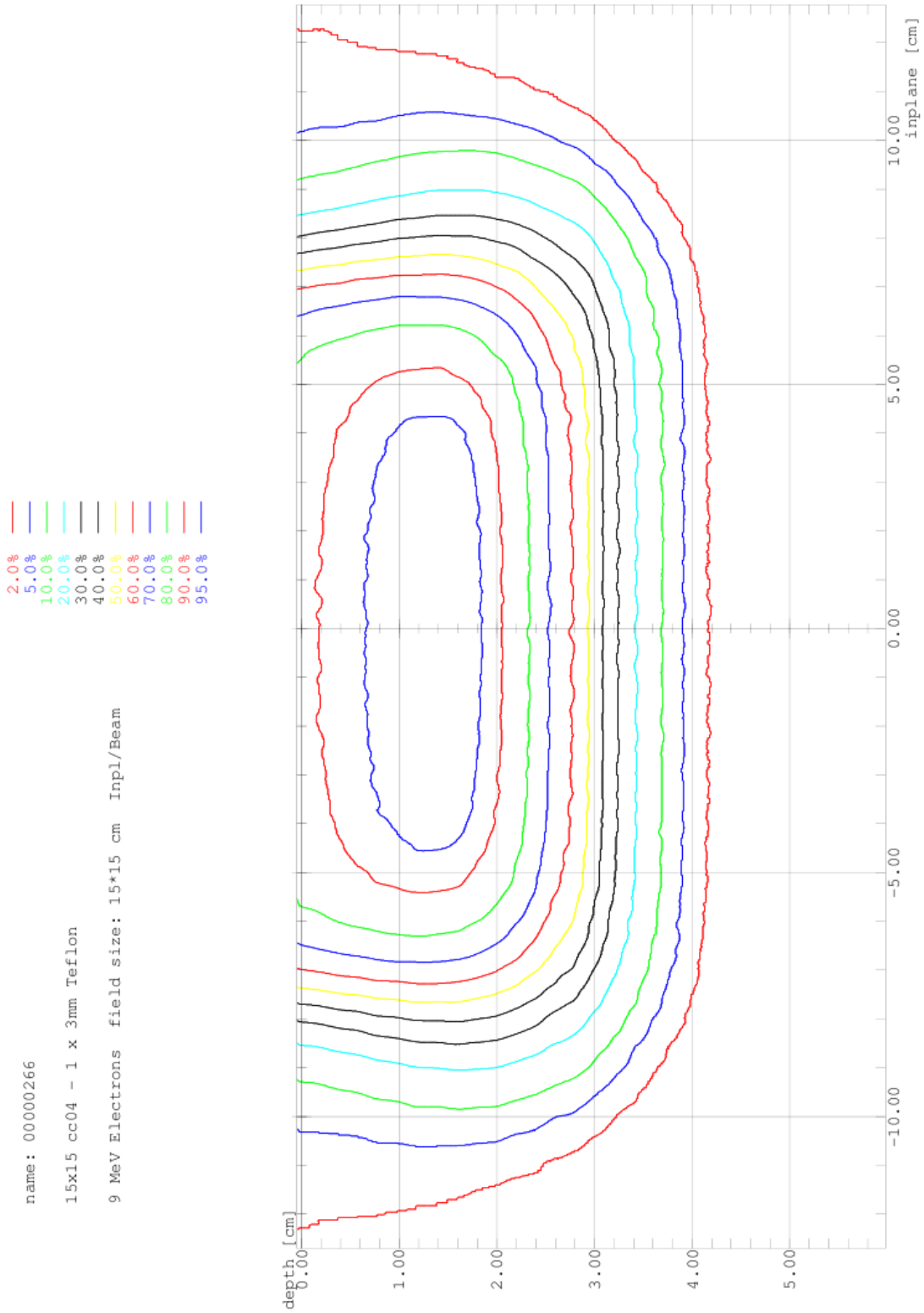

Illustration 55: Full Bolus 9MeV 1x3mm Teflon for Table 17

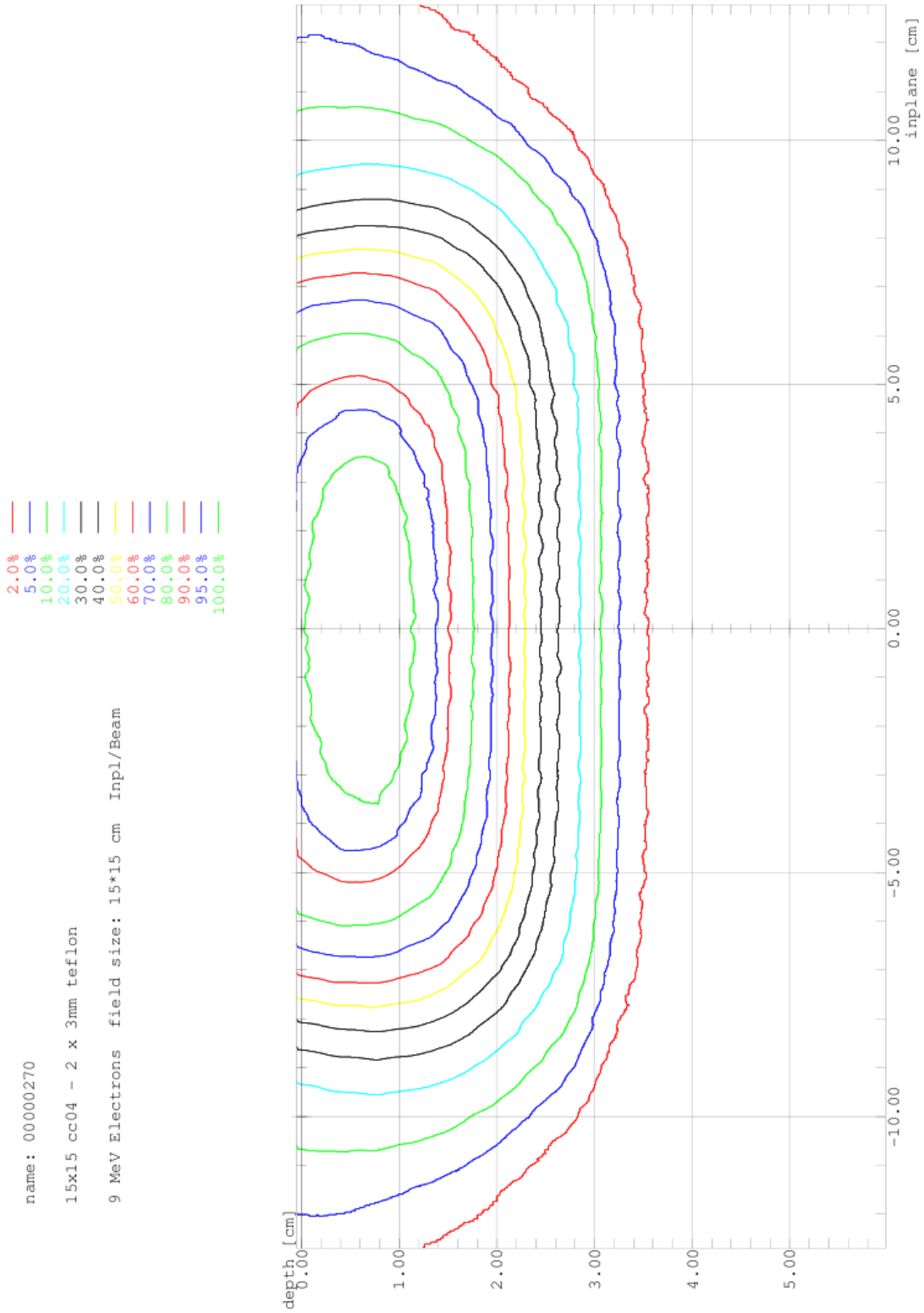

Illustration 56: Full Bolus 9MeV 2x3mm Teflon for Table 17

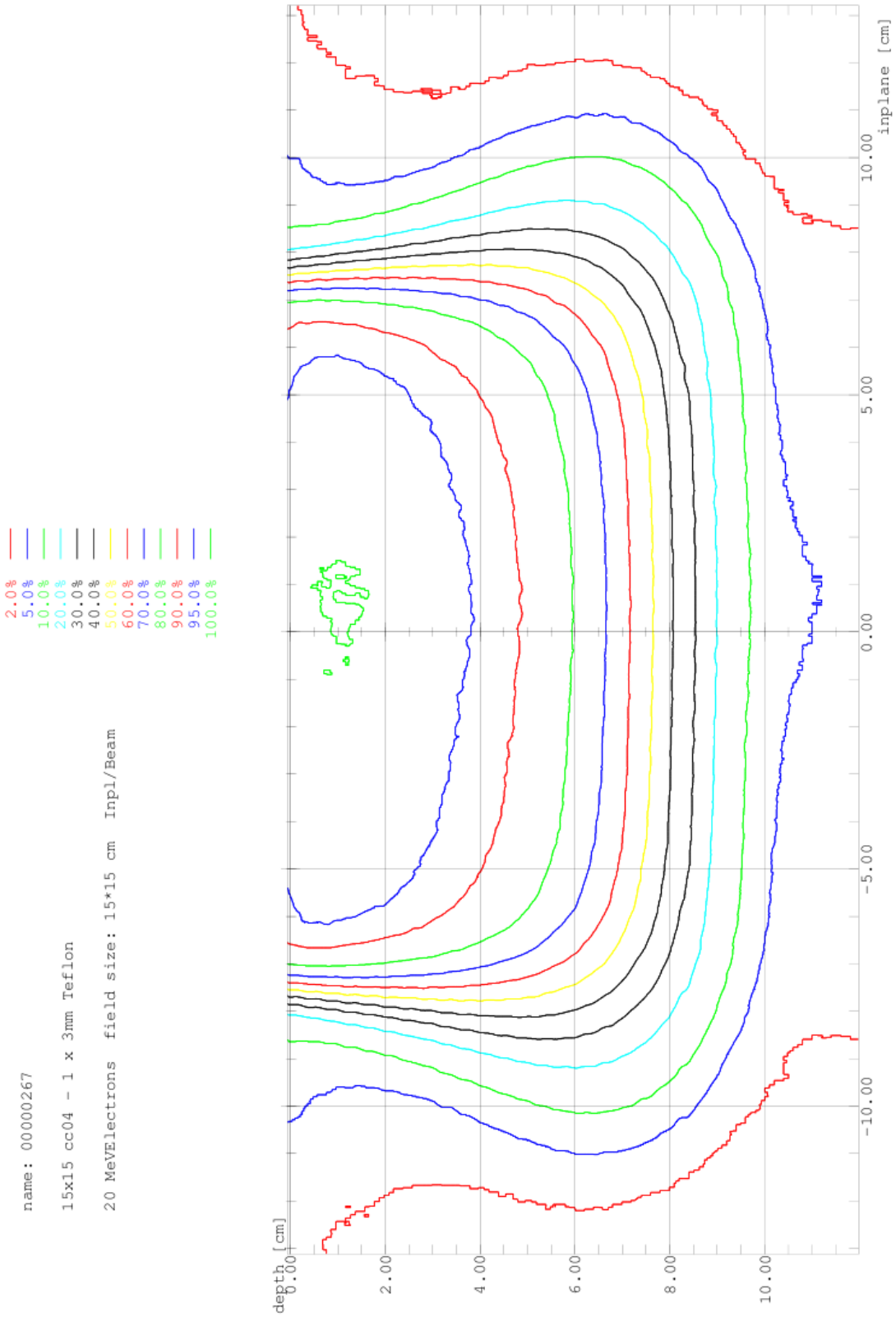

Illustration 57: Full Bolus 20MeV 1x3mm Teflon for Table 17

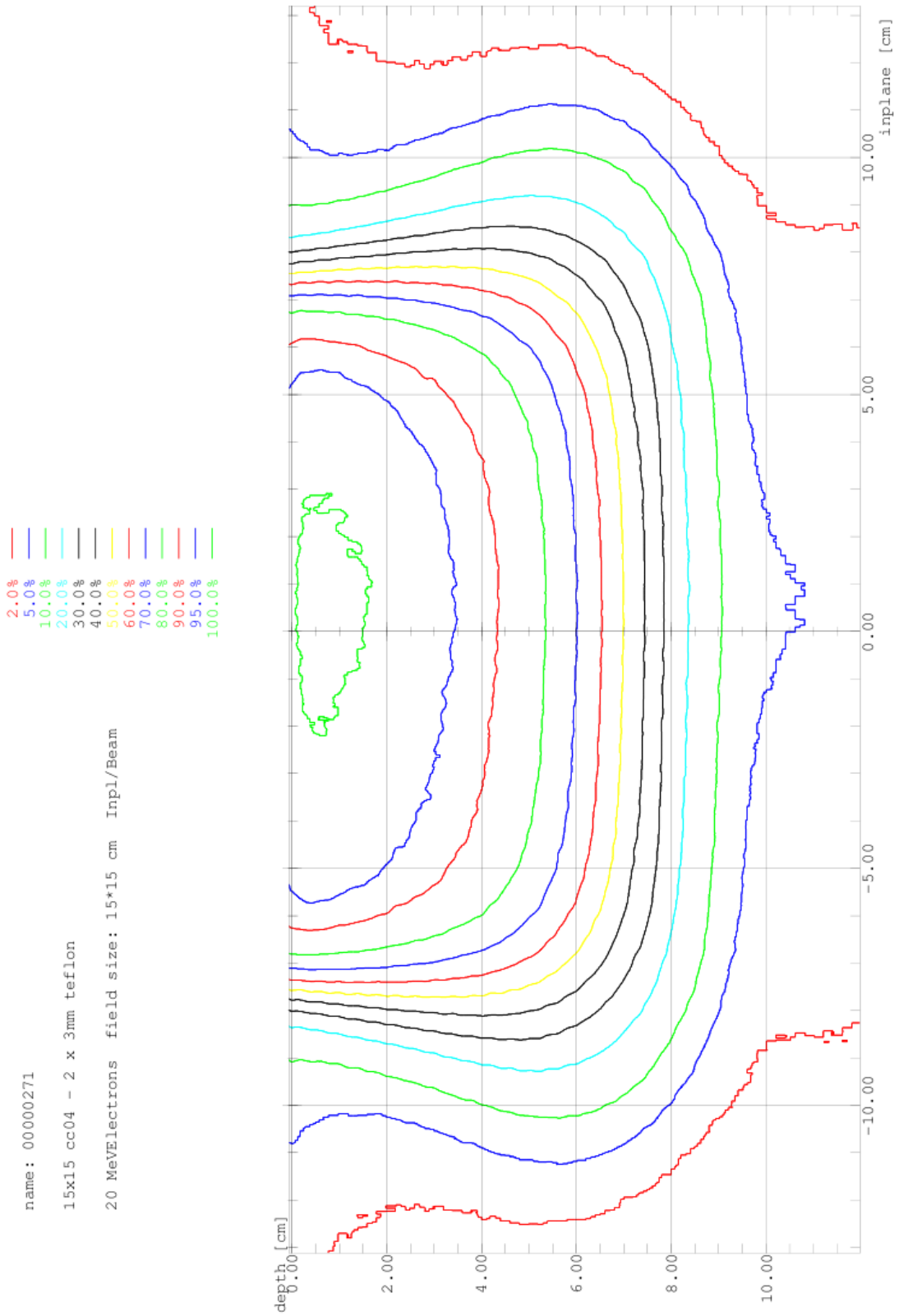

Illustration 58: Full Bolus 20MeV 2x3mm Teflon for Table 17

A.3.1.3 Bolus on Applicator FULL BOLUS – ALUMINIUM 9 & 20MeV

- **Illustration 59: Full Bolus on Applicator Depth Ionisation - Aluminium 9MeV from Table 19**
- **Illustration 60: Full Bolus on Applicator Depth Ionisation - Aluminium 20MeV from Table 20**
- **Illustration 61: Full Bolus 9MeV 2.5mm Aluminium for Table 21**
- **Illustration 62: Full Bolus 9MeV 5.0mm Aluminium for Table 21**
- **Illustration 63: Full Bolus 20MeV 2.5mm Aluminium for Table 21**
- **Illustration 64: Full Bolus 20MeV 5.0mm Aluminium for Table 21**

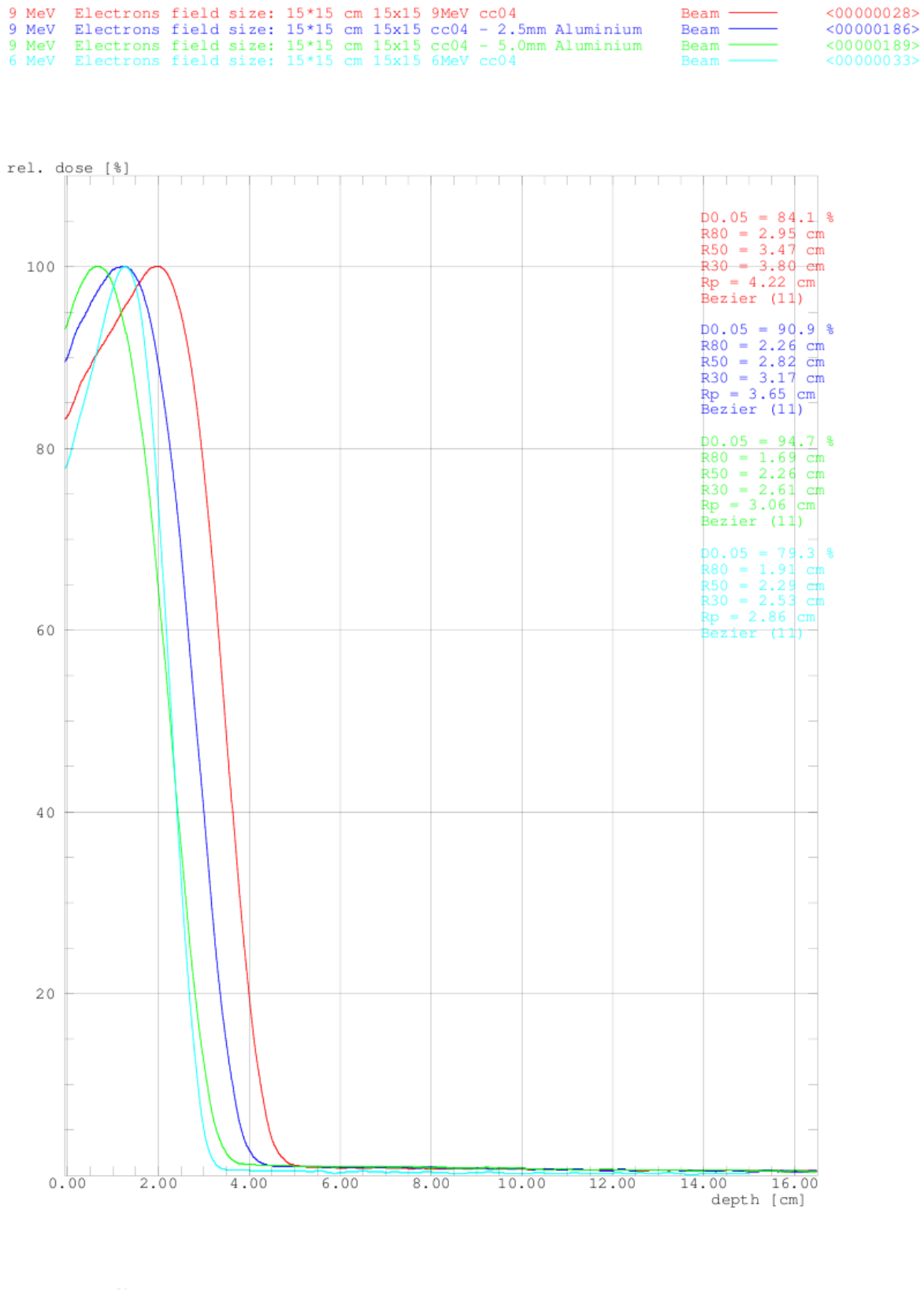

Illustration 59: Full Bolus on Applicator Depth Ionisation - Aluminium 9MeV from Table 19

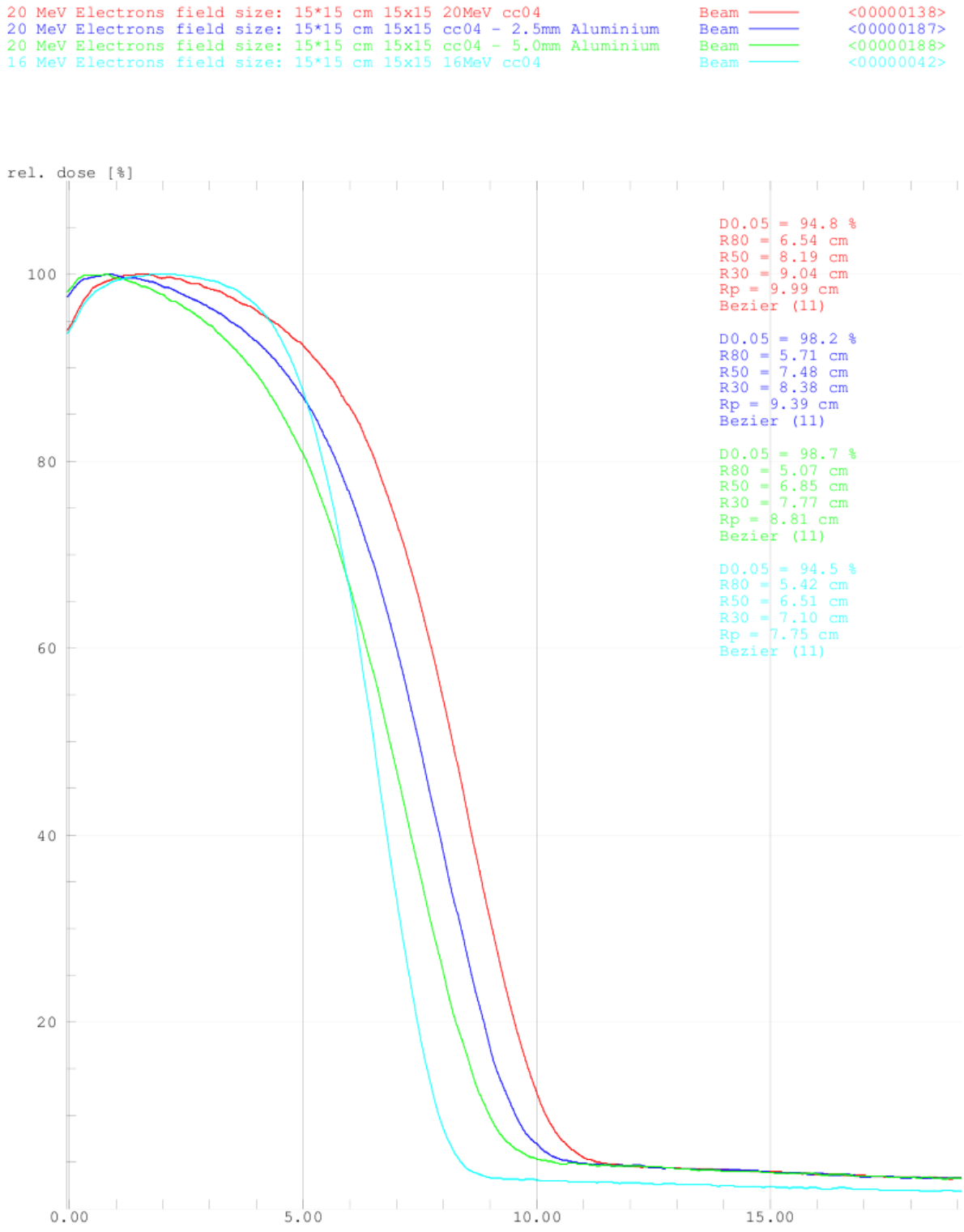

Illustration 60: Full Bolus on Applicator Depth Ionisation - Aluminium 20MeV from Table 20

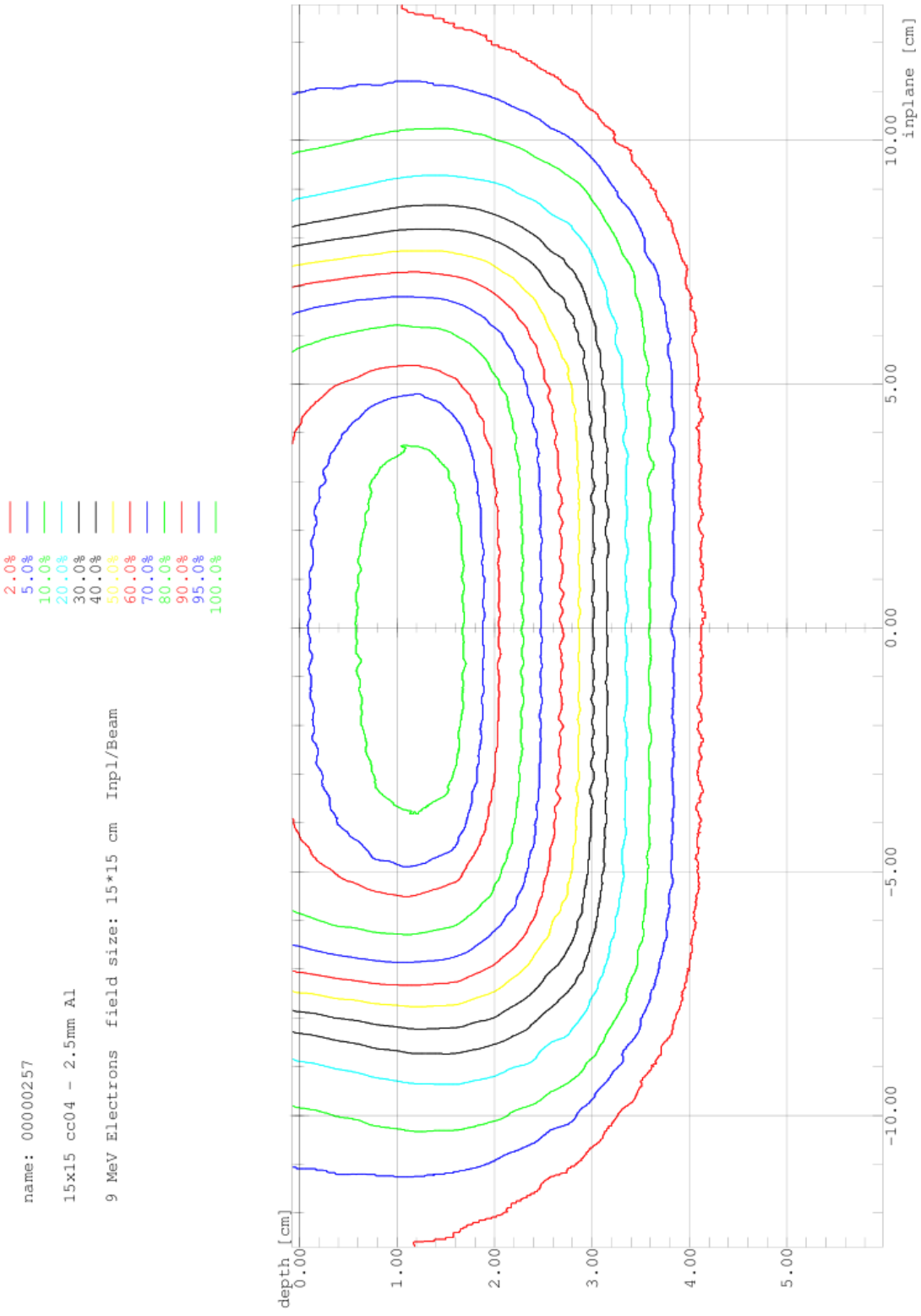

Illustration 61: Full Bolus 9MeV 2.5mm Aluminium for Table 21

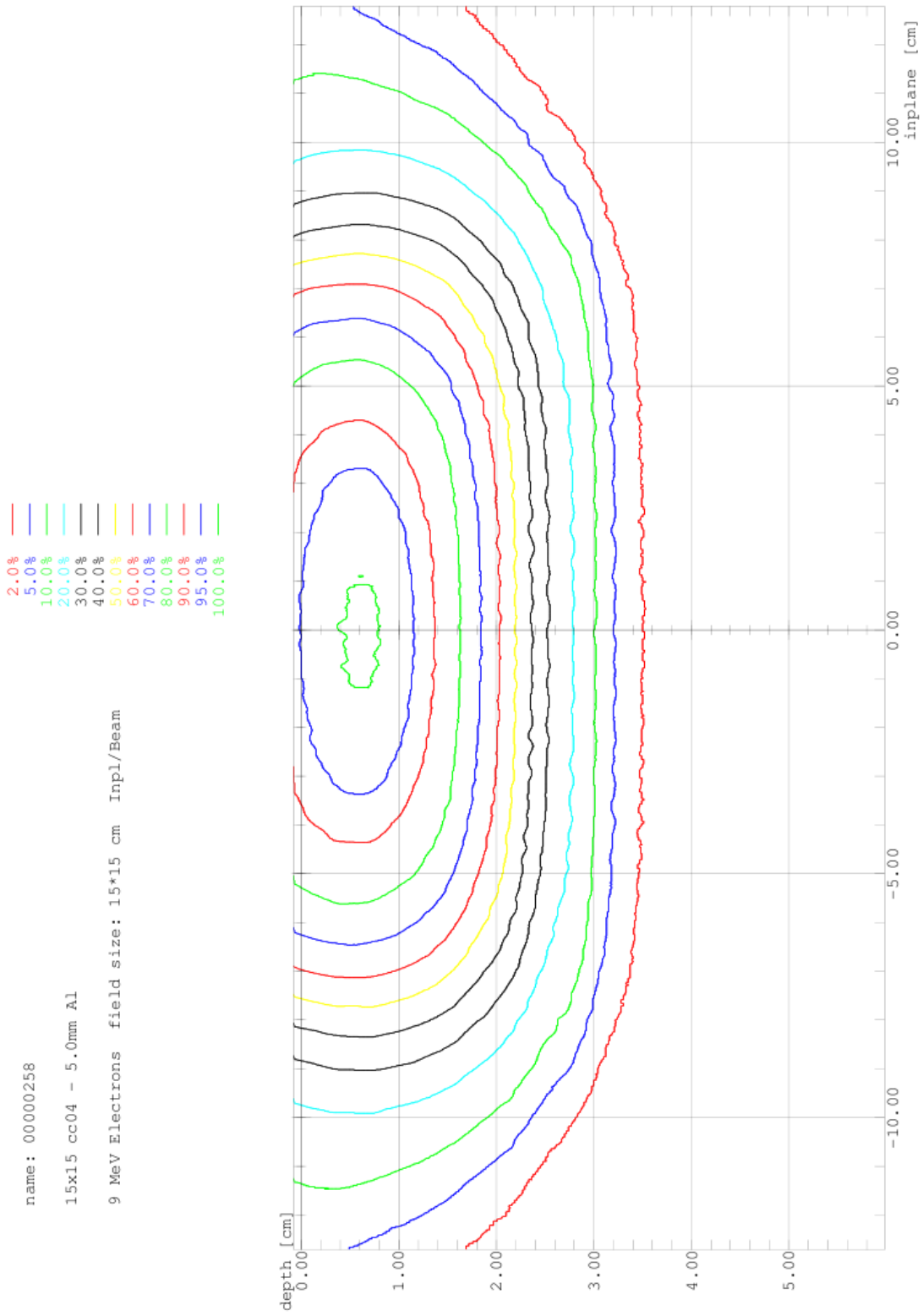

Illustration 62: Full Bolus 9MeV 5.0mm Aluminium for Table 21

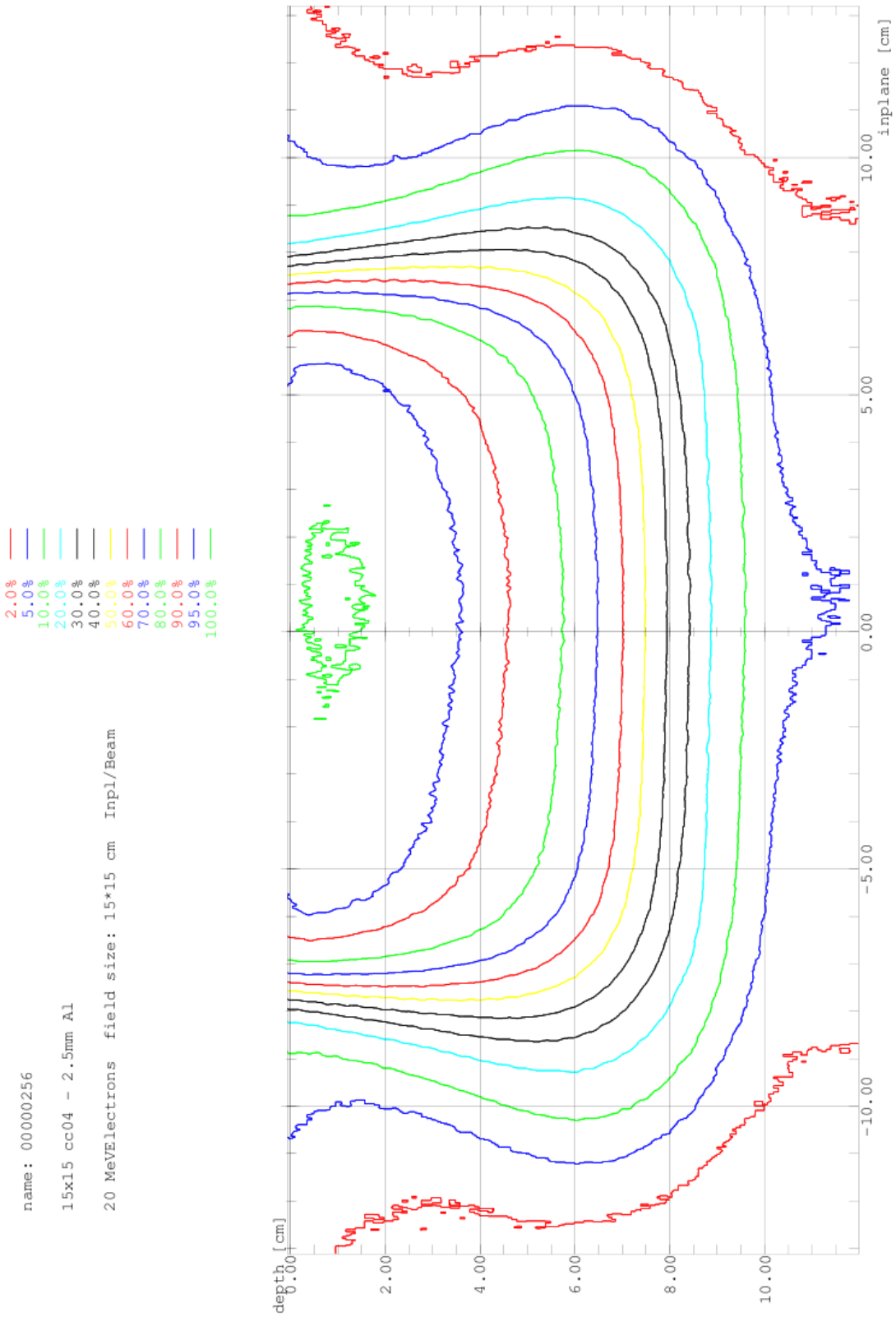

Illustration 63: Full Bolus 20MeV 2.5mm Aluminium for Table 21

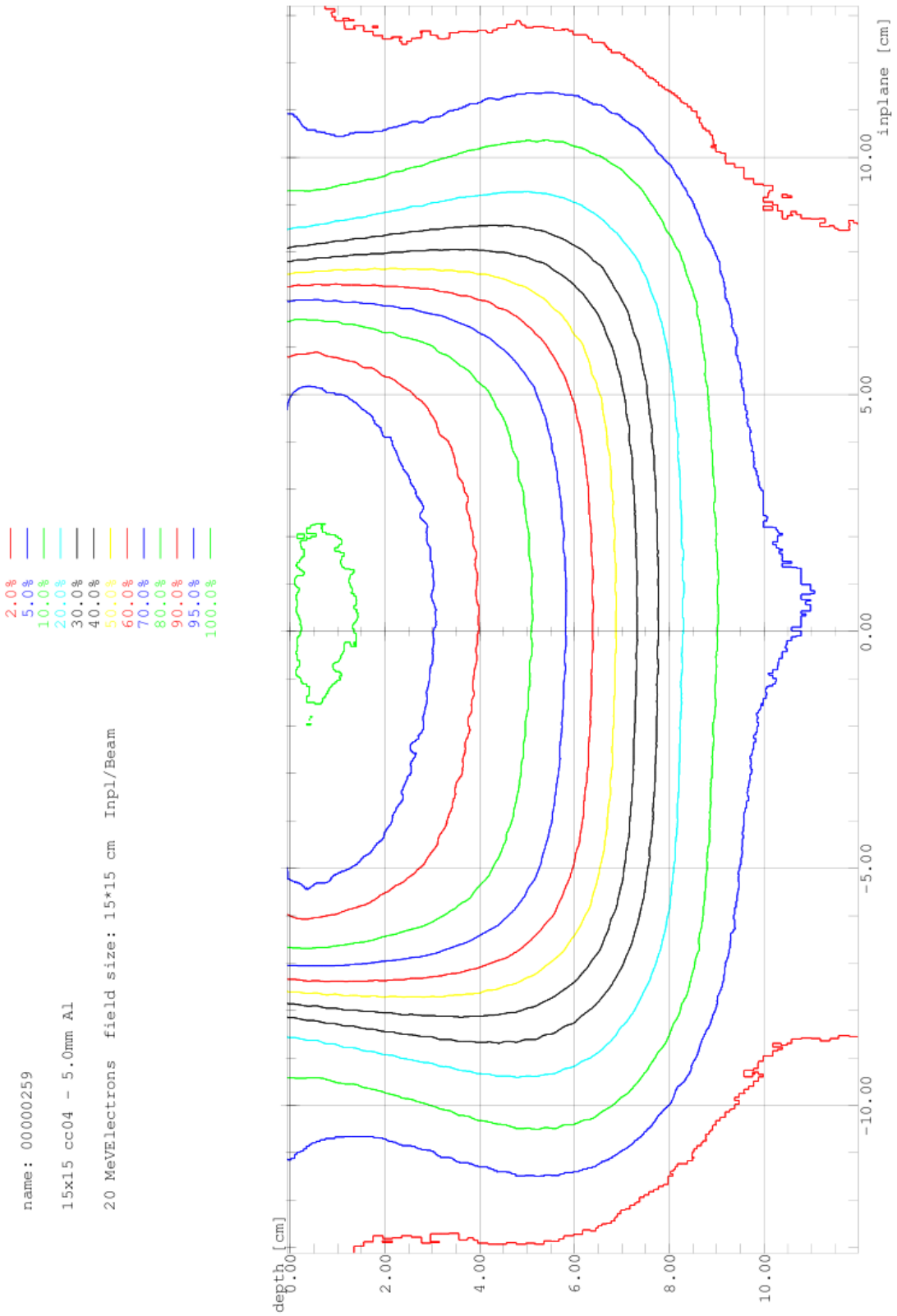

Illustration 64: Full Bolus 20MeV 5.0mm Aluminium for Table 21

A.3.2.1 Bolus on Applicator PARTIAL BOLUS – PERSPEX 9 & 20MeV

- **Illustration 65: Partial Bolus Perspex Depth Ionisation - Central Axis – 9MeV from Table 23**
- **Illustration 66: Partial Bolus Perspex Depth Ionisation - +3.5cm inplane – 9MeV from Table 23**

- **Illustration 67: Partial Bolus Perspex Depth Ionisation - Central Axis – 20MeV from Table 24**
- **Illustration 68: Partial Bolus Perspex Depth Ionisation - +3.5cm inplane – 20MeV from Table 24**

- **Illustration 69: Partial Bolus 9MeV 1x6mm Perspex for Table 25**
- **Illustration 70: Partial Bolus 9MeV 2x6mm Perspex for Table 25**
- **Illustration 71: Partial Bolus 9MeV 3x6mm Perspex for Table 25**
- **Illustration 72: Partial Bolus 20MeV 1x6mm Perspex for Table 25**
- **Illustration 73: Partial Bolus 20MeV 2x6mm Perspex for Table 25**
- **Illustration 74: Partial Bolus 20MeV 3x6mm Perspex for Table 25**

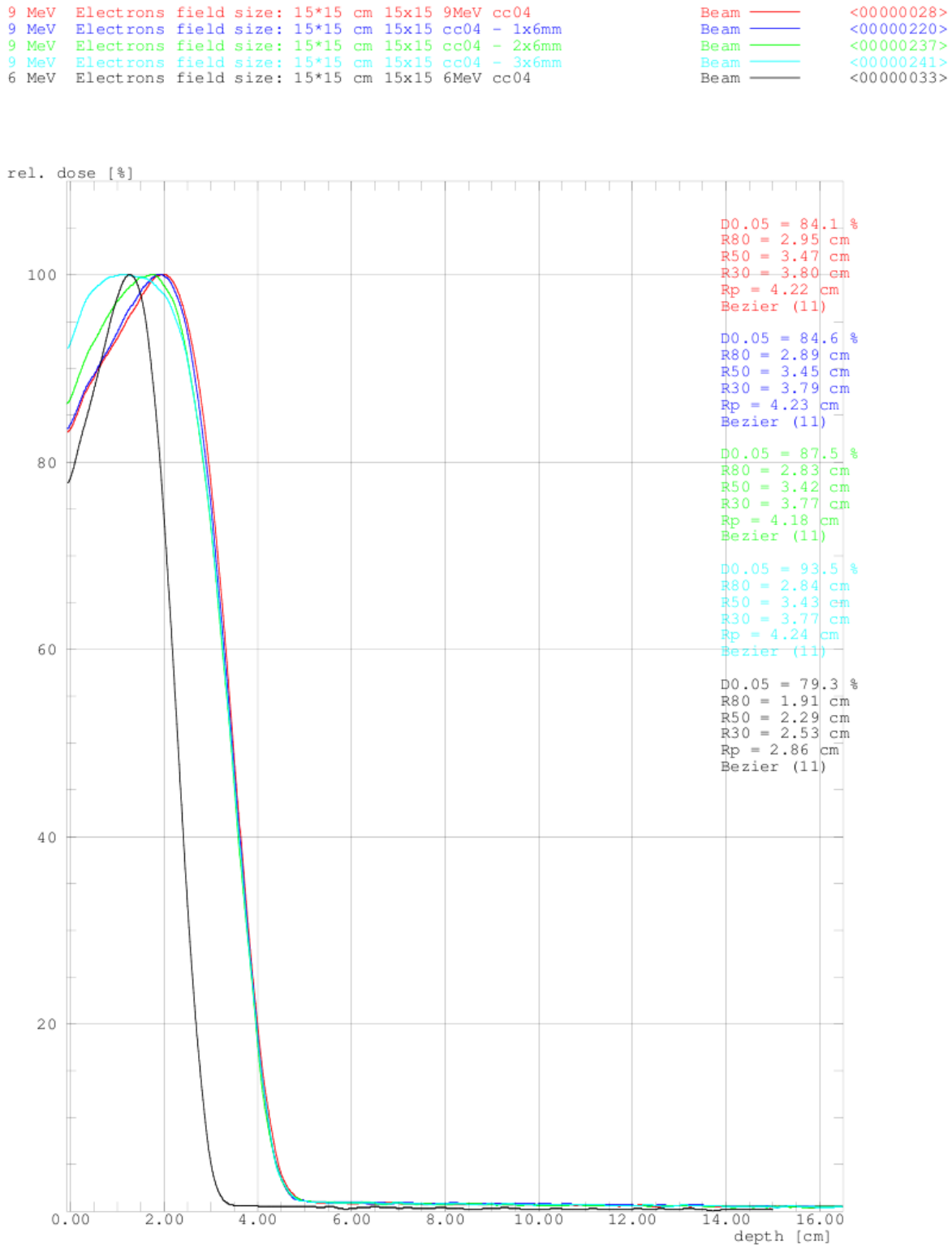

Illustration 65: Partial Bolus Perspex Depth Ionisation - Central Axis – 9MeV from Table 23

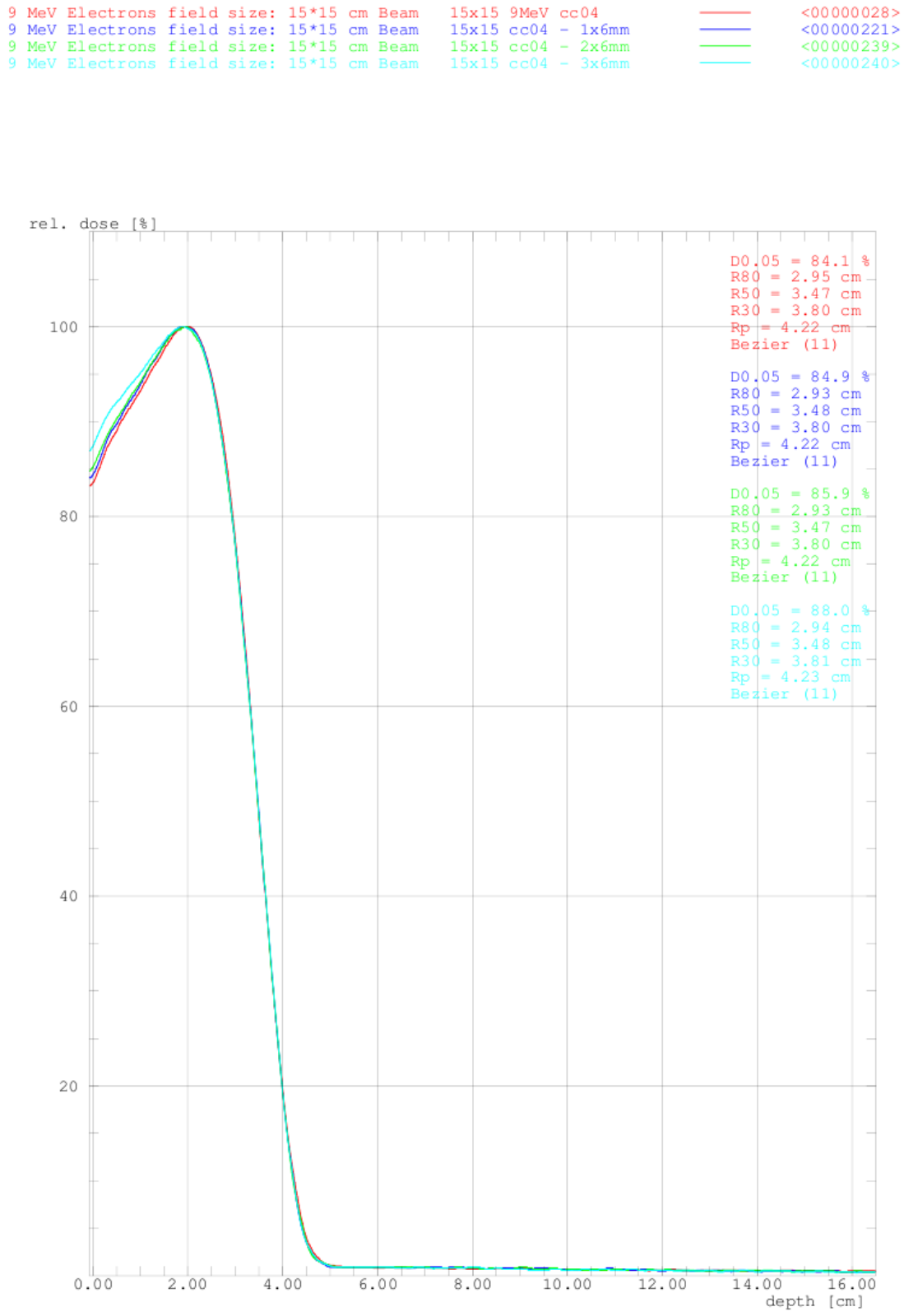

Illustration 66: Partial Bolus Perspex Depth Ionisation - +3.5cm inplane – 9MeV from Table 23

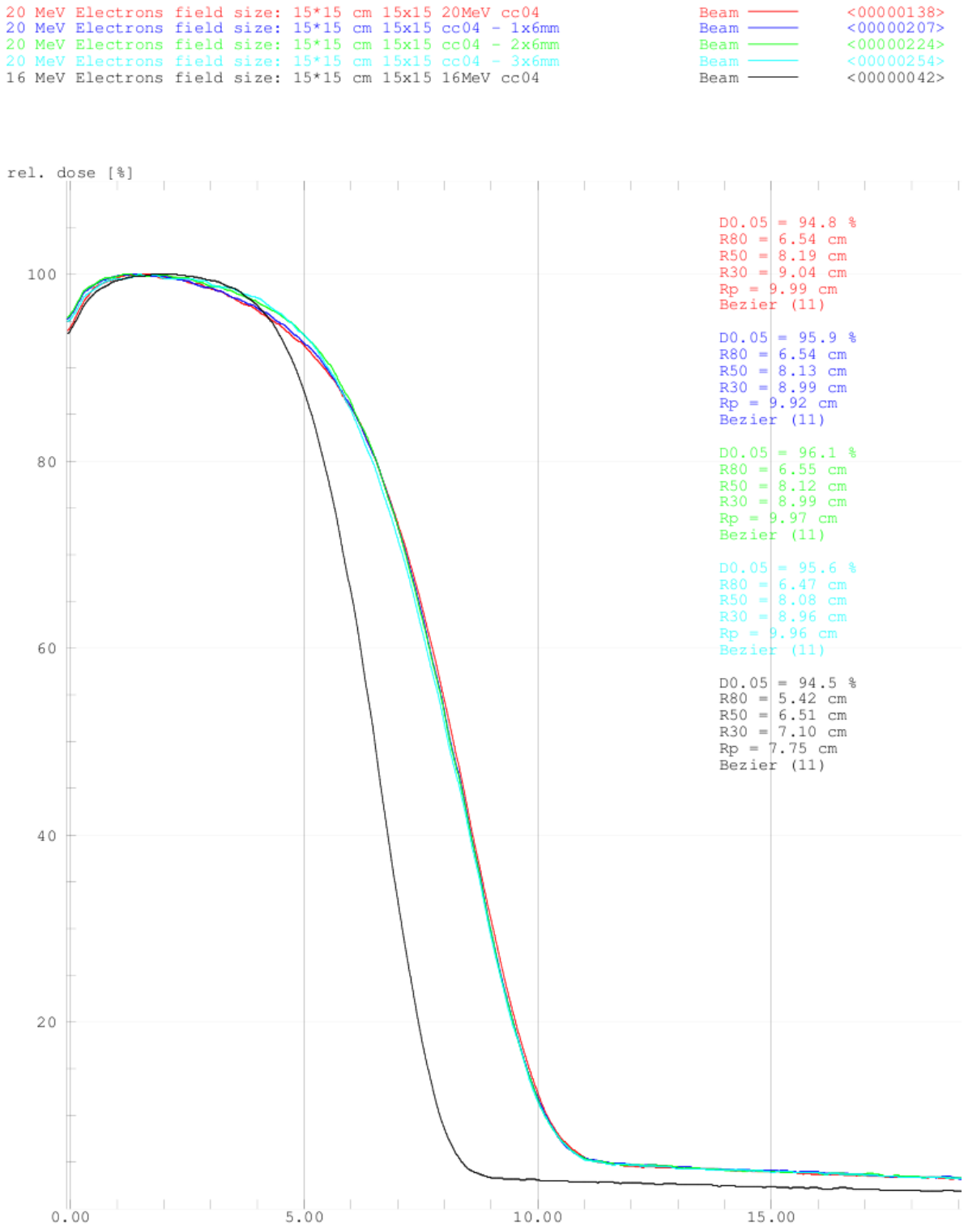

Illustration 67: Partial Bolus Perspex Depth Ionisation - Central Axis – 20MeV from Table 24

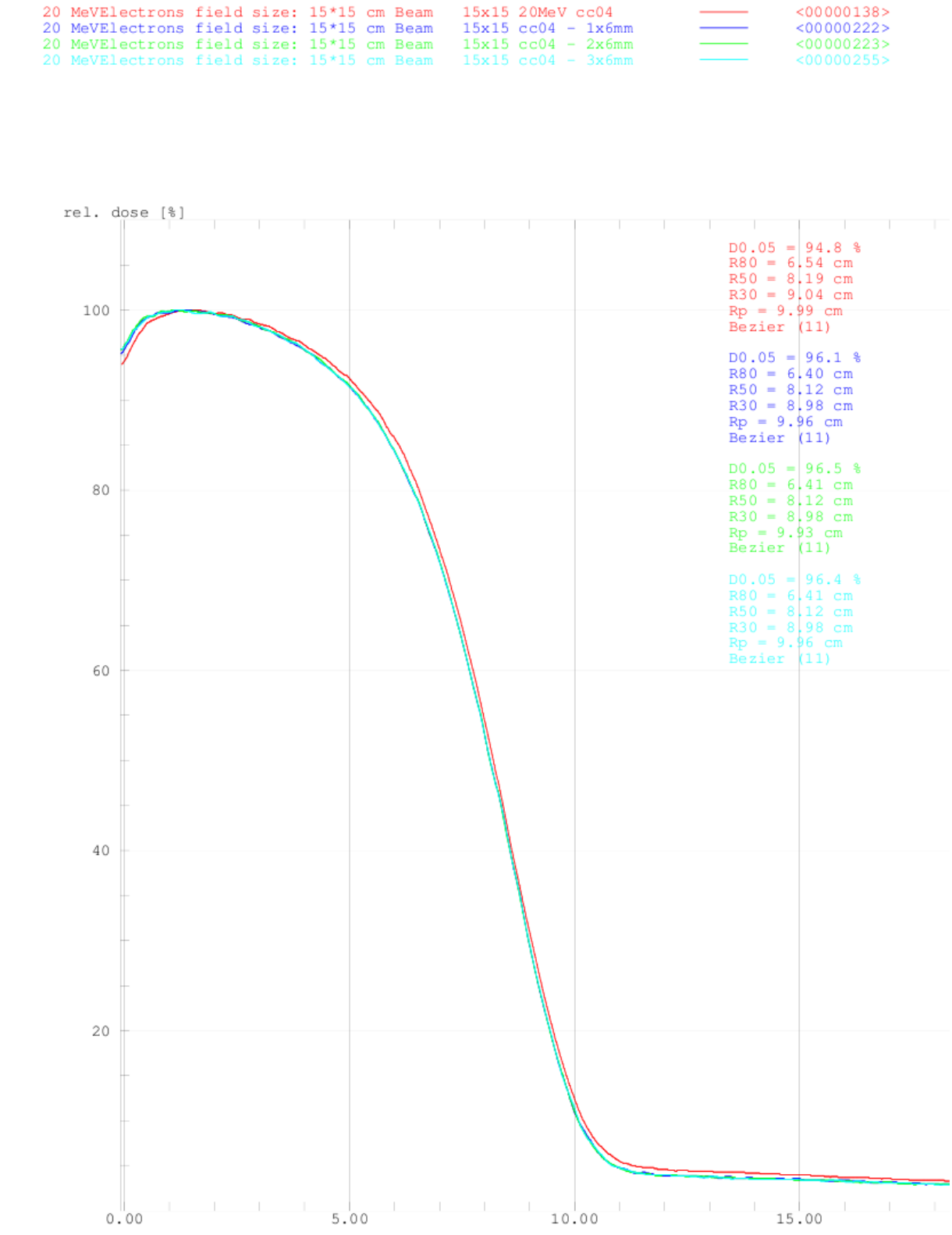

Illustration 68: Partial Bolus Perspex Depth Ionisation - +3.5cm inplane – 20MeV from Table 24

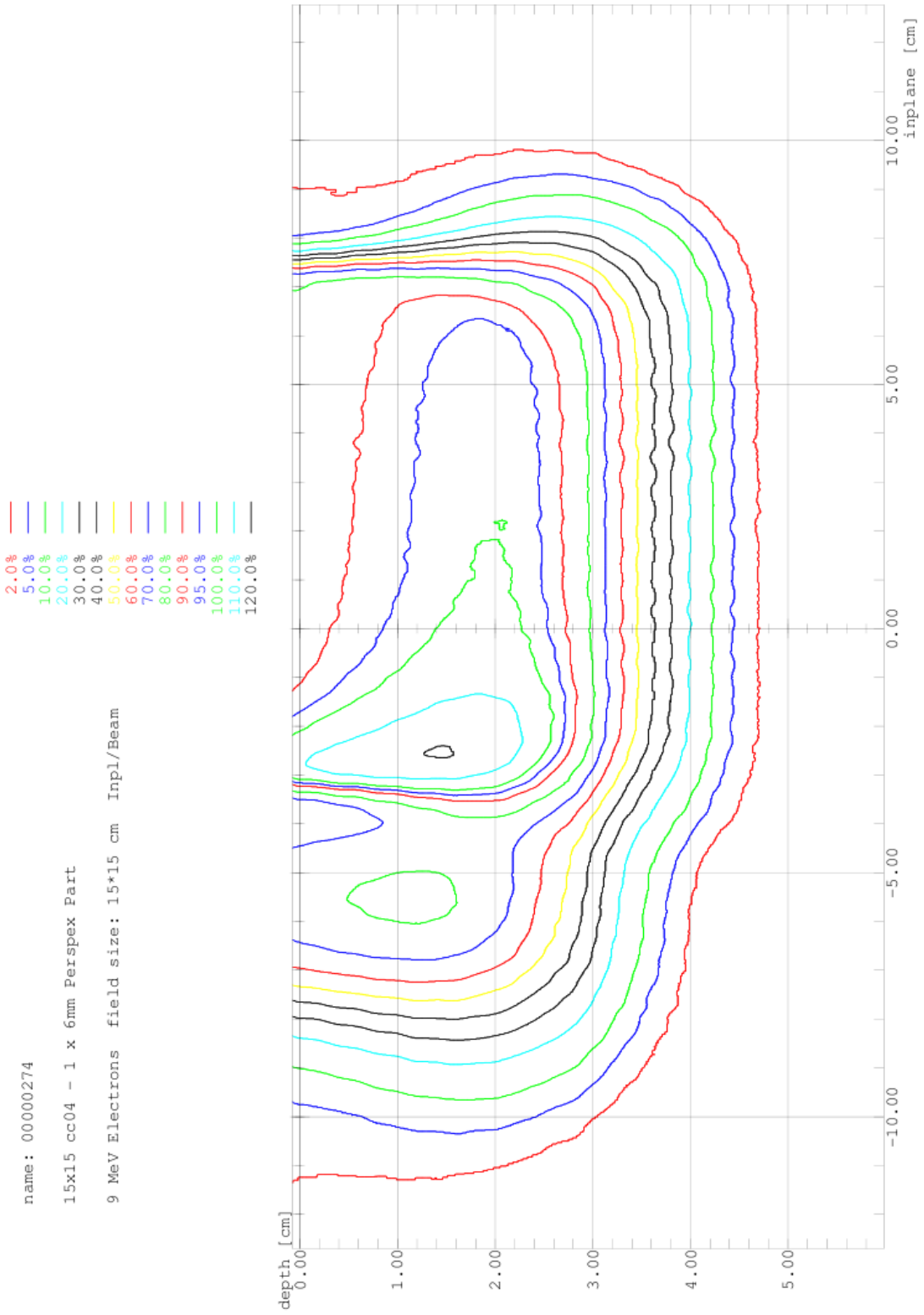

Illustration 69: Partial Bolus 9MeV 1x6mm Perspex for Table 25

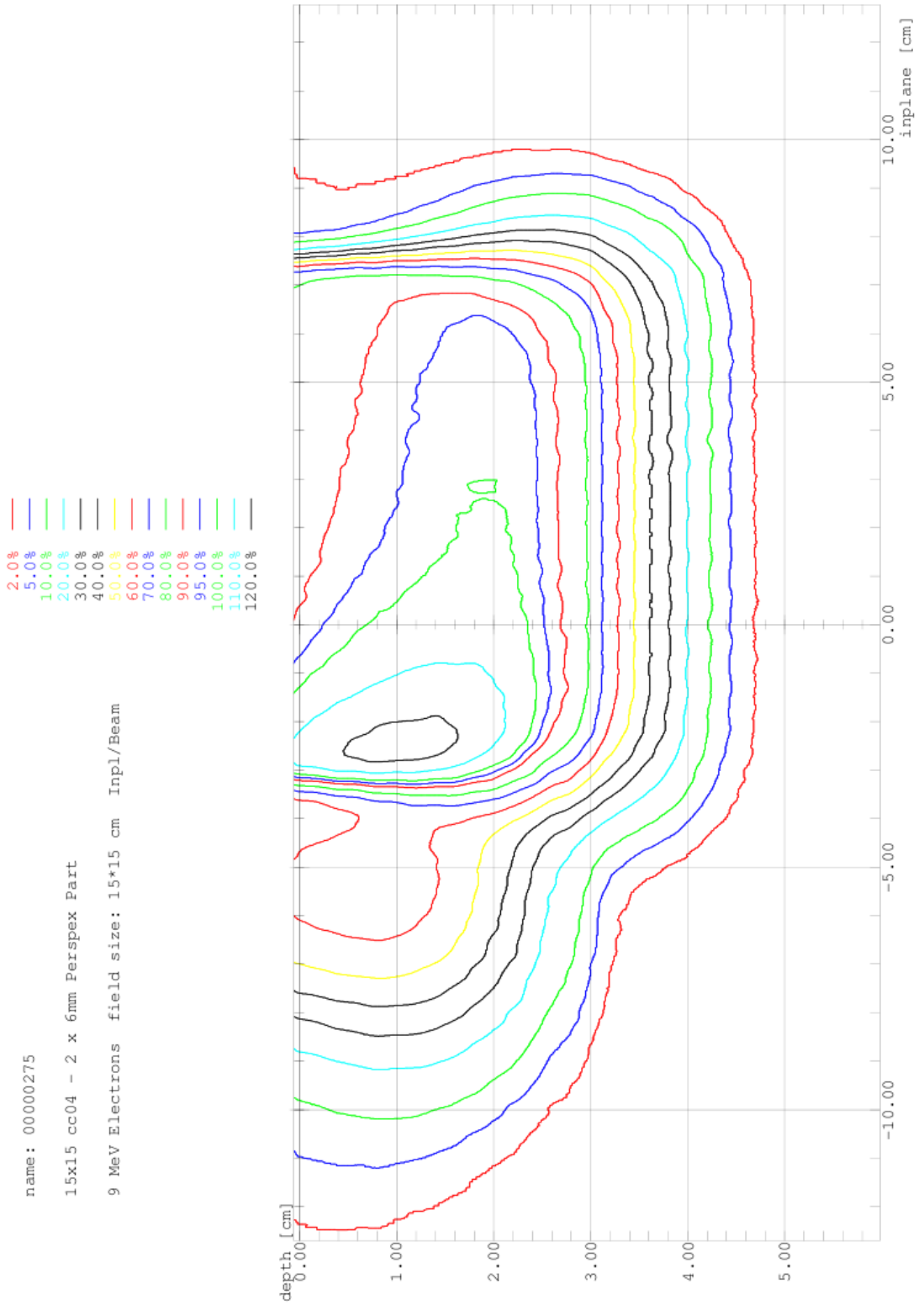

Illustration 70: Partial Bolus 9MeV 2x6mm Perspex for Table 25

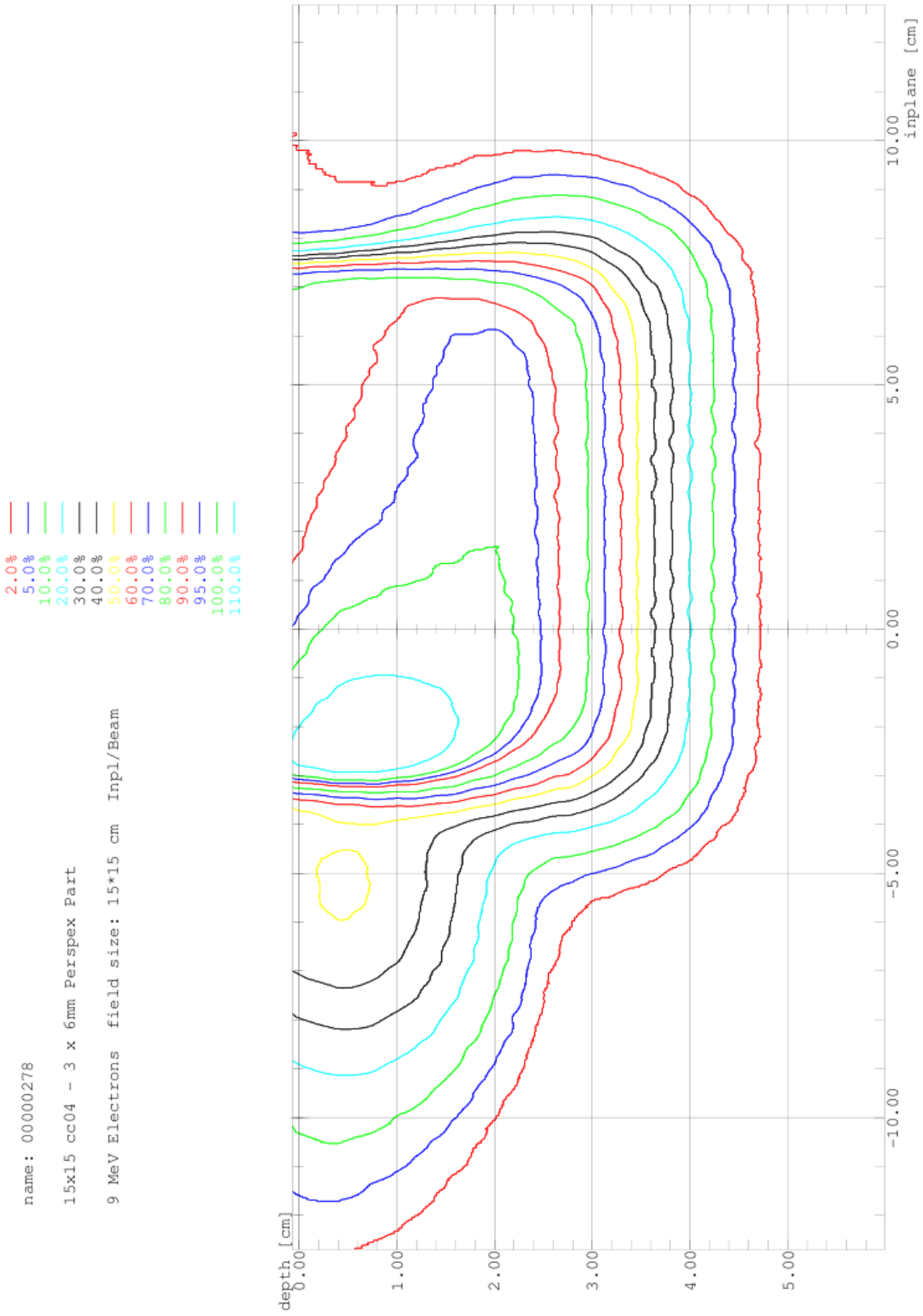

Illustration 71: Partial Bolus 9MeV 3x6mm Perspex for Table 25

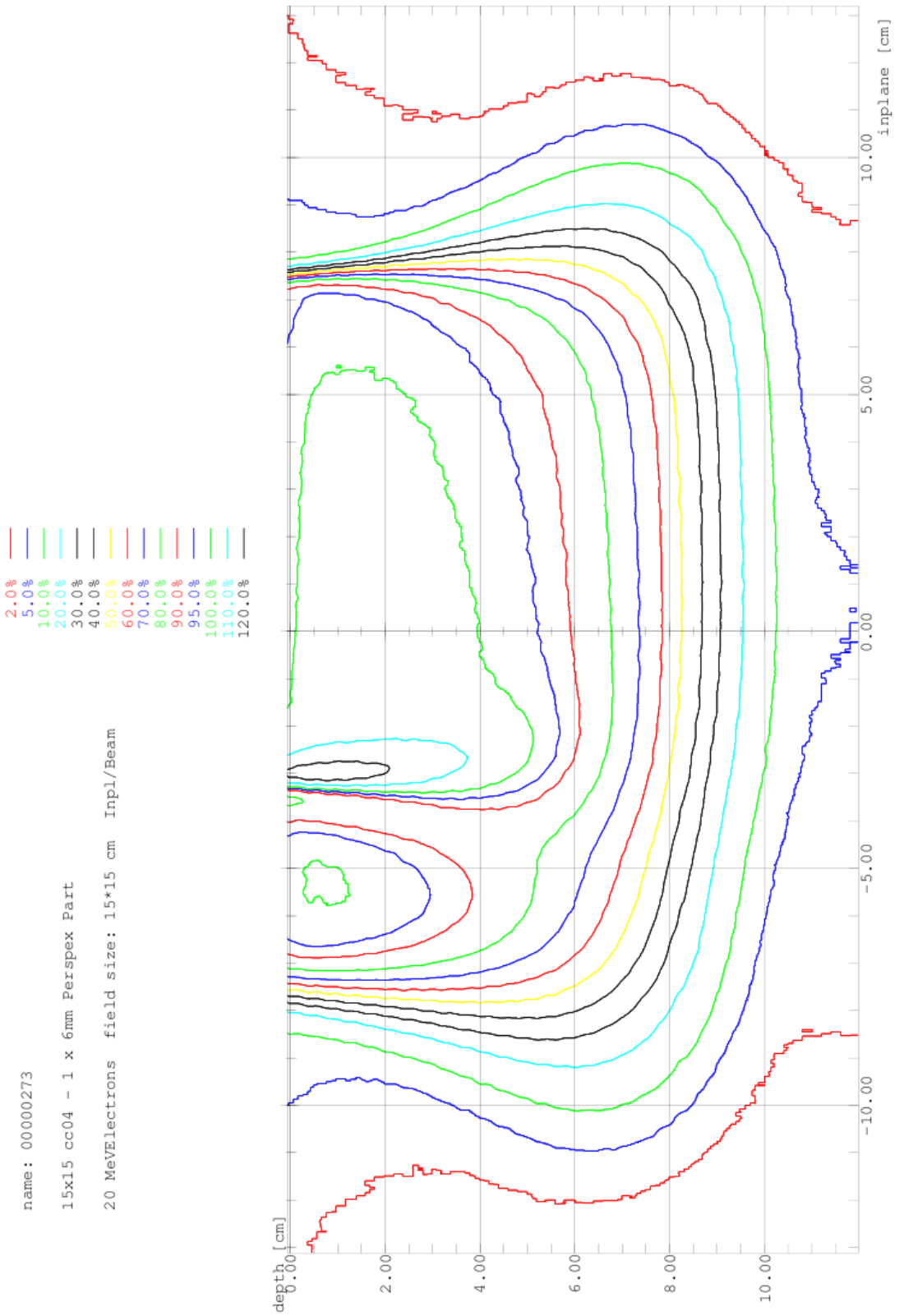

Illustration 72: Partial Bolus 20MeV 1x6mm Perspex for Table 25

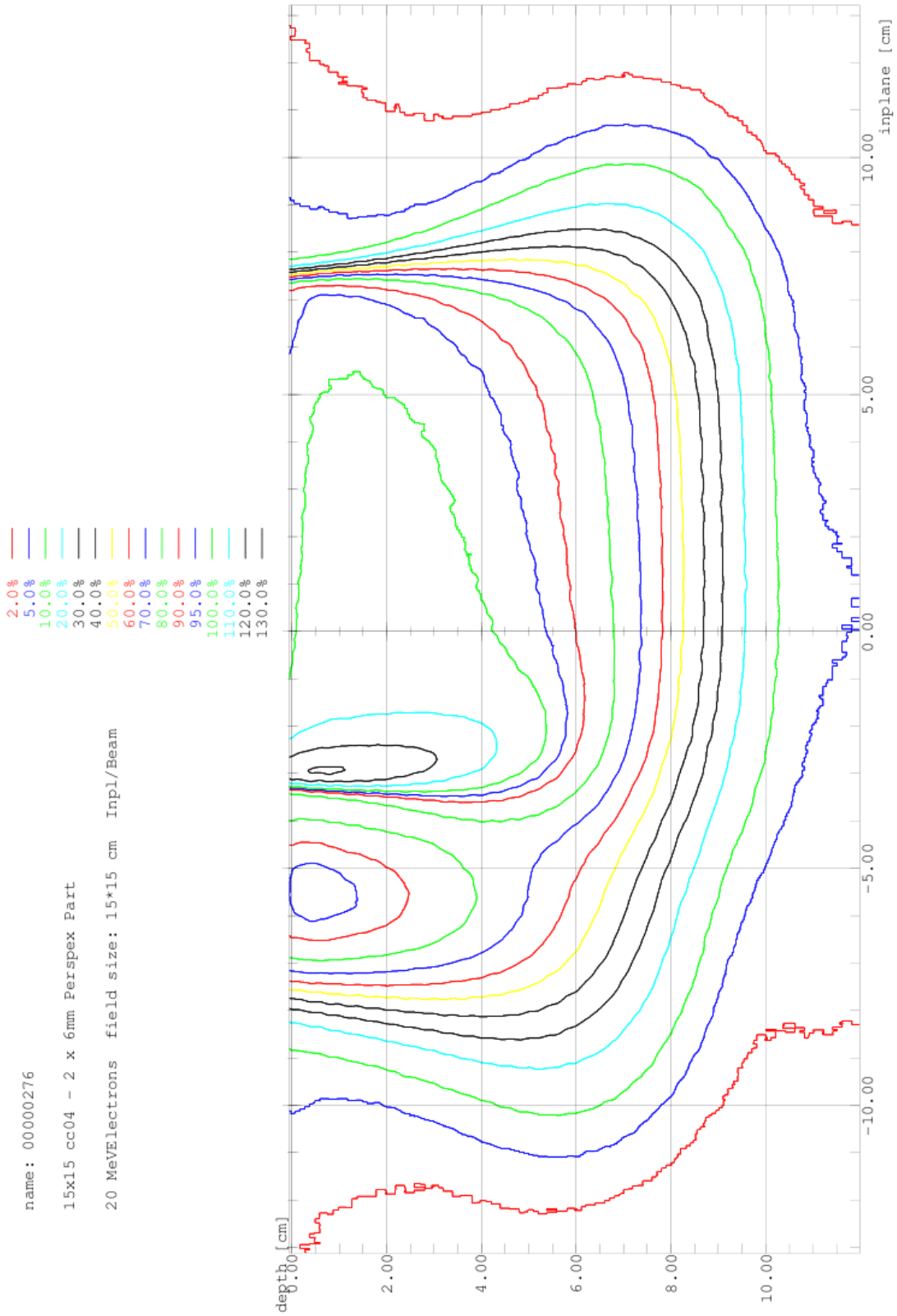

Illustration 73: Partial Bolus 20MeV 2x6mm Perspex for Table 25

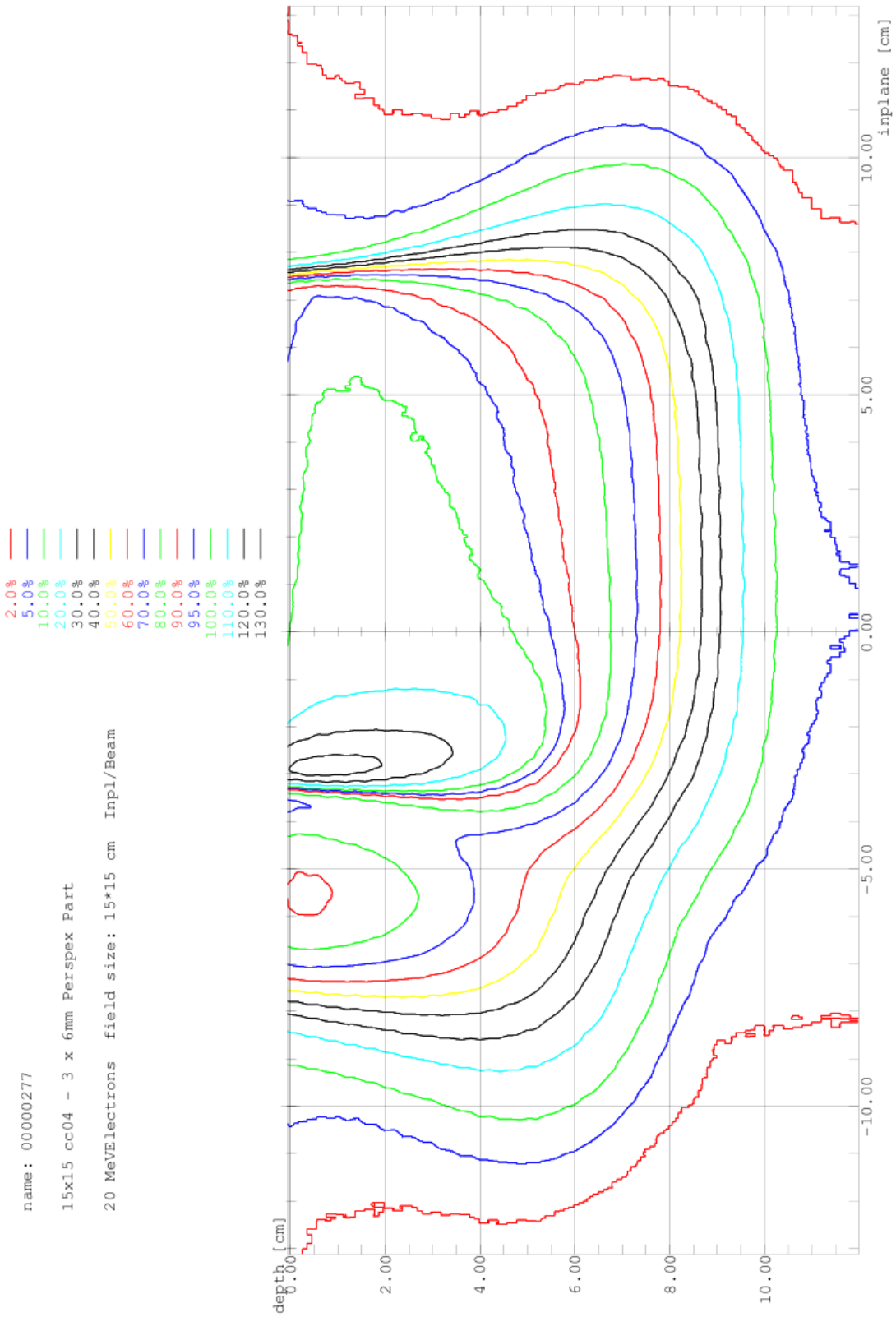

Illustration 74: Partial Bolus 20MeV 3x6mm Perspex for Table 25

A.3.2.2 Bolus on Applicator PARTIAL BOLUS – TEFLON 9 & 20MeV

- **Illustration 75: Partial Bolus Teflon Depth Ionisation - Central Axis – 9MeV from Table 28**
- **Illustration 76: Partial Bolus Teflon Depth Ionisation - +3.5cm inplane – 9MeV from Table 28**

- **Illustration 77: Partial Bolus Teflon Depth Ionisation - Central Axis – 20MeV from Table 29**
- **Illustration 78: Partial Bolus Teflon Depth Ionisation - +3.5cm inplane – 20MeV from Table 29**

- **Illustration 79: Partial Bolus 9MeV 1x3mm Teflon for Table 30**
- **Illustration 80: Partial Bolus 9MeV 2x3mm Teflon for Table 30**
- **Illustration 81: Partial Bolus 9MeV 2x5mm Teflon for Table 30**
- **Illustration 82: Partial Bolus 20MeV 1x3mm Teflon for Table 30**
- **Illustration 83: Partial Bolus 20MeV 2x3mm Teflon for Table 30**
- **Illustration 84: Partial Bolus 20MeV 2x5mm Teflon for Table 30**

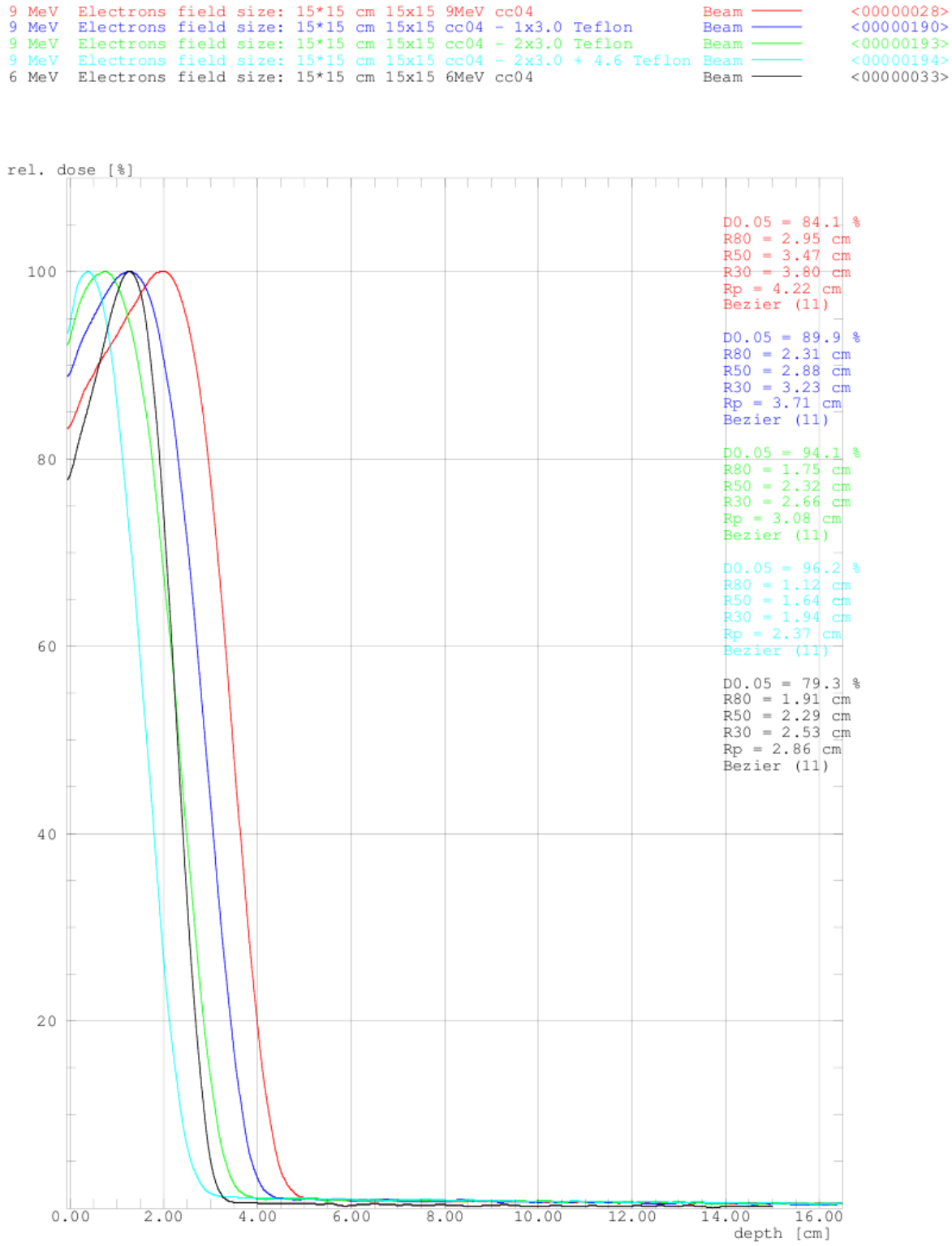

Illustration 75: Partial Bolus Teflon Depth Ionisation - Central Axis – 9MeV from Table 28

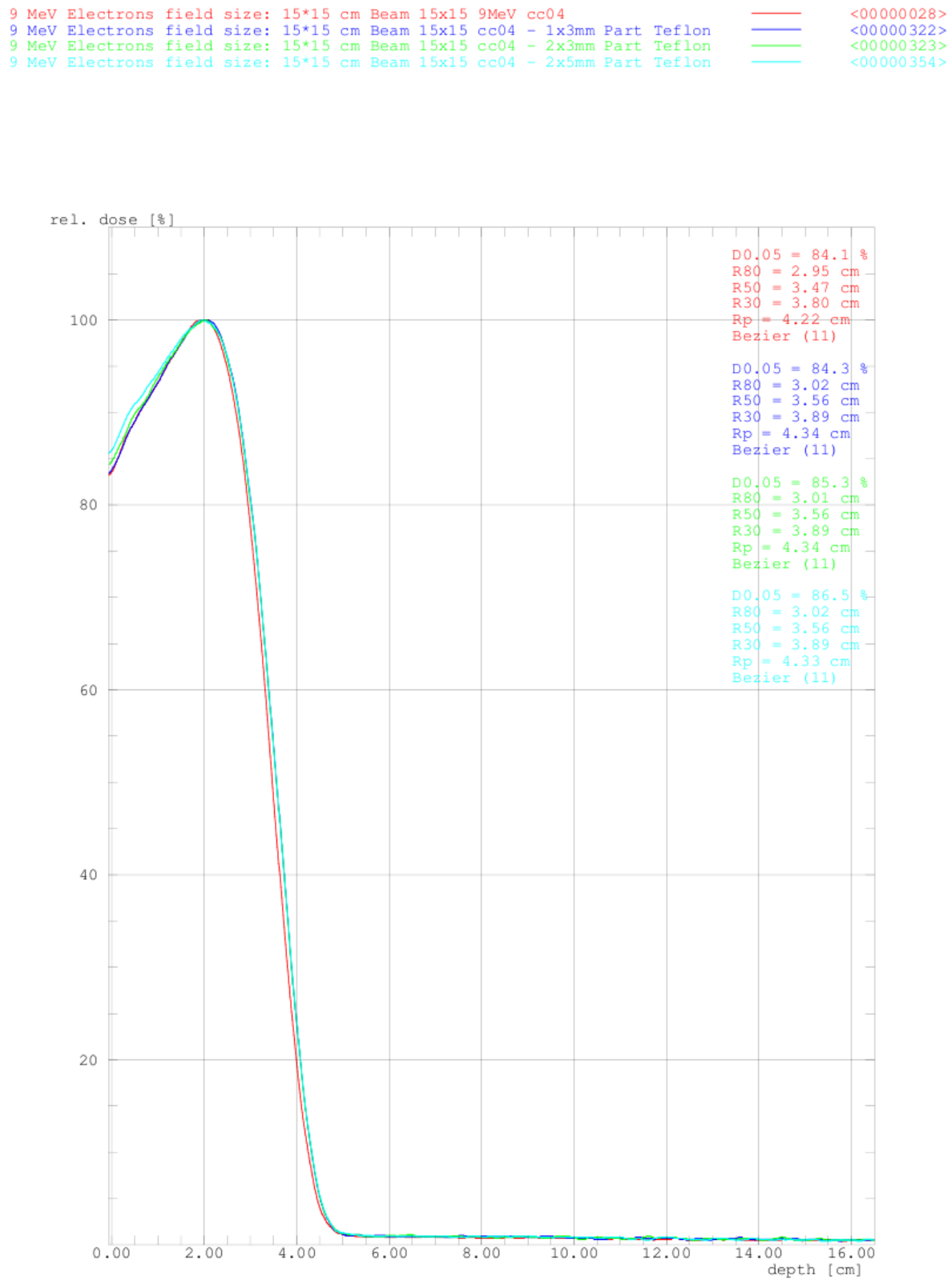

Illustration 76: Partial Bolus Teflon Depth Ionisation - +3.5cm inplane – 9MeV from Table 28

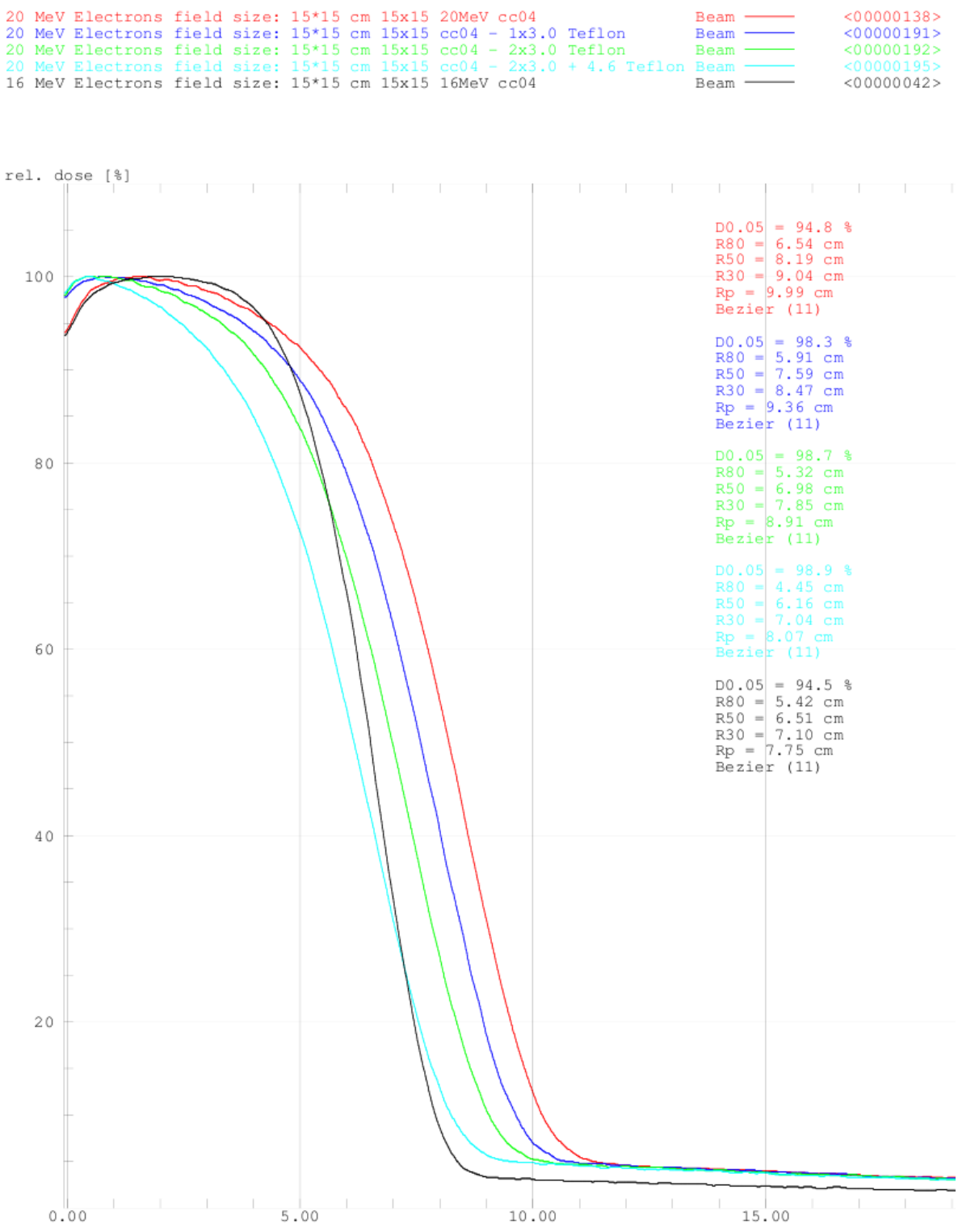

Illustration 77: Partial Bolus Teflon Depth Ionisation - Central Axis – 20MeV from Table 29

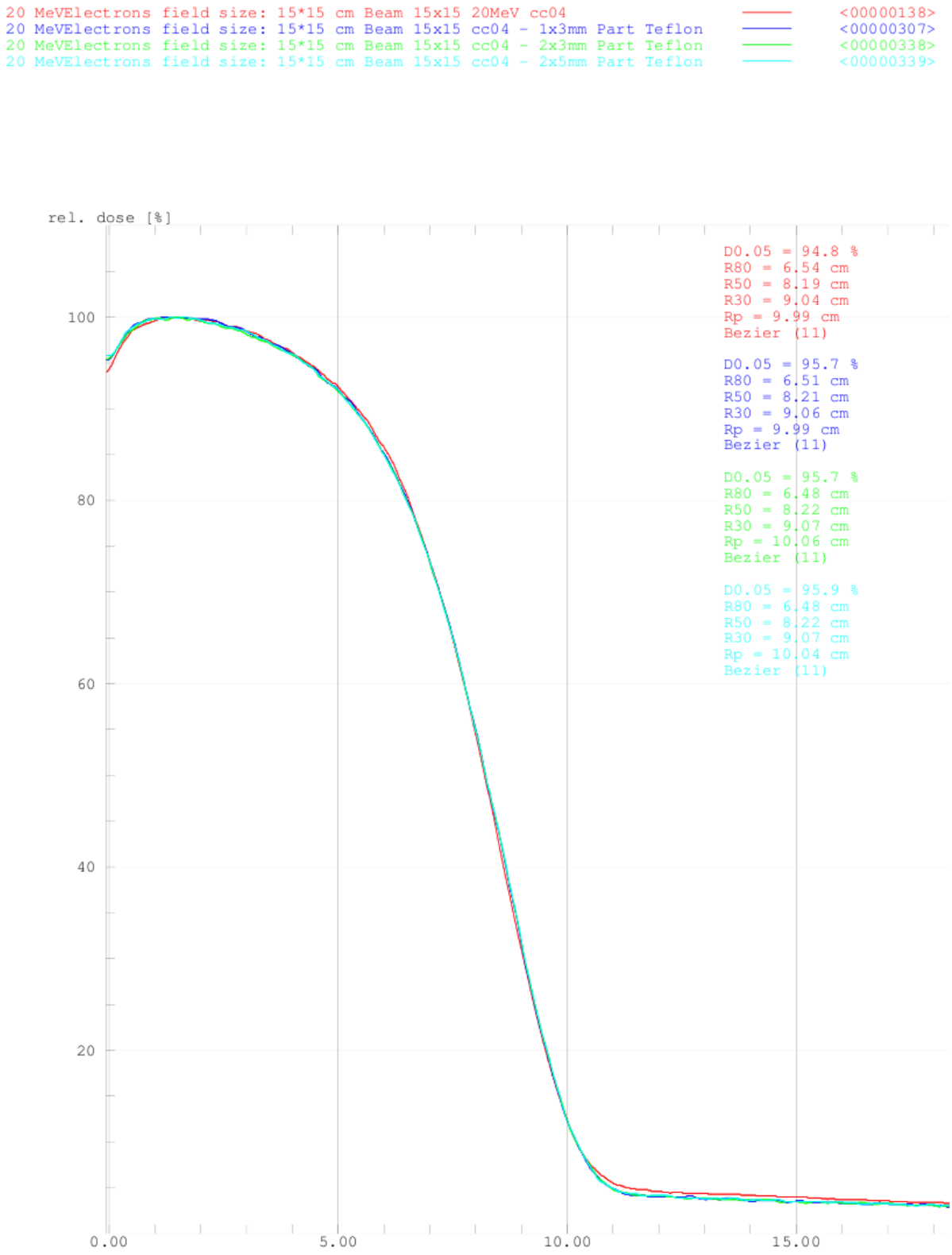

Illustration 78: Partial Bolus Teflon Depth Ionisation - +3.5cm inplane – 20MeV from Table 29

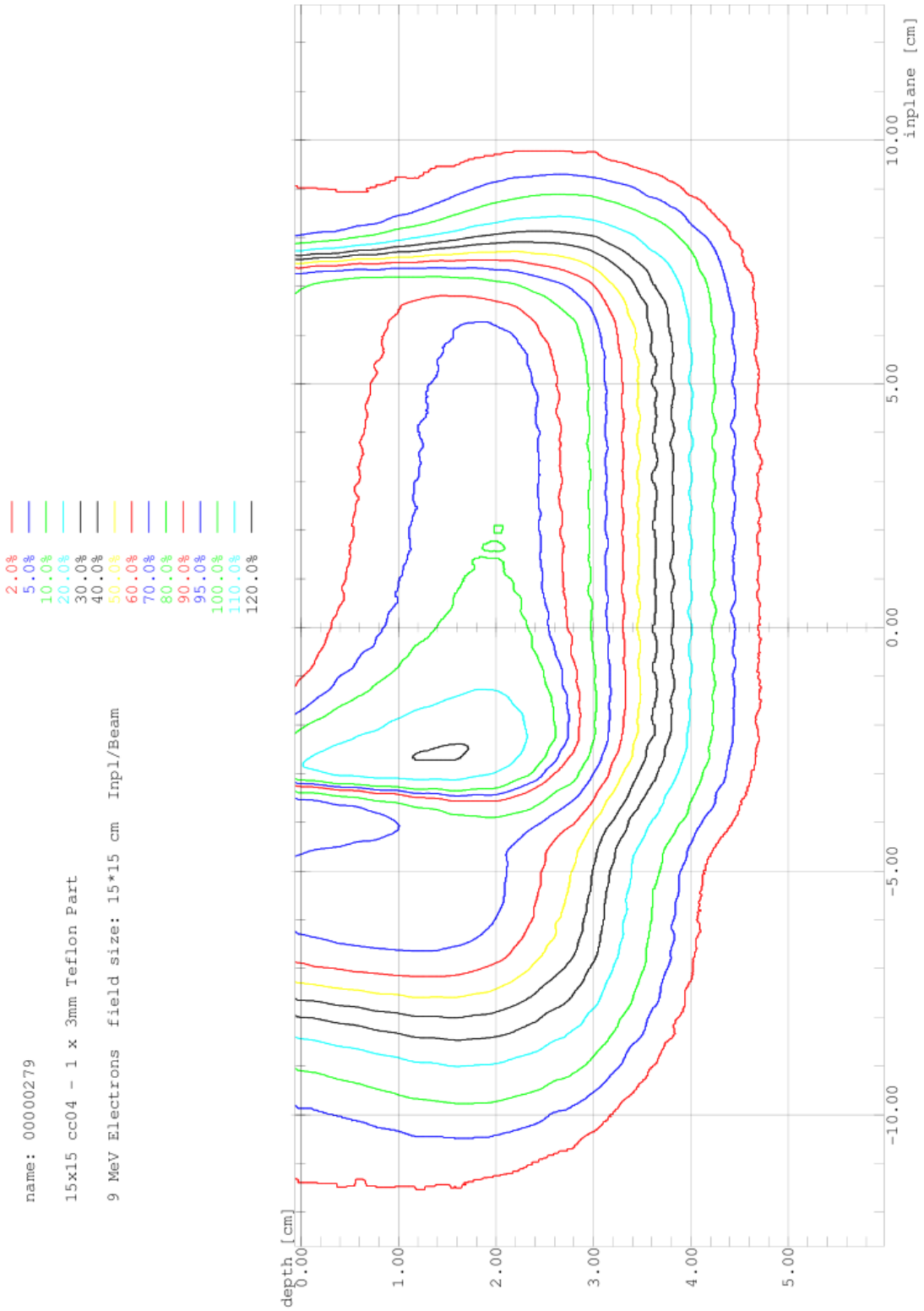

Illustration 79: Partial Bolus 9MeV 1x3mm Teflon for Table 30

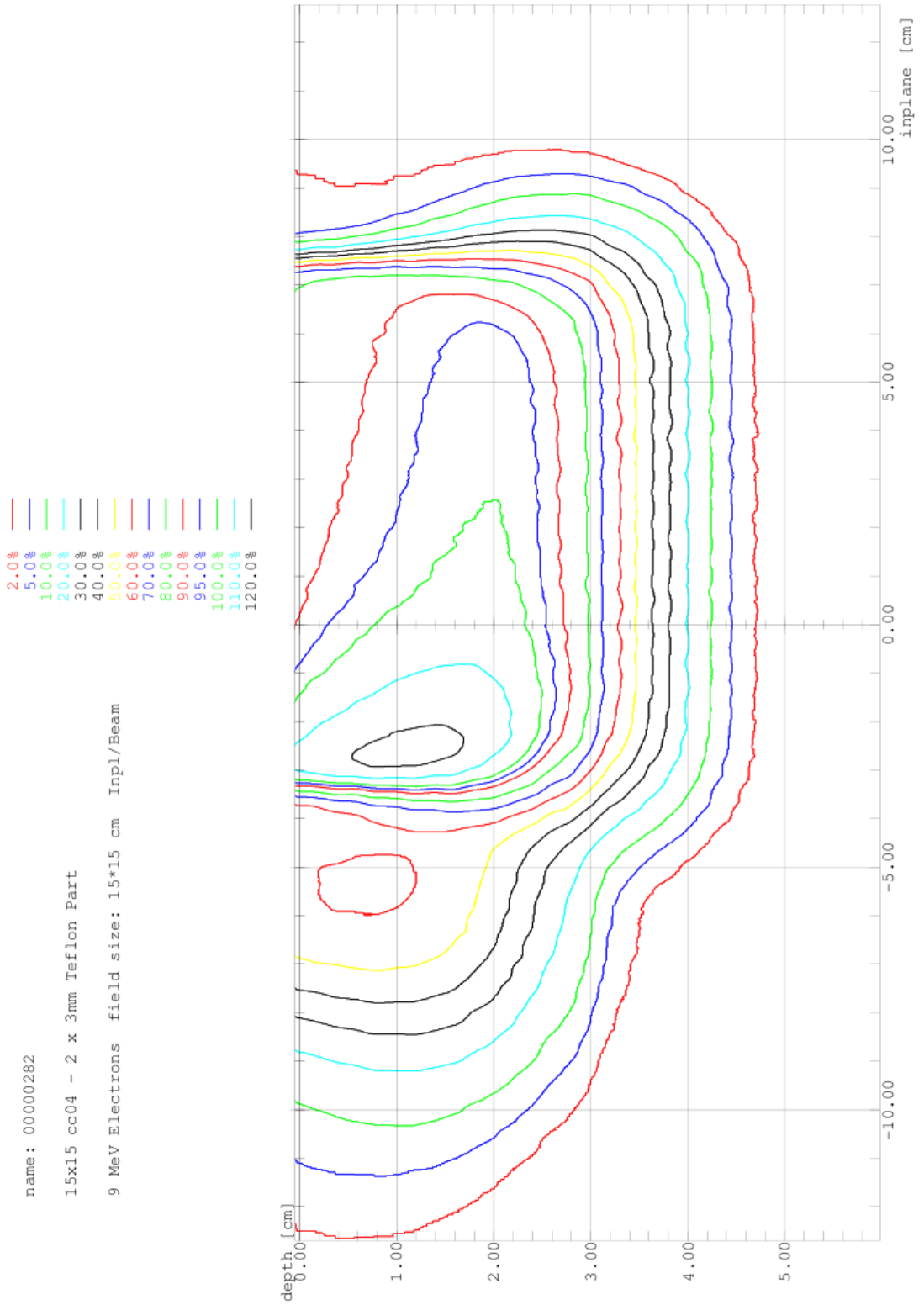

Illustration 80: Partial Bolus 9MeV 2x3mm Teflon for Table 30

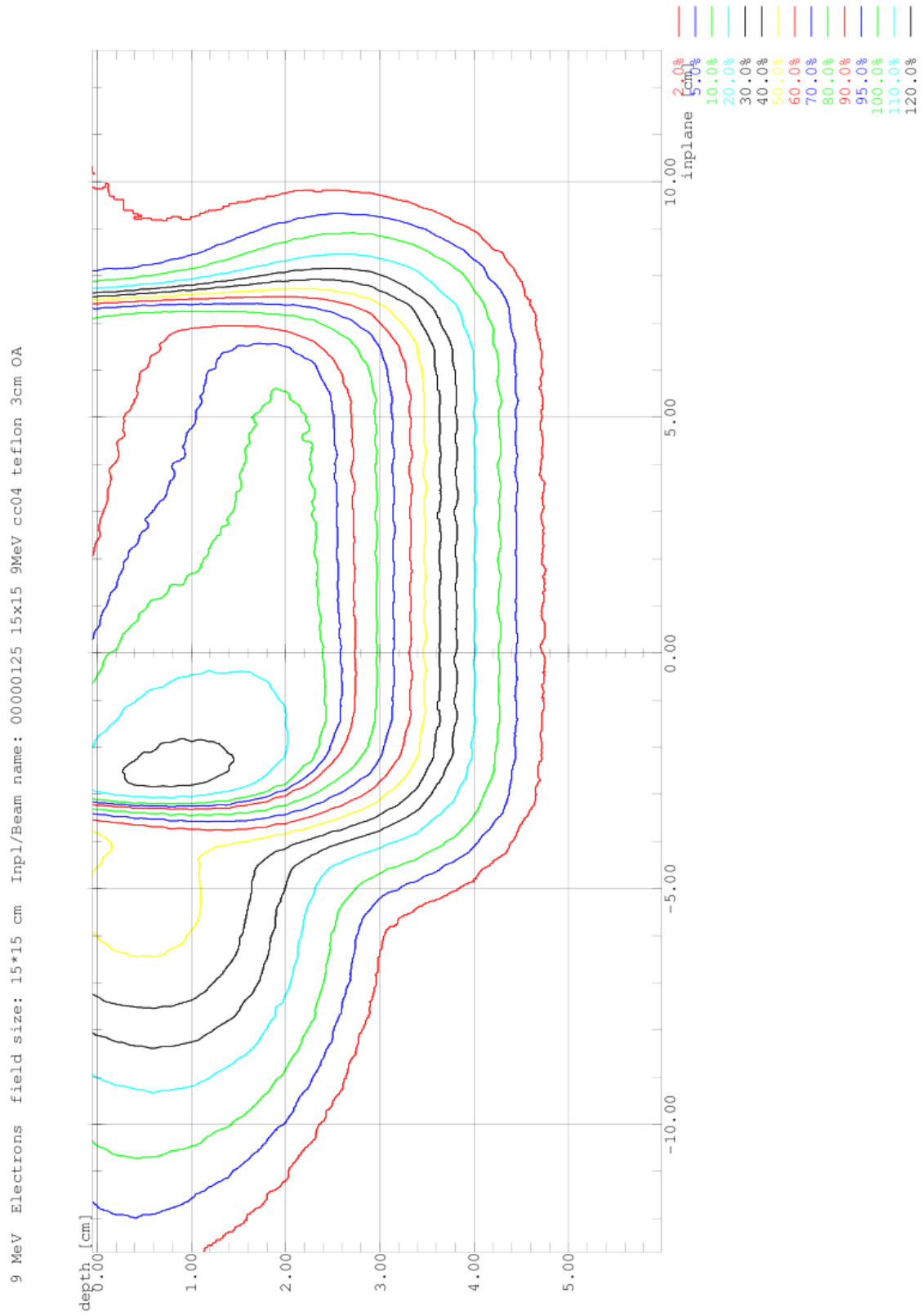

Illustration 81: Partial Bolus 9MeV 2x5mm Teflon for Table 30

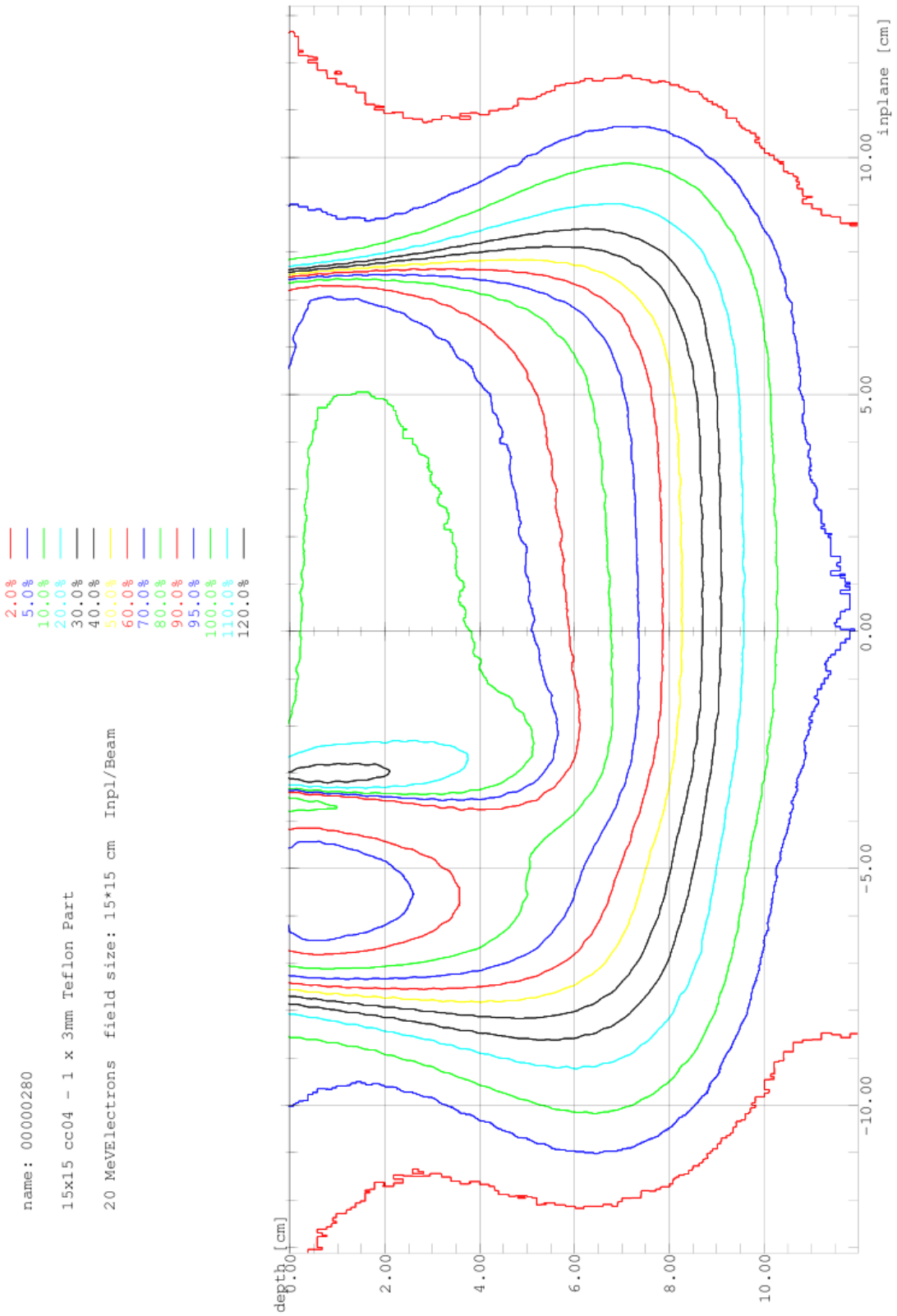

Illustration 82: Partial Bolus 20MeV 1x3mm Teflon for Table 30

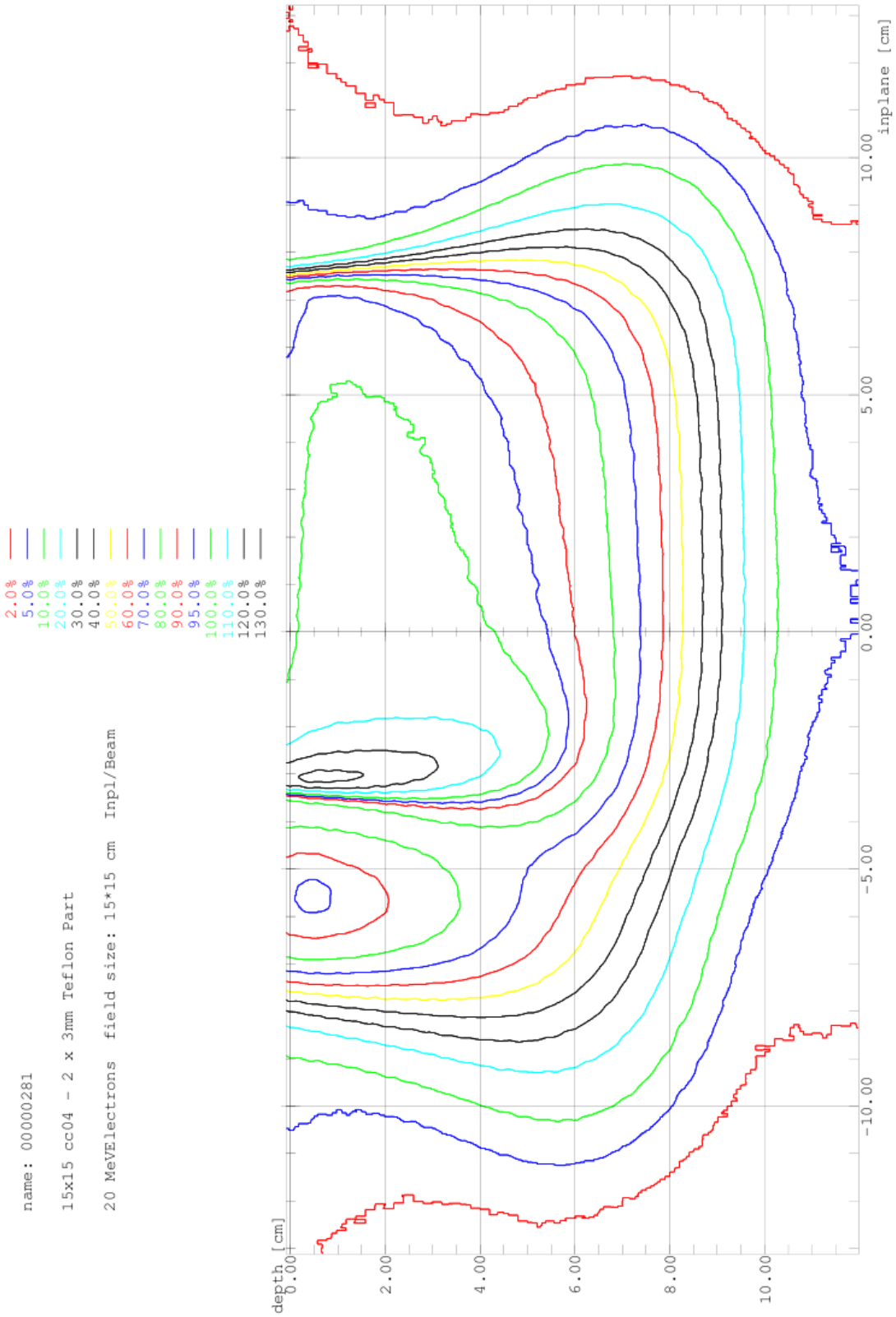

Illustration 83: Partial Bolus 20MeV 2x3mm Teflon for Table 30

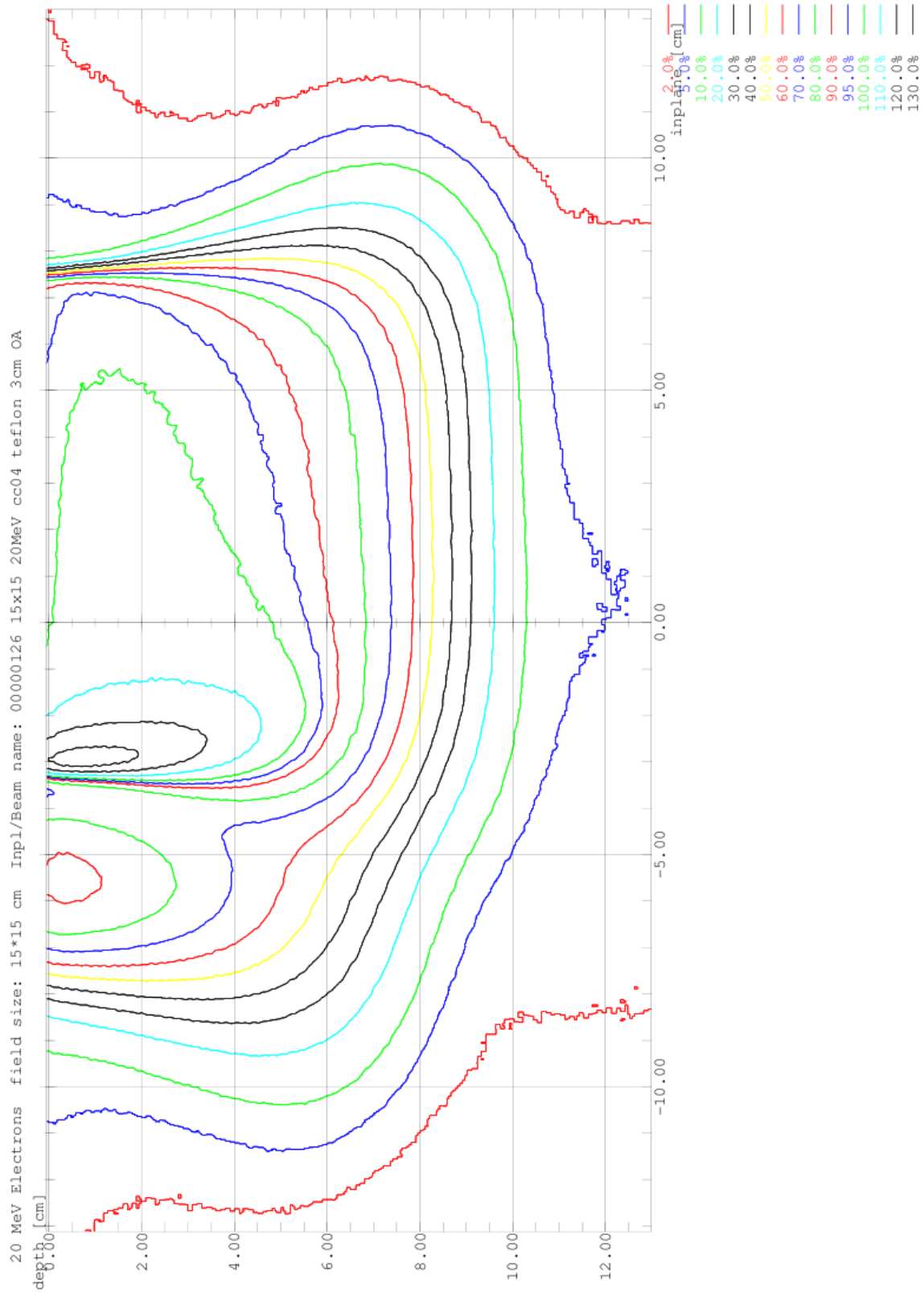

Illustration 84: Partial Bolus 20MeV 2x5mm Teflon for Table 30

A.3.2.3 Bolus on Applicator PARTIAL BOLUS – ALUMINIUM 9 & 20MeV

- **Illustration 85: Partial Bolus Aluminium Depth Ionisation - Central Axis – 9MeV from Table 33**
- **Illustration 86: Partial Bolus Aluminium Depth Ionisation - +3.5cm inplane – 9MeV from Table 33**

- **Illustration 87: Partial Bolus Aluminium Depth Ionisation - Central Axis – 20MeV from Table 34**
- **Illustration 88: Partial Bolus Aluminium Depth Ionisation - +3.5cm inplane – 20MeV from Table 34**

- **Illustration 89: Partial Bolus 9MeV 2.7mm Aluminium for Table 35**
- **Illustration 90: Partial Bolus 9MeV 5.1mm Aluminium for Table 35**
- **Illustration 91: Partial Bolus 20MeV 2.7mm Aluminium for Table 35**
- **Illustration 92: Partial Bolus 20MeV 5.1mm Aluminium for Table 35**

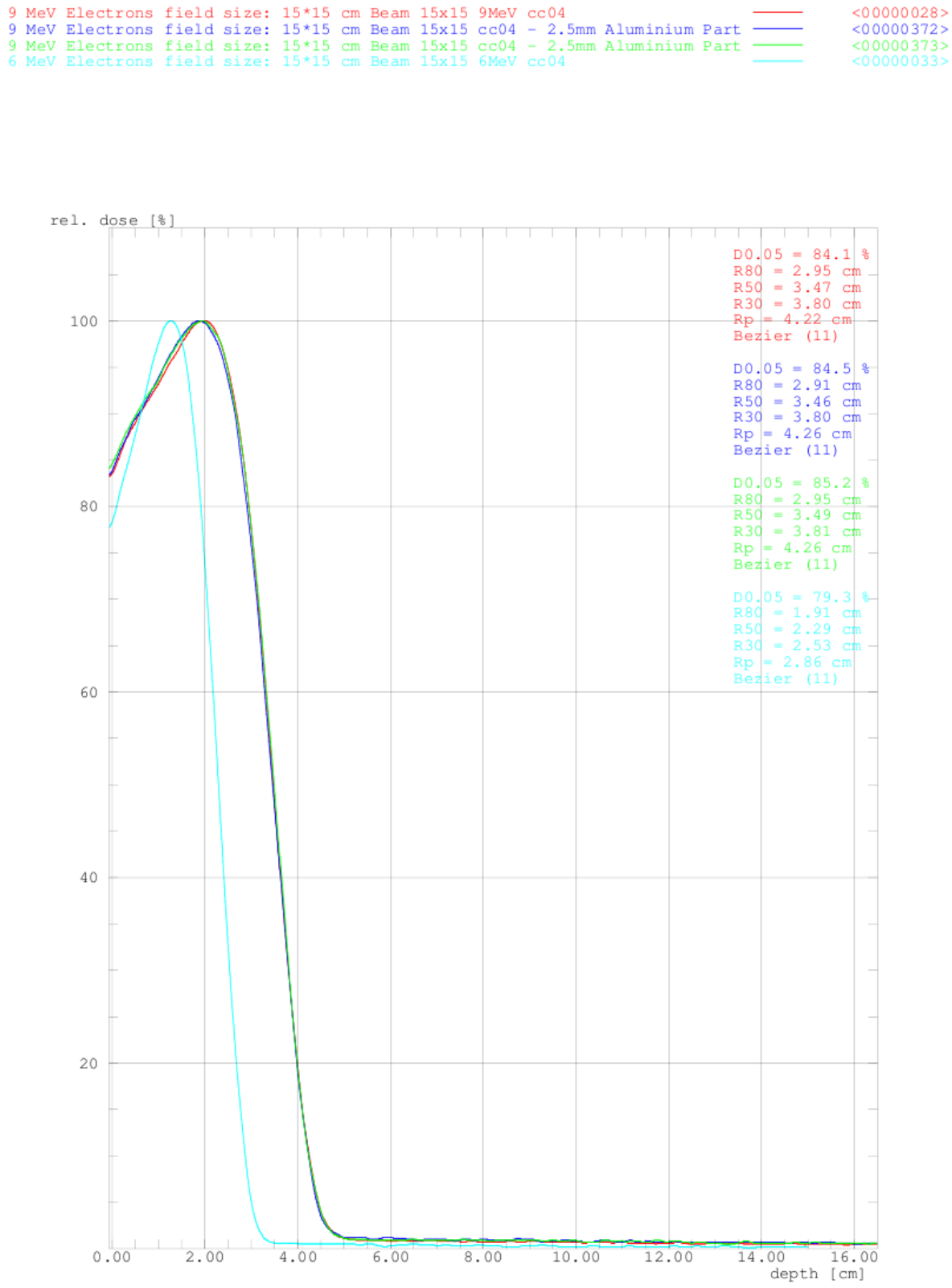

Illustration 85: Partial Bolus Aluminium Depth Ionisation - Central Axis – 9MeV from Table 33

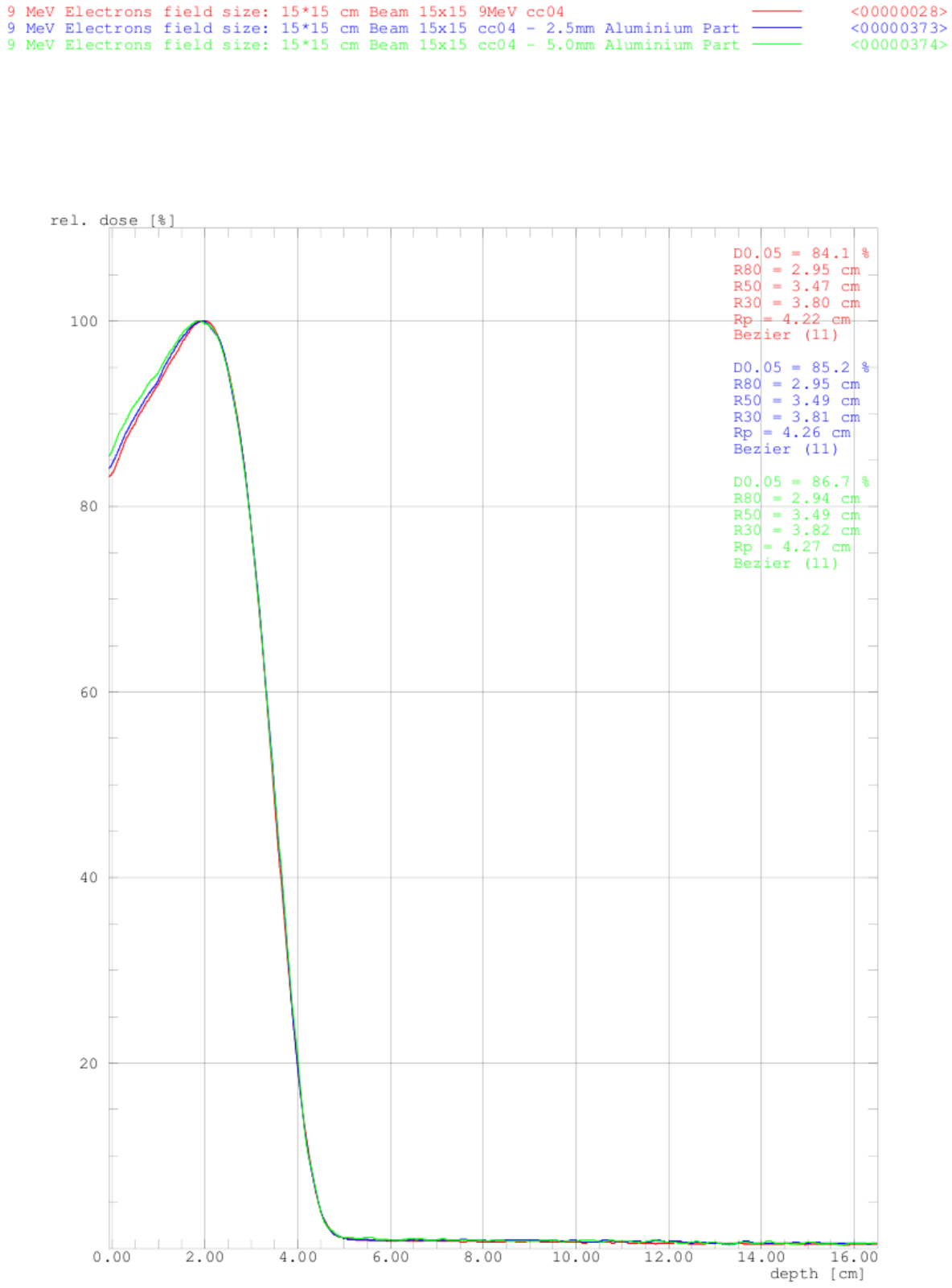

Illustration 86: Partial Bolus Aluminium Depth Ionisation - +3.5cm inplane – 9MeV from Table 33

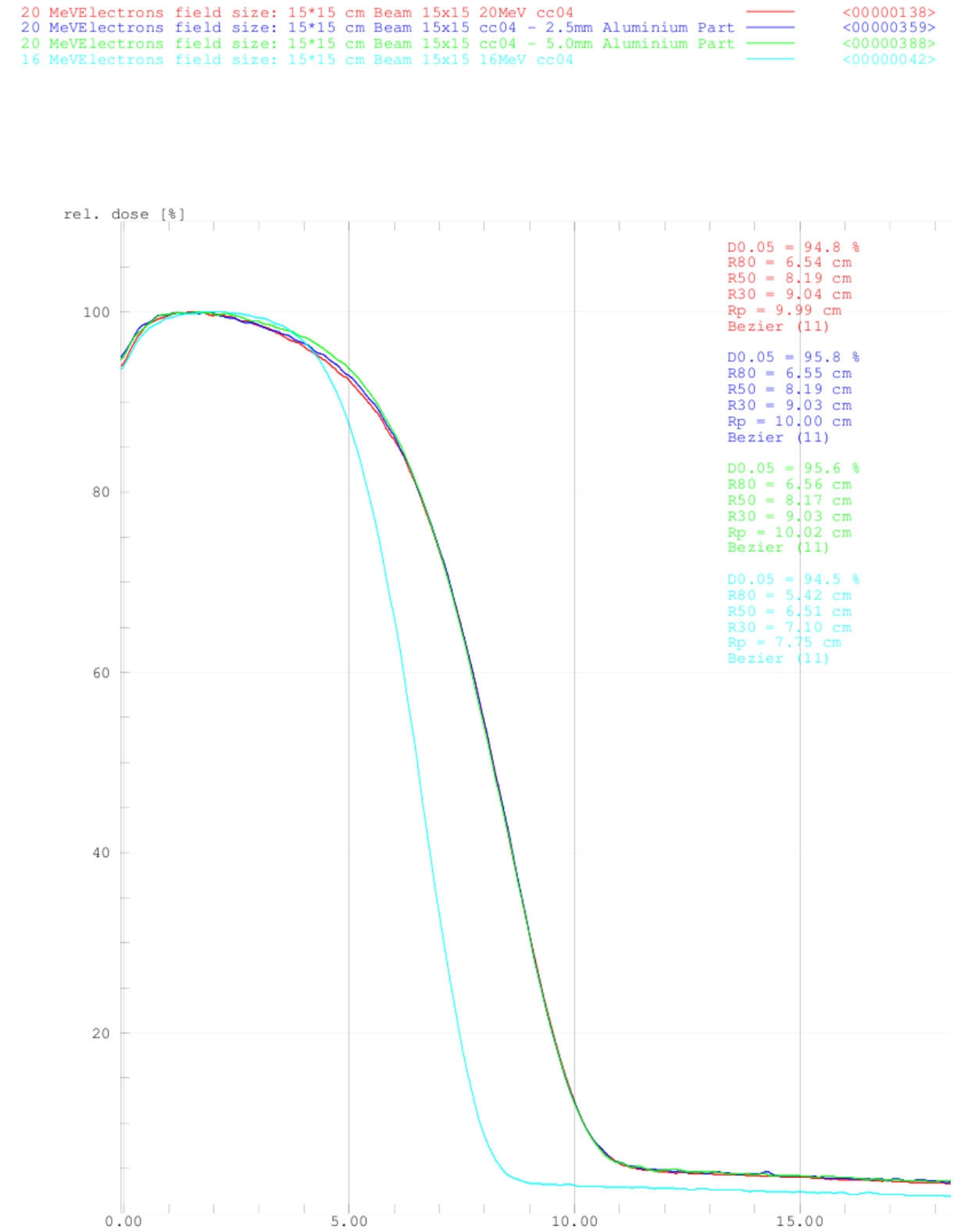

Illustration 87: Partial Bolus Aluminium Depth Ionisation - Central Axis – 20MeV from Table 34

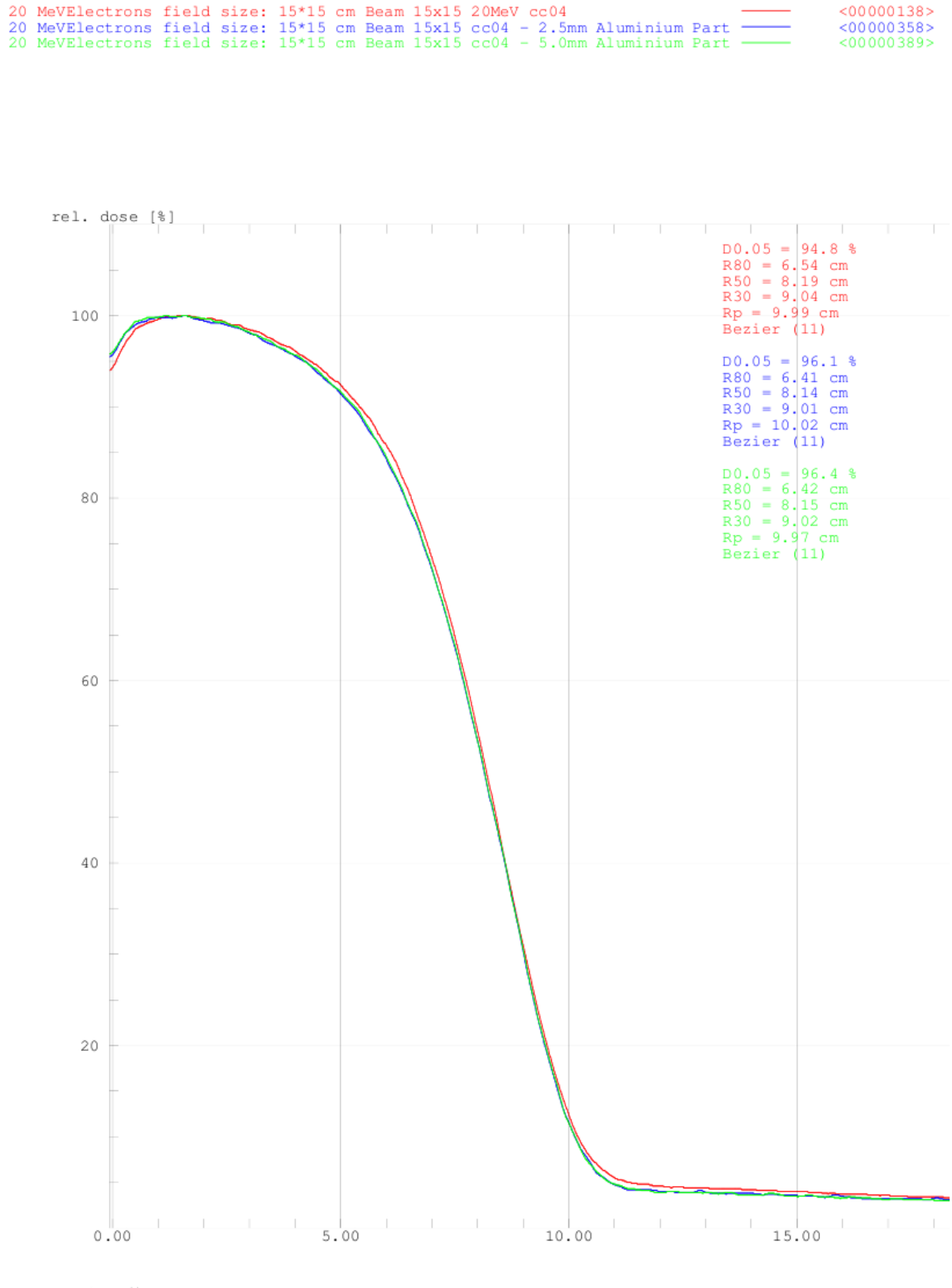

Illustration 88: Partial Bolus Aluminium Depth Ionisation - +3.5cm inplane – 20MeV from Table 34

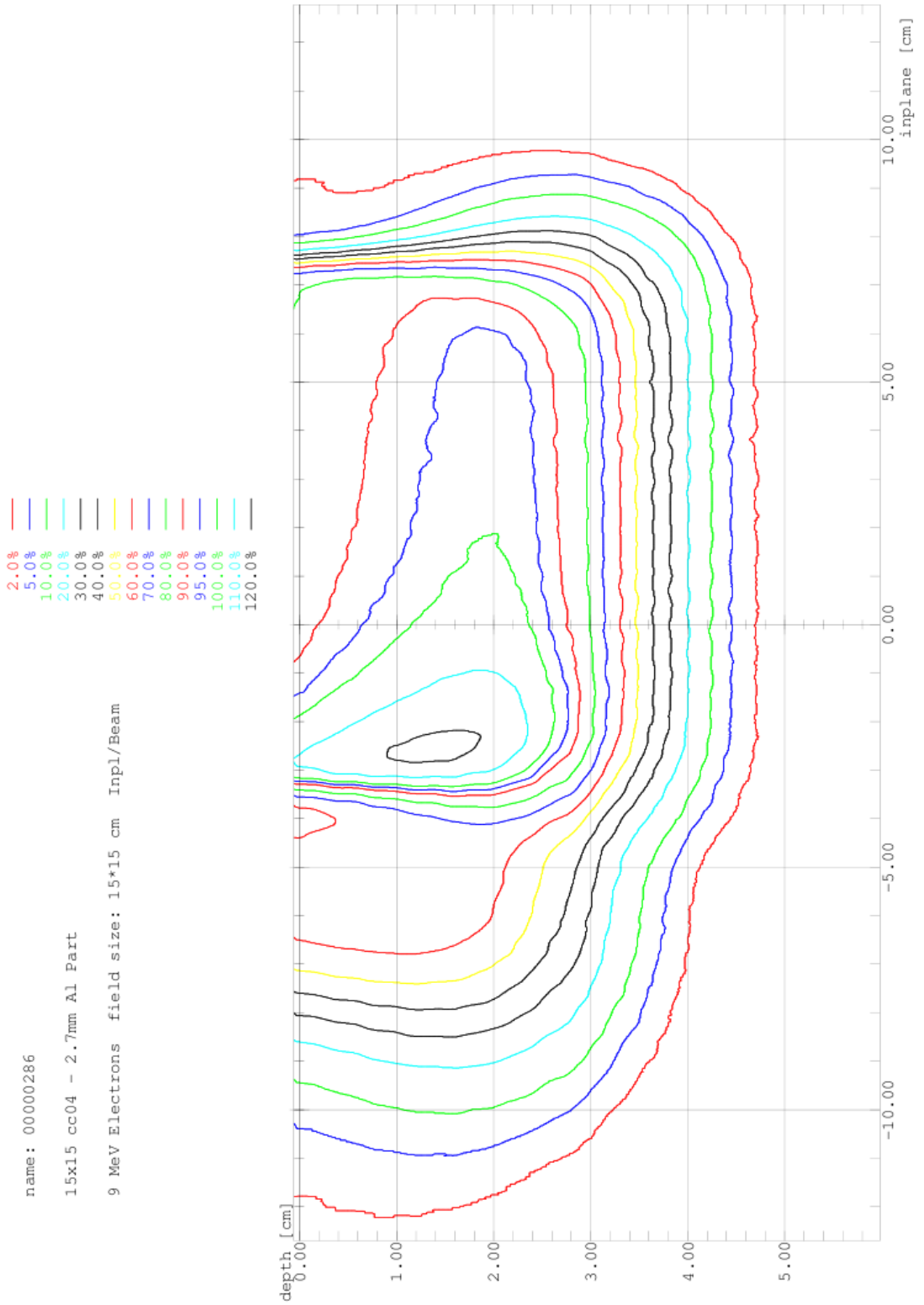

Illustration 89: Partial Bolus 9MeV 2.7mm Aluminium for Table 35

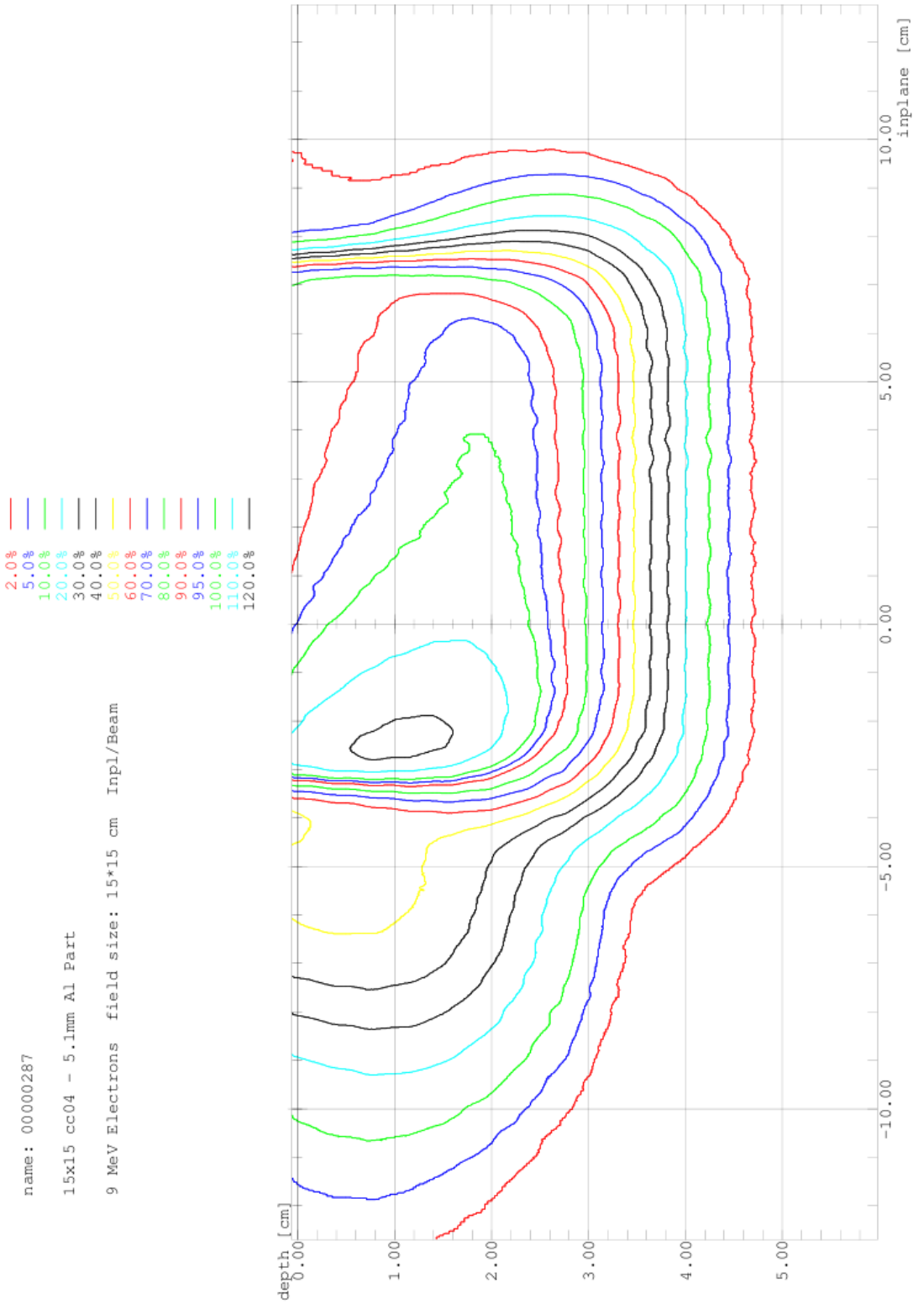

Illustration 90: Partial Bolus 9MeV 5.1mm Aluminium for Table 35

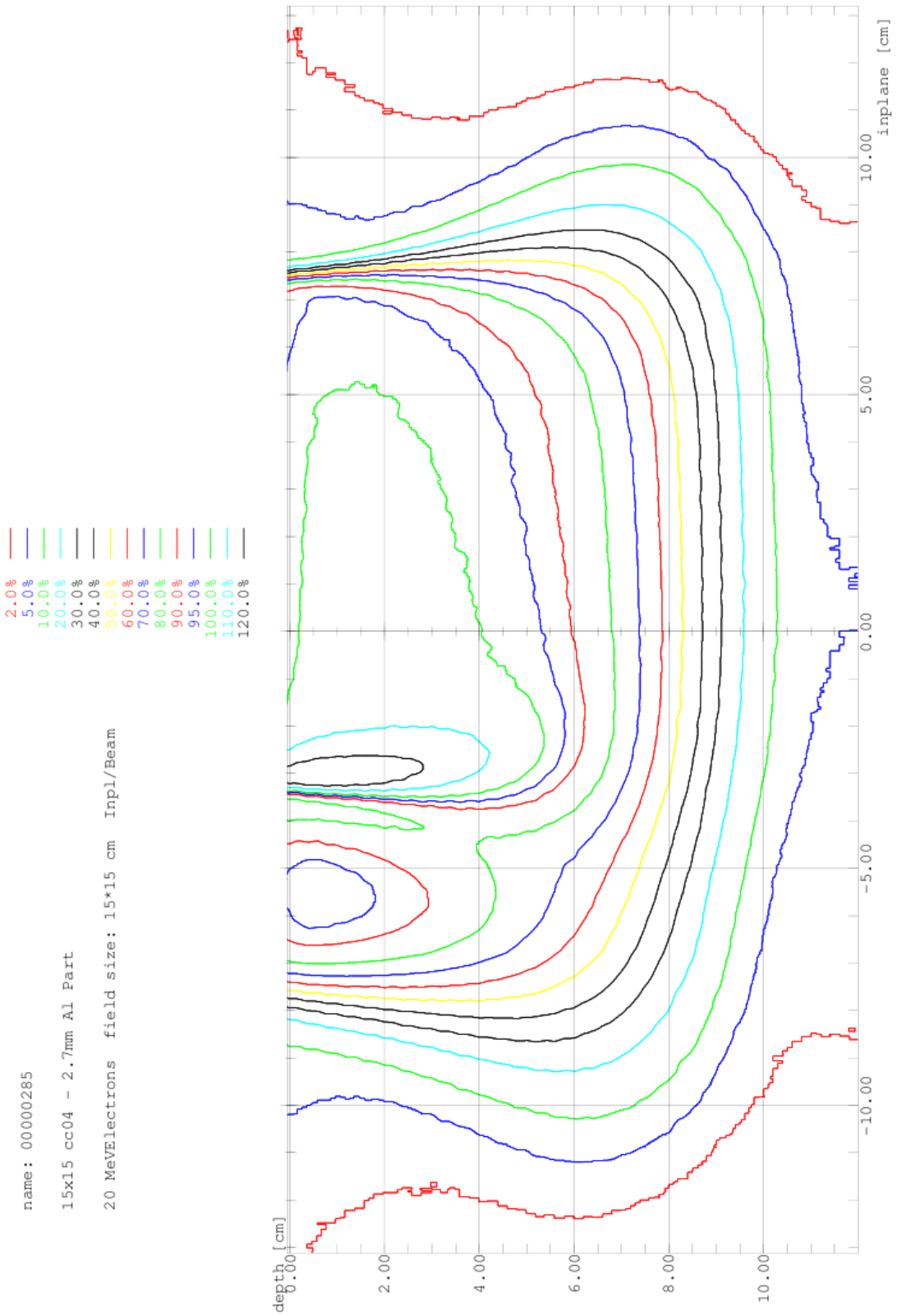

Illustration 91: Partial Bolus 20MeV 2.7mm Aluminium for Table 35

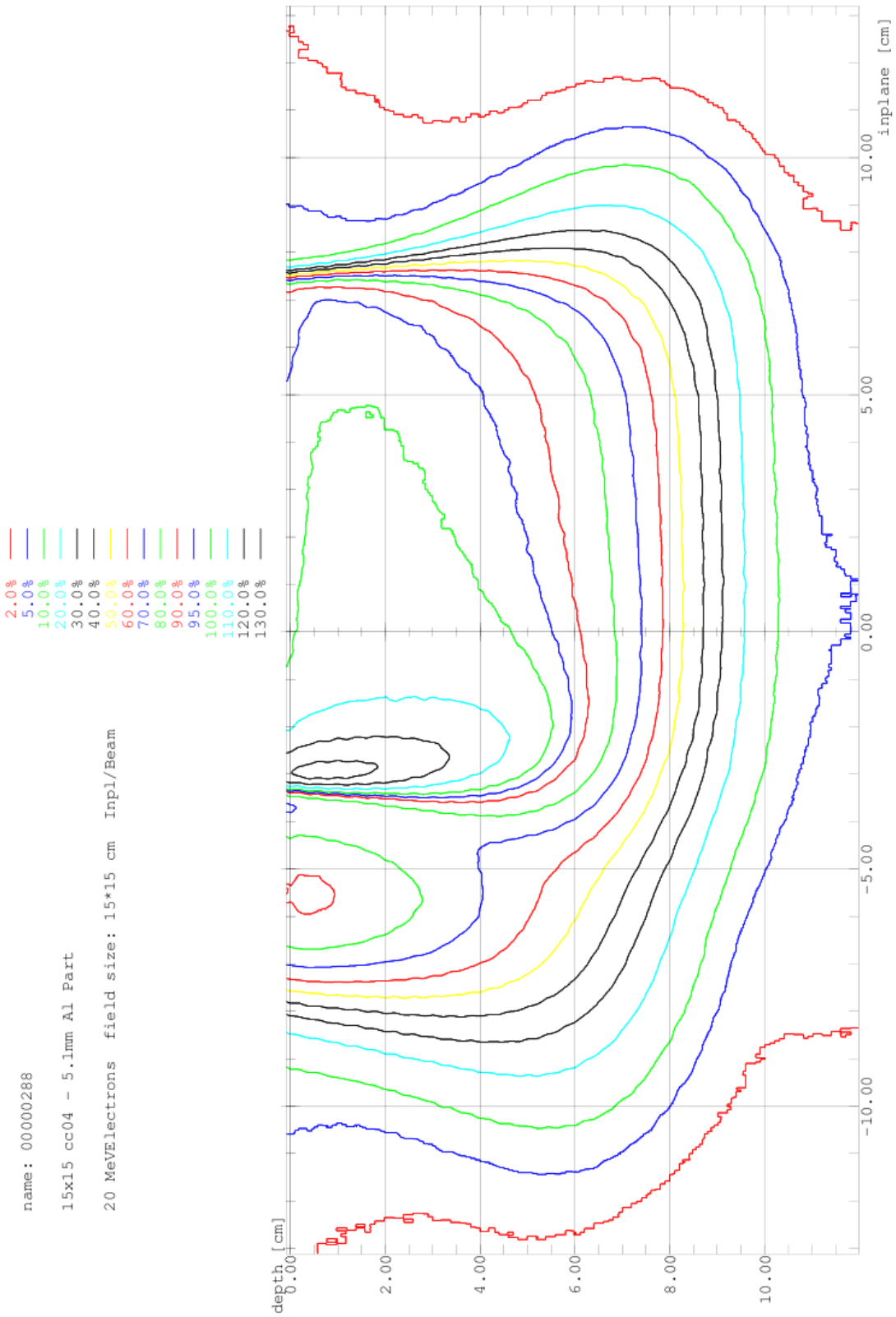

Illustration 92: Partial Bolus 20MeV 5.1mm Aluminium for Table 35

A3.2.2 Bolus on Applicator STRIP BOLUS – TEFLON 9 & 20MeV

- **Illustration 93: Strip Bolus Teflon Depth Ionisation - Open, -4cm, CA,+4cm inplane – 9MeV from Table 38**
- **Illustration 94: Strip Bolus Teflon Depth Ionisation - Open, -4cm, CA,+4cm inplane – 9MeV from Table 39**

- **Illustration 95: Strip Bolus 9MeV 2x5mm Teflon for Table 40**
- **Illustration 96: Strip Bolus 20MeV 2x5mm Teflon for Table 40**

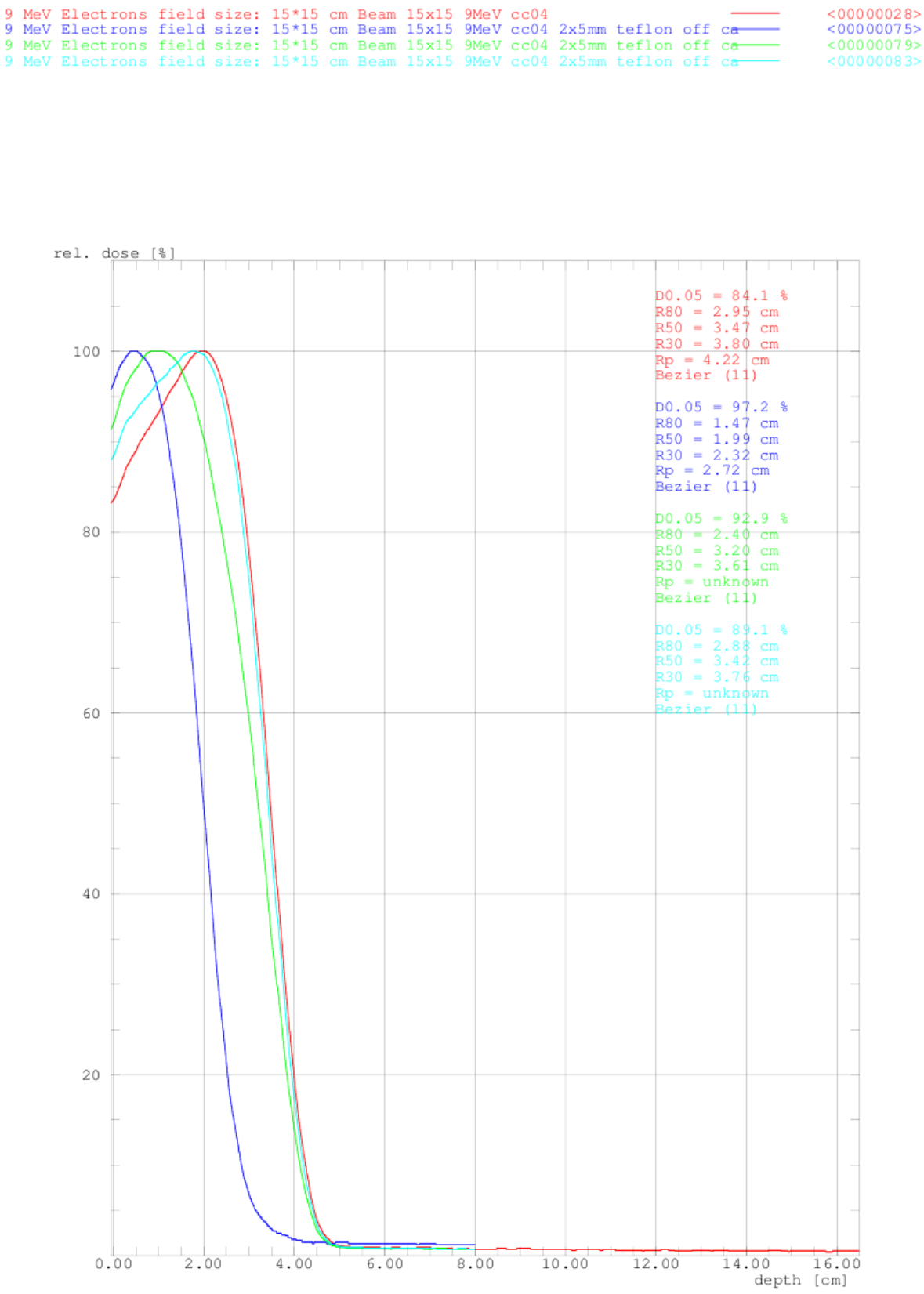

Illustration 93: Strip Bolus Teflon Depth Ionisation - Open, -4cm, CA,+4cm inplane – 9MeV from Table 38

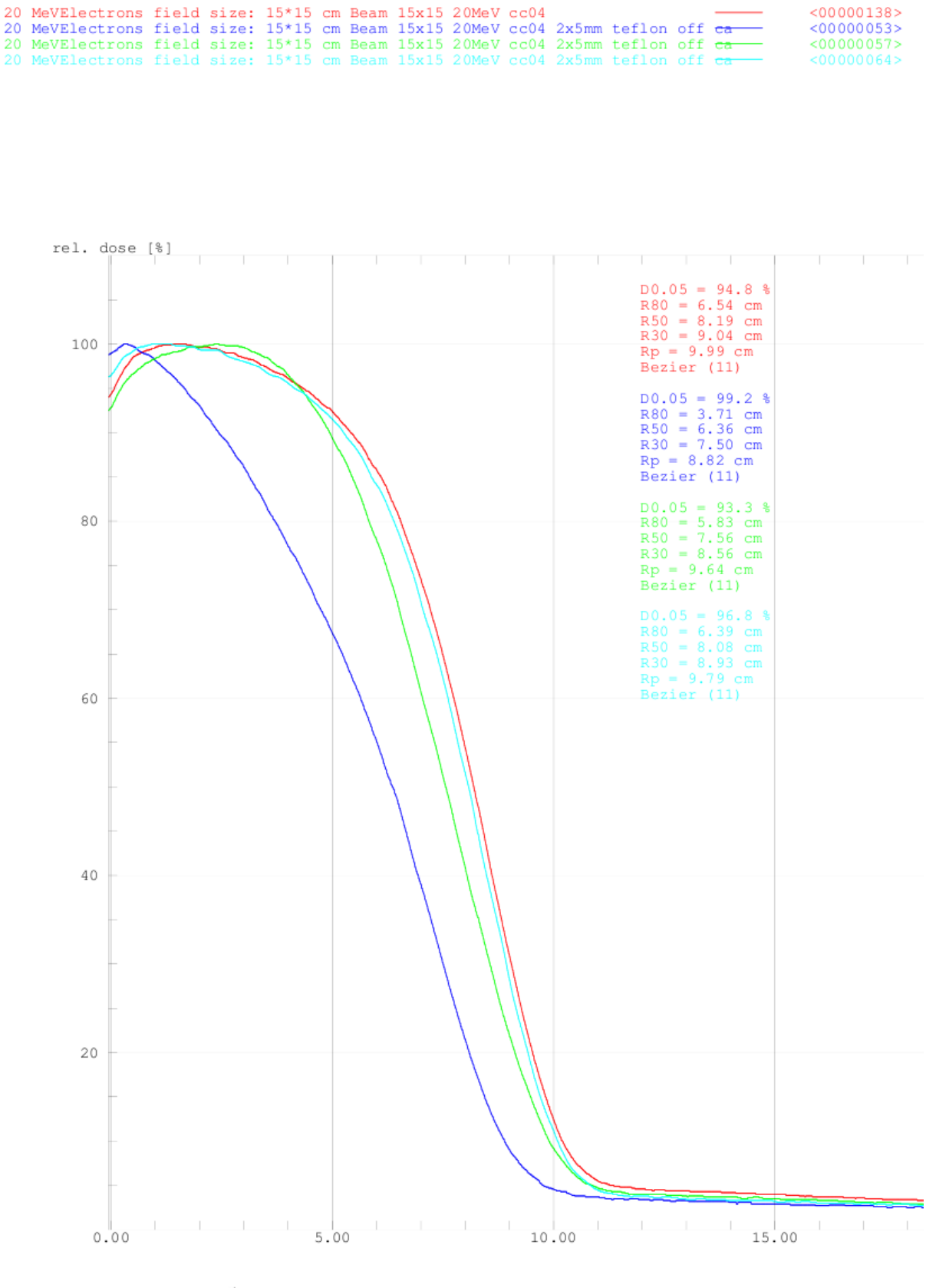

Illustration 94: Strip Bolus Teflon Depth Ionisation - Open, -4cm, CA,+4cm inplane – 9MeV from Table 39

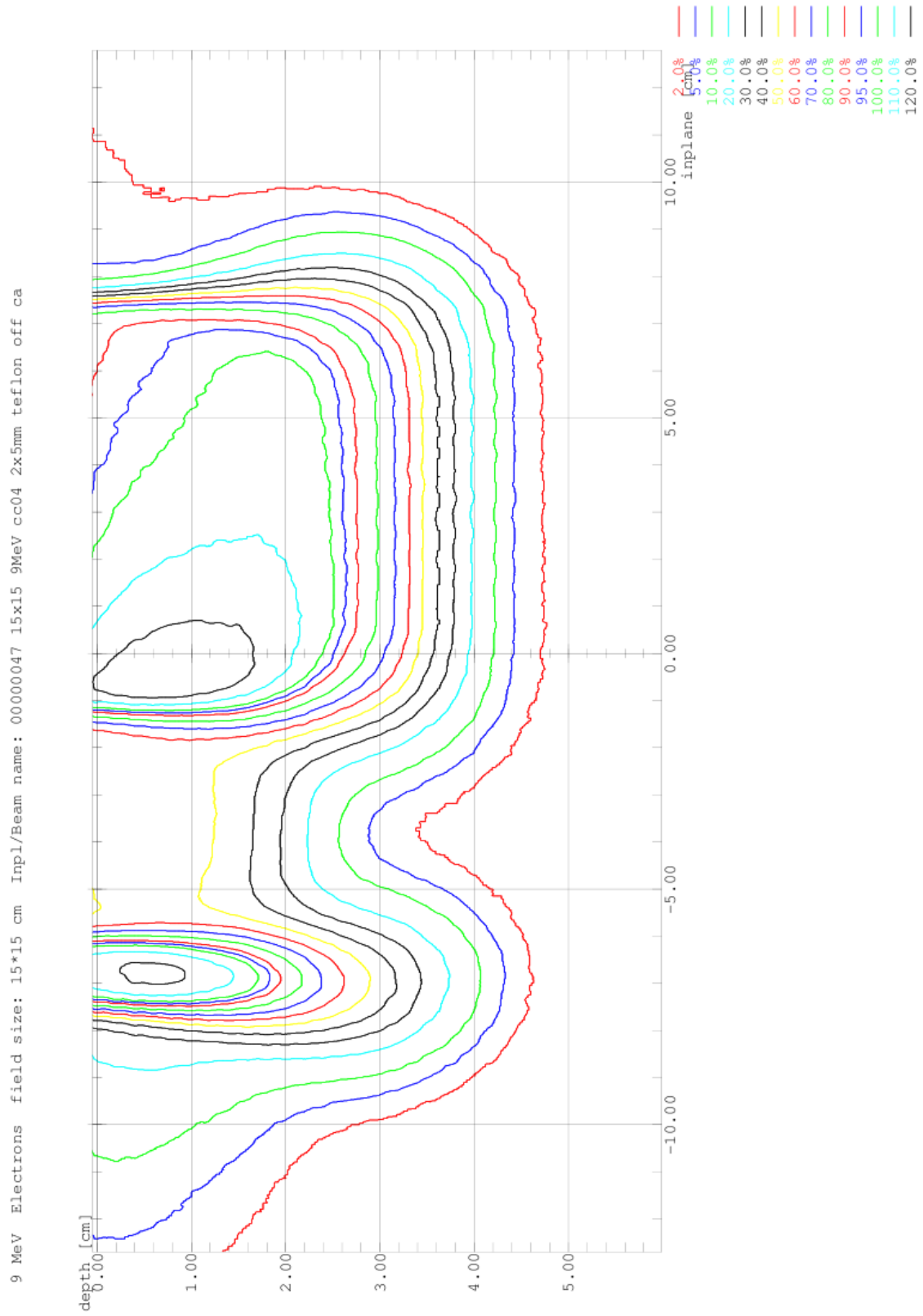

Illustration 95: Strip Bolus 9MeV 2x5mm Teflon for Table 40

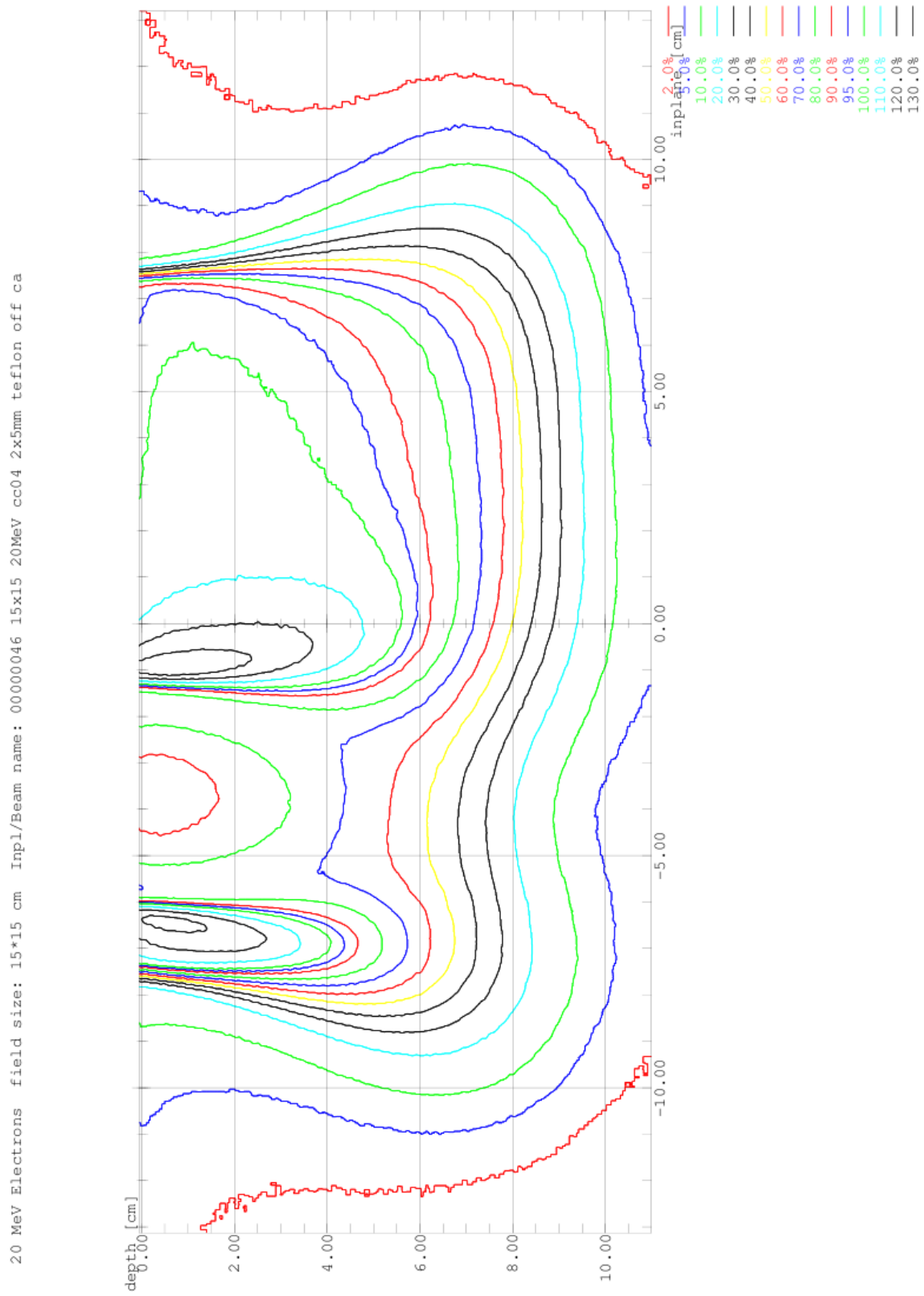

Illustration 96: Strip Bolus 20MeV 2x5mm Teflon for Table 40

A3.4.1 Bolus on Applicator HIGHER Z GRIDS Aluninium & Stainless Steel 9 & 20MeV

- **Illustration 97: Depth Ionisation Scans Higher Z Grids 9MeV.pdf from Table 42**
- **Illustration 98: Depth Ionisation Scans Higher Z Grids 20MeV.pdf from Table 43**

- **Illustration 99: Aluminium Mesh on Applicator 1xsheet 9MeV from Table 44**
- **Illustration 100: Aluminium Shim on Applicator 1xsheet 9MeV from Table 44**
- **Illustration 101: Aluminium Shim on Applicator 2xsheet 9MeV from Table 44**
- **Illustration 102: Aluminium Mesh on Applicator 1xsheet 20MeV from Table 44**
- **Illustration 103: Aluminium Sheet on Applicator 1xsheet 20MeV from Table 44**
- **Illustration 104: Aluminium Sheet on Applicator 2xsheet 20MeV from Table 44**

- **Illustration 105: Stainless Steel Mesh on Applicator Depth Ionisation 9MeV from Table 46**
- **Illustration 106: Stainless Steel Mesh on Applicator Depth Ionisation 20MeV from Table 47**

- **Illustration 107: Stainless Steel Mesh on Applicator 1xsheet 9MeV for Table 48**
- **Illustration 108: Stainless Steel Mesh on Applicator 2xsheet 9MeV for Table 48**
- **Illustration 109: Stainless Steel Mesh on Applicator 3xsheet 9MeV for Table 48**
- **Illustration 110: Stainless Steel Mesh on Applicator 4xsheet 9MeV for Table 48**
- **Illustration 111: Stainless Steel Mesh on Applicator 1xsheet 20MeV for Table 48**
- **Illustration 112: Stainless Steel Mesh on Applicator 2xsheet 20MeV for Table 48**
- **Illustration 113: Stainless Steel Mesh on Applicator 3xsheet 20MeV for Table 48**
- **Illustration 114: Stainless Steel Mesh on Applicator 4xsheet 20MeV for Table 48**

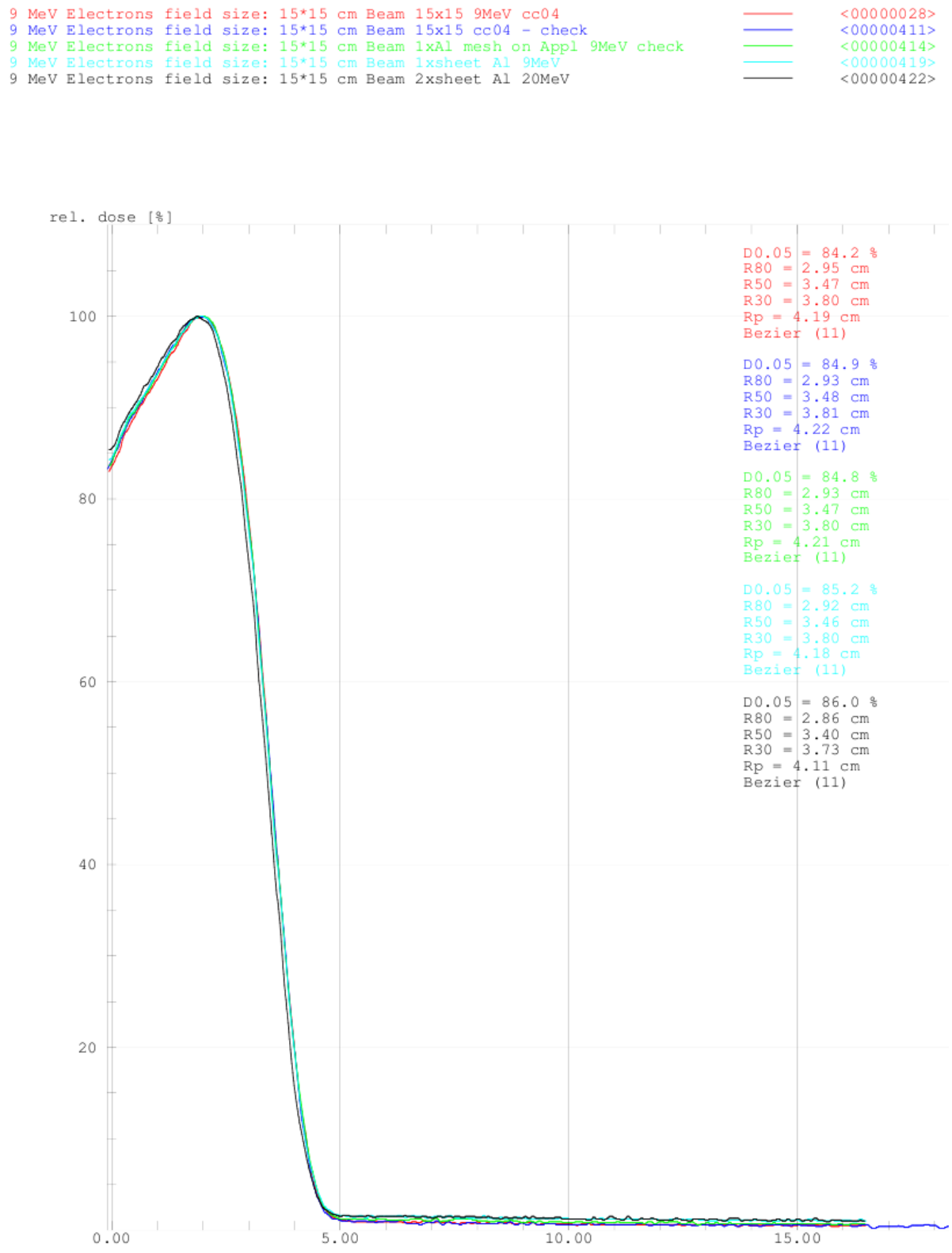

Illustration 97: Depth Ionisation Scans Higher Z Grids 9MeV.pdf from Table 42

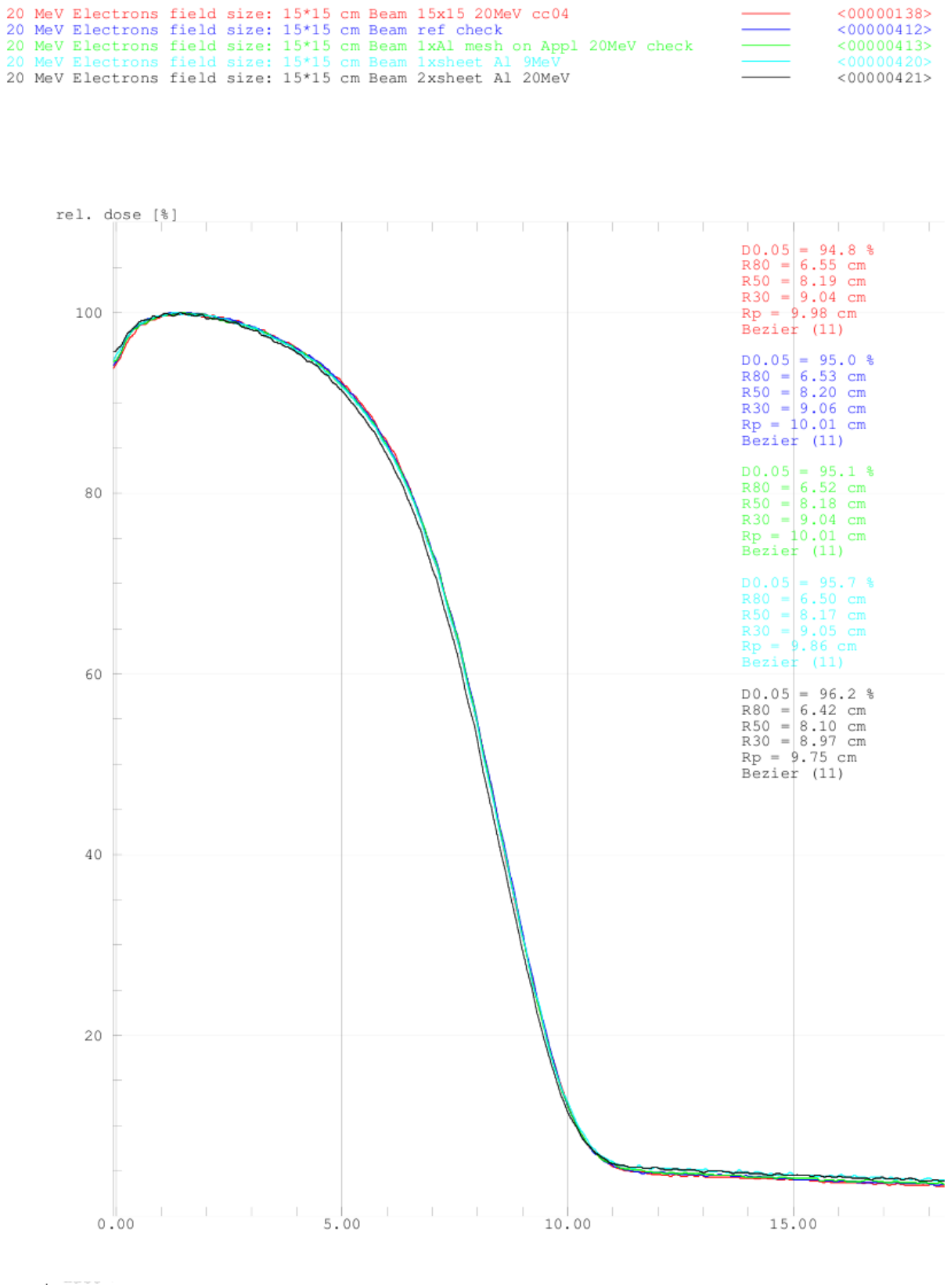

Illustration 98: Depth Ionisation Scans Higher Z Grids 20MeV.pdf from Table 43

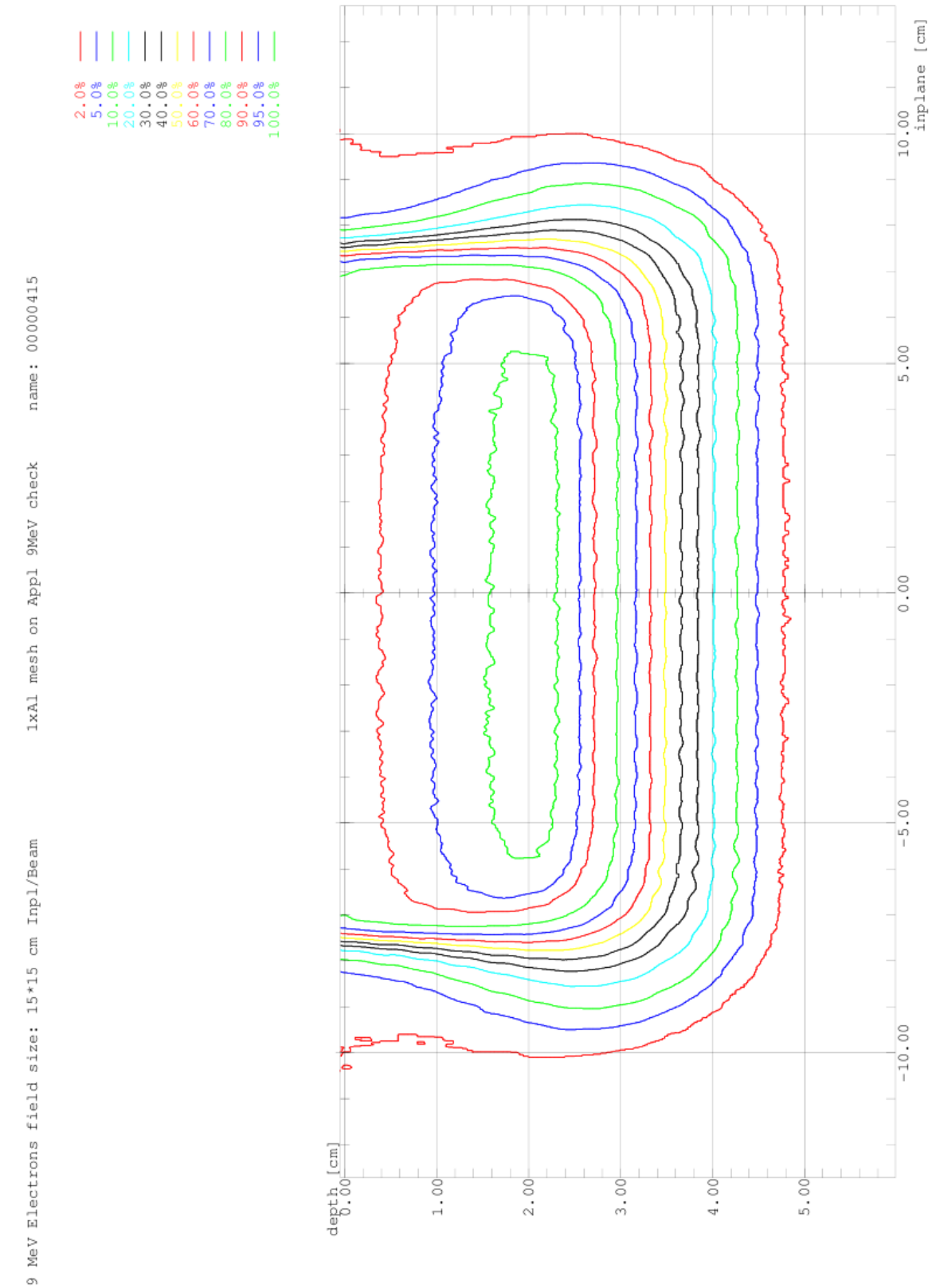

Illustration 99: Aluminium Mesh on Applicator 1xsheet 9MeV from Table 44

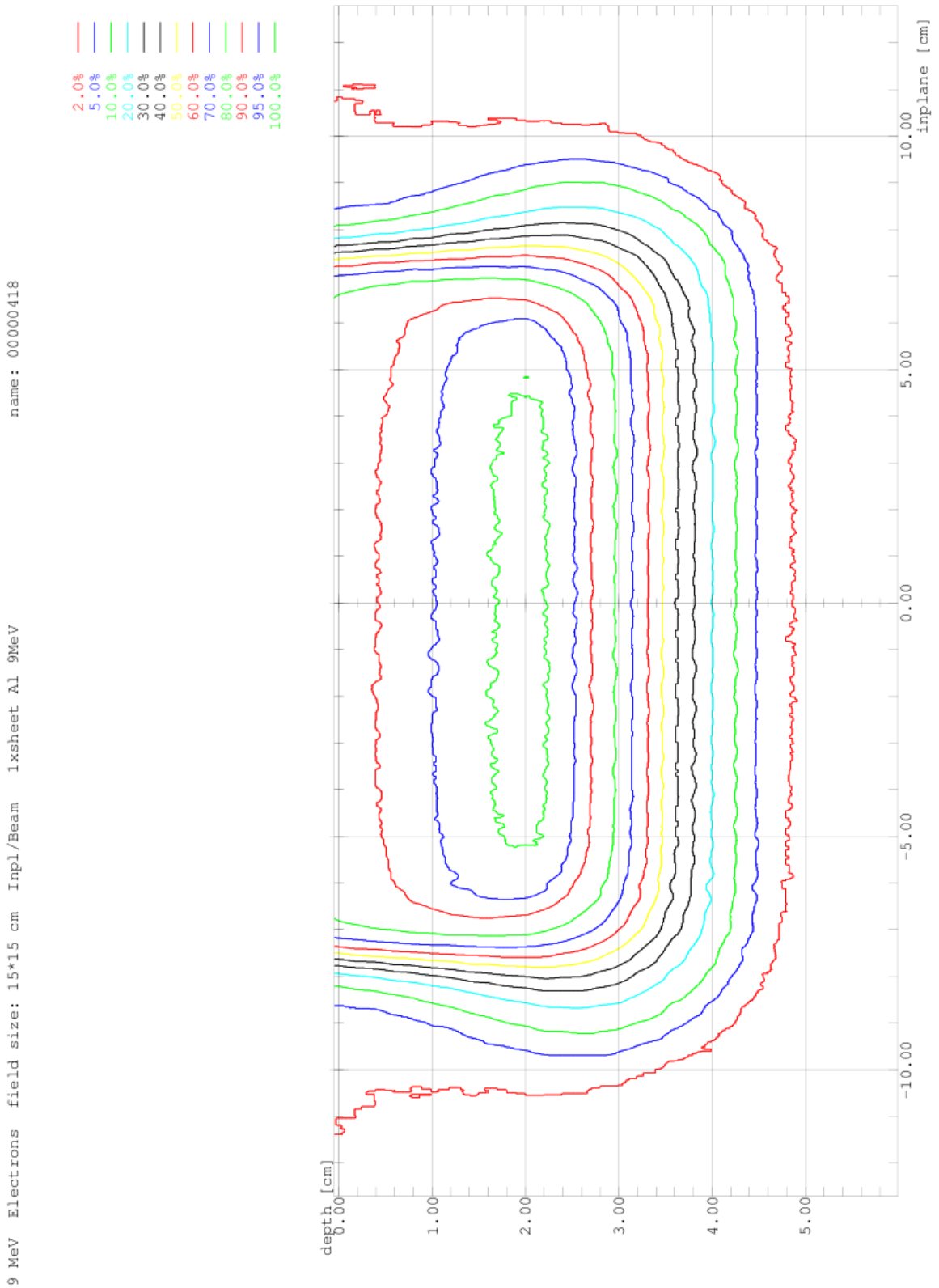

Illustration 100: Aluminium Shim on Applicator 1xsheet 9MeV from Table 44

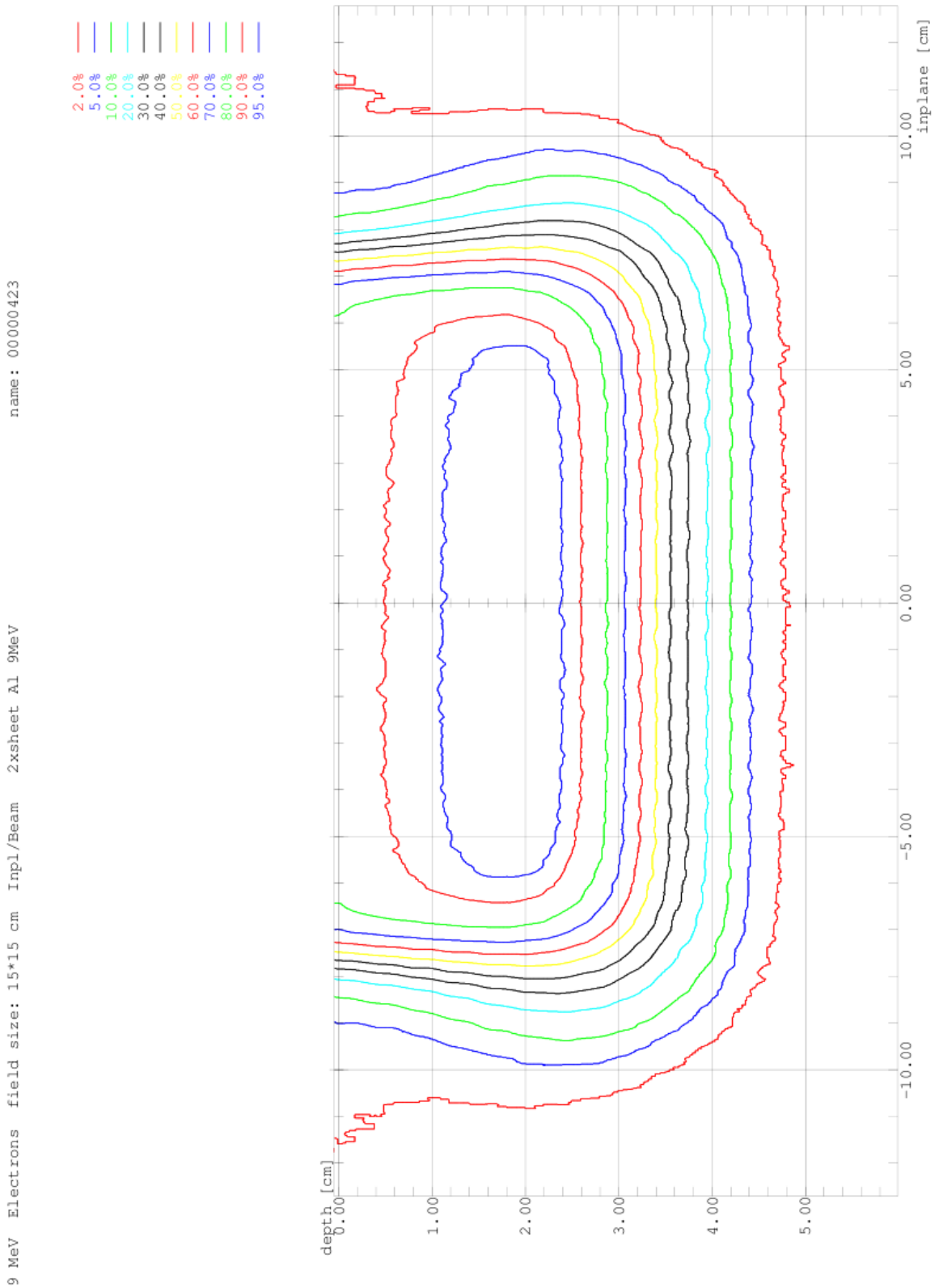

Illustration 101: Aluminium Shim on Applicator 2xsheet 9MeV from Table 44

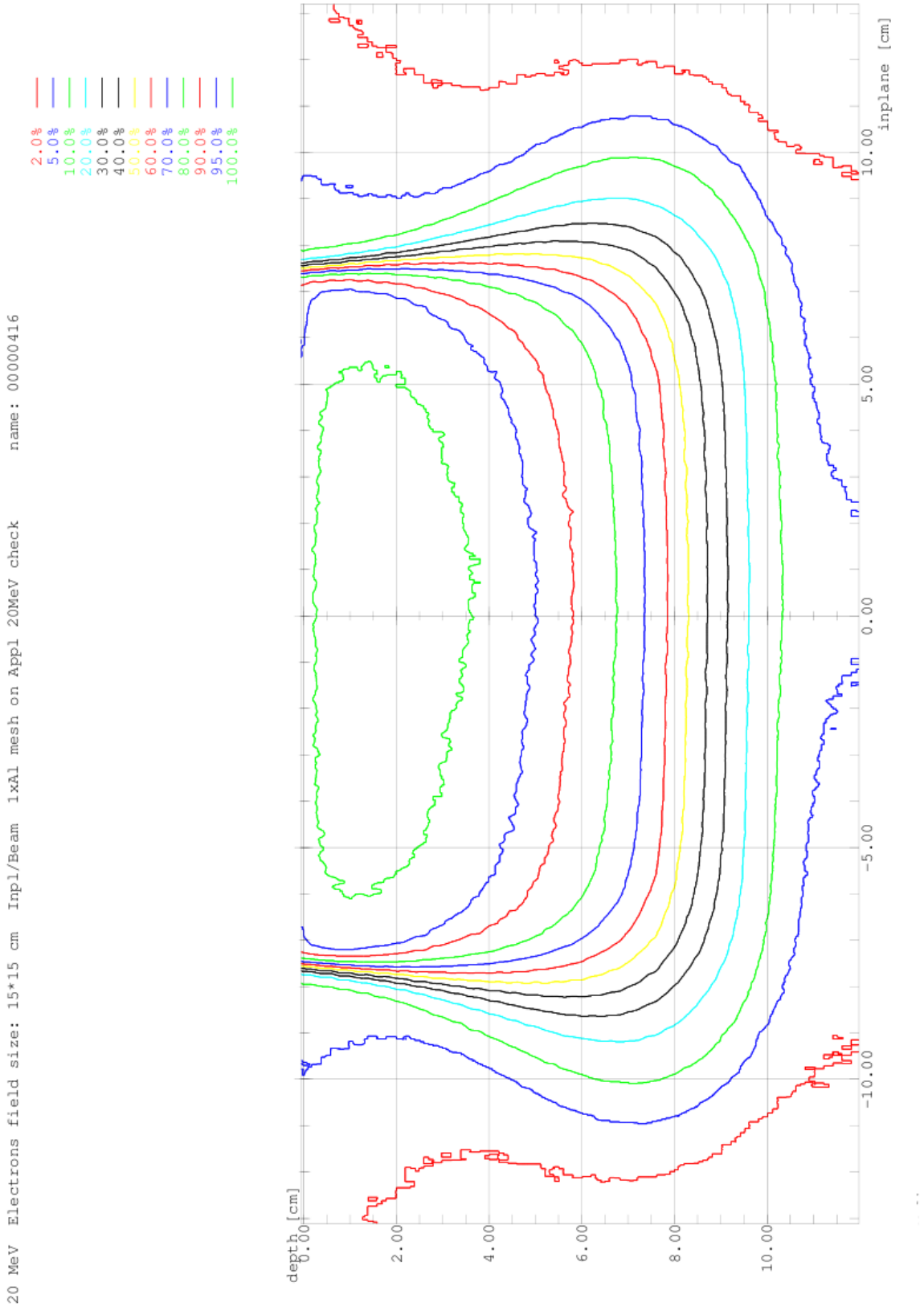

Illustration 102: Aluminium Mesh on Applicator 1xsheet 20MeV from Table 44

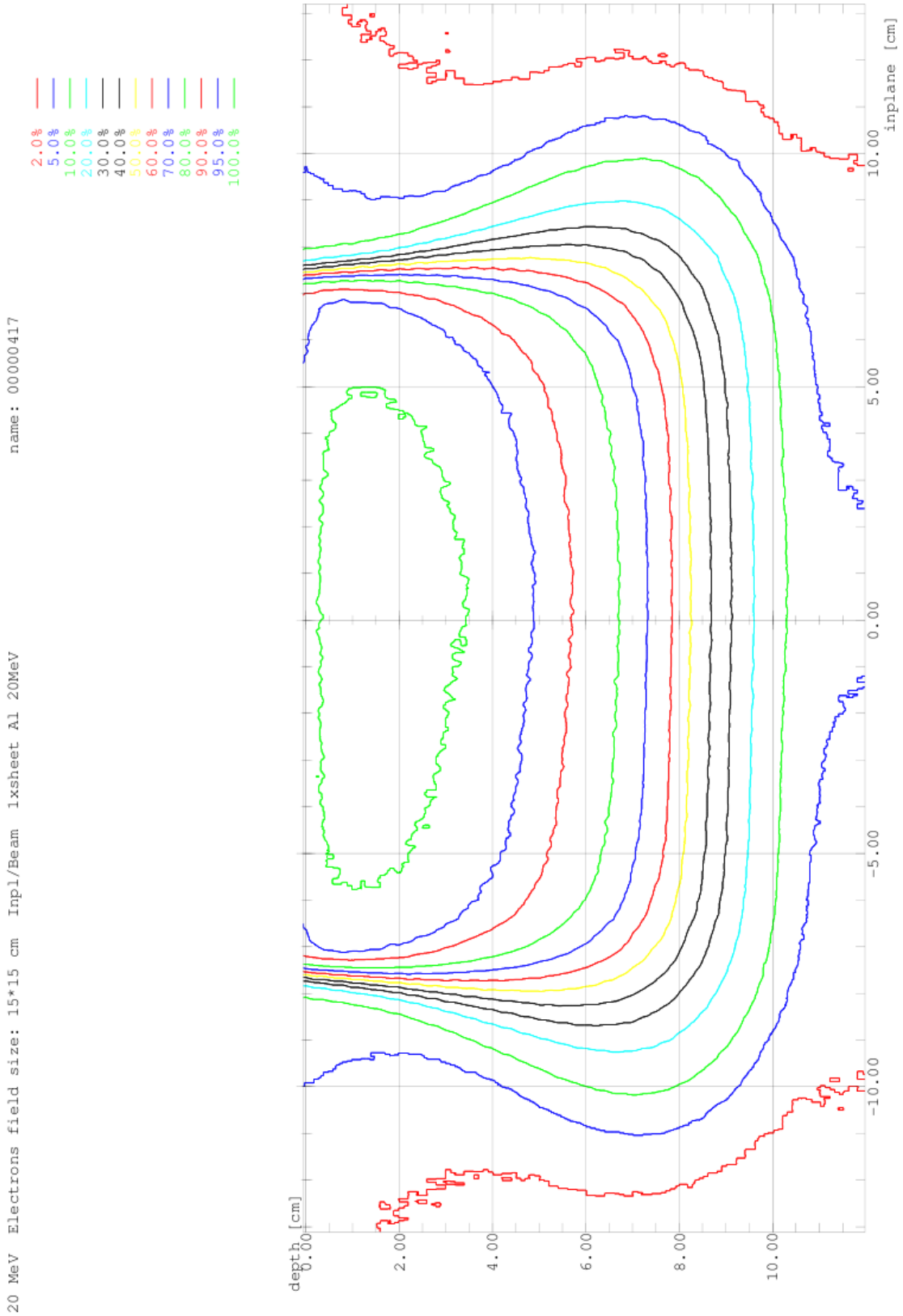

Illustration 103: Aluminium Sheet on Applicator 1xsheet 20MeV from Table 44

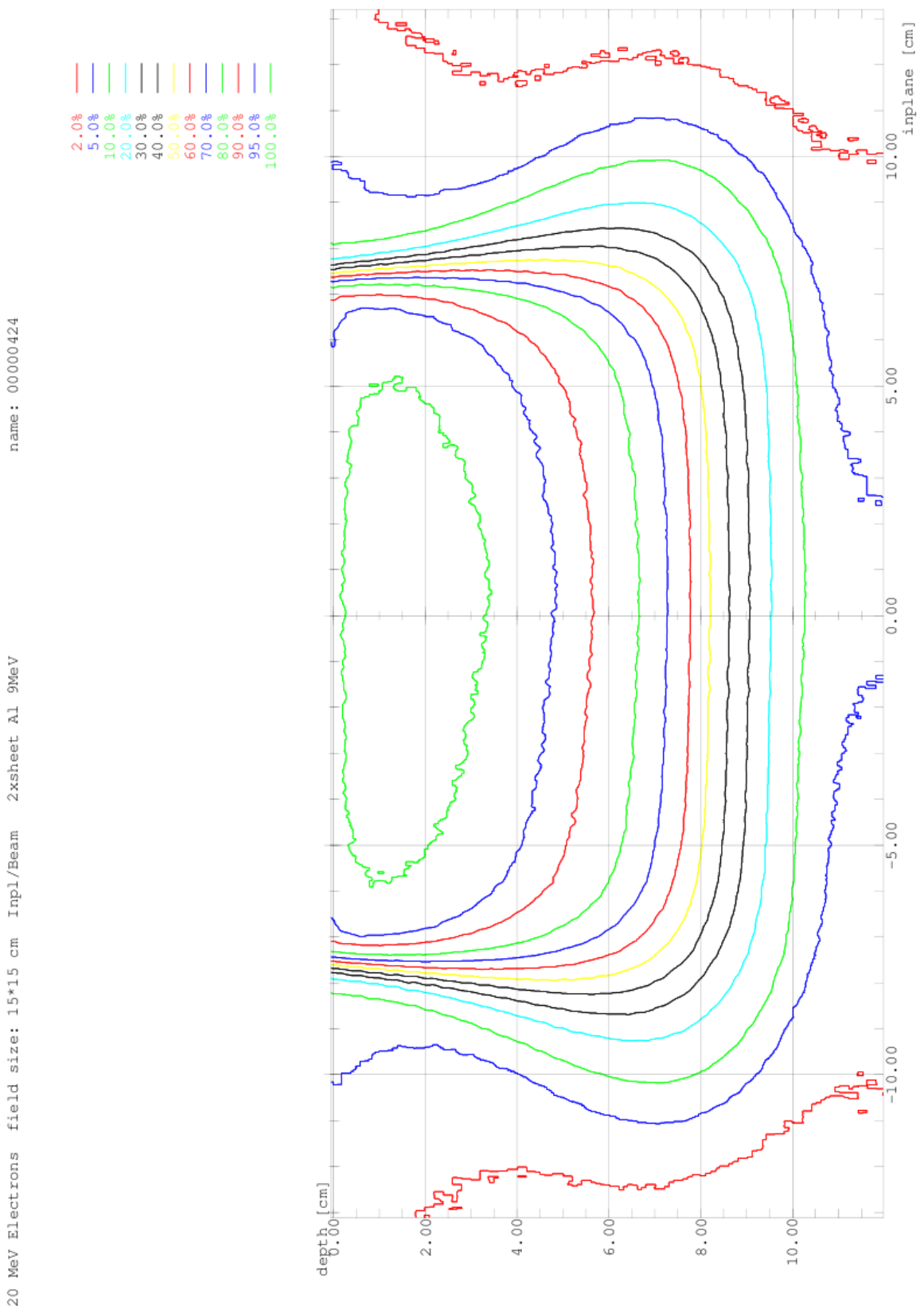

Illustration 104: Aluminium Sheet on Applicator 2xsheet 20MeV from Table 44

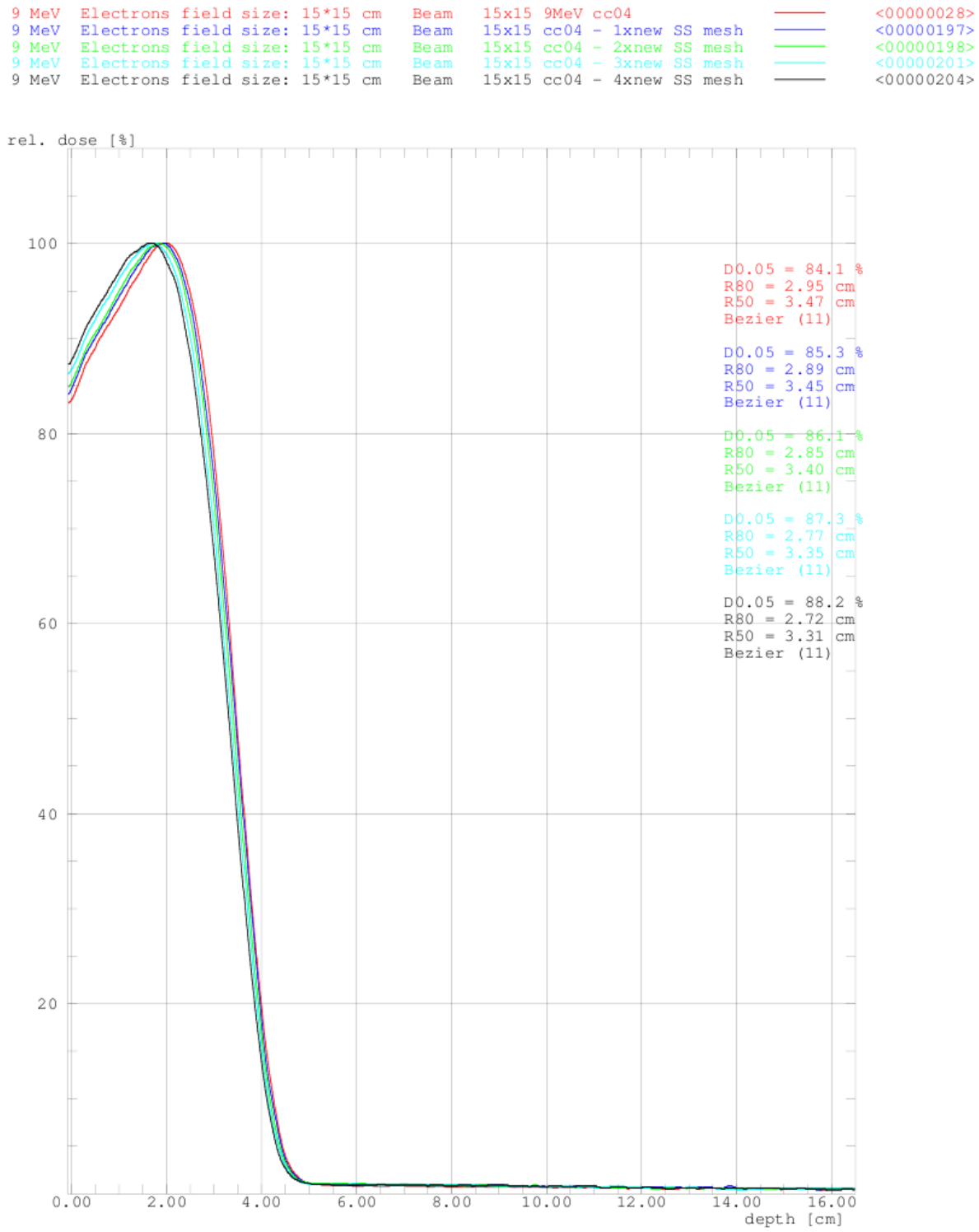

Illustration 105: Stainless Steel Mesh on Applicator Depth Ionisation 9MeV from Table 46

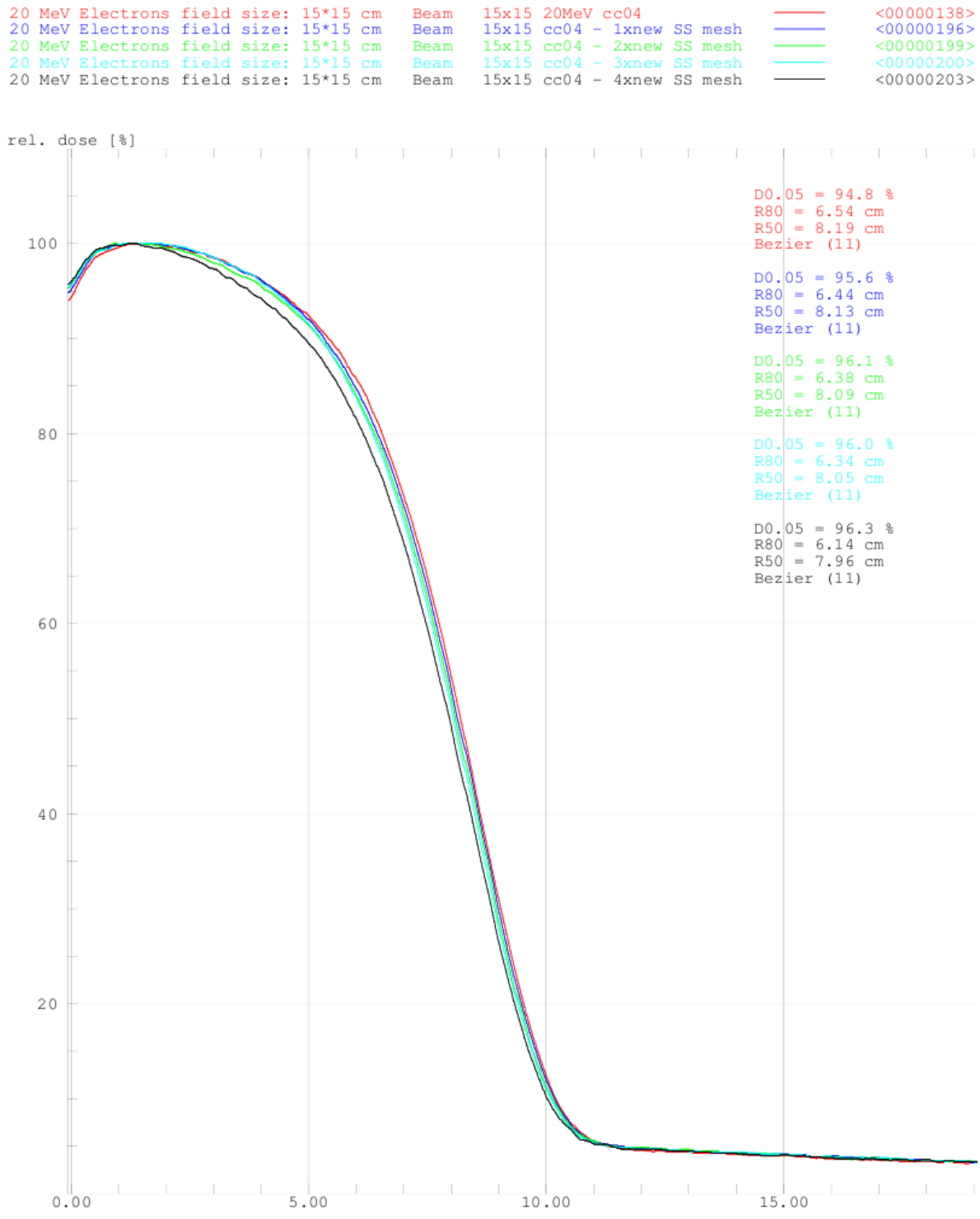

Illustration 106: Stainless Steel Mesh on Applicator Depth Ionisation 20MeV from Table 47

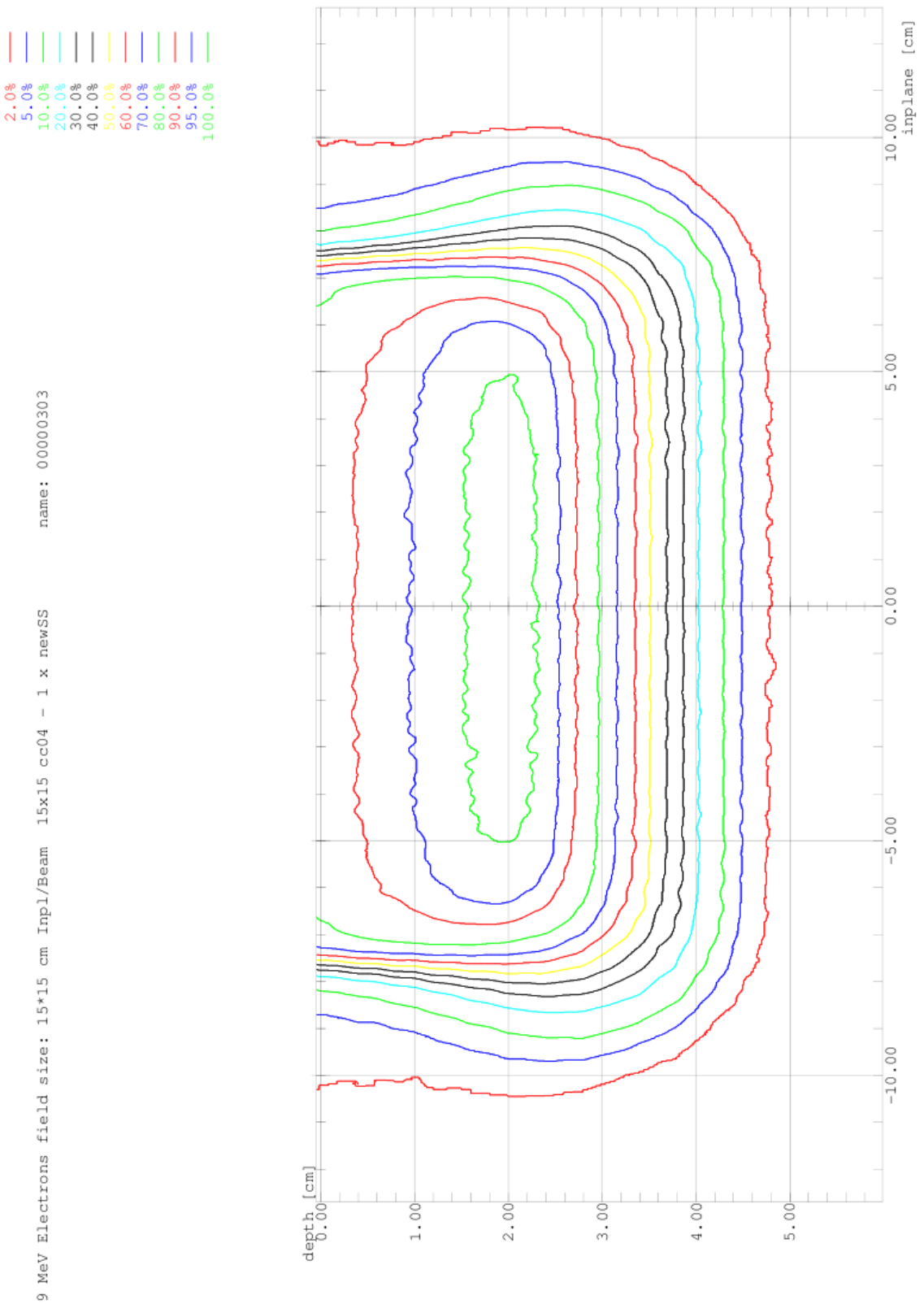

Illustration 107: Stainless Steel Mesh on Applicator 1xsheet 9MeV for Table 48

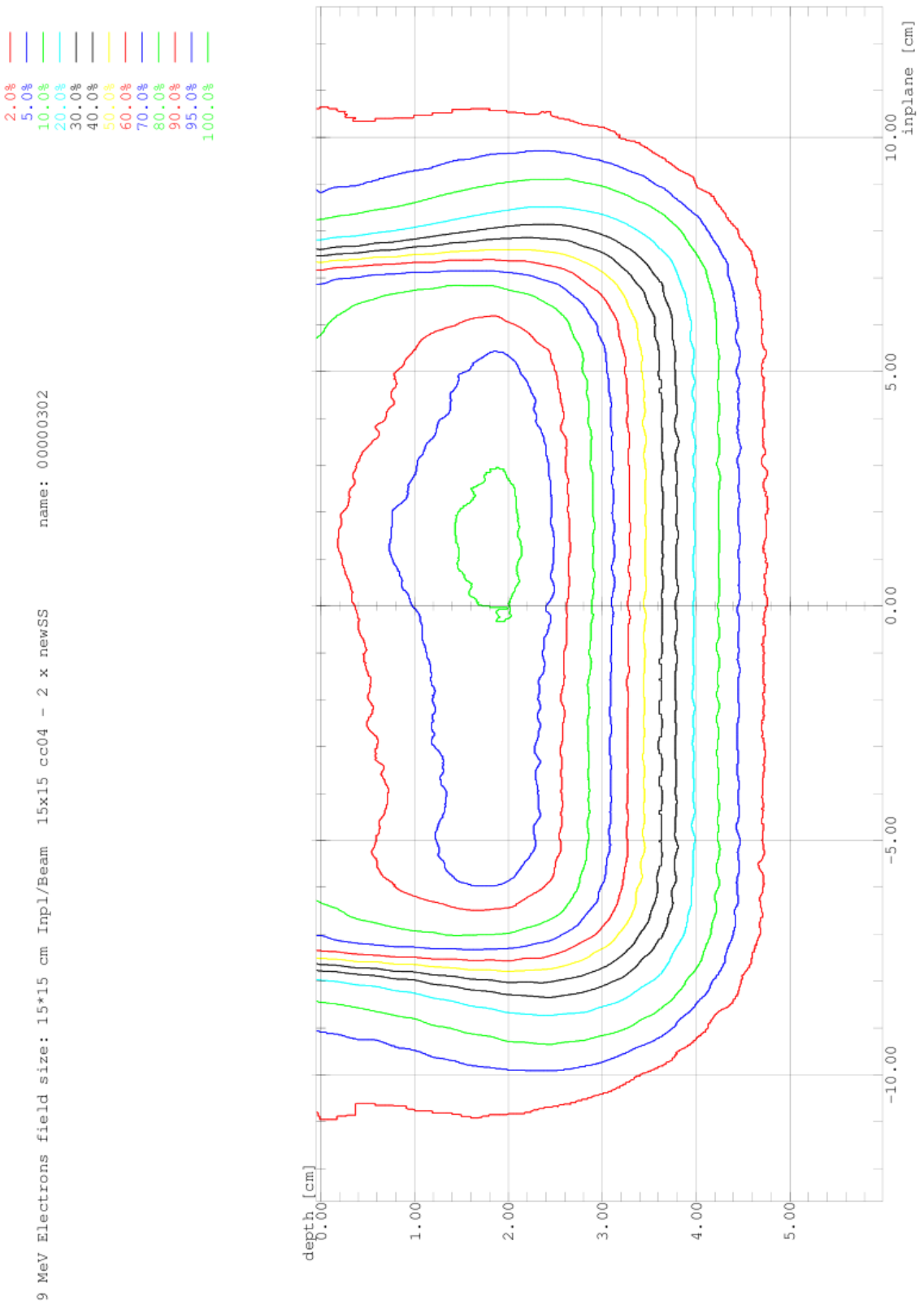

Illustration 108: Stainless Steel Mesh on Applicator 2xsheet 9MeV for Table 48

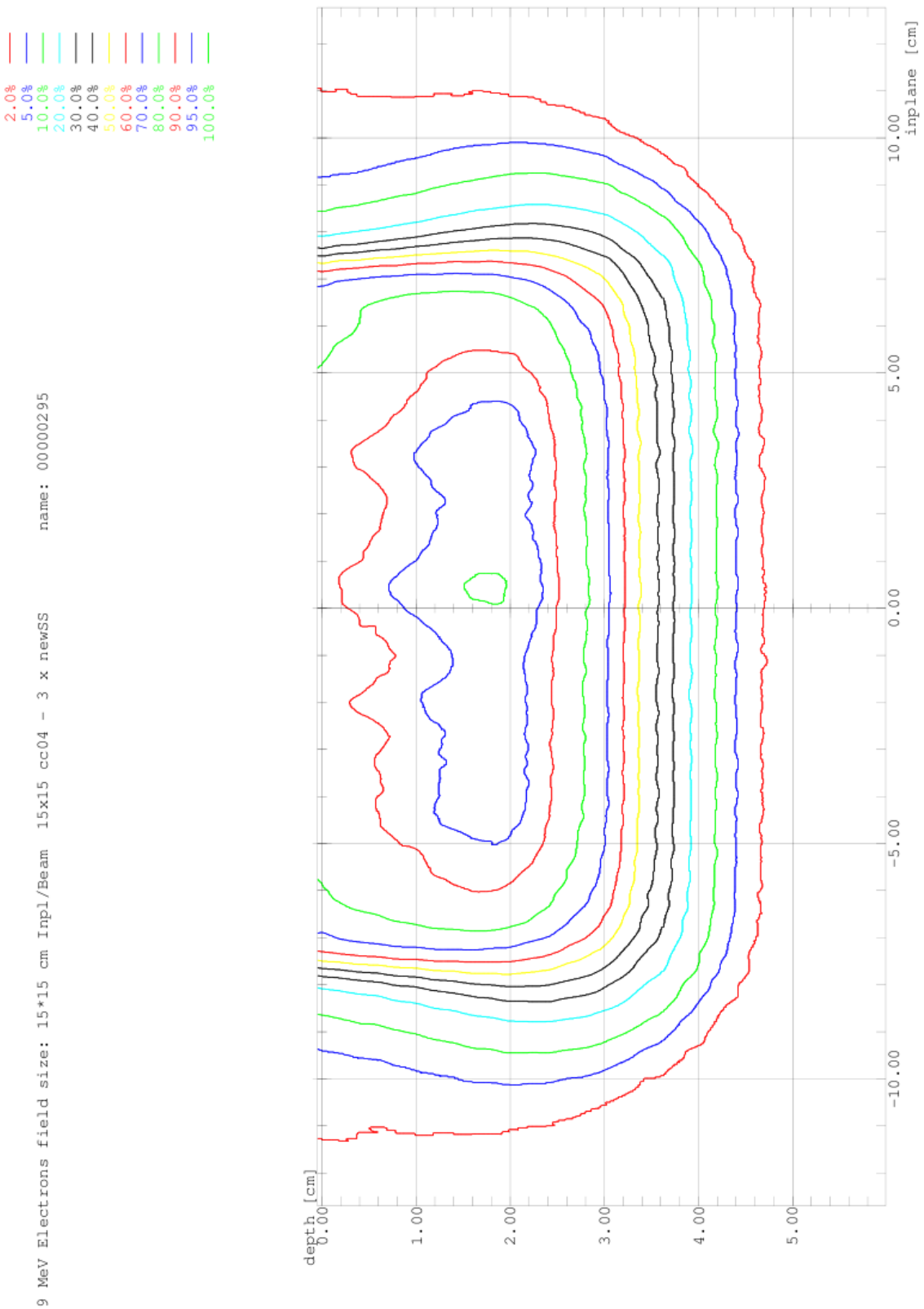

Illustration 109: Stainless Steel Mesh on Applicator 3xsheet 9MeV for Table 48

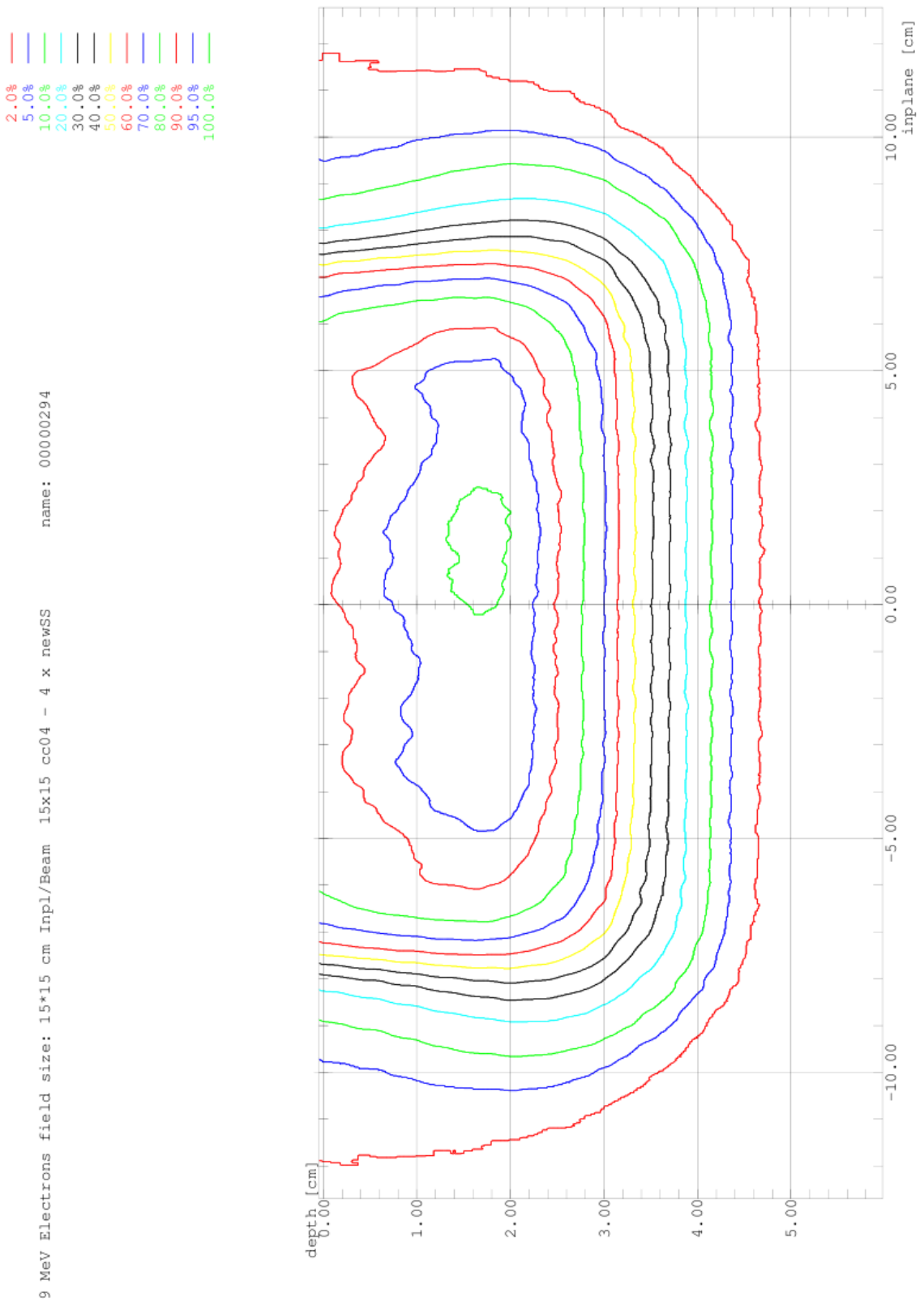

Illustration 110: Stainless Steel Mesh on Applicator 4xsheet 9MeV for Table 48

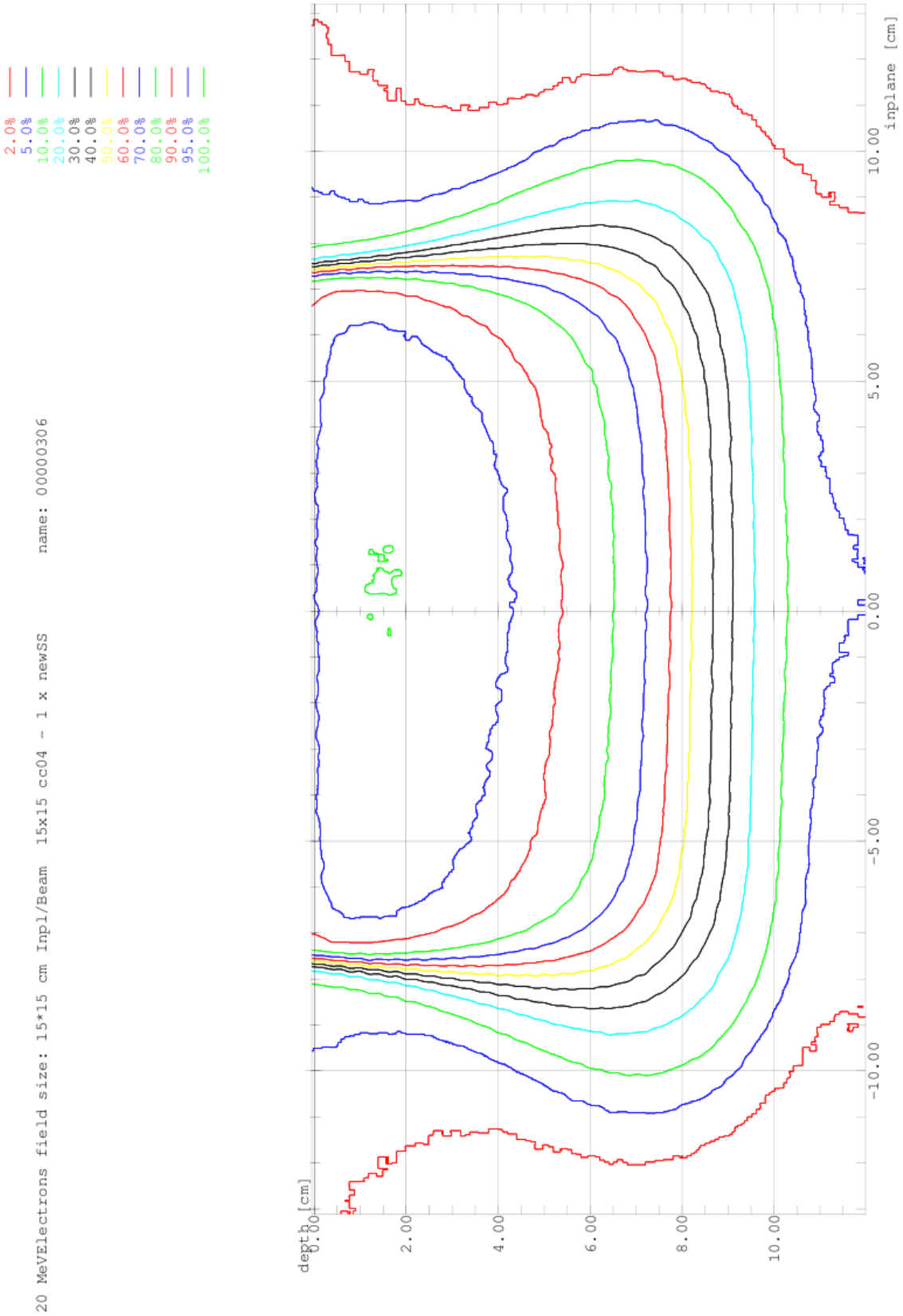

Illustration 111: Stainless Steel Mesh on Applicator 1xsheet 20MeV for Table 48

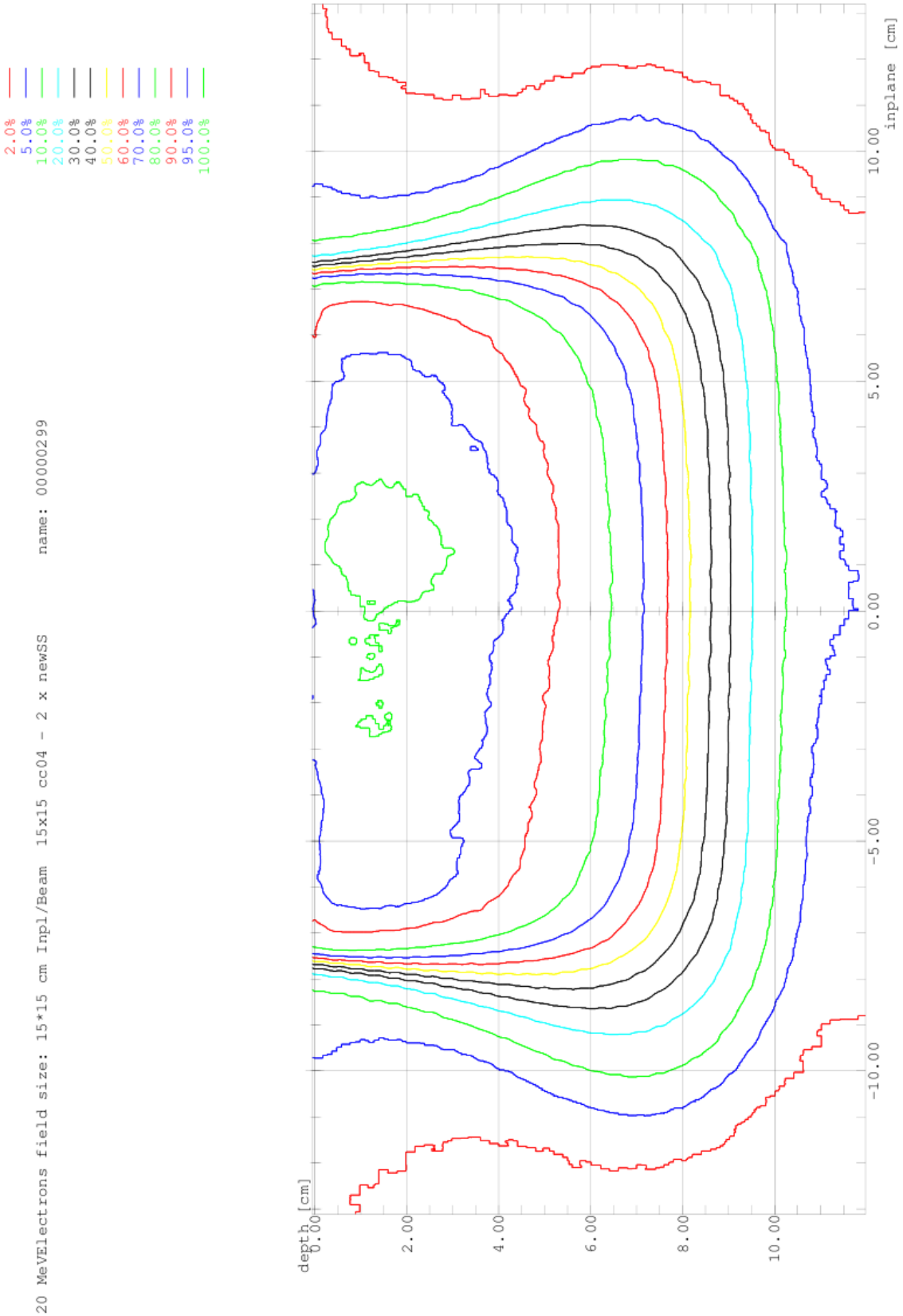

Illustration 112: Stainless Steel Mesh on Applicator 2xsheet 20MeV for Table 48

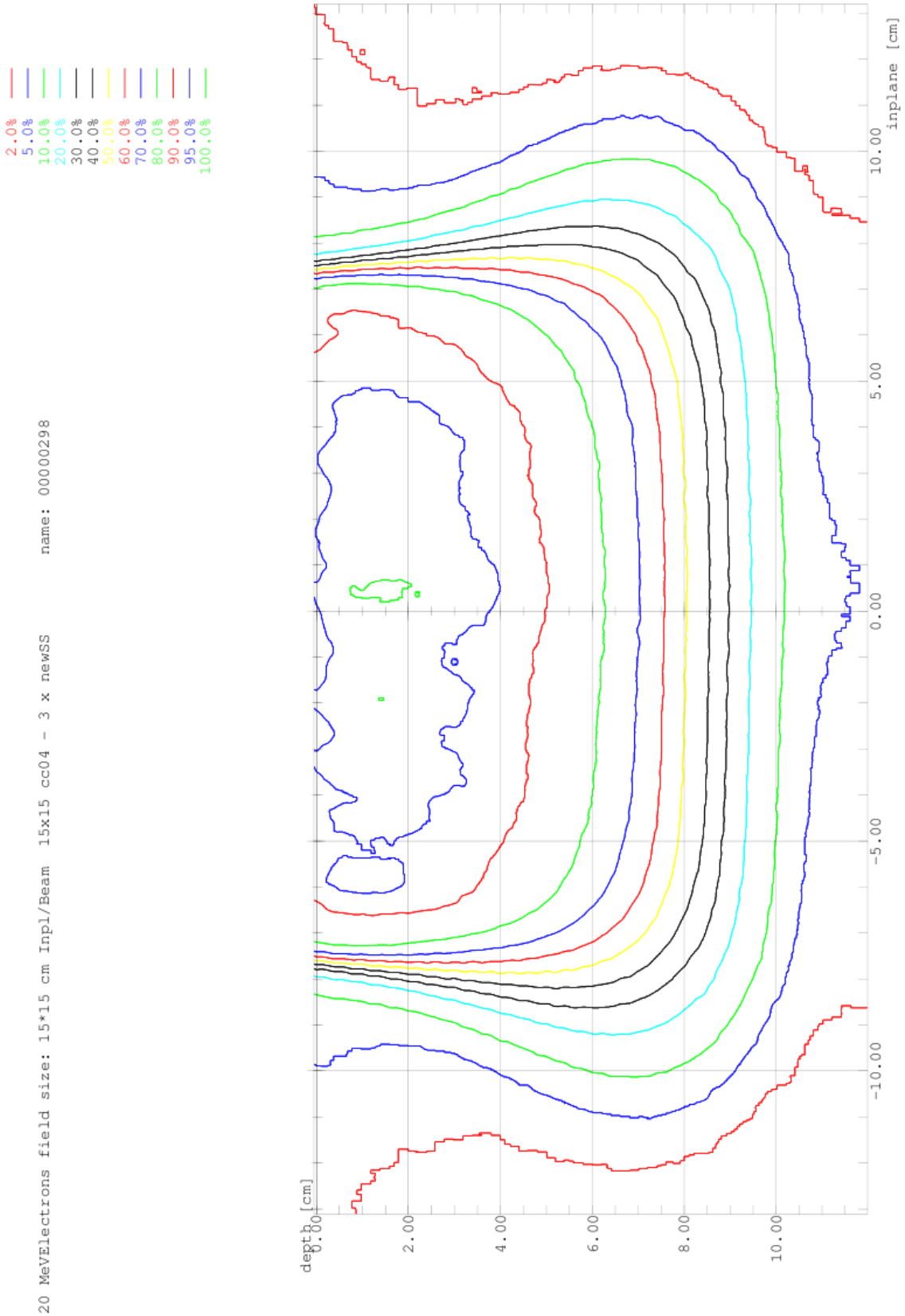

Illustration 113: Stainless Steel Mesh on Applicator 3xsheet 20MeV for Table 48

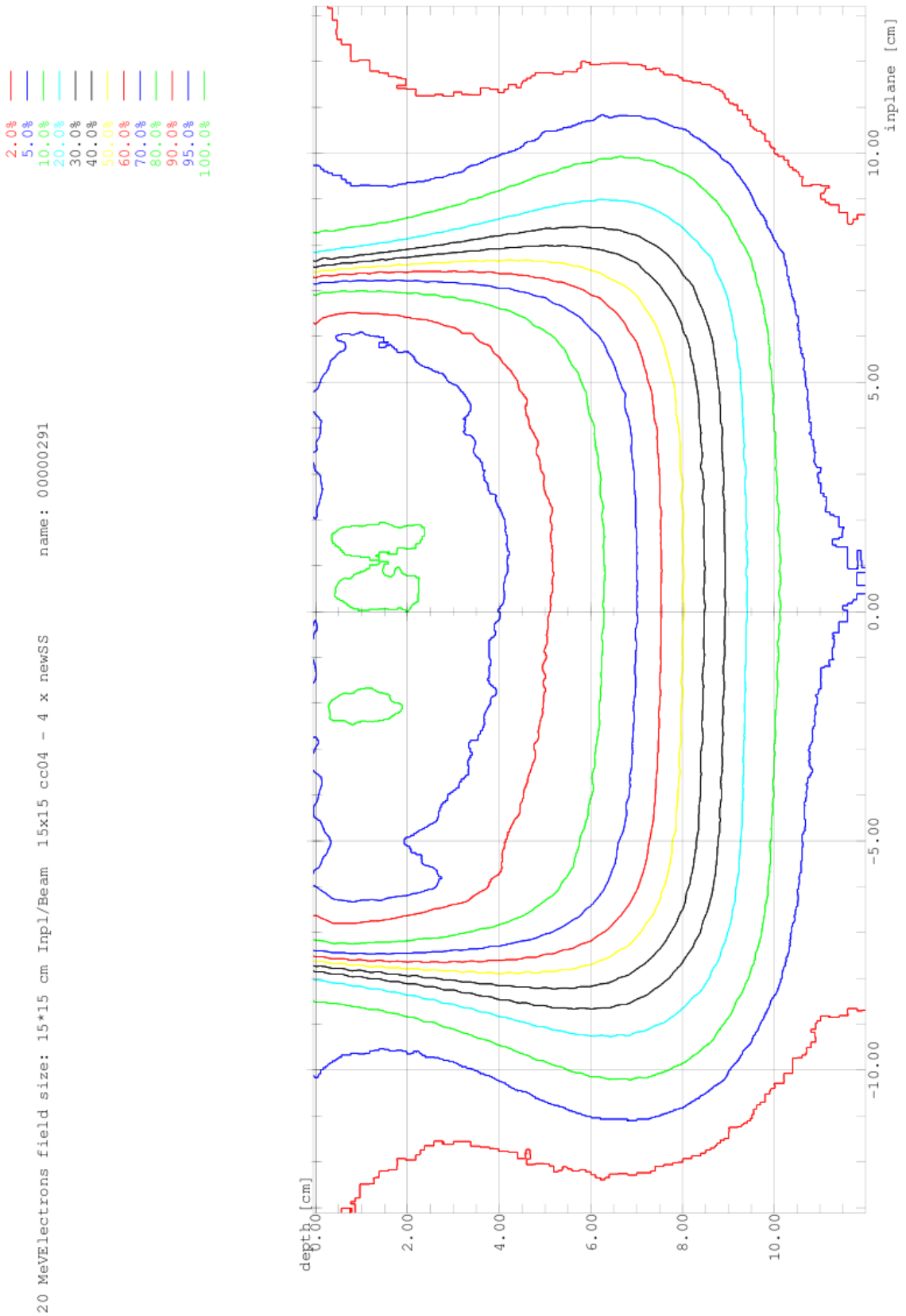

Illustration 114: Stainless Steel Mesh on Applicator 4xsheet 20MeV for Table 48

A3.4.1 Bolus on Surface Perspex & Teflon 9 & 20MeV

- **Illustration 115: Perspex Bolus on Surface Depth Ionisation 9MeV from Table 50**
- **Illustration 116: Perspex Bolus on Surface Net 1xSheet 9MeV for Table 51**
- **Illustration 117: Perspex Bolus on Surface Net 2xSheet 9MeV for Table 51**
- **Illustration 118: Perspex Bolus on Surface Net 3xSheet 9MeV for Table 51**

- **Illustration 119: Bolus on Surface Teflon 1, 2 x5mm sheet Depth Ionisation 9MeV for Table 53**
- **Illustration 120: Bolus on Surface Teflon 1, 2 x5mm sheet Depth Ionisation 20MeV for Table 54**
-

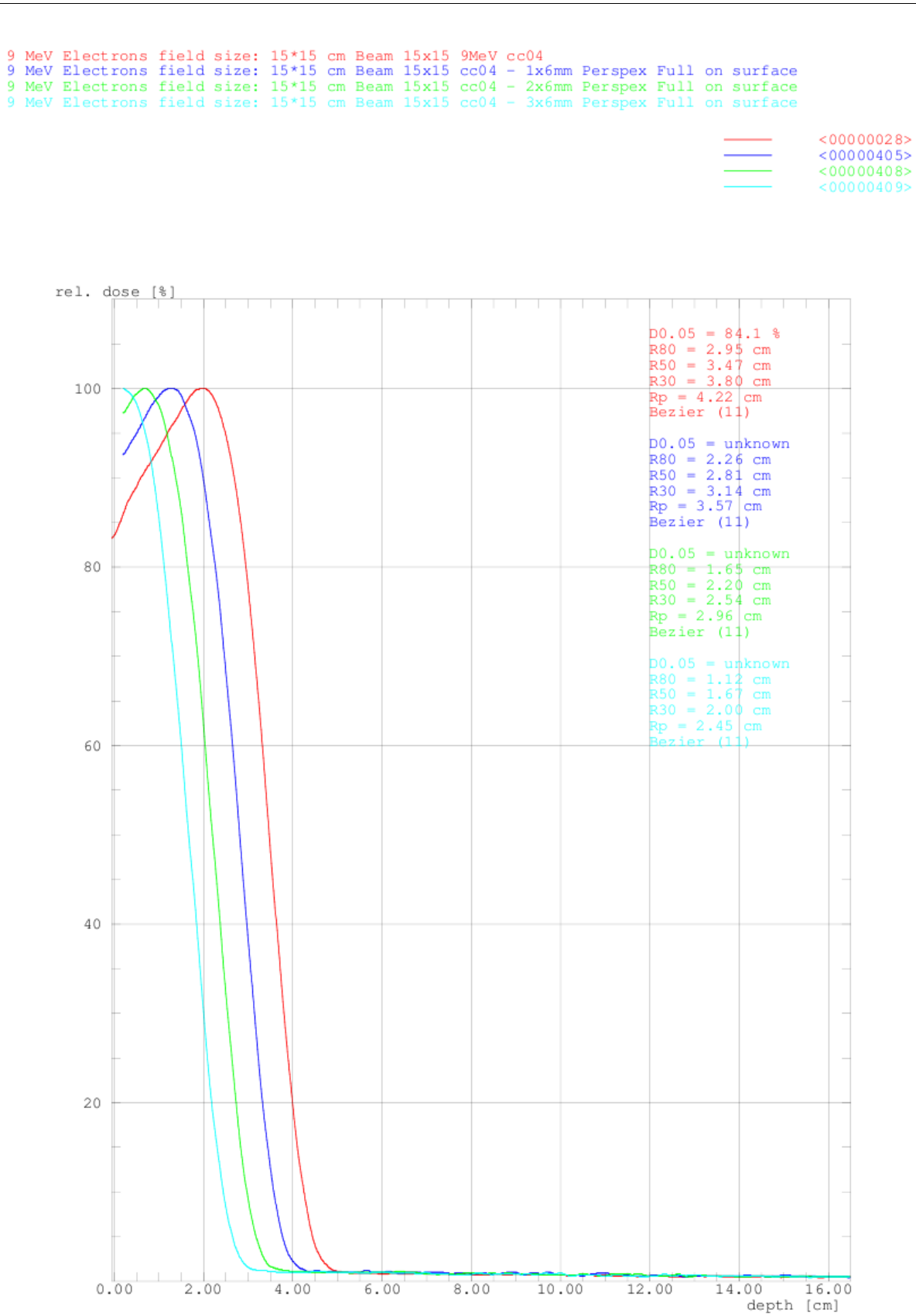

Illustration 115: Perspex Bolus on Surface Depth Ionisation 9MeV from Table 50

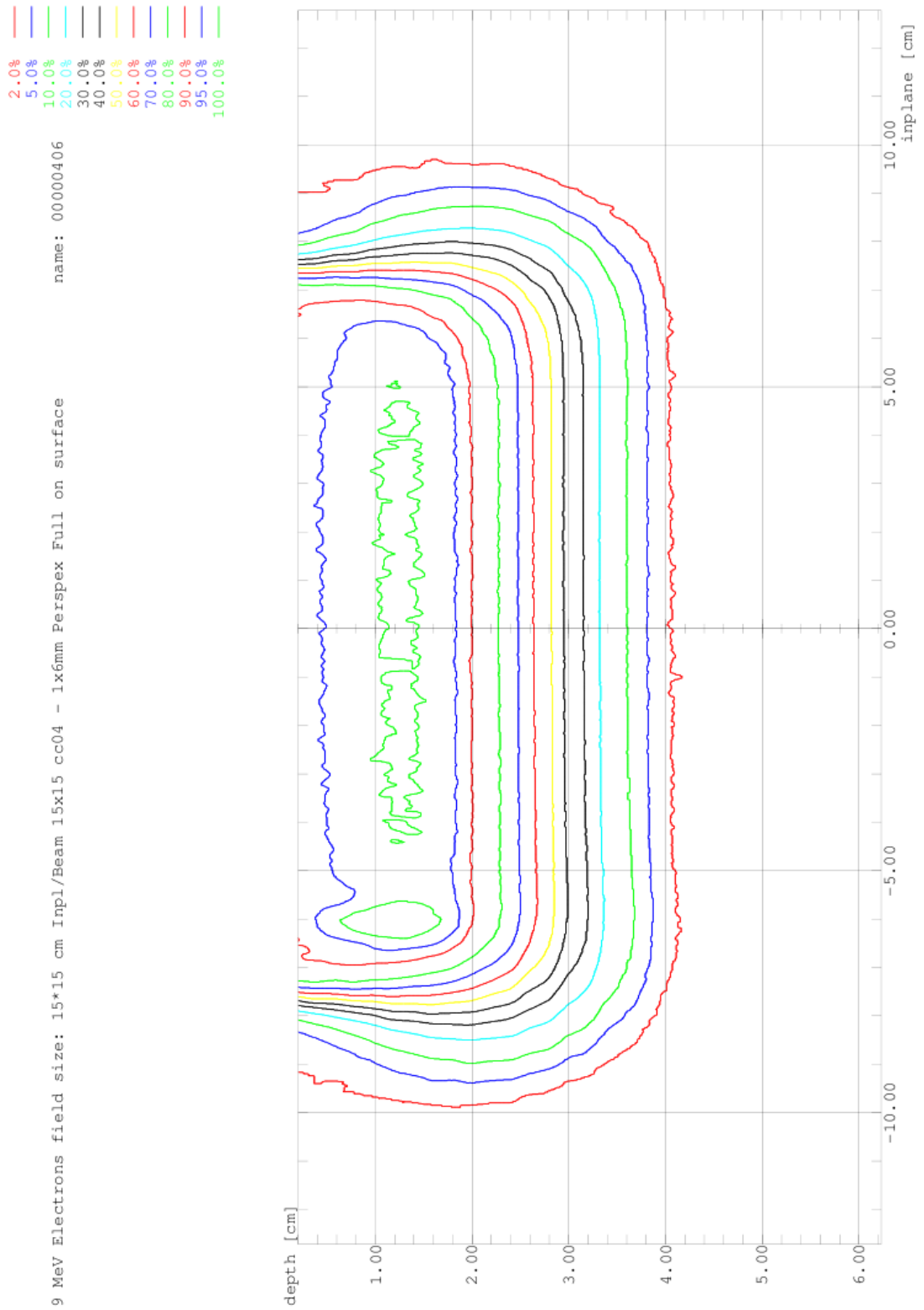

Illustration 116: Perspex Bolus on Surface Net 1xSheet 9MeV for Table 51

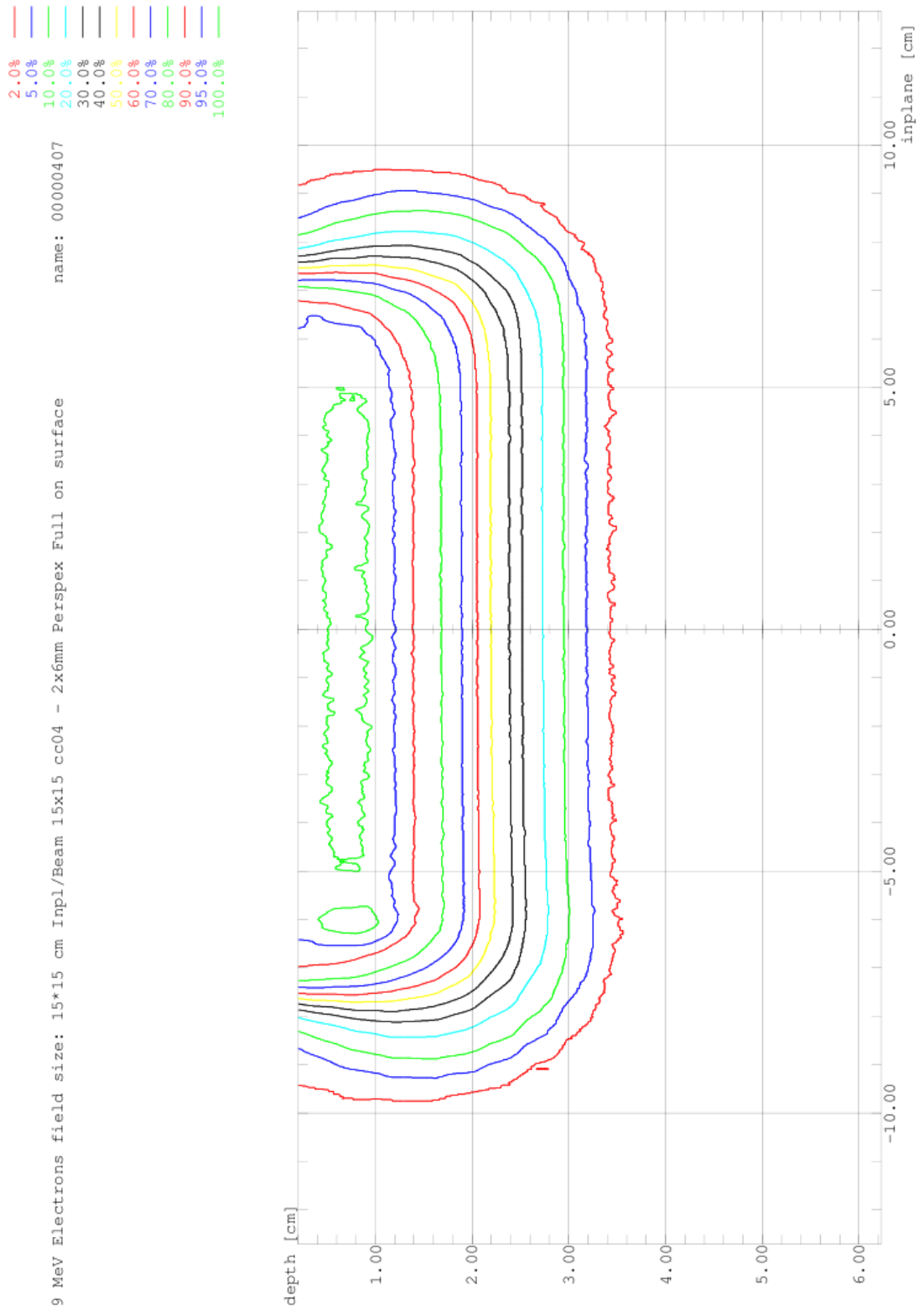

Illustration 117: Perspex Bolus on Surface Net 2xSheet 9MeV for Table 51

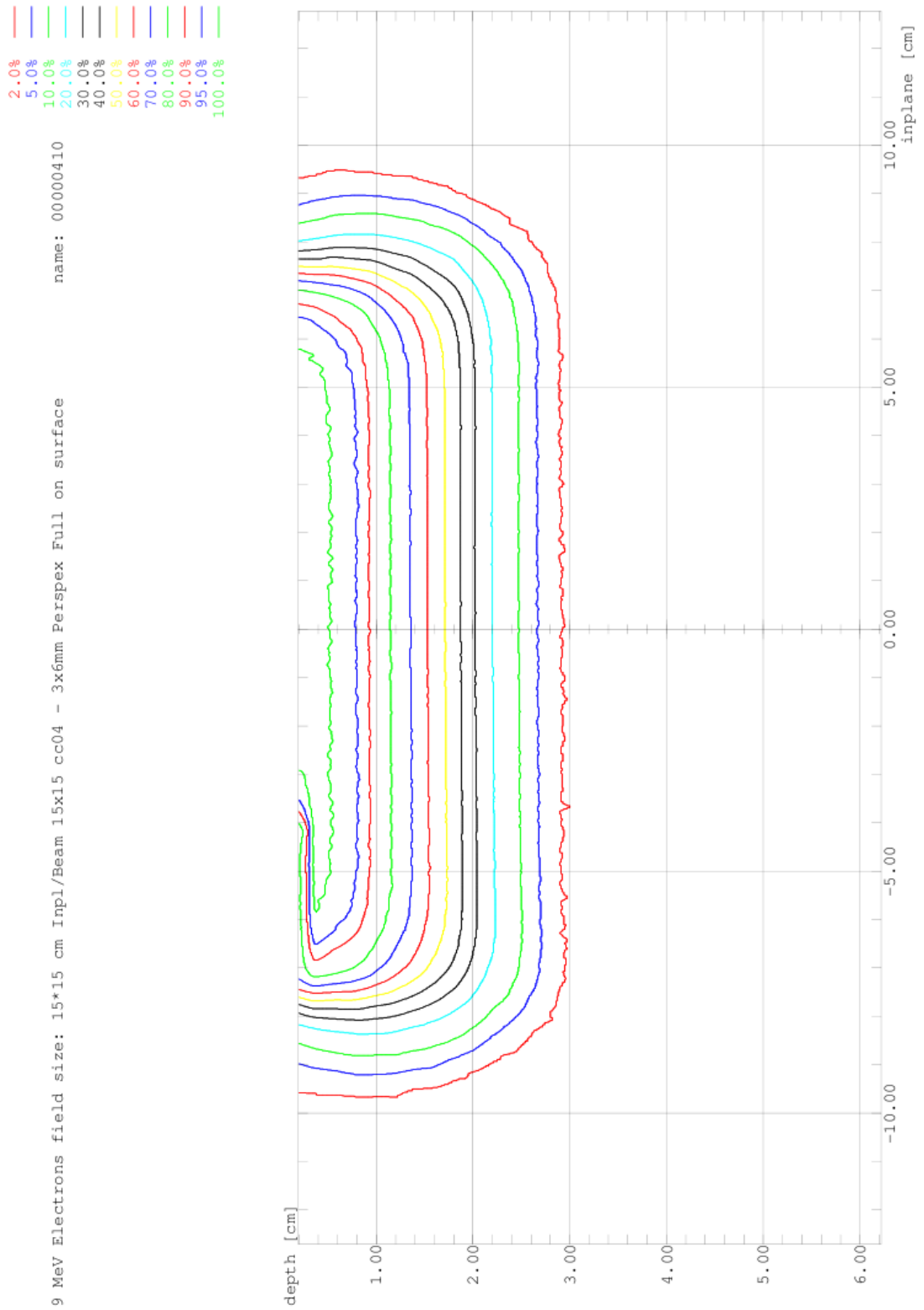

Illustration 118: Perspex Bolus on Surface Net 3xSheet 9MeV for Table 51

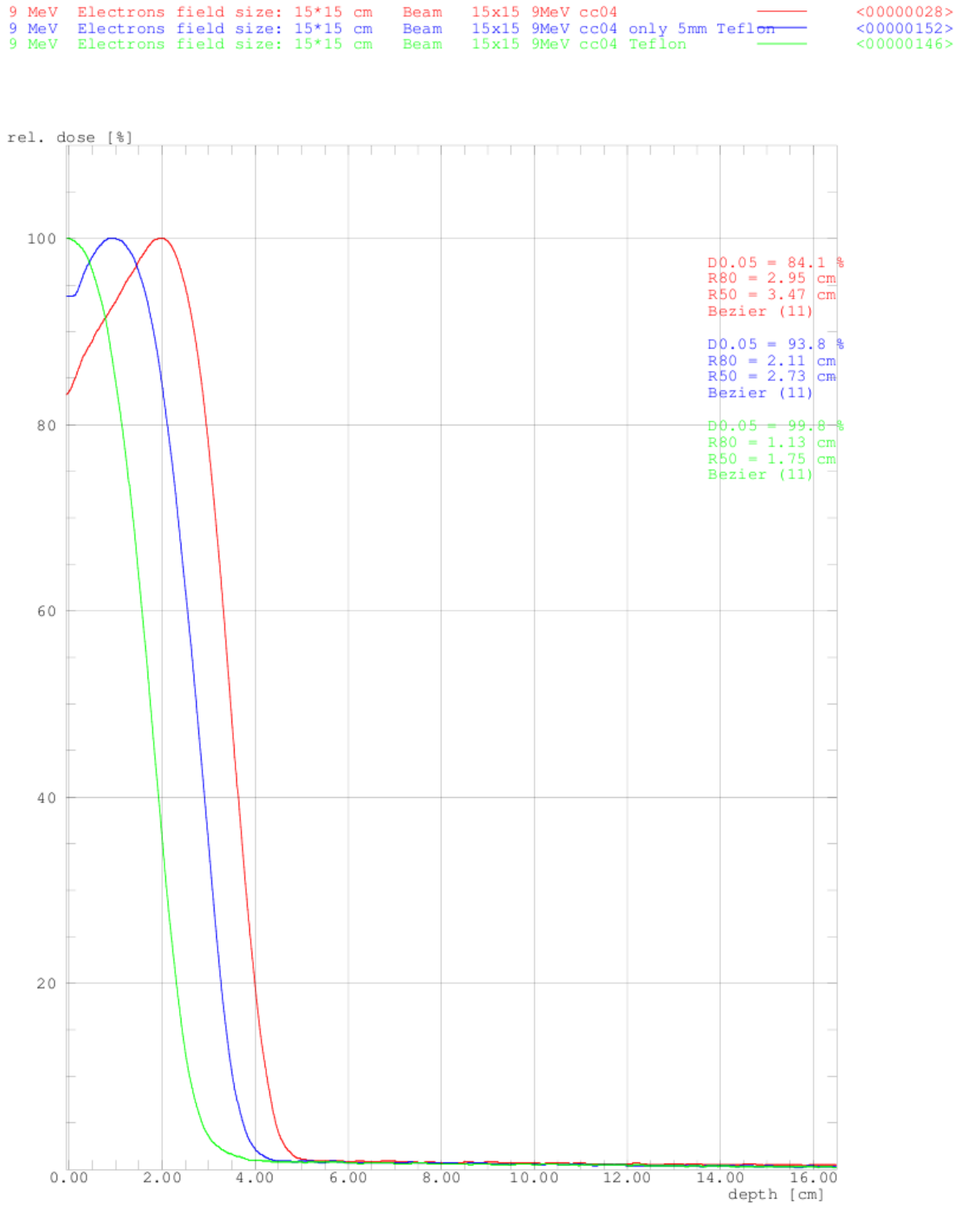

Illustration 119: Bolus on Surface Teflon 1, 2 x5mm sheet Depth Ionisation 9MeV for Table 53

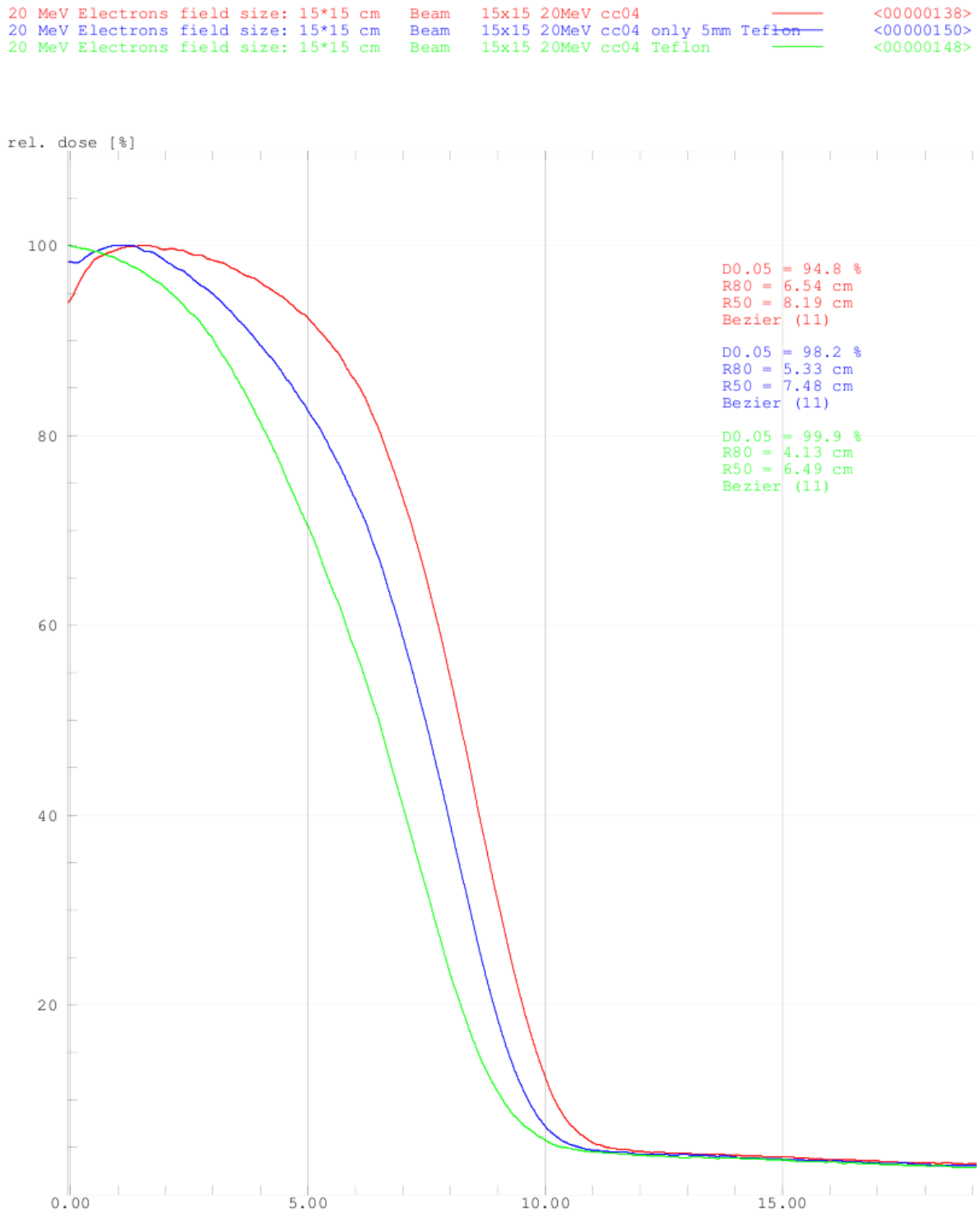

Illustration 120: Bolus on Surface Teflon 1, 2 x5mm sheet Depth Ionisation 20MeV for Table 54

Page intentionally left blank

A3.4.1 Full Bolus on Applicator Perspex 9 & 20MeV

- **Illustration 121: Full Bolus Perspex with 9MeV surface shift 0.6cm**
- **Illustration 122: Full Bolus Perspex with 9MeV surface shift 1.22cm**
- **Illustration 123: Full Bolus Perspex with 9MeV surface shift 1.83cm**

- **Illustration 124: Full Bolus Perspex with 20MeV surface shift 0.6cm**
- **Illustration 125: Full Bolus Perspex with 20MeV surface shift 1.27cm**
- **Illustration 126: Full Bolus Perspex with 20MeV surface shift 1.9cm**
-
-
-
-

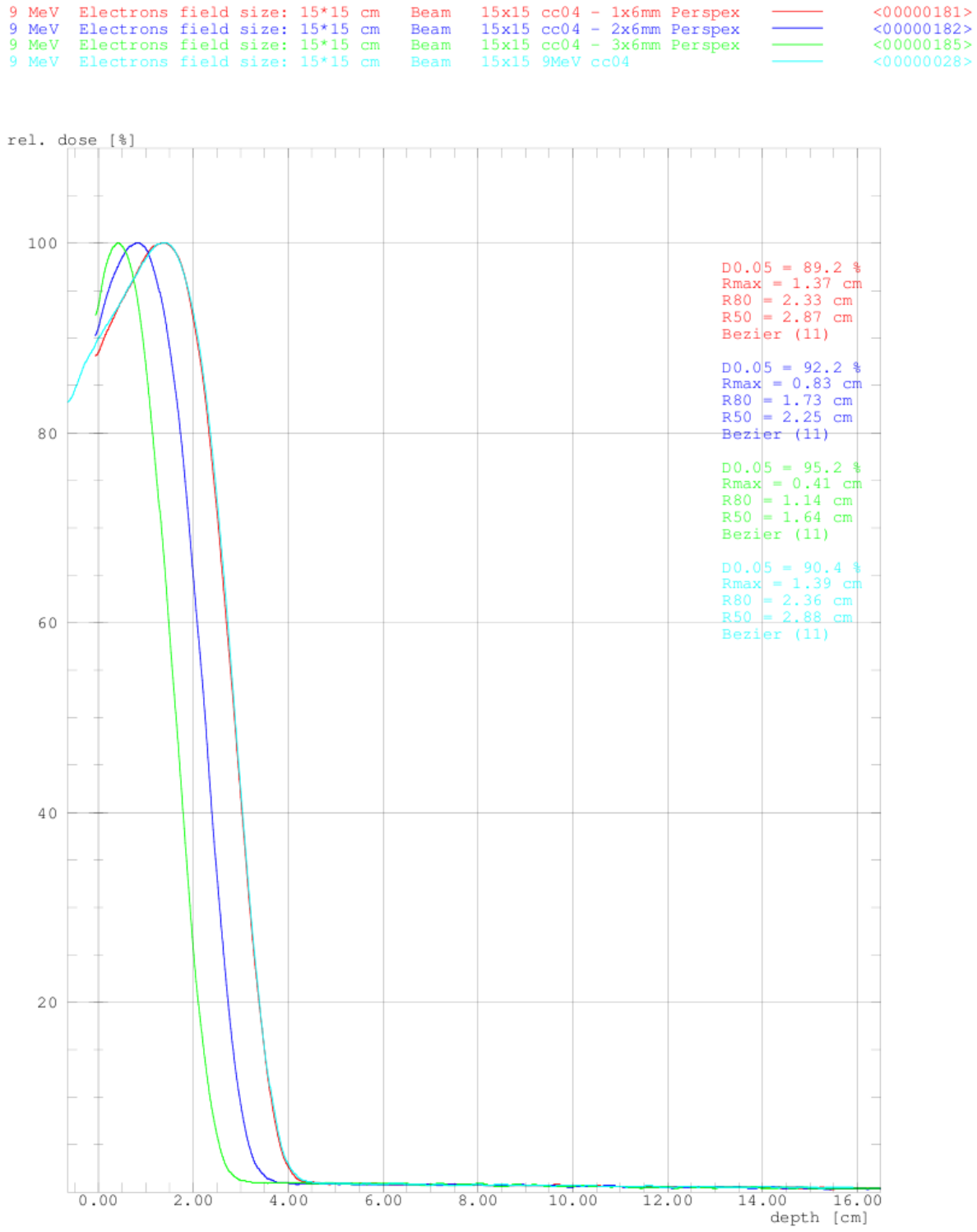

Illustration 121: Full Bolus Perspex with 9MeV surface shift 0.6cm

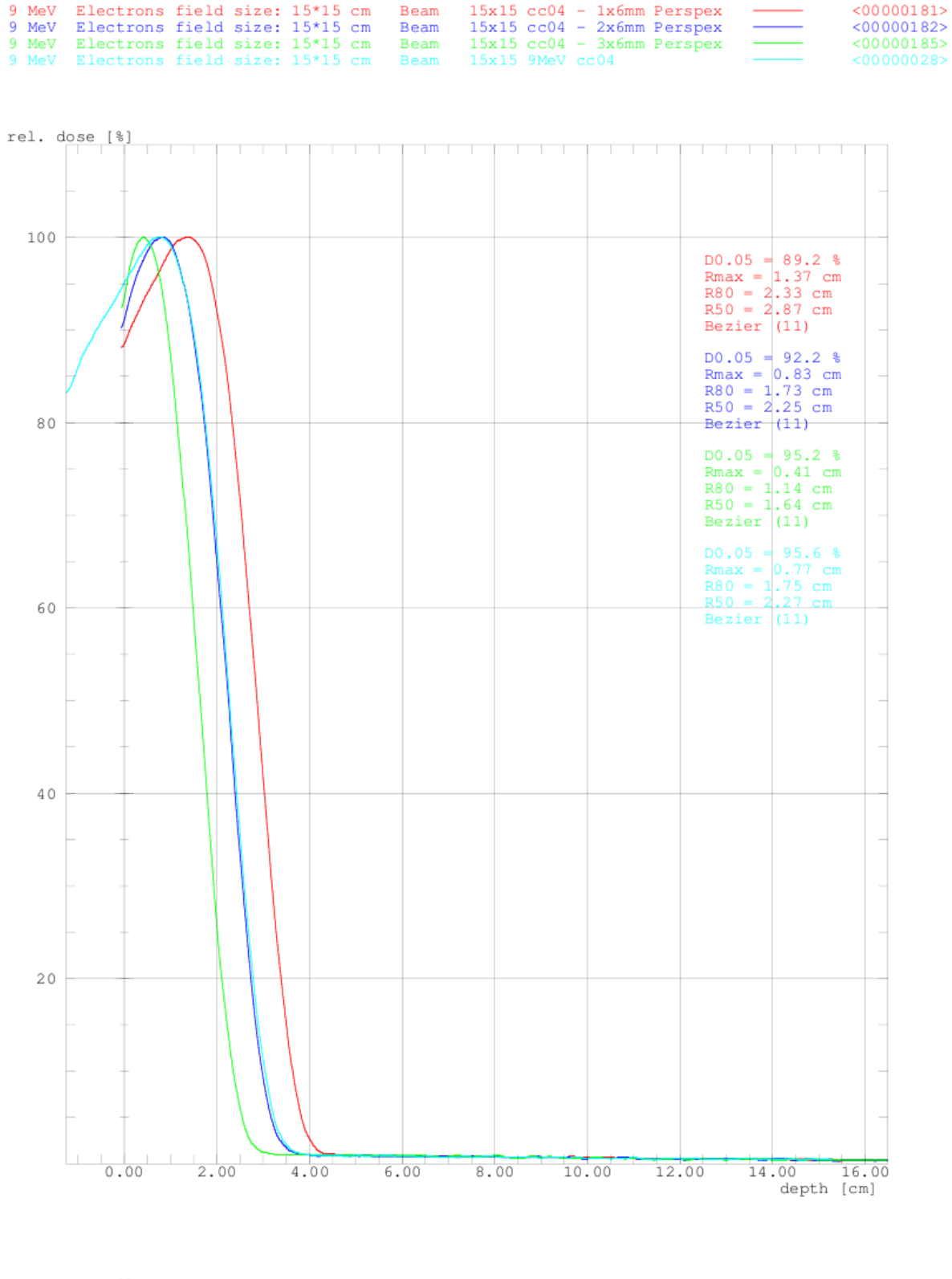

Illustration 122: Full Bolus Perspex with 9MeV surface shift 1.22cm

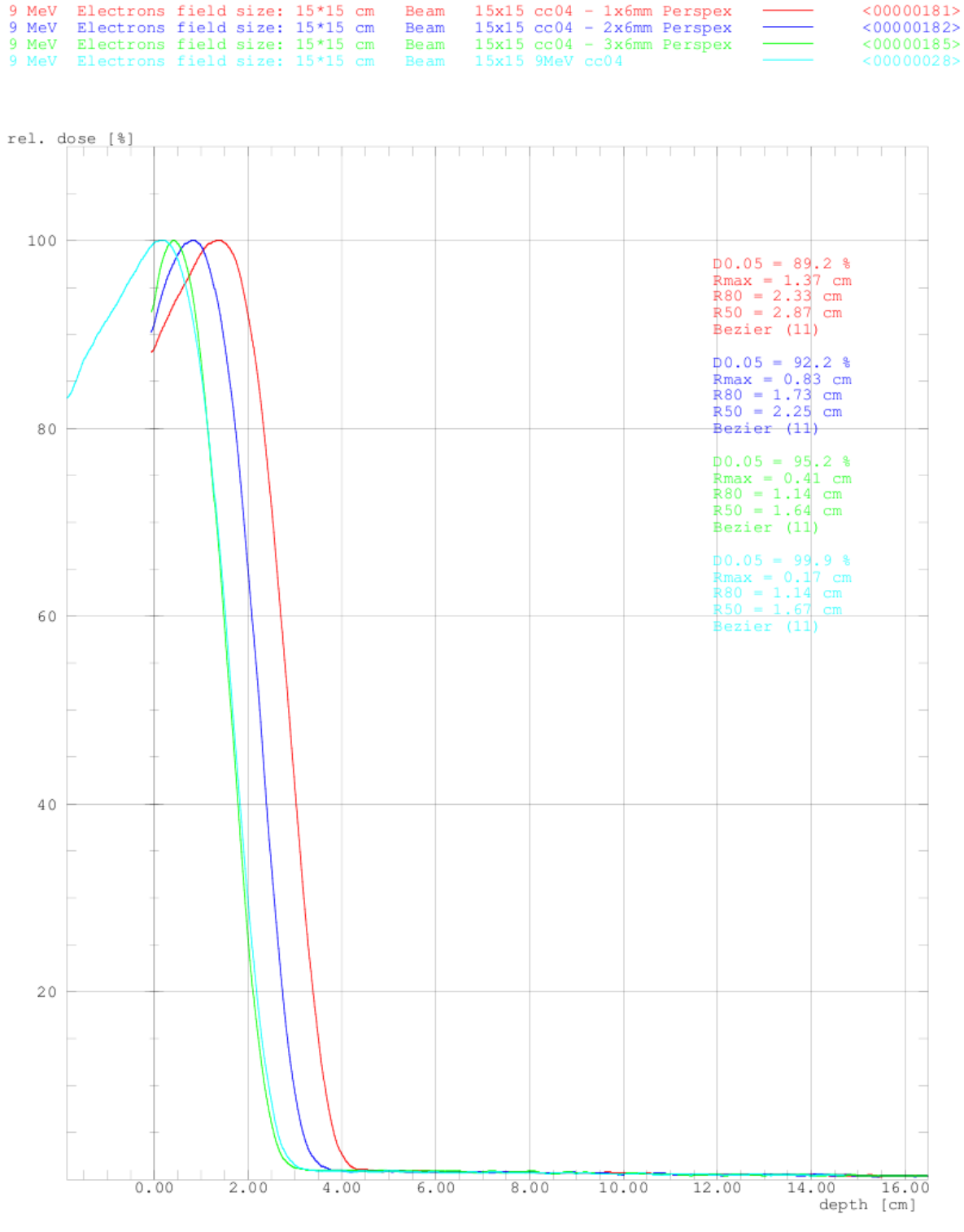

Illustration 123: Full Bolus Perspex with 9MeV surface shift 1.83cm

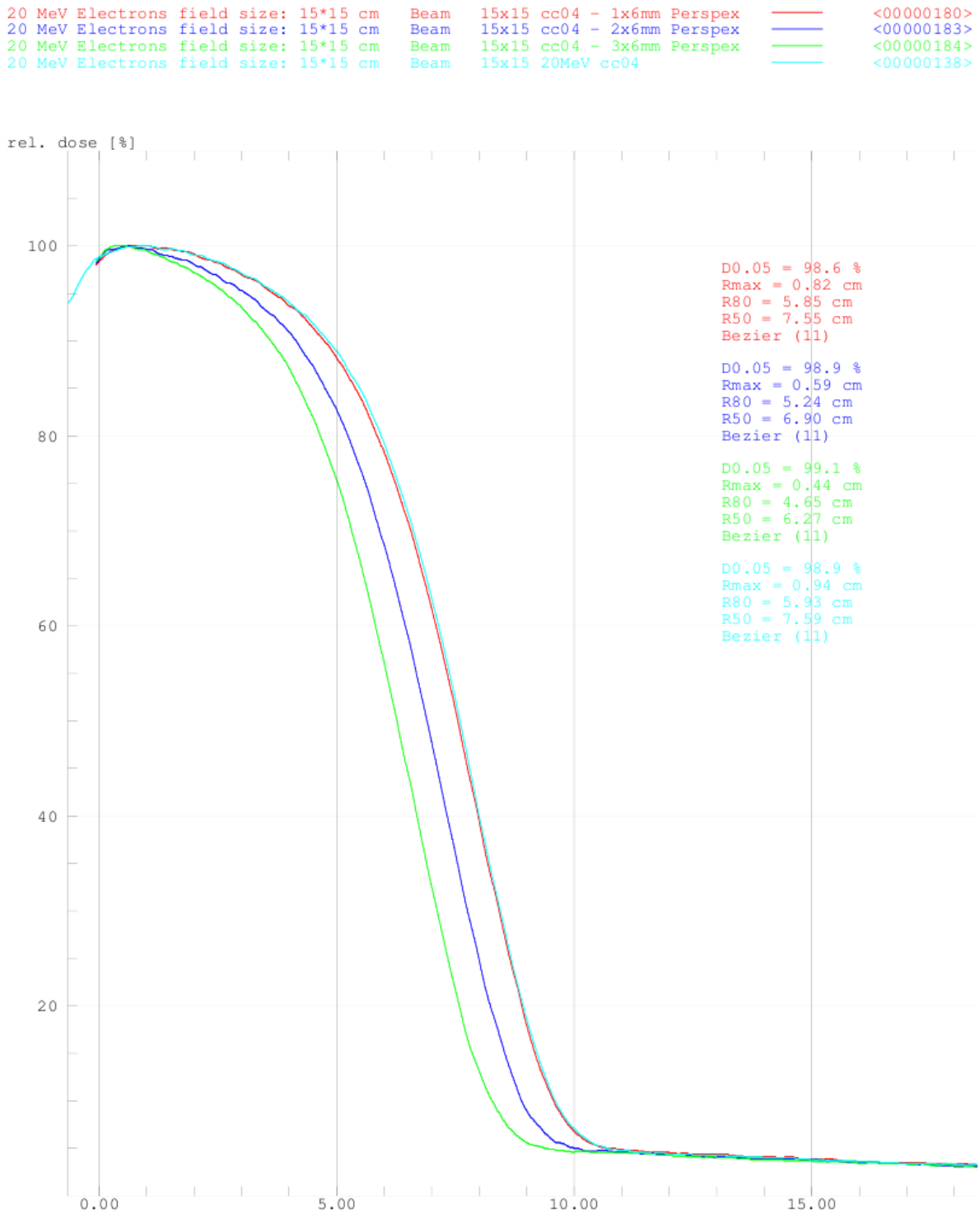

Illustration 124: Full Bolus Perspex with 20MeV surface shift 0.6cm

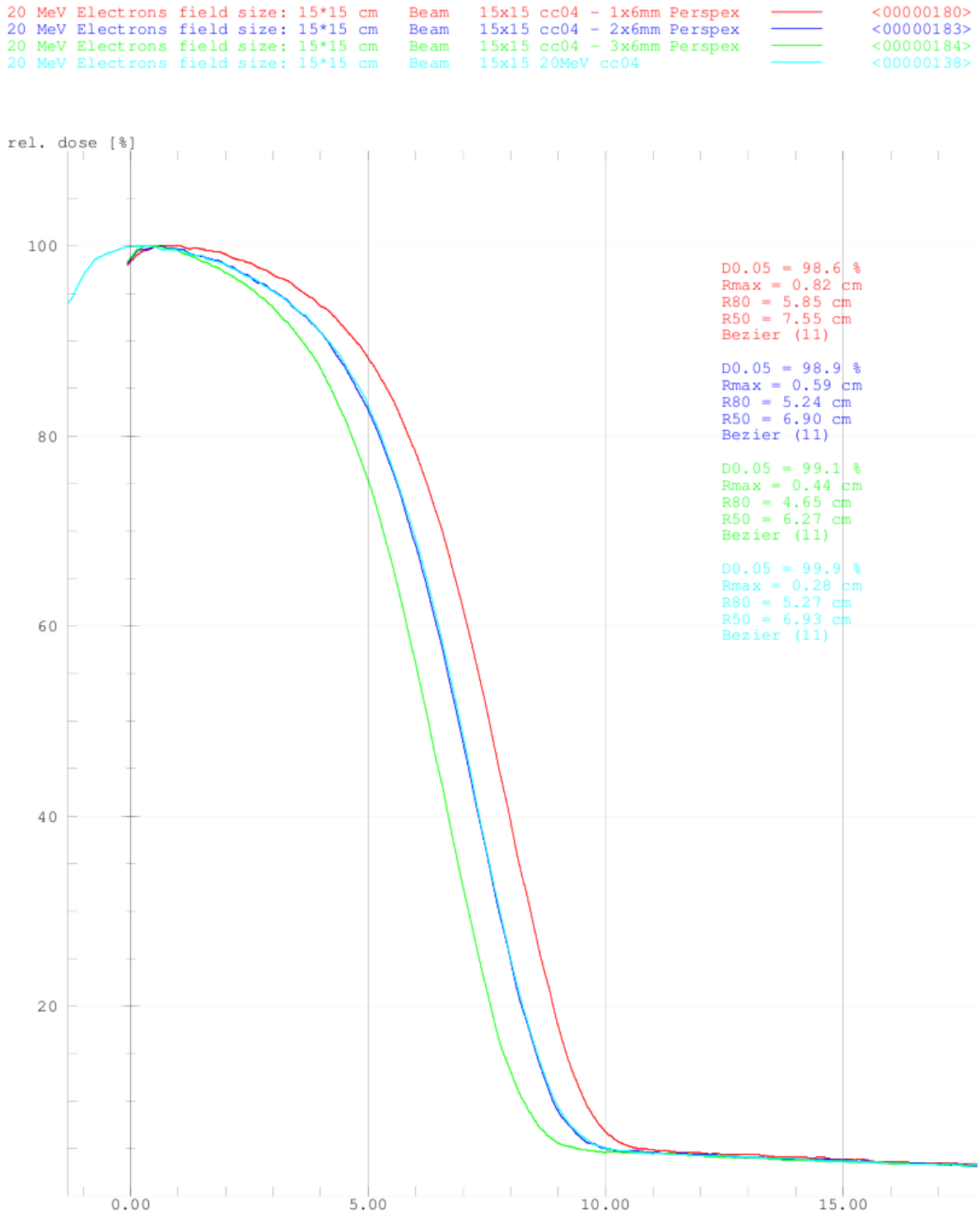

Illustration 125: Full Bolus Perspex with 20MeV surface shift 1.27cm

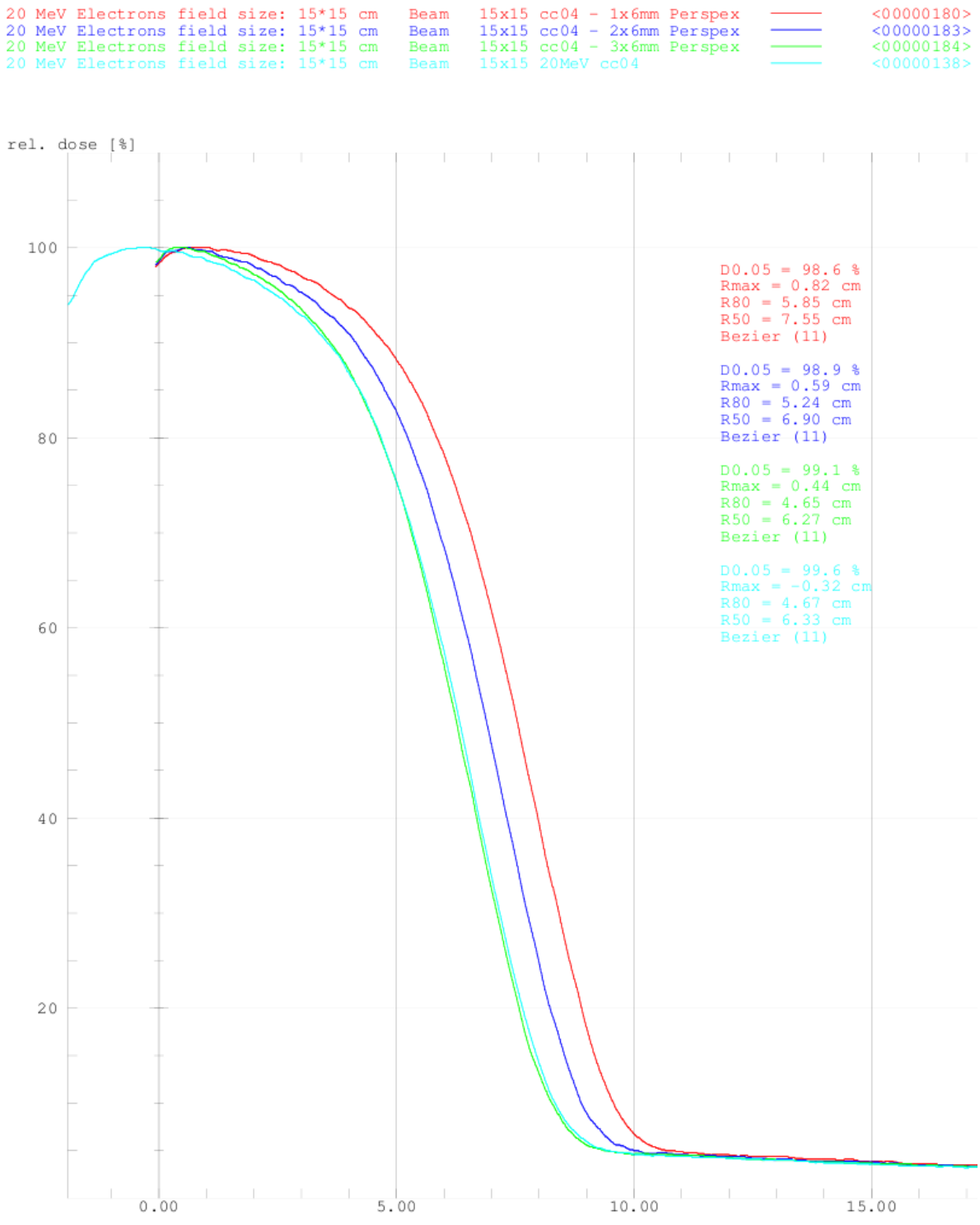

Illustration 126: Full Bolus Perspex with 20MeV surface shift 1.9cm

A3.4.2 Full Bolus on Applicator Teflon 9 & 20MeV

- **Illustration 127: Full Bolus Teflon with 9MeV surface shift 0.6cm**
- **Illustration 128: Full Bolus Teflon with 9MeV surface shift 1.15cm**
- **Illustration 129: Full Bolus Teflon with 9MeV surface shift 1.83cm**
-
- **Illustration 130: Full Bolus Teflon with 20MeV surface shift 0.58cm**
- **Illustration 131: Full Bolus Teflon with 20MeV surface shift 1.19cm**
- **Illustration 132: Full Bolus Teflon with 20MeV surface shift 2.1cm**

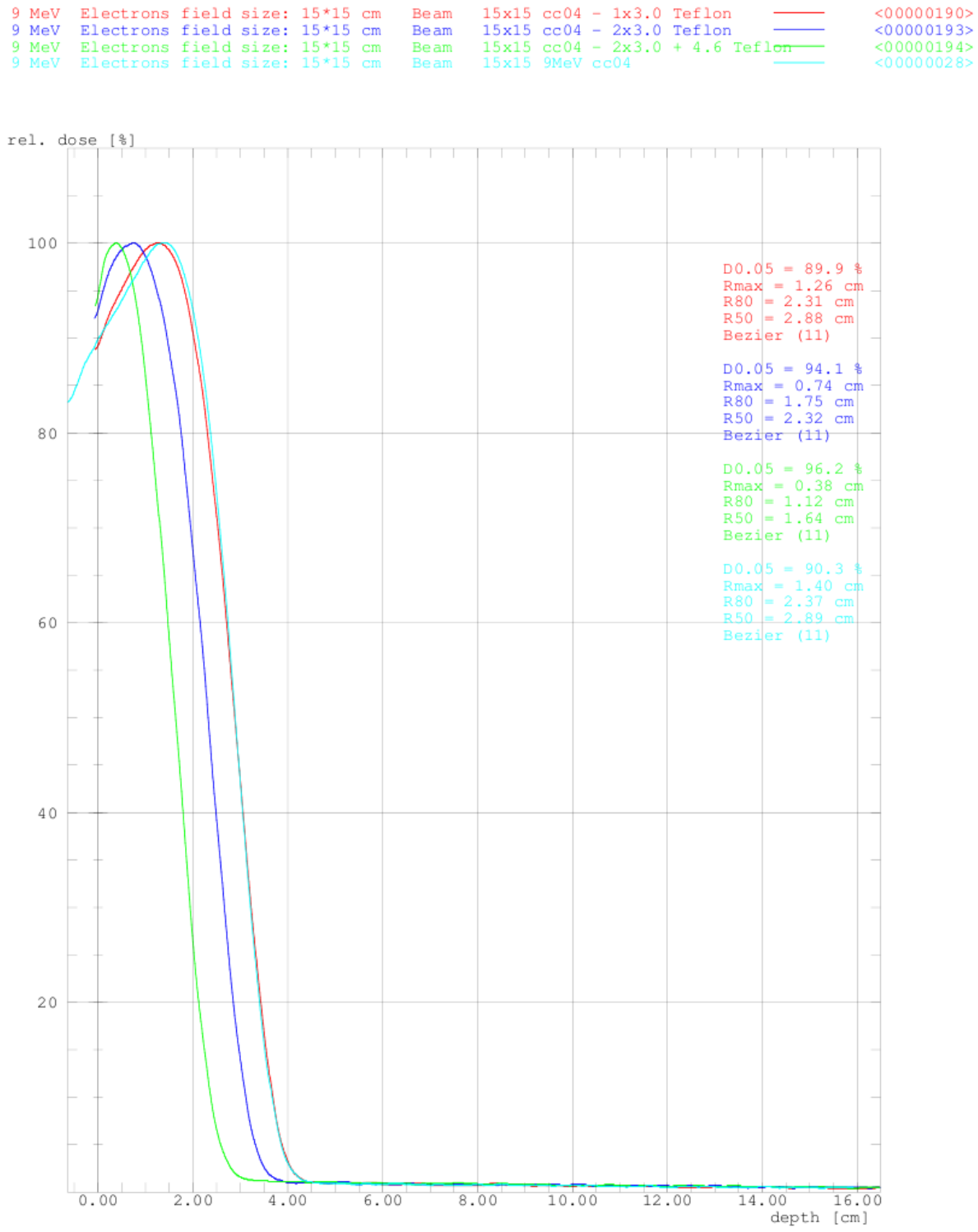

Illustration 127: Full Bolus Teflon with 9MeV surface shift 0.6cm

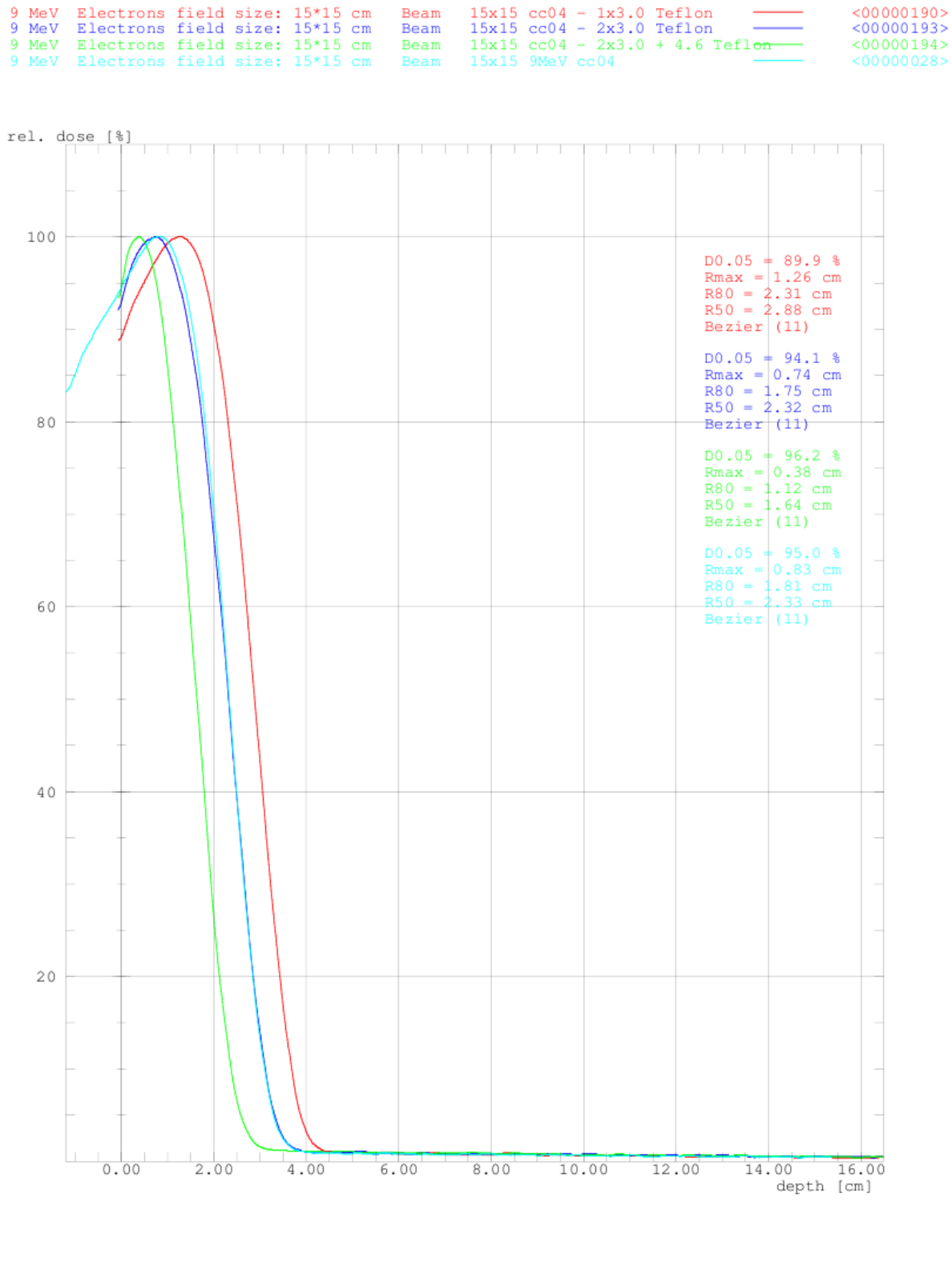

Illustration 128: Full Bolus Teflon with 9MeV surface shift 1.15cm

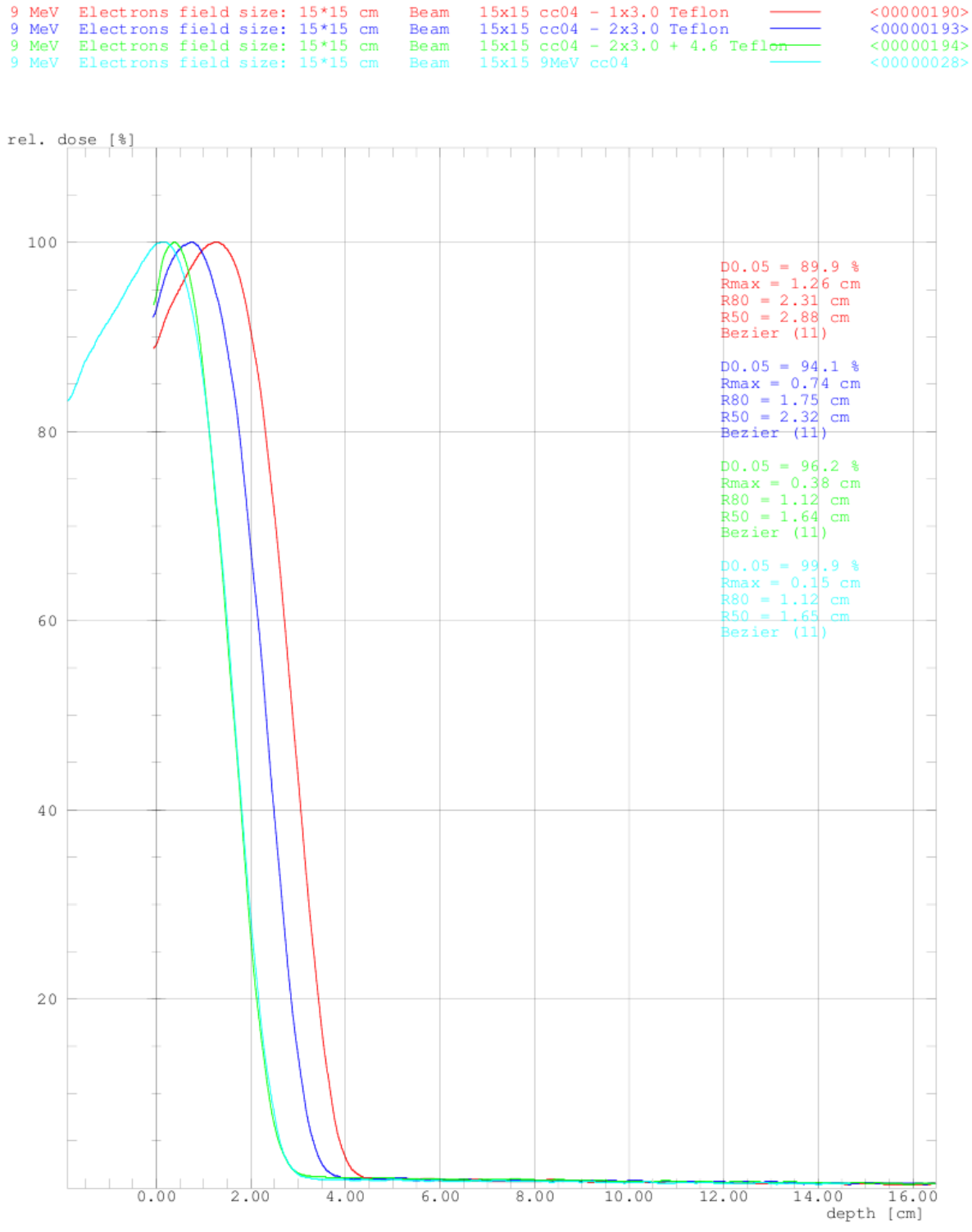

Illustration 129: Full Bolus Teflon with 9MeV surface shift 1.83cm

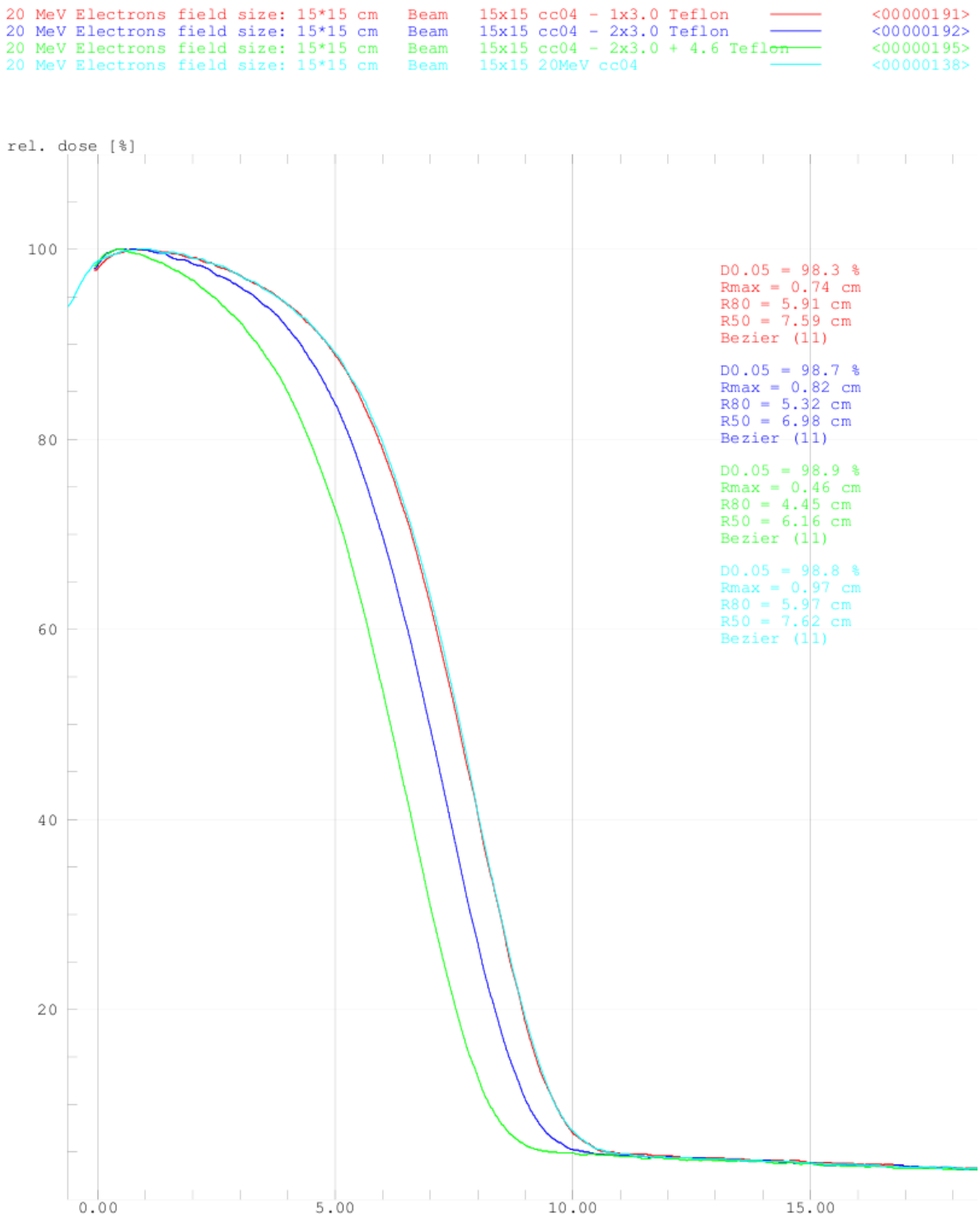

Illustration 130: Full Bolus Teflon with 20MeV surface shift 0.58cm

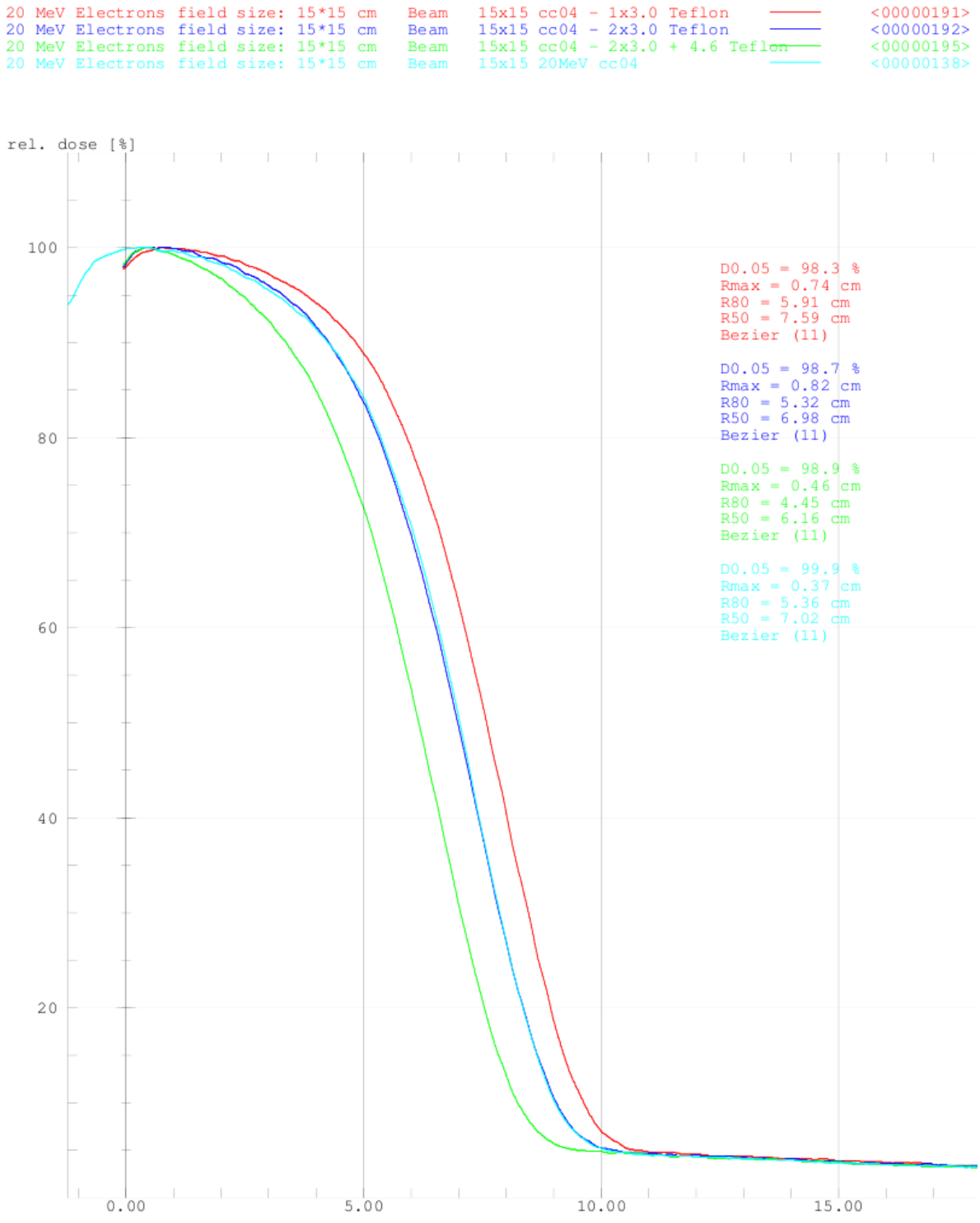

Illustration 131: Full Bolus Teflon with 20MeV surface shift 1.19cm

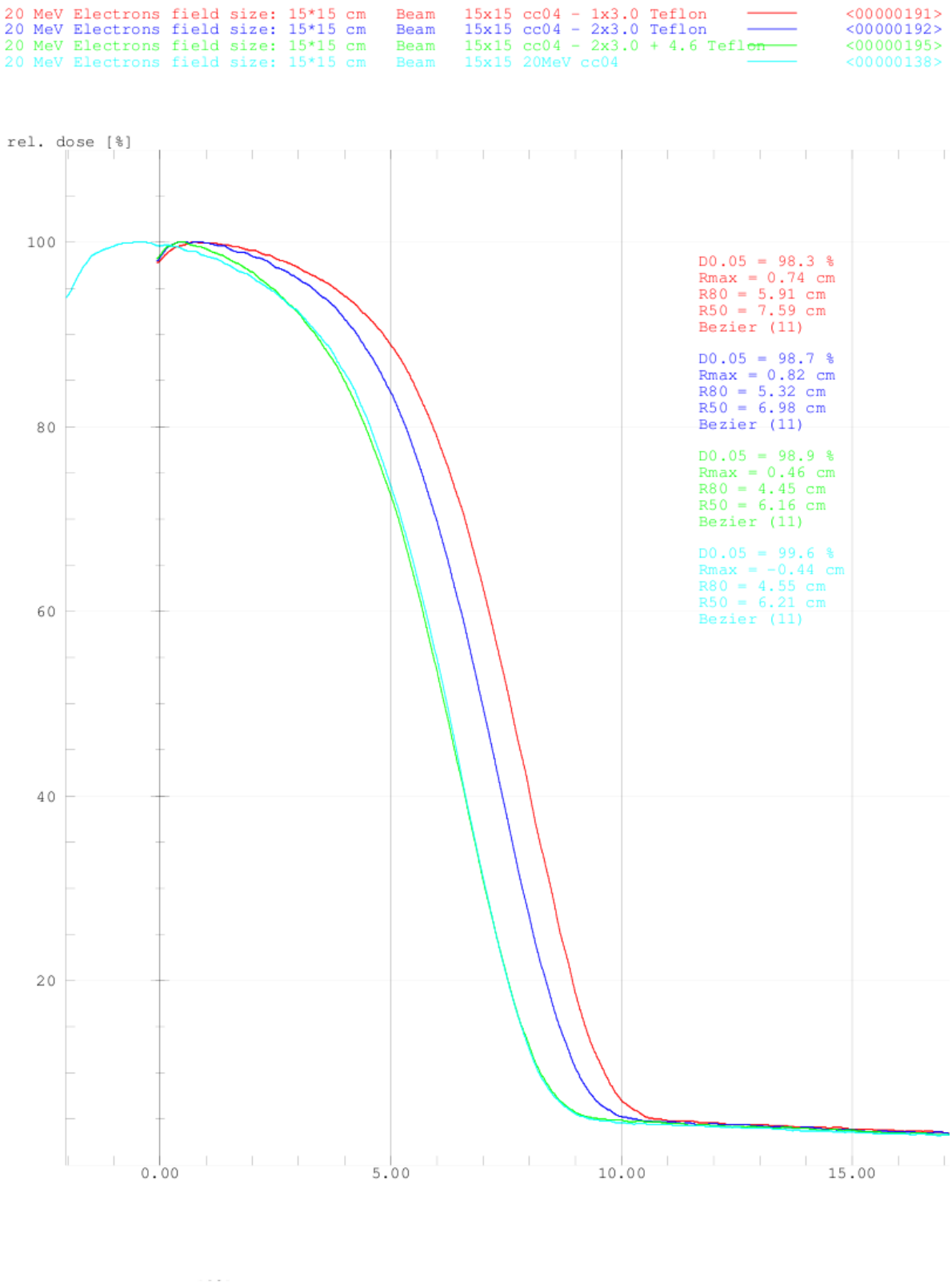

Illustration 132: Full Bolus Teflon with 20MeV surface shift 2.1cm

A3.4.3 Full Bolus on Applicator Aluminium 9 & 20MeV

- **Illustration 133: Full Bolus Aluminium with 9MeV surface shift 0.65cm**
- **Illustration 134: Full Bolus Aluminium with 9MeV surface shift 1.21cm**
-
- **Illustration 135: Full Bolus Aluminium with 20MeV surface shift 0.69cm**
- **Illustration 136: Full Bolus Aluminium with 20MeV surface shift 1.32cm**

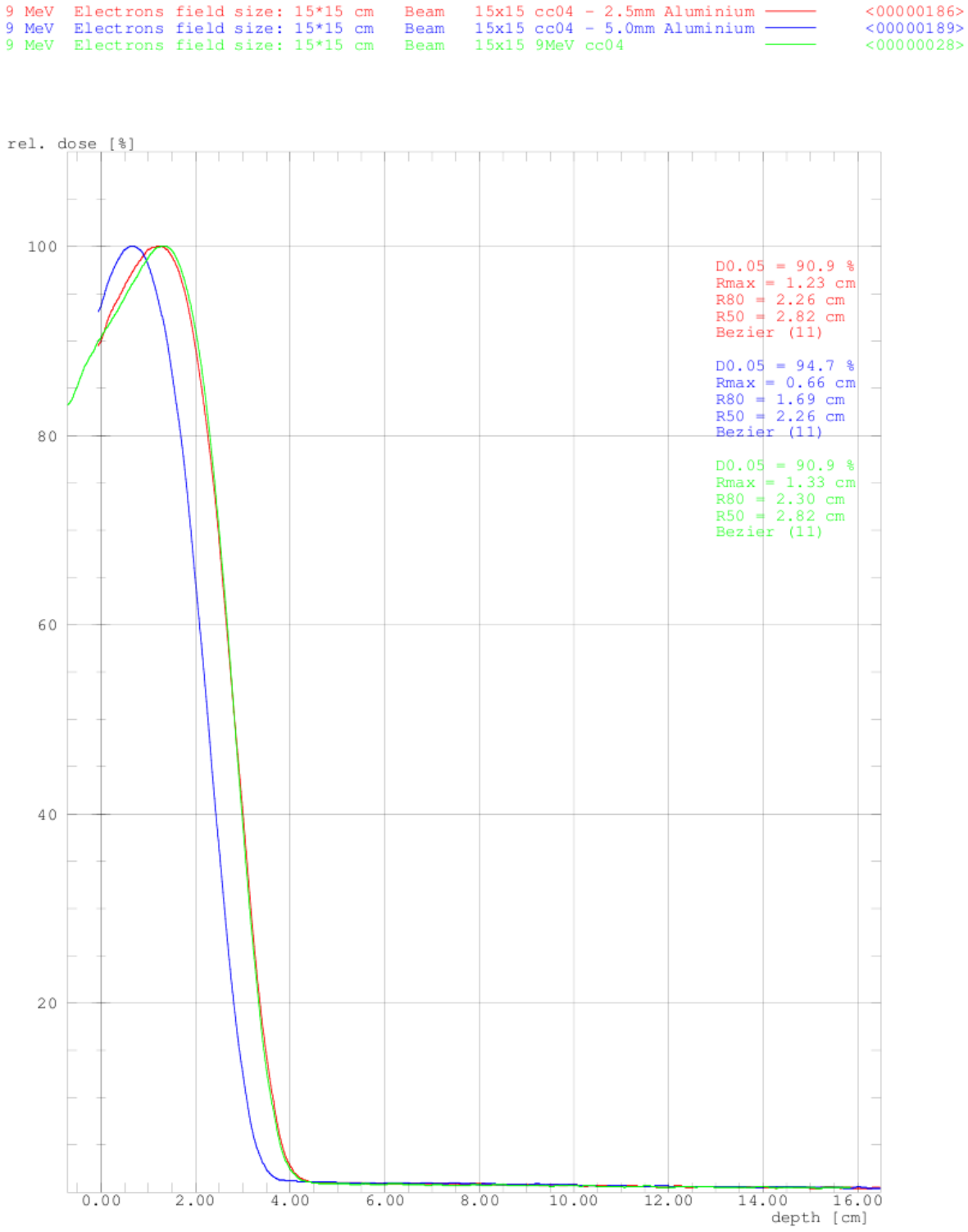

Illustration 133: Full Bolus Aluminium with 9MeV surface shift 0.65cm

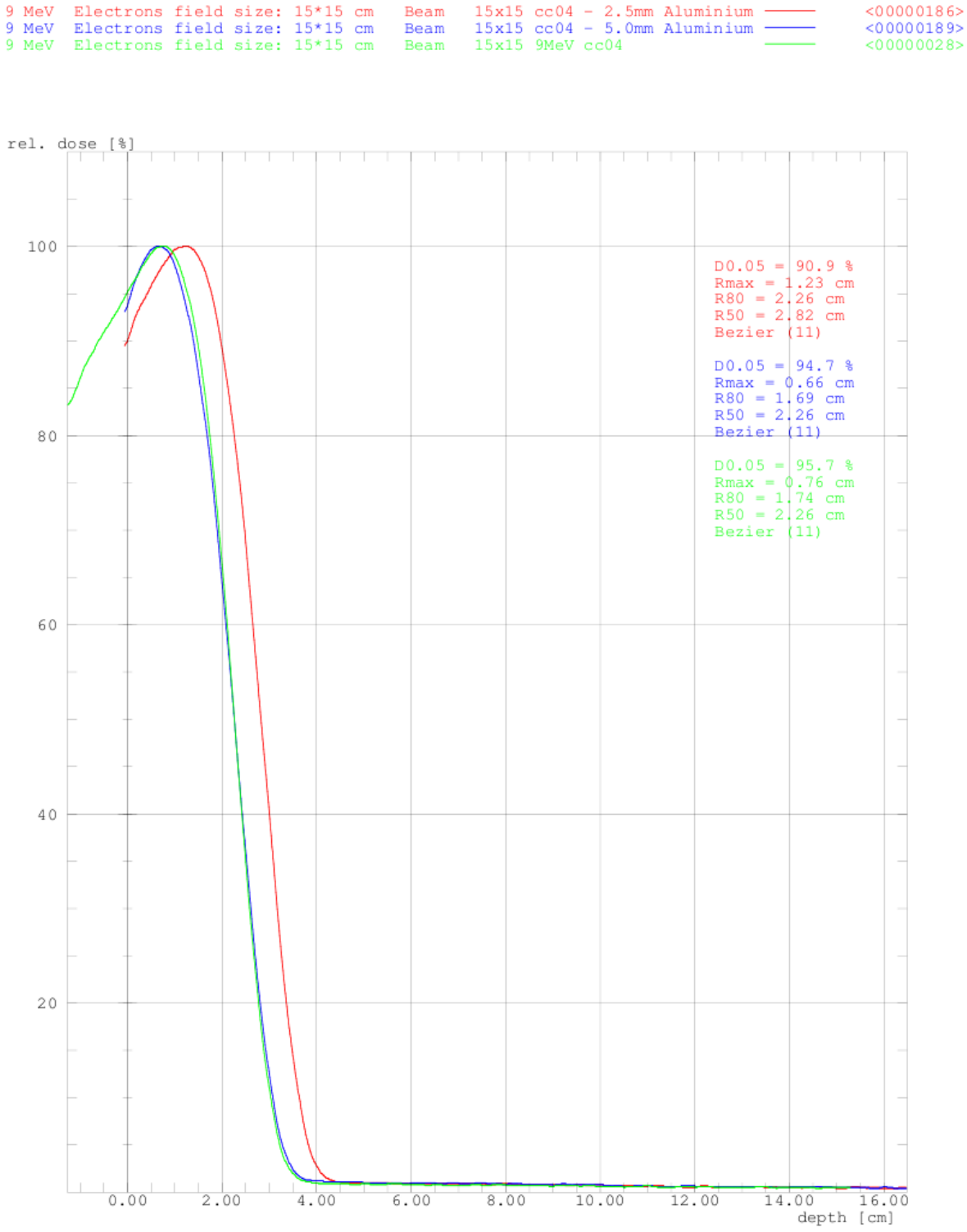

Illustration 134: Full Bolus Aluminium with 9MeV surface shift 1.21cm

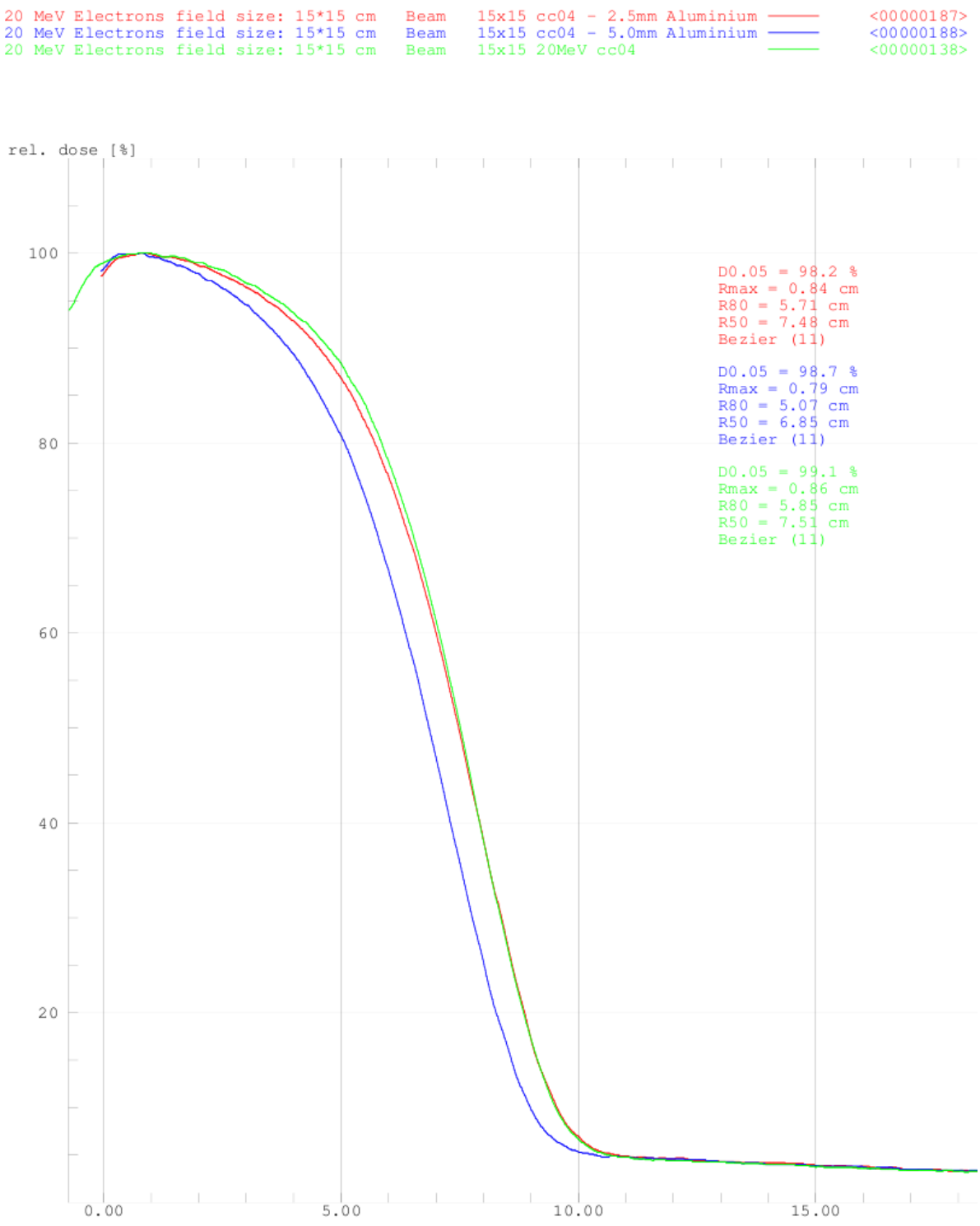

Illustration 135: Full Bolus Aluminium with 20MeV surface shift 0.69cm

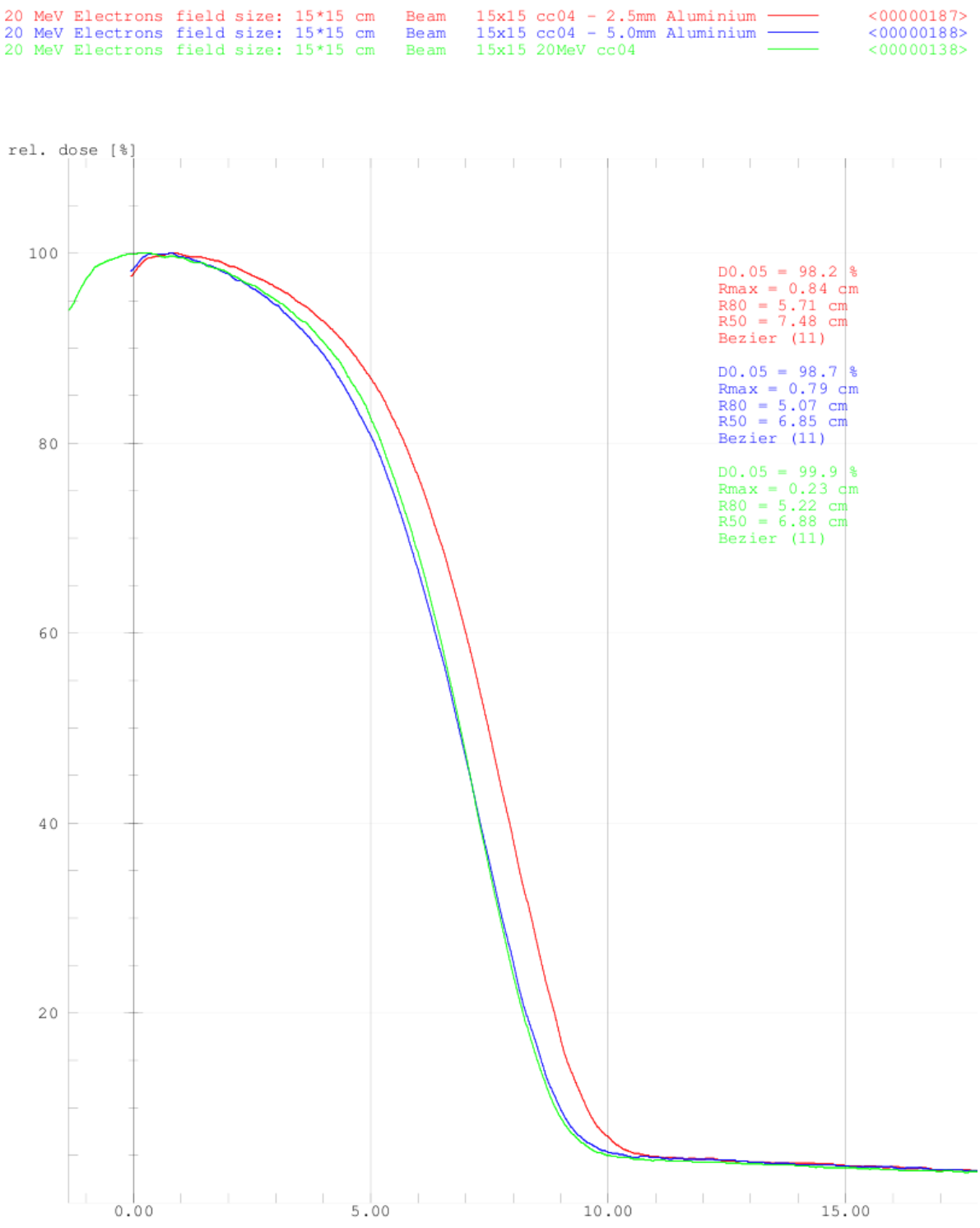

Illustration 136: Full Bolus Aluminium with 20MeV surface shift 1.32cm

Page intentionally left blank